Theoretical and Experimental Investigations of Passive and Ultrasound-Enhanced Transdermal Drug Delivery

by

Joseph Kushner, IV

Submitted to the Department of Chemical Engineering in partial fulfillment of the requirements for the degree of

Doctor of Philosophy in Chemical Engineering

at the

MASSACHUSETTS INSTITUTE OF TECHNOLOGY

September 2006
[Feb'ruary 2007]

Author.....
Department of Chemical Engineering
September 7, 2006

Certified by.....
Daniel Blankschtein
Professor, Thesis Supervisor

.....
Robert Langer
Professor, Thesis Supervisor

Accepted by.....
William Deen
Professor of Chemical Engineering
Chairman, Committee for Graduate Students

Theoretical and Experimental Investigations of Passive and Ultrasound-Enhanced Transdermal Drug Delivery

by

Joseph Kushner, IV

Submitted to the Department of Chemical Engineering on September 7, 2006
in Partial Fulfillment of the Requirements for the Degree of
Doctor of Philosophy in Chemical Engineering

Abstract

In the initial investigation of this thesis, Fick's second law of diffusion was modified to describe both the transient, and the steady-state, transdermal transport of hydrophilic permeants through unbranched, aqueous pore channels. This new transport model, combined with dual radiolabeled diffusion experiments, was then used to separately evaluate how the porosity, the tortuosity, and the hindrance factor of the aqueous pore channels that exist in the skin varied as the extent of skin perturbation due to simultaneous treatment of the skin with low-frequency ultrasound (US) and a chemical enhancer, the surfactant sodium lauryl sulfate (SLS), and as the radius of the hydrophilic permeant delivered across the skin, were increased. This investigation revealed that the values of the hindrance factor and of the tortuosity decreased as the radius of the hydrophilic permeant increased, and that the value of the porosity of the aqueous pore channels increased as the extent of skin perturbation due to the application of US increased. This last result suggested that low-frequency US primarily enhances the transport of hydrophilic permeants by increasing the fraction of the skin surface occupied by the aqueous pore channels.

This modeling approach was next applied to the passive delivery of hydrophobic permeants through the *branched* pathways located in the intercellular lipid bilayer domain of untreated stratum corneum (SC), the outermost layer of the skin. The existence of these branched pathways led to the development of a new theoretical model, the Two-Tortuosity Model, which requires two tortuosity factors to account for: 1) the effective diffusion path length, and 2) the total volume of the branched, intercellular transport pathways, both of which may be evaluated from known values of the SC structure. After validating the Two-Tortuosity model with simulated SC diffusion experiments in FEMLAB (a finite element software package), the vehicle-bilayer partition coefficient, K_b, and the lipid bilayer diffusion coefficient, D_b, in untreated human SC were evaluated using this new model for two hydrophobic permeants, naphthol ($K_b = 233 \pm 44$, $D_b = 1.6*10^{-7} \pm 0.3*10^{-7}$ cm^2/s) and testosterone ($K_b = 100 \pm 14$, $D_b = 1.8*10^{-8} \pm 0.2*10^{-8}$ cm^2/s). This investigation demonstrated that the new proposed method to evaluate K_b and D_b is more direct than previous methods, in which SC permeation experiments were combined with octanol-water partition experiments, or with SC solute release experiments, to evaluate K_b and D_b.

Previous studies on ultrasound-mediated transdermal drug delivery had hypothesized that the discrete regions which form on the surface of skin treated with low-frequency US in the

presence of a colored permeant are regions of high permeability. To test this hypothesis, full-thickness pig skin was treated simultaneously with low-frequency US and SLS in the presence of a hydrophilic fluorescent permeant, sulforhodamine B (SRB), which was used to observe the location of the hypothesized localized transport regions (LTRs) and of the surrounding regions of US-treated skin (the non-LTRs). After US-pretreatment, diffusion masking experiments, a novel experimental method in which hydrophobic vacuum grease was selectively applied to the skin surface, demonstrated that the permeability of calcein, another hydrophilic fluorescent permeant, in the LTRs was ~80-fold greater than in the non-LTRs. Furthermore, measurements of the skin electrical resistivity in both the LTRs and the non-LTRs revealed significant decreases relative to the skin electrical resistivity in untreated skin (~5000-fold and ~170-fold, respectively), suggesting that two levels of significant structural perturbation exist in skin treated simultaneously with ultrasound and SLS. Finally, an analysis of the porosity-to-tortuosity ratio values suggested that transcellular transdermal transport pathways exist within the LTRs.

To confirm the results of the previous investigation, the transdermal delivery of SRB and of rhodamine B hexyl ester (RBHE), a fluorescent hydrophobic permeant, in skin treated with low-frequency ultrasound (US) and/or a chemical enhancer (SLS) relative to untreated skin (the control) was analyzed with dual-channel two-photon microscopy (TPM). An analysis of the average fluorescence intensity profiles as a function of skin depth, obtained from the TPM images, revealed that SRB and RBHE penetrated beyond the stratum corneum and into the viable epidermis only in the LTRs of US-treated and of US/SLS-treated skin. Further analysis of the average fluorescence intensity profiles and of the enhancements in the vehicle-skin partition coefficient, the intensity gradient, and the effective diffusion path length confirmed that a chemical enhancer was required in the coupling medium during US-treatment to obtain two significant levels of increased penetration of SRB and RBHE into the skin. Finally, by comparing the heights and the widths of the fluorescence intensity peaks obtained from the dual-channel TPM images, the existence of transcellular pathways was confirmed in the LTRs of US-treated and of US/SLS-treated skin for SRB and RBHE, as well as in SLS-treated skin for SRB.

In the final investigation of this thesis, the differences in the hindrance factor, the porosity, and the tortuosity of the aqueous pore channels located in the LTRs and in the non-LTRs were evaluated for the delivery of four hydrophilic permeants (urea, mannitol, raffinose, and inulin) using the transport model developed in the initial investigation of this thesis combined with dual radiolabeled diffusion masking experiments. In this analysis, three different idealized cases were examined. In the first case, where the porosity and the tortuosity were assumed to be independent of the permeant radius, the hindrance factor, and, therefore, the average pore radius, was found to be statistically larger in the LTRs than in the non-LTRs. In the second case, where a distribution of pore radii was assumed to exist in the skin, no meaningful results could be obtained due to the large variation in the shape of the distribution of pore radii used in the analysis. In the final case, where infinitely large aqueous pores were assumed to exist in the skin, the value of the porosity of the LTRs was found to be 3- to 8-fold larger than that of the non-LTRs, while there little difference was found in the values of the tortuosity of the LTRs and of the non-LTRs.

Thesis Advisor: Daniel Blankschtein
Title: Professor of Chemical Engineering

Thesis Advisor: Robert Langer
Title: Institute Professor

Acknowledgements

The completion of this thesis would not have been possible without the assistance of many individuals that I am grateful to have worked with over the course of my thesis studies. At the top of this list are my thesis advisors, Bob Langer and Daniel Blankschtein, who served as excellent guides on my Ph.D. journey and provided an immeasurable source of ideas and feedback on my contributions to the transdermal project. I also owe thanks to the other members of my thesis committee, Bill Deen from MIT and Barbara Gilchrest from Boston University, who provided me support and guidance in their respective areas of expertise. Thanks to Hua Tang, whose mentoring during my first year was an invaluable component of getting me started on the right path to a successful thesis. Many thanks as well to the other past and present members of the Blankschtein and Langer Labs who helped in providing a stimulating work environment. Also, a special thanks to Daekeun Kim and Peter So for their collaboration on the microscopy studies, without which that project could not have been successfully completed. Finally, thanks to the National Institute of Health and to the Institute of Soldier Nanotechnologies for providing financial support of my thesis research.

All of the work and stress that comes with completing a Ph.D. thesis would be impossible to manage without the company of a good group of friends to trade research–related trials and tribulations as well as the happier moments of life. To Kristin, Heather, Nick, Roger, Mary Beth, Marianne, Jason (Karlaj), Jason (Chopster), Greg and the rest of my friends in the ChemE department, for providing the laughter to make the daily grind a little easier to endure. To Mike, Lori, Ashley, Shawn, Liz, Kate, Brian and the Tech Catholic Community, for providing a community to deepen my faith over these many

years. To the Hampshire Street Poker Club and the Boston Poker Tour, for providing hours upon hours of entertainment and a few extra dollars in my pocket. To Adam, Suzanne, and John Paul, for being wonderful housemates and dear friends.

Finally, these acknowledgements would not be complete without honoring those most dear to me, my family, both immediate and extended. To my parents, Pat and Joe, and to my brother and sisters, Michael, Maria, Ann, and Barbara, for their constant love and support during these many years. To my in-laws, Rick and Gail and their children Christina, Carolyn, and Matthew, for taking in a home-sick boy from Arizona and welcoming me into their family. To my grandparents and the rest of my extended family, for always being there to lend a hand when it was needed. And, saving the best for last, to the two special ladies in my life. To my daughter, Veronica, whose love for her "daddy-man" carried me through the final months of this thesis, thank you for all of your smiles and giggles. To my wife, Jennifer, who has given me so much love and support during the last five years, there are no words sufficient to thank you for all that you have done for me and for our family. This thesis is dedicated to them.

Table of Contents

List of Figures

List of Tables

Chapter 1

Introduction

1.1 Overview of Transdermal Drug Delivery

1.1.1 Historical Development and Current Status of Transdermal Drug Delivery (TDD) in Industry

Transdermal Drug Delivery (TDD) is the process in which drugs are administered to a patient through the skin, either for topical or systemic application. In recent years, TDD has become a viable alternative to traditional methods of drug administration, including injections and oral delivery. Since the approval of the first transdermal patch in 1981 to prevent the nausea and vomiting associated with motion sickness, the FDA has approved more than 35 transdermal patch products for 13 drug molecules.[1] The US transdermal market approached $1.2 billion in 2001 and was based on 11 drug molecules (see Table 1-1): fentanyl, nitroglycerin, estradiol, ethinyl estradiol, norethindrone acetate, testosterone, clonidine, nicotine, lidocaine, prilocaine, and scopolamine.[1] Figure 1-1 gives a breakdown of the contribution of each drug to the global TDD market, which was valued at $2.4 billion in sales in 2001. During the time that this thesis was completed, two additional transdermal patch products containing norelgestromin and oxybutynin

have been made available by the FDA for clinical use. [1] Additionally, the global TDD market has grown remarkably in the last few years. In 2005, the value of the market was estimated at $12.4 billion, and it is projected to increase to $21.5 billion in 2010 and to $31.5 billion in 2015.[2] Approximately 90 companies are currently active in developing transdermal technologies.[2]

Table 1-1: Drugs Currently Delivered for Therapeutic Applications Using Transdermal Methods.[3,4]

Drug Name	Molecular Weight	Log $K_{O/W}$	Uses
Estradiol	272.4	3.86	hormone replacement
Testosterone	288.4	3.31	hormone replacement
Fentanyl	336.5	4.37	pain management
Lidocaine	234.3	2.48	local anesthetic
Scopolamine	303.4	1.24	motion sickness
Nicotine	162.2	1.17	smoking cessation
Nitroglycerin	227.4	1.62	vasodilation
Ethynil Estradiol	296.0	3.73	hormone replacement
Clonidine	230.9	2.27	antihypertensive
Prilocaine	220.3	2.42	local anesthetic
Oxybutin	357.4	4.68	bladder control

1.1.2 Advantages of TDD over Conventional Methods of Drug Delivery

Some of the advantages of TDD over traditional methods of drug delivery which account for the growing interest of pharmaceutical companies and clinicians in TDD include: 1) avoiding first-pass metabolism effects in the harsh environment of the gastrointestinal

(GI) tract, which pose a limitation for oral delivery, 2) offering a painless alternative to injections, 3) enabling controlled release of the drug for both systemic and topical delivery, and 4) increased patient compliance with drug dosing schedules – a patient can apply a single drug-containing patch to the skin to have drug delivery occur over an extended period of time (hours, days, weeks, etc.), thus eliminating the need to administer repeated injections or take oral medications. However, despite these advantages, the use of TDD as an alternative to traditional methods of drug delivery has been limited thus far to low molecular weight (<400 Da) hydrophobic drugs (log $K_{o/w}$ >1), as shown in Table 1-1, due to the barrier properties of the skin.

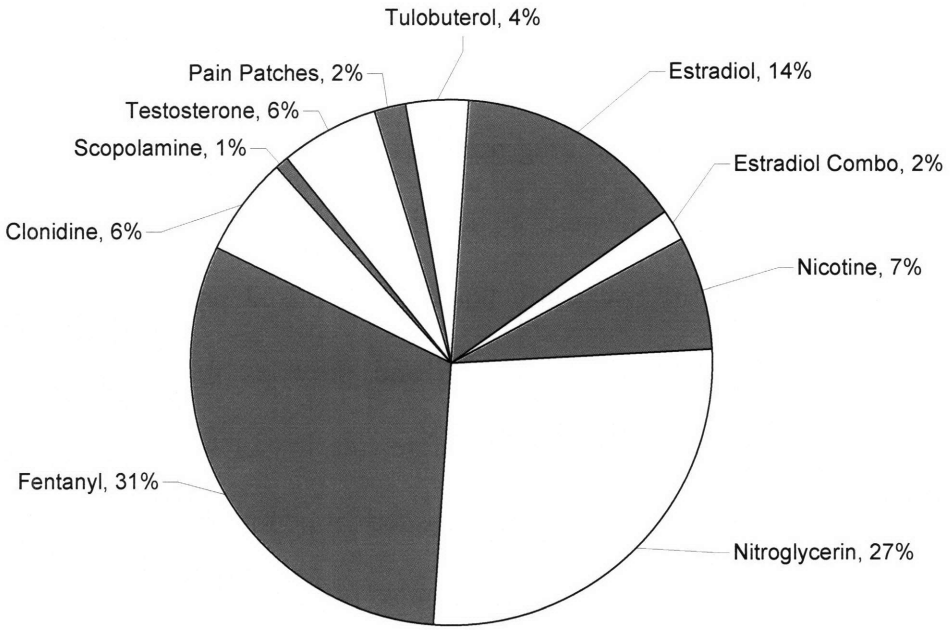

Figure 1-1: Breakdown of Global TDD market circa 2001. The total market value is estimated to be $2.4 billion. [1]

1.1.3 Impact of the Structure of the Skin on TDD

The barrier properties of the skin can be understood by examining the structure of the skin. The skin is composed of three primary layers – the stratum corneum, the viable epidermis, and the dermis (see Figure 1-2). The stratum corneum is the thinnest layer of the skin having a thickness of 10-20 μm in humans, while the viable epidermis and the dermis have thickness of 100-200 μm and 1-4 mm, respectively.[5] Even though it is the thinnest layer, the stratum corneum functions as the primary barrier to TDD. The stratum corneum consists of corneocytes, which are thin, polyhedral-shaped, dead cells filled with cross-linked keratin fibers, and a matrix of lipid lamellar bilayers, which together are arranged in a brick-and-mortar structure (see Figure 1-3). This tightly packed brick-and-mortar structure of corneocytes and highly-ordered lipid bilayers is the main source of the resistance to transdermal diffusion in the stratum corneum. The corneocytes are considered to be impermeable to drug transport due to the extensive amount of keratin cross-linking within the corneocytes.[5] In addition, a thin (15 nm) cornified cell envelope, composed of a mixture of covalently bound cross-linked protein filaments and lipid molecules, surrounds the corneocyte cells and provides further resistance to drug diffusion into the corneocyte cells.[5] Therefore, the intercellular lipid lamellar bilayer domain is widely believed to the primary transdermal permeation pathway under passive transport conditions.[6-8] The stratum corneum also presents an additional barrier function for hydrophilic molecules due the hydrophobic nature of the intercellular lipid lamellar bilayer domain. This characteristic property makes it difficult for hydrophilic molecules to partition into the intercellular regions of the stratum corneum.

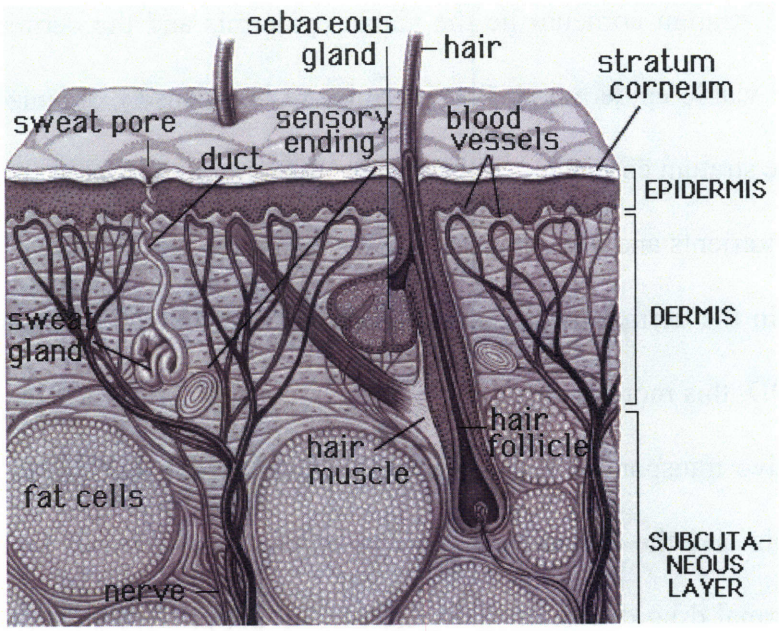

Figure 1-2: Sketch of the cross-section of the skin.

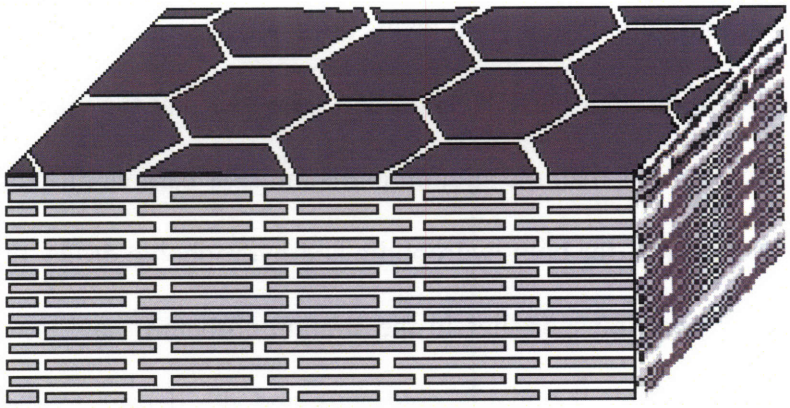

Figure 1-3: Schematic representation of the brick-and-mortar model of the Stratum Corneum (SC). Corneocytes (depicted in gray) are shown with their characteristic hexagonal shape and are contained within the lamellar lipid bilayers (depicted in white). In humans, the thickness of the SC ranges from 10 – 20 μm, and typically consists of 15 interlocking layers of corneocytes.

Beneath the stratum corneum lie the viable epidermis and the dermis layers of the skin. Both the viable epidermis and the dermis are less densely organized skin layers, compared to the stratum corneum.[5] This structural feature of the viable epidermis and the dermis allows nutrients and waste products to be easily transported via diffusion between the capillaries in the dermal layer and the living cells of the viable epidermis. For the purposes of TDD, this more open structure of the viable epidermis and the dermis allows for easy diffusive transport of both hydrophilic and hydrophobic drugs. As such, the viable epidermis and the dermis are not considered to be the rate-limiting layers in passive transdermal drug diffusion, and therefore, do not provide any resistance to drug transport. Additionally, the physicochemical properties of the viable epidermis and the dermis differ from those of the stratum corneum. The viable epidermis and the dermis have been shown to be more hydrophilic as compared to the stratum corneum. However, the increased hydrophilicity of these two layers does not significantly hinder the transport of hydrophobic drugs through these layers, due to the fact that the viable epidermis and the dermis are more porous than the stratum corneum. For passive diffusion through the skin, it is widely accepted, for both hydrophilic and hydrophobic drugs, that the primary resistance to transdermal transport lies in the stratum corneum,[9] and, once this layer is traversed, diffusion through the viable epidermis and the dermis to the capillaries is comparatively easy. Therefore, to increase the permeability of the skin to allow delivery of hydrophilic and hydrophobic drugs at therapeutic levels, it is necessary to either: 1) find a drug transport route which bypasses the stratum corneum, or 2) perturb the structure of the stratum corneum to reduce the resistance of the stratum corneum to transdermal transport.

As Figure 1-2 shows, there are other structures in the skin - hair follicles, sweat glands, and sebaceous glands – which may be used to bypass the stratum corneum and to deliver drugs directly into the viable epidermis and dermis layers of the skin. Sebaceous glands are found within hair follicles and have a skin surface density of 57-100 sites per cm^2 of the skin.[5] Their combined skin surface area fraction is approximately $1/1000^{th}$ of the skin surface.[5] Sweat glands are present in the skin in greater density, approximately 100-200 sites per cm^2 of the skin.[5] However, sweat glands only take up $1/10{,}000^{th}$ of the skin surface area.[5] From the work of Johnson *et al.*,[3] the permeable, intercellular regions of the stratum corneum occupy approximately $1/500^{th}$ of the skin surface area, a similar order-of-magnitude to the surface fraction of the skin occupied by hair follicles and sebaceous glands.[5] Therefore, the intercellular route and the follicular route may both be significant for passive transdermal transport in native skin samples. Since only a small fraction of the skin surface is taken up by each delivery route, an impractically large amount of skin area would be required to deliver a therapeutic dose of a desired drug using transdermal methods.

1.1.4 Current Methods for Reducing the Barrier Properties of the Skin to Improve TDD

Since the two possible routes of transdermal delivery discussed in Section 1.1.3 occupy such a small fraction of the skin surface area, transdermal delivery rates could be increased several hundred fold if it were possible to perturb the stratum corneum to utilize a larger fraction of the skin surface area for transdermal drug transport. Increasing transdermal delivery rates is the motivation behind research in methods to enhance

transdermal drug delivery. Therefore, to deliver such compounds at therapeutic levels, several methods have been developed to make the skin more permeable to drug transport – (i) electroporation,[10-15] (ii) iontophoresis,[16-22] (iii) chemical enhancers,[23-27] (iv) sonophoresis,[27-33] (v) microneedles,[34-36] and (vi) laser-ablation.[37]

Each of the above methods attempts to either alter or bypass the highly-organized structure of the stratum corneum, or to provide an additional driving force to increase transdermal delivery rates. Electroporation increases drug transport across the skin through the creation of temporary aqueous pores in the stratum corneum formed by the application of pulsed electric voltages.[10-15] Iontophoresis enhances drug transport by means of electrophoresis, in which polar and charged molecules are pushed through the skin by the applied electric field, or to produce enhanced diffusion.[16-22] Chemical enhancers utilize several mechanisms by which drug transport is enhanced. These mechanisms include: (i) enhancing drug solubility in the donor solution,[23] (ii) modifying the partitioning of the drug between the donor solution and the SC,[24] and (iii) disrupting the lipid lamellar bilayers and connective proteins that make the SC a tight barrier to drug transport.[25] Microneedles offer a painless alternative to traditional injections.[34-36] In this technique, very small, short needles are pressed into the skin surface.[34-36] The needles are designed such that they only penetrate into the viable epidermis or the dermis, effectively bypassing the stratum corneum, and resulting in no pain for the patient.[34-36] Delivery methods with this technique include: 1) the desired drug can be loaded into the microneedle prior to insertion into the skin, 2) the drug can be coated on the microneedle surface, and 3) the drug can be injected into the skin, through the microneedle, once it has

been inserted into the skin. In laser-ablation methods, the stratum corneum is physically removed from the desired skin delivery site, thus enabling enhanced delivery methods.[37] Sonophoresis, the transdermal enhancement technique that is the focus of this thesis, uses ultrasound to enhance transdermal drug transport. Ultrasound (US) corresponds to any sound wave with a frequency higher than 20 kHz. The ultrasound wave can be characterized by the frequency and the amplitude of the sound wave oscillations. Figure 1-4 presents a sketch of the typical experimental setup used for the application of ultrasound on the skin. The ultrasound is generated by passing an electrical AC signal, from a signal generator, through a piezo-electric crystal (e.g. the transducer) at the desired frequency and amplitude. As shown in Figure 1-4, a coupling medium in the donor chamber is required to transmit the ultrasound wave from the transducer to the skin. Without an appropriate coupling medium (i.e. a material with an acoustic impedance similar to that of the skin), the ultrasound wave will be reflected off the skin surface rather than being able to penetrate into the skin, thus minimizing the effectiveness of the ultrasound on the skin. Previous studies (see Section 1.2) have demonstrated that sonophoresis enhances drug transport primarily by inducing acoustic cavitation bubble formation, both in the skin and in the coupling medium.[32] Implosion of the acoustic cavitation bubbles in, and near, the skin surface leads to the onset of violent shockwaves that can disrupt the tight structure of the SC. When these implosions occur near the skin surface, microjets are formed and are directed toward the skin surface, which drives the drug solution into the disrupted SC.[32] Additionally, operation of ultrasound in the coupling medium can create acoustic streaming of the coupling medium fluid.[32] If a

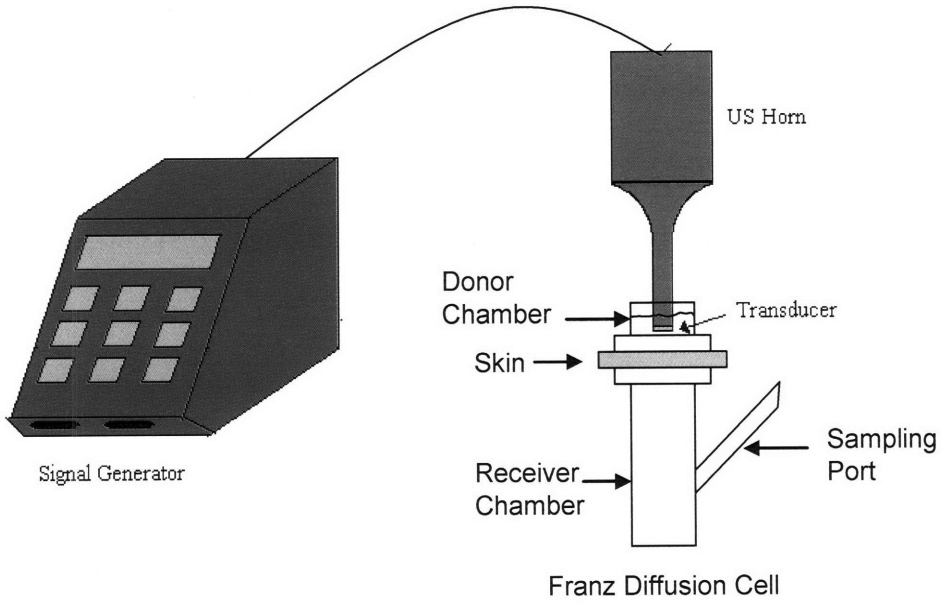

Figure 1-4: Schematic representation of the typical experimental setup used in sonophoresis. The signal generator is programmable, allowing different duty cycles and intensities to be selected. The signal from the generator is amplified before it is transferred to the transducer through the US horn. The transducer in this setup is screwed into the tip of the horn, and can be replaced as needed to ensure proper function.

drug is included in the coupling medium during sonophoresis, the acoustic streaming can also contribute to enhanced delivery of the drug into the skin.[32]

Currently, the preferred method of sonophoresis in transdermal drug delivery involves pre-treating the skin with ultrasound to perturb the structure of the stratum corneum followed by passive delivery of the desired drug from a patch through the ultrasound pre-treated skin site. In all the above enhancement techniques, the skin is not exposed to the external environment, both during application of the enhancing technique

and during delivery of the desired drug, to prevent the possibility of infectious agents entering into the skin through the weakened skin sites. Each of these enhancement techniques has yielded successful results in increasing the skin permeability in order to facilitate drug transport. Additionally, combinations of these enhancement methods have been attempted with some synergistic effects observed, resulting in even greater enhancements of TDD.[24, 28, 38-40]

1.2 Literature Review

In this section, I review the previous work conducted on the ultrasound TDD project by two former students in our group – Samir Mitragotri and Hua Tang. Additionally, I will also include a brief review of published work that is relevant to the experimental and the theoretical work that I undertook for my thesis. In my discussions of the previous work, both done by our group and discussed in the literature, I will highlight the issues that remain unresolved which impact our understanding of ultrasound-mediated transdermal drug delivery.

1.2.1 Ph.D. Thesis of Samir Mitragotri

Mitragotri began his thesis studies by conducting a mechanistic investigation of sonophoresis to determine which of several ultrasound-related phenomena (cavitation, thermal effects, convective velocities, and mechanical effects) were responsible for the observed transport enhancements of drugs delivered across ultrasound-exposed skin.[41] These studies were carried out in the high frequency (1-3 MHz) ultrasound region, also referred to as the therapeutic region, which is typically used for ultrasound imaging and

dental care, as well as over a range of intensities from 0-2 W/cm^2.[41] The findings from his experimental analysis indicated that *cavitation taking place in the SC appears to be the dominant phenomenon contributing to ultrasound enhancement of TDD*, through the action of cavitation bubbles disordering the lipid bilayers in the stratum corneum.[41] Additional theoretical studies further indicated that the observed enhancement factor depended mostly on the passive permeant diffusion coefficient.[41]

Having concluded that cavitation events within the keratinocytes of the stratum corneum were the primary enhancement mechanism, Mitragotri examined low-frequency sonophoresis studies in an effort to increase the enhancement factors that exposure of the skin to ultrasound could provide.[41] The rationale for conducting studies in the low-frequency range (20 kHz) was that cavitation events vary inversely with acoustic frequency.[41] Accordingly, cavitation events are more likely to occur at lower ultrasonic frequencies, resulting in increased cavitation and greater enhancements in transdermal drug permeabilities.[41] *In vitro* studies using a variety of permeants showed enhancements in the range of 3-fold to 5000-fold in the permeability of a drug when compared to its passive permeability.[41] *In vivo* studies showed enhancements in drug permeability of near 300-fold for salicylic acid in hairless rats.[41] Since the increase in cavitation events that lead to an increase in transdermal drug permeability also lead to an increase in disordering of the stratum corneum, histological and safety tests were conducted to determine if low-frequency ultrasound exposure was safe for the skin.[41] These tests showed that no long-term damage was produced in the stratum corneum or in the underlying tissue at the conditions used for the low-frequency ultrasound experiments (20 kHz, 125 mW/cm^2, 100 msec pulses applied every second).[41]

Following the results of the high-frequency studies, Mitragotri proposed that, at low frequency, enhancement occurs as a result of cavitation disrupting the lipid bilayers of the stratum corneum.[41] Additionally, he proposed that aqueous channels, which can further facilitate the transport of hydrophilic permeants across the hydrophobic stratum corneum, may form within the lipid bilayers from water supplied by the keratinocytes.[41] Finally, Mitragotri illustrated the potential utility of sonophoresis in TDD by conducting experiments for the transdermal delivery of proteins and other high molecular weight permeants.[41] These experiments showed that low-frequency sonophoresis was able to enhance the transport of these large, hydrophilic permeants by several orders of magnitude.[41]

1.2.2 Ph.D. Thesis of Hua Tang

Tang continued the work on the ultrasound TDD project identifying four major areas of the project that required further study after the completion of Mitragotri's work: (1) justifying the selection of various *in vitro* skin membrane models for low-frequency sonophoresis studies, (2) determining the primary mechanisms of ultrasound enhancement at low-frequency conditions, specifically focusing on characterizing the role of cavitation, (3) developing a model to predict sonophoresis effects for hydrophilic permeants from knowledge of the ultrasound parameters and the physicochemical properties of the permeants, and (4) studying the effects of LFS on living skin samples.[42]

In her studies of the correlation between *in vivo* and various *in vitro* skin models, Tang discovered that *in vivo* and *in vitro* skin models react to low-frequency sonophoresis at different rates.[42] Because of this important finding, no correlation was

observed between the *in vivo* and the *in vitro* (full-thickness skin, split-thickness skin, and heat-stripped skin) skin models at equivalent ultrasound energy doses.[42] However, when skin electrical resistance was used instead of the ultrasound energy dose as the comparative factor, a correlation was observed between the permeability values obtained from the *in vivo* and the different *in vitro* skin models having the same electrical resistances.[42] This correlation makes it possible to use data from *in vitro* skin models to predict what would occur *in vivo*.[42]

To characterize the role of cavitation in low-frequency sonophoresis, Tang conducted two different sets of permeability experiments.[42] First, using a custom-made high pressure cell, she investigated how the transdermal drug permeability changed as pressure was increased.[42] It is known that increases in pressure reduce cavitation events, and therefore, Tang hypothesized (and observed) that increases in pressure would reduce the transdermal drug permeability due to decreased cavitation in the high-pressure cell.[42] Once cavitation was found to be a key mechanism in low-frequency sonophoresis, the exact location of the cavitation events – inside or outside the skin membrane – needed to be determined.[42] By using a highly viscous coupling medium (castor oil) to suppress cavitation events outside the skin, Tang demonstrated that, for low-frequency sonophoresis, cavitation events occur outside the skin layer.[42] This is fundamentally different from the previous findings of Mitragotri *et al.* using high-frequency sonophoresis,[43] where it was concluded that cavitation takes place inside the skin.[42] Additionally, Tang determined that high-velocity microjets, resulting from the collapse of transient cavitation bubbles in the vicinity of the skin surface, are most responsible for permeabilizing the skin.[42] This key finding is not only fundamentally important, but will

also drive future practical research in low-frequency sonophoresis to identify ways to maximize cavitation activity outside the skin in the vicinity of the skin surface in order to maximize transdermal drug permeabilities.

Two theoretical models were developed by Tang in the course of her thesis work – one for predicting the steady-state transdermal drug permeability from measurements taken during the transient diffusion phase, and the second to characterize the skin porous pathway of hydrophilic permeants, including accounting for the role of convection, during low-frequency sonophoresis. A two-parameter Fickian diffusion model (with constant parameter values) was developed to predict the steady-state transdermal drug permeability from transient diffusion data, and was found to be applicable in the case of hydrophobic permeants.[44] In the case of hydrophilic permeants, although the model did not work quantitatively, it allowed Tang to develop an understanding of hydration effects on the polar pathway that affects the transdermal permeability of hydrophilic compounds. The aqueous pore pathway model was found to be able to predict the rate of drug penetration across the skin, in addition to characterizing the effect of ultrasound on the skin microscopic transport properties (specifically, the effective pore radius in the skin and the ratio of skin porosity to tortuosity).[45]

Finally, Tang conducted *in vivo* experiments using the low-frequency ultrasound protocols and showed, through histological studies, that low-frequency sonophoresis is indeed safe for living tissue.[31]

More recently, Tang uncovered the existence of discrete "red spot" regions in skin treated with low-frequency ultrasound (20 kHz) in the presence of sulforhodamine B (SRB), a red fluorescent dye, as the model permeant while studying the permeation

pathways of this model compound using two-photon microscopy.[42] Based on visual observations of skin samples treated with low-frequency ultrasound in the presence of SRB, it was hypothesized that the observed "red spots" were regions of high transdermal permeability.[42] As a result of this hypothesis, the "red spots" are referred to as localized transport regions (LTRs).[42] *In order to test this hypothesis, I compared the permeability and skin electrical resistance measurements of the LTRs formed during pre-treatment of the skin with low-frequency sonophoresis with the surrounding regions of ultrasound-treated skin.* If these LTRs are indeed regions of high permeability, then it would be possible to further increase transdermal permeation rates if the red spots could be formed uniformly over the entire surface of the ultrasound-treated skin sample.

1.2.3 Effects of Ultrasound and Surfactants on TDD

Mitragotri *et al.* conducted a study of the synergistic effect of low-frequency ultrasound and the surfactant, sodium lauryl sulfate (SLS), on transdermal drug transport.[38] Their findings indicate that addition of SLS into the coupling medium during ultrasound exposure greatly increases the enhancement of transdermal drug delivery when compared to permeability studies without SLS in the coupling medium by two mechanisms: (1) ultrasound drives more SLS into the skin, and (2) ultrasound enhances dispersion of SLS within the skin.[38] While the presence of SLS during ultrasound treatment of the skin increases the perturbation of the skin, it has also been demonstrated by sonochemical oxidation KI to I_2 that the rate of cavitation may be reduced by half when SLS is included in the coupling medium.[46] This observed reduction in cavitation rate in the presence of SLS is countered by an increase in the velocity of the microjet formed after implosion of

a transient cavitation event when a surfactant is present in the coupling medium. For example, it has been found that a four-fold decrease in the surface tension of the coupling medium can result in a 50-fold increase in the velocity of the microjets produced after the transient cavitation bubbles collapse.[47] As stated in the work by Tang, microjet formation seems to be the primary effect of cavitation that leads to increased permeability of the skin.[32] Therefore, even though SLS seems to reduce the rate of cavitation in the coupling medium during ultrasound treatment of the skin, the greater increase in microjet velocity from the collapse of transient cavitation events translates into increased perturbation of skin treated with ultrasound in the presence of a surfactant. In the context of the experimental work conducted in this thesis, the advantage of using SLS in my experiments lies in being able to permeabilize the skin faster, which will allow a larger number of experiments to be conducted in a shorter period of time.

Tezel *et al.* have recently conducted two interesting studies.[29,40] The first study examines the effects of ultrasound frequency on sonophoresis. In this work, some initial observations on how the appearance of localized transport regions (LTRs) varies with frequency were made – a single LTR was observed at 20 kHz while multiple LTRs were observed at ~40 and ~60 kHz, and no LTRs were observed above 60 kHz.[29] Additionally, it was suggested that the optimal frequency for drug delivery is 58.9 kHz.[29] However, this conclusion was based solely on skin electrical resistance measurements and not on actual drug permeability measurements. In addition, given the widely-accepted belief that cavitation is the primary mechanism of transdermal enhancement, this proposed optimum value of ~60 kHz appears to contradict cavitation as the sole enhancing mechanism, since cavitation is inversely proportional to ultrasound frequency,

and it would be expected therefore that the optimal frequency would occur at ~20 kHz. *Therefore, there is a need for further investigation into the mechanisms responsible for ultrasound enhancement of transdermal drug delivery.*

The second study involves a fundamental analysis of the synergistic effect of ultrasound and surfactants on transdermal drug delivery. In this study, it was discovered that 12-carbon tail surfactants are most disruptive to the skin passively, while 14-carbon tail surfactants are most disruptive to the skin in the presence of ultrasound.[40] Furthermore, charged surfactants appear to have a greater enhancing effect than neutral surfactants.[40] Additional studies were also conducted using surfactant mixtures which resulted in varied results.[40] Mixtures of surfactants provide a possible means to increase transdermal drug permeability enhancements, as it has been shown that surfactant mixtures can interact synergistically to reduce the surface tension of the mixed surfactant solution to values which are lower than those of the pure surfactant solutions at equivalent surfactant concentrations.[48] The surface tension lowering using surfactant mixtures would increase microjet velocity, and thereby potentially increase the drug permeability enhancements, while reducing the exposure of the skin to irritating surfactants. Additionally, lowering the surface tension should also reduce the cavitation threshold, making it easier for cavitation events to occur.[38]

1.2.4 Safety of Sonophoresis

In determining the safety of low-frequency sonophoresis, Boucaud *et al.* have conducted some interesting work exploring the safety threshold in freshly excised human skin samples. Their findings, applicable to ultrasound at 20 kHz only, indicate the existence

of an intensity maximum of 2.5 W/cm^2 under pulsed or continuous ultrasound operation, before skin damage occurs.[49] Other safety analyses[50,51] have shown that damage occurs in *in vivo* hairless rat and mice skin at lower ultrasound intensities (1.0 W/cm^2), indicating that these would not be good models for human skin. This further justifies the selection of pig and human skin as acceptable models for use in the experiments conducted in this thesis.

1.2.5 Visualization of Transdermal Permeation Pathways

Several researchers have conducted studies to determine the pathways followed by permeants to traverse the SC and other skin layers, for both passive and ultrasound-enhanced drug delivery. Based on work conducted on passive permeation, it was concluded that permeation of polar molecules through the skin occurs via the intercellular route, specifically through pathways lined with lipid molecules containing polar head groups.[6-8] The pore radius of these pathways has been estimated to be on the order of 1 nm.[8,52] In addition to elucidating the likely pathway for polar permeant transport under passive conditions, the work of these groups has also clarified the structure of the lipid bilayers of the stratum corneum and outlined several useful techniques, including chemical staining and a host of electron microscopy methods, for visualizing the permeation pathways within the skin.[6-8] There is also evidence that the intercellular permeation pathway exists when ultrasound is applied to the skin.[53-55] Menon and Elias found that, at high frequency, ultrasound acts to connect segregated lacunar domains within the skin, creating a temporary network of channels which both polar and nonpolar permeants may use to traverse the skin barrier.[54] However, all the ultrasound permeation

pathway visualization studies in the literature have been conducted at high frequency (MHz range). Since the focus of this thesis is on the low-frequency range of ultrasound, it will be necessary to evaluate the types of transdermal pathways present in skin treated with low-frequency ultrasound.

A relatively new technique, two-photon microscopy, shows excellent promise as a new method not only for determining permeation pathways, but also for determining enhancement factors. Recent work by Yu *et al.* has demonstrated the value of this technique in investigating the *in vitro* permeation of both hydrophobic and hydrophilic permeants in the presence of a chemical enhancer (oleic acid).[56] Using two-photon microscopy, it is possible to visualize the concentration of the permeant throughout the skin sample in 3 dimensions. This makes it possible to determine the exact location of the permeants throughout the skin sample. This technique, which has yet to be extensively applied to low-frequency sonophoresis, would allow visualization of the differences in the permeation pathways of the LTRs and the unenhanced regions of an ultrasound-treated skin sample (the non-LTRs). Additionally, valuable quantitative information on the enhancements of the probe diffusion path length through the skin, the probe diffusion coefficient, and the probe vehicle-to-skin partition coefficient can be obtained from an analysis of the TPM data. *The permeation pathway and enhancement information obtained from TPM imaging of the LTRs and the non-LTRs would be useful in furthering our understanding of the mechanisms of formation of these regions in ultrasound-treated skin.*

1.2.6 Fundamental Modeling of Transdermal Transport

Most of the modeling work conducted on predicting transdermal drug permeability of hydrophobic and hydrophilic permeants is applicable only to passive delivery conditions. For hydrophobic permeants, several empirical models,[57-61] whose important parameters are the molecular weight and the octanol-water partition coefficient of the permeant, were tested for accuracy by Wilschut *et al.* in 1995, and it was found that the revised Robinson model was most accurate for *in vitro* permeation experiments with human skin samples.[62] Recently, Mitragotri has developed a predictive model for determining the permeability of small hydrophobic solutes (MW<500) across the stratum corneum using Scaled-Particle Theory,[63] which relates the work required to create cavities in the lipid bilayers to the lipid density, the lipid order parameters, and the solute radius.[64] Other researchers have attempted to use the structural parameters of the stratum corneum to model transdermal delivery through the hydrophobic intercellular regions of the SC.[3, 65-69] However, there has been some difficulty in developing a first-principles model of hydrophobic (intercellular) transport through the stratum corneum. The primary difficulty has been in obtaining agreement in the values of the steady-state permeability and the diffusion lag time to steady-state.[3] *In order to improve our understanding of intercellular transport in the stratum corneum, it will be necessary to develop an improved model for transdermal transport in the intercellular regions of the stratum corneum which will successfully predict both steady-state permeability values and the diffusion lag time to steady-state.* By applying this improved model of intercellular transport in the stratum corneum to ultrasound-treated skin samples, it will be possible to better understand the role of intercellular diffusion in ultrasound-treated skin samples.

For hydrophilic permeants, the aqueous pore pathway model is the primary theoretical model used to describe hydrophilic transdermal transport. This model has been used to describe hydrophilic transdermal transport in untreated skin samples, as well as in skin samples perturbed by ultrasound,[46,70] chemical enhancers,[71,72] and iontophoresis.[73] A key feature of the model is the inclusion of the aqueous pore radius in the model equations. With this feature, hydrophilic permeability data can be analyzed to determine the size of the aqueous pores in the skin, thereby allowing comparisons between untreated skin and enhanced (by sonophoresis or other methods) skin. Such comparisons can shed light on the mechanisms of transdermal enhancement of hydrophilic permeant delivery. Specifically, it is possible to determine whether the aqueous pores in the skin increase in size as the skin is enhanced, or if more aqueous pores of the same size are generated by the enhancing method used on the skin. *For the case of LTR formation in ultrasound-treated skin, interpreting permeability data from the LTRs and the non-LTRs with the porous pathway would make it possible to determine the mechanism of how the skin is enhanced by ultrasound in these regions of ultrasound-treated skin.*

However, there is currently some debate in the literature on the proper application of the aqueous pore pathway, specifically on how to characterize the aqueous pore sizes in the skin. There are currently two methods for characterizing the aqueous pores in the skin. The first, used by Peck *et al.*[72] and Tang *et al.*,[45] assumes that the aqueous pores in the skin can be described sufficiently by a single, average aqueous pore radius. The value of the average aqueous pore radius is a structural property of the skin and is independent of the size of the permeant delivered through the skin. The second, used by

Tezel *et* al.,[70] assumes that there is a distribution of aqueous pore sizes in the skin. In this case, the average aqueous pore radius increases as the size of the permeant increases (and vice versa), since smaller permeants can access a larger fraction of the total aqueous pore distribution relative to larger permeants. While there is experimental data to suggest that a distribution of aqueous pores may be a more accurate representation of the aqueous pore pathways in the skin, some other assumptions in the model of Tezel *et al.* on the behavior of the porosity and the tortuosity of the aqueous pore pathways as the skin is treated with ultrasound need to be verified. *Therefore, before applying the aqueous pore pathway to the LTRs and the non-LTRs of ultrasound-treated skin, it is first necessary to re-examine the assumptions and analysis techniques of the aqueous pore pathway hypothesis to determine how best to characterize the porosity, the tortuosity, and the size distribution of the aqueous pores in both untreated and ultrasound-treated skin.*

1.3 Thesis Objectives

This thesis will address three major issues that remain unresolved, based on the review of the available TDD literature presented in Section 1.2, that are relevant to furthering our mechanistic understanding of ultrasound-mediated TDD.

The first issue investigates in further detail the use of the porous pathway hypothesis to understand the mechanisms by which ultrasound enhances the transdermal transport of hydrophilic drugs. Specifically, the goals of these studies are: 1) to determine if the porous pathway hypothesis is a valid model for interpreting experimental data for the transdermal delivery of hydrophilic drugs over a wide range of drug molecular weights, and 2) to use the porous pathway hypothesis, if it is indeed valid, to

examine how ultrasound alters the skin structure, resulting in the well-documented enhancement of hydrophilic drug transdermal transport in ultrasound-treated skin samples.

The second issue focuses on the fundamental modeling of drug transport through the intercellular regions of the stratum corneum. Since the intercellular regions of the stratum corneum are hydrophobic in nature due to the presence of the lipid lamellar bilayers, this particular transdermal modeling investigation is primarily applicable to hydrophobic drugs. However, it has been demonstrated that the corneocyte cells of untreated stratum corneum are essentially impermeable to both hydrophobic and hydrophilic drugs due the presence of the cornified envelope which surrounds the corneocyte cells.[5] Therefore, it has been hypothesized, and subsequently demonstrated, that hydrophilic molecules also utilize the intercellular transport pathway in untreated stratum corneum.[6-8] For hydrophilic permeants delivered in ultrasound-treated skin, it has been hypothesized that transcellular pathways may be present in the stratum corneum as a result of treatment of the skin with ultrasound (both in the presence and in the absence of surfactant). The goal of this investigation is to develop a fundamental model of drug transport through the intercellular regions of the stratum corneum based on the structure of the stratum corneum. By using the results of this model to determine a maximum intercellular stratum corneum permeation rate for hydrophilic permeant delivery, it will be possible to determine indirectly whether intercellular or transcellular permeation pathways are present in skin samples which have been treated with low-frequency ultrasound.

The third issue examines how the formation of hypothesized LTRs in ultrasound-treated skin samples impacts our understanding of the transport mechanisms underlying ultrasound-mediated transdermal drug delivery. The goals of this study include: 1) verifying that the hypothesized LTRs are, in fact, localized regions of high permeability in ultrasound-treated skin samples compared to the surrounding regions of less permeable ultrasound-treated skin (the non-LTRs), 2) using Two-Photon Microscopy to visualize the location of a model hydrophilic and a model hydrophobic drug to examine the types of transdermal pathways present in the LTRs and in the non-LTRs of ultrasound-treated skin samples, and 3) using the porous pathway hypothesis to interpret transport data through the LTRs and the non-LTRs in ultrasound-treated skin samples to gain mechanistic insights into how a single ultrasound dose is able to perturb the structure of the skin to two significantly different levels.

Addressing these three issues, which were discussed in the literature review presented in Section 1.2, will further our understanding of the fundamental transport processes relevant to ultrasound-mediated TDD. Additionally, deeper investigations into the porous pathway model and into intercellular stratum corneum transport models will further our understanding of the basic fundamental principles that are relevant in transdermal drug delivery.

1.4 Thesis Overview

The remaining chapters of this thesis cover, in detail, investigations into the three issues concerning ultrasound-mediated transdermal drug delivery discussed in Section 1.3.

Chapter 2 presents a theoretical and experimental investigation into the use of the porous pathway hypothesis to describe the transdermal transport of hydrophilic drugs. In previous studies of ultrasound-mediated hydrophilic drug transport, the transdermal transport of a single hydrophilic drug and skin electrical resistivity measurements were analyzed in the context of the porous pathway hypothesis to characterize the nature of the hypothesized aqueous pore pathways in both ultrasound-treated and untreated skin samples. In Chapter 2, two hydrophilic drugs of differing molecular weight were delivered *simultaneously* through untreated human full-thickness skin, heat-stripped human dermis, and ultrasound-treated human full-thickness skin, in conjunction with skin electrical resistivity measurements. This experimental data was analyzed using the model of porous pathway transport as it applies to the time-dependent solution to Fick's Second Law of diffusion. By simultaneously delivering two hydrophilic drugs across the same skin sample, it was possible to use the Fickian form of the porous pathway hypothesis to evaluate the following critical drug transport properties - the porosity, the tortuosity, and the diffusive hindrance factor - for each hydrophilic drug in each type of skin sample examined. Finally, using the skin electrical resistivity as a quantitative measure of the structural perturbation in the skin due to ultrasound exposure, it was possible to evaluate how these important transport properties changed as a function of ultrasound exposure.

Chapter 3 presents an analysis of drug transport in the intercellular regions of the stratum corneum. Building on previous structure-based models for the transport of drugs through the intercellular regions of the stratum corneum, a new model was developed for drug transport in the intercellular regions of the stratum corneum which accounts for the existence of parallel diffusion pathways in the stratum corneum. The results of the model

derivation indicated that two tortuosity factors, one accounting for the total amount of intercellular space and the second accounting for the impact of parallel diffusion pathways on the diffusive flux, are required in the time-dependent solution to Fick's Second Law for diffusion through the intercellular regions of the stratum corneum. This new model was then validated against data from simulated stratum corneum diffusion experiments conducted with the finite element software package, FEMLAB. The new model for transport through the intercellular regions of the stratum corneum was also useful for evaluating the vehicle-to-lipid partition coefficient, K_b, and the diffusion coefficient, D_b, for hydrophobic drugs from a *single permeation experiment*, which represents an improvement over previous experimental methods used to obtain values of K_b and D_b.

Chapter 4 presents an experimental verification that the hypothesized localized transport regions formed in skin samples treated with low-frequency ultrasound are indeed localized regions of high transdermal transport. Analysis of the passive transport of calcein, a hydrophilic permeant, through the LTRs and non-LTRs of ultrasound pre-treated pig full-thickness skin samples was achieved with a novel experimental technique: diffusion masking experiments. A colored hydrophilic permeant penetrating into the skin was used as a marker to indicate the locations of the LTRs and the non-LTRs on the skin. Separate skin electrical resistivity measurements of the LTRs and the non-LTRs were used to verify the results obtained from the calcein transport experiments. Values of the porosity/tortuosity ratio for the LTRs and the non-LTRs were obtained from the electrical resistivity measurements and compared to the porosity/tortuosity ratio for the intercellular regions of the skin, obtained in Chapter 3, to

determine whether intercellular or transcellular pathways were present in the LTRs and the non-LTRs of ultrasound-treated skin.

Chapter 5 presents further analysis on the LTRs and the non-LTRs generated with low-frequency sonophoresis. In Chapter 5, two-photon microscopy was used to visualize the transdermal pathways within the LTRs and the non-LTRs in human full-thickness skin. The primary goal of this study was to observe the location in the skin of a fluorescent hydrophilic permeant, SRB, with TPM imaging to determine whether intercellular or transcellular pathways are the primary route of delivery within the LTRs and the non-LTRs. These images were used to confirm results obtained from an analysis of the experimental data in Chapter 4. In this study, four cases were examined: 1) untreated skin, 2) surfactant-treated skin, 3) ultrasound-treated skin, and 4) ultrasound and surfactant treated skin. In addition to evaluating the types of pathways traversed by the model hydrophilic permeant, it was also possible to generate profiles of intensity as a function of skin depth. These profiles allowed determination of enhancements in the surface partitioning and in the concentration gradient in the skin relative to the untreated skin case, which can provide useful clues to the mechanism of enhancement of the skin induced by the surfactant and/or ultrasound. While Chapter 4 examined the creation of the LTRs and the non-LTRs in the presence of the hydrophilic probe, SRB, in Chapter 5, the delivery of a model hydrophobic probe, RBHE, was also examined for each of the fours cases listed above. This additional investigation was conducted to compare the transdermal transport pathways traversed by hydrophilic and by hydrophobic drugs in the presence of ultrasound treatment, as well as to examine any differences in the

enhancements of the transdermal transport properties resulting from the three skin enhancing methods.

Chapter 6 presents an application of the porous pathway model to the LTRs and the non-LTRs of ultrasound-treated skin. In this study, the methods and results of Chapter 2 were applied to permeability data obtained from the LTRs and the non-LTRs in full-thickness human skin generated by ultrasound in the presence of the hydrophilic probe, SRB. The goal of this study was to examine the differences between the transport properties associated with the aqueous pores formed by ultrasound in the LTRs and the non-LTRs. By evaluating the porosity, the tortuosity, and the diffusive hindrance factor for the LTRs and the non-LTRs in the context of the porous pathway model, it was possible to examine the differences in these transport properties of the two different regions of ultrasound-treated skin. As with the TPM imaging studies presented in Chapter 5, this analysis provided useful clues as to how the skin was perturbed in a heterogeneous manner from a single ultrasound treatment.

Chapter 7 completes the presentation of this thesis with a summary of the thesis work done and a brief exploration of some potential areas for continuing future research in the field of ultrasound-enhanced transdermal drug delivery.

1.5 References

1. Gordon RD and Peterson TA. 2003. 4 Myths about transdermal drug delivery. Drug Deliv Tech 3(4):44-50.
2. Transdermal Drug Delivery - Technologies, Markets, and Companies. Jain PharmaBiotech 2006.
3. Johnson ME, Blankschtein D, and Langer R. 1997. Evaluation of solute permeation through the stratum corneum: Lateral bilayer diffusion as the primary transport mechanism. J Pharm Sci 86:1162-1172.
4. Wishart DS et al. 2006. DrugBank: A comprehensive resource for in silico drug discovery and exploration. Nucleic Acids Res. 34:D668-D672.
5. Walters KA and Roberts MS. 2002. The structure and function of the skin. Drug and the Pharmaceutical Sciences: Dermatological and Transdermal Formulations. 119:1-39.
6. Hou SYE, Mitra AK, White SH, Menon GK, Ghadially R, and Elias PM. 1991. Membrane structures in normal and essential fatty acid deficient stratum corneum: characterization by ruthenium tetroxide staining and X-ray diffraction. J Invest Derm 96:215-223.
7. Bodde HE, van der Brink I, Koerten HK, and de Haan FHN. 1991. Visualization of in vitro percutaneous penetration of mercuric chloride; transport through intercellular space versus cellular uptake through desmosomes. J Cont Rel 15:227-236.

8. Sznitowska M, Janciki S, and Williams AC. 1998. Intracellular of Intercellular Localization of the Polar Pathway across Stratum Corneum. J Pharm Sci 87:1109-1114.

9. Williams A. 2003. Transdermal and Topical Drug Delivery: From Theory to Clinical Practice. Pharmaceutical Press. Pg. 5.

10. Pliquett UF, Zewert TE, Chen T, Langer R, Weaver JC. 1996. Imaging of fluorescent molecule and small ion transport through human stratum corneum during high voltage pulsing: Localized transport regions are involved. Biophys Chem 58:185-204.

11. Zewert TE, Pliquett UF, Langer R, Weaver JC. 1995. Transdermal transport of DNA antisense oligonucleotides by electroporation. Biochem Biophys Res Co 212:286-292.

12. Vanbever R, Pliquett UF, Preat V, Weaver JC. 1999. Comparison of the effects of short, high-voltage and long, medium-voltage pulses on skin electrical and transport properties. J Cont Rel 60:35-47.

13. Gowrishankar TR, Herdon TO, Vaughan TE, Weaver JC. 1999. Spatially constrained localized transport regions due to skin electroporation. J Cont Rel 60:101-110.

14. Sharma A, Kara M, Smith FR, Krishnan TR. 2000. Transdermal drug delivery using electroporation. I. Factors influencing in vitro delivery of terazosin hydrochloride in hairless rats. J Pharm Sci 89:528-535.

15. Sharma A, Kara M, Smith FR, Krishnan TR. 2000. Transdermal drug delivery using electroporation. II. Factors influencing skin reversibility in electroporative delivery of terazosin hydrochloride in hairless rats. J Pharm Sci 89:536-544.

16. Prausnitz MR, Aura Gimm J, Guy RH, Langer R, Weaver JC, Cullander C. 1996. Imaging regions of transport across human stratum corneum during high-voltage and low-voltage exposures. J Pharm Sci 85:1363-1370.

17. Kochhar C, Imanidis G. 2003. In vitro transdermal iontophoretic delivery of leuprolide – mechanisms under constant voltage application. J Pharm Sci 92:84-96.

18. Turner NG, Guy RH. 1997. Iontophoretic transport pathways: Dependence on penetrant physicochemical properties. J Pharm Sci 86:1385-1389.

19. Bath BD, Scott ER, Phipps JB, White HS. 2000. Scanning electrochemical microscopy on iontophoretic transport in hairless mouse skin. Analysis of the relative contributions of diffusion, migration, and electroosmosis of transport in hair follicles. J Pharm Sci 89:1537-1549.

20. Curdy C, Kalia YN, Guy RH. 2001. Non-invasive assessment of the effects of iontophoresis on human skin in-vivo. J Pharm Pharmacol 53:769-777.

21. Kalia YN, Nonato LB, Guy RH. 1996. The effect of iontophoresis on skin barrier integrity: non-invasive evaluation by impedance spectroscopy and transepidermal water loss. Pharm Res 13:957-960.

22. Kalia YN, Guy RH. 1997. Interaction between penetration enhancers and iontophoresis: effect on human skin impedance in vivo. J Cont Rel 44:33-42.

23. Moser K, Kriwet K, Froehlilch N, Kalia YN, Guy RH. 2001. Permeation enhancement of a highly lipophilic drug using supersaturated systems. J Pharm Sci 90:607-616.

24. Mitragotri S. 2000. Synergistic effect of enhancers for transdermal drug delivery. Pharm Res 17:1354-1359.

25. Mitragotri S. 2001. Effect of bilayer disruption on transdermal transport of low-molecular weight hydrophobic solutes. Pharm Res 18:1018-1023.

26. Yu B, Kim KH, So PTC, Blankschtein D, Langer R. 2003. Visualization of oleic acid-induced transdermal diffusion pathways using two-photon fluorescence microscopy. J Invest Derm 120:448-455.

27. Johnson ME, Mitragotri S, Patel A, Blankschtein D, Langer R. 1996. Synergistic effects of chemical enhancers and therapeutic ultrasound on transdermal drug delivery. J Pharm Sci 85:670-678.

28. Tezel A, Sens A, Tuchscherer J, Mitragotri S. 2002. Synergistic effect of low-frequency ultrasound and surfactants on skin permeability. J Pharm Sci 91:91-100.

29. Tezel A, Sens A, Tuchscherer J, Mitragotri S. 2001. Frequency dependence of sonophoresis. Pharm Res 18:1694-1700.

30. Tezel A, Sens A, Mitragotri S. 2002. A theoretical analysis of low-frequency sonophoresis: Dependence of transdermal transport pathways on frequency and energy density. Pharm Res 19:1841-1846.

31. Tang H, Blankschtein D, Langer R. 2002. Effects of low-frequency ultrasound on the transdermal permeation of mannitol: Comparative studies with in vivo and in vitro skin. J Pharm Sci 91:1776-1794.

32. Tang H, Wang CCJ, Blankschtein D, Langer R. 2002. An investigation of the role of cavitation in low-frequency ultrasound-mediated transdermal drug transport. Pharm Res 19:1160-1169.

33. Alvarez-Román R, Merino G, Kalia YN, Naik A, Guy RH. 2003. Skin permeability enhancement by low-frequency sonophoresis: Lipid extraction and transport pathways. J Pharm Sci 92:1138-1146.

34. Henry S, McAllister DV, Allen MG, Prausnitz MR. 1998. Microfabricated microneedles: A novel approach to transdermal drug delivery. J Pharm Sci 87:922-925.

35. Trebotich D, Zahn JD, Prabhakarpandian B, Liepmann D. 2003. Modeling of microfabricated microneedles for minimally invasive drug delivery, sampling and analysis. Biomed Microdevices 5:245-251.

36. McAllister DV, Wang PM, Davis SP, Park JH, Canatella PJ, Allen MG, Prausnitz MR. 2003. Microfabricated needles for transdermal delivery of macromolecules and nanoparticles: Fabrication methods and transport studies P Natl Acad Sci USA 100: 13755-13760.

37. Zharov VP, Latyshev AS. 1998. Laser ultrasonic transport of drugs in living tissues. Ann Ny Acad Sci 858: 66-73.

38. Mitragotri S, Ray D, Farrell J, Tang H, Yu B, Kost J, Blankschtein D, and Langer RS. 2000. Synergistic effect of low-frequency ultrasound and sodium lauryl sulfate on transdermal transport. J Pharm Sci 89:892-900.

39. Le L, Kost J, Mitragotri S. 2000. Combined effect of low-frequency ultrasound and iontophoresis: applications for transdermal heparin delivery. Pharm Res 17:1151-1154.

40. Mitragotri S, Ray D, Farrell J, Tang H, Kost J, and Langer RS. 1999. Enhancement of transdermal transport using low-frequency ultrasound in combination with surfactants. Proceed Int'l Symp Control Rel Bioact Mater 26:176-177.

41. Mitragotri S. Ultrasound-Mediated Transdermal Drug Delivery: Mechanisms and Applications. Ph.D. Thesis, Mass. Inst. of Tech. (1996).

42. Tang H. Low-Frequency Sonophoresis in Transdermal Drug Delivery. Ph.D. Thesis, Mass. Inst. of Tech. (2001).

43. Mitragotri S, Edwards DA, Blankschtein D, and Langer RS. A mechanistic study of ultrasonically-enhanced transdermal drug delivery. J Pharm Sci 84:697-706 (1995).

44. Tang H, Blankschtein D, and Langer RS. 2002. Prediction of steady-state skin permeabilities of polar and nonpolar permeants across excised pig skin based on measurements of transient diffusion: characterization of hydration effects on the skin porous pathway. J Pharm Sci 91:1891-1907.

45. Tang H, Mitragotri S, Blankschtein D, Langer RS. 2001. Theoretical description of transdermal transport of hydrophilic permeants: application to low-frequency sonophoresis. J Pharm Sci 90:545-568.

46. Lavon I, Grossman M, and Kost J. 2005. The nature of ultrasound-SLS synergism during enhanced transdermal transport. J. Cont. Rel. 107:484-494.

47. Krasovitski B and Kimmel E. 2001. Gas bubble pulsation in a semi-confined space subjects to ultrasound. J Acoust Soc Am 109:891-898.

48. Mulqueen, M. 2001. Theoretical and Experimental Investigation of the Equilibrium and Dynamic Interfacial Behavior of Mixed Surfactant Solutions. Ph.D. Thesis, Mass. Inst. of Tech.

49. Boucaud A, Montharu J, Lebertre M, Patat F, Vaillant L, Machet L. 1999. Biological effects of low frequency ultrasound on the skin. IEEE Ultrasonics Symposium.

50. Boucaud A, Montharu J, Garrigue MA, Machet L, Patat F, Vaillant L. 2000. Low frequency sonophoresis of insulin: an in vivo study. Congres Annuel de Recherche en Dermatologie, Lyon, France.

51. Yamashita N, Tachibana K, Ogawa K, Tsujita N, Tomita A. 1997. Scanning electron microscopic evaluation on the skin surface after ultrasound exposure. The Anatomical Record 247:455-461.

52. Hatanaka T, Manabe E, Sugibayashi K, Morimoto Y. 1994. An application of the hydrodynamic pore theory to percutaneous absorption of drugs. Pharm Res 11:654-658.

53. Menon GK, Bommannan DB, Elias PM. 1994. High-frequency sonophoresis: permeation pathways and structural basis for enhanced permeability. Skin Pharmacol 7:130-139.

54. Menon GK and PM Elias. 1997. Morphological basis for a pore-pathway in mammalian stratum corneum. Skin Pharmacol 10:235-246.

55. Bommannan D, Menon GK, Okuyama H, Elias PM, Guy RH. 1992. Sonophoresis II: examination of the mechanism(s) of ultrasound-enhanced transdermal delivery. Pharm Res 9:1043-1047.

56. Yu B, Dong C, So PTC, Blankschtein D, Langer RS. 2001. In vitro visualization and quantification of oleic acid induced changes in transdermal transport using two-photon fluorescence microscopy. J Invest Dermatol 117:16-25.

57. Brown SL and Rossi JE. 1989. A simple method for estimating dermal absorption of chemicals in water. Chemosphere 19:1989-2001.

58. Fiserova-Bergerova V, Pierce JT, and Droz PO. 1990. Dermal absorption potential of industrial chemicals: criteria for skin notation. Am J Ind Med 17:617-635.

59. McKone TE and Howd RA. 1992. Estimating dermal uptake of nonionic organic chemicals from water and soil. I. Unified fugacity-based models for risk assessments. Risk Anal 12:543-557.

60. Robinson PJ. A Composite Model for Predicting Dermal Penetration in Vivo. Human and Environmental Safety Division. The Proctor and Gamble Company.

61. Guy RH and Potts RO. 1993. Penetration of industrial chemicals across the skin: A predictive model. Am J Ind Med 23:711-719.

62. Wilschut A, ten Berge WF, Robinson PJ, and McKone TE. 1995. Estimating skin permeation: the validation of five mathematical skin permeation models. Chemosphere 30:1275-1296.

63. Mitragotri S. 2002. A theoretical analysis of permeation of small hydrophobic solutes across the stratum corneum based on scaled particle theory. J Pharm Sci 91:744-752.

64. Mitragotri S, Johnson ME, Blankschtein D, and Langer RS. 1999. An analysis of the size selectivity of solute partitioning, diffusion, and permeation across lipid bilayers. Biophys J 77:1268-1283.

65. Michaels AS, Chandraskeran SK, Shaw JE. 1975. Drug permeation through human skin: theory and in vitro experimental measurement. Am Inst Chem Eng J 21:985-996.

66. Cussler E, Hughes S, Ward W, and Aris R. 1988. Barrier membranes. J Memb Sci 38:161-174.

67. Lange-Lieckfeldt R and Lee G. 1992. Use of a model lipid matrix to demonstrate the dependence of the stratum corneum's barrier properties on its internal geometry. J Cont Rel 20:183-194.

68. Edwards DA and Langer R. 1994. A linear theory of transdermal transport phenomena. J Pharm Sci 83:1315-1334.

69. Frasch HF and Barbero AM. 2003. Steady-state flux and lag time in the stratum corneum lipoid pathway: Results from finite element models. J Pharm Sci 92: 2196-2207.

70. Tezel A, Sens A, and Mitragotri S. 2003. Description of transdermal transport of hydrophilic solutes during low-frequency sonophoresis based on a modified porous pathway model. J Pharm Sci. 92: 381-393.

71. Li SK, Suh W, Parikh HH, Ghanem AH, Mehta SC, Peck KD, and Higuchi WI. 1998. Lag time data for characterizing the pore pathway of intact and chemically pretreated human epidermal membrane. Int J Pharm. 170: 93-108.

72. Peck KD, Ghanem AH, and Higuchi WI. 1994. Hindered diffusion of polar molecules through and effective pore radii estimates of intact and ethanol treated human epidermal membrane. Pharm Res 11:1306-1314.

73. Song Y, Li SK, Peck KD, Zhu HG, Ghanem AH, and Higuchi WI. 2002. Human epidermal membrane constant conductance iontophoresis: alternating current to obtain reproducible enhanced permeation and reduced lag times of a nonionic polar permeant. Int J Pharm 232: 45-57.

Chapter 2

Evaluation of the Porosity, the Tortuosity, and the Hindrance Factor for the Transdermal Delivery of Hydrophilic Permeants in the Context of the Aqueous Pore Pathway Hypothesis using Dual Radiolabeled Permeability Experiments

2.1 Introduction

Modeling the transport of hydrophilic permeants across the skin membrane is essential to understanding transdermal drug delivery (TDD). A particular challenge in this area of TDD involves understanding the mechanism of hydrophilic permeant delivery across the stratum corneum (SC). As discussed in Chapter 1, the SC is the outermost layer of the skin, typically having a thickness of 10-20 μm, and consists of a brick-and-mortar structure of impermeable corneocyte cells (the bricks) and intercellular lamellar lipid bilayer domains (the mortar) (see Figure 1-3).[1] Primarily because of its lipophilic nature due to the presence of the lipid bilayers in the intercellular regions,[1] the SC exhibits

increased resistance to the permeation of hydrophilic compounds as compared to the permeation of hydrophobic compounds. Because of this observed difference in the SC permeation rates of hydrophobic and hydrophilic compounds, it has been proposed that hydrophobic and hydrophilic permeants traverse the SC along different permeation pathways. Hydrophobic permeants traverse the SC primarily along the intercellular lipid lamellar domains (see Chapter 3 for details),[2-6] while hydrophilic permeants are believed to traverse the SC, as well as the viable epidermis and the dermis, along aqueous pore pathways.[7-11]

The aqueous pore pathway hypothesis has been developed as a model to describe the transport of hydrophilic solutes through the aqueous pore pathways of the skin. The basic assumption of this model is that the transport of hydrophilic permeants across the skin occurs through cylindrical aqueous channels, or pores, that traverse the skin barrier (see Figure 2-1).[9-11] Because the radii of the hypothesized aqueous pores may be similar to the radii of the aqueous permeants which are delivered across the skin, equations from hindered transport[12] have previously been incorporated into the model equations characterizing the aqueous pore pathway hypothesis.[9-11] While there has been no direct evidence for the physical existence of aqueous pore channels in the SC to date, some researchers have claimed that the presence of an aqueous pore pathway can be inferred from evidence of connected lacunar domains within the lipid lamellar bilayers,[7,8,13,14] or from the presence of defects in the lipid lamellar bilayers of the intercellular regions of the SC.[10,15] Despite the lack of direct physical evidence for the existence of the aqueous pore pathways in the SC, the porous pathway hypothesis has been used extensively to study the permeation of hydrophilic permeants across the SC.[9-11, 16-20]

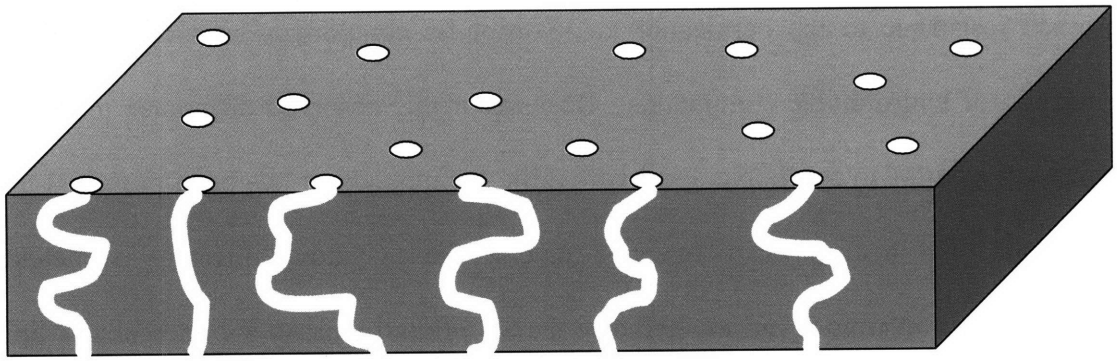

Figure 2-1: Sketch of the hypothesized cylindrical aqueous pore channels (shown in white) which traverse the skin barrier (shown in grey).

One of the main reasons that transdermal transport models for hydrophilic permeants, which are based on the aqueous pore pathway hypothesis, continue to be useful in the field of hydrophilic transdermal transport is their ability to evaluate several key transport parameters characterizing the structural features of the hypothesized aqueous pores. These include: 1) the fraction of the skin surface occupied by the aqueous pore channels, ε, (i.e. the porosity), 2) the tortuosity, τ, of the aqueous pore channels present in the skin, and 3) the average aqueous pore radii, or the distribution of aqueous pore radii, of the hypothesized aqueous pore channels, which determines the amount of hindrance experienced by a hydrophilic permeant diffusing through an aqueous pore channel in the skin. Previously, Peck *et al.* used the aqueous pore pathway hypothesis to determine the *average aqueous pore radius* in untreated and in ethanol-treated human epidermal membrane from permeability experiments using four small hydrophilic permeants – urea (MW = 60.1 Da, log $K_{O/W}$ = -2.75), mannitol (MW = 182.2 Da, log $K_{O/W}$ = -3.10), sucrose MW = 342.3 Da, log $K_{O/W}$ = -3.67), and raffinose (MW = 504.4

Da, log $K_{O/W}$ = -3.67) (see Section 2.2.1 for model details).[9] Tang *et al.* used the aqueous pore pathway hypothesis in conjunction with principles of electrochemistry to demonstrate that the permeability of small hydrophilic permeants (mannitol and sucrose) can be predicted from measurements of the skin electrical resistance.[10] These studies allowed for the determination of the *average aqueous pore radius* and the *porosity-to-tortuosity ratio*, (ε/τ), in untreated and in ultrasound-treated full-thickness pig skin and human epidermal membrane (see Section 2.2.2 for model details).[10] Tezel *et al.* extended the work of Tang *et al.* by modifying the aqueous pore pathway hypothesis to account for the possible existence of a *distribution of aqueous pore radii* in the skin. This modification was required to account for deviations from the model equations in the aqueous pore pathway hypothesis proposed by Tang *et al.* observed in permeability experiments in the case of larger hydrophilic permeants (i.e. inulin (MW = 5000 Da, log $K_{O/W}$ = -2.75) and dextran (MW = 70,000 Da, log $K_{O/W}$ = -2.75)).[11] This modification also allowed prediction of the permeability of larger hydrophilic permeants in untreated and in ultrasound-treated skin using skin electrical resistance measurements. Moreover, this modification to the aqueous pore pathway hypothesis made by Tezel *et al.* allowed for the separate evaluation of the *porosity*, ε, and the *tortuosity*, τ, rather than of the ratio, (ε/τ) (see Section 2.2.3 for model details).[11] In addition, the studies with ultrasound-enhanced skin conducted by Tang *et al.* and by Tezel *et al.* suggested that permeability enhancement of the skin structure is due to the creation of more pores having the same pore size distribution as that in untreated skin samples, and not due to the creation of larger or smaller pores than those observed in untreated skin samples.[10,11]

However, there are some model assumptions made by Tang *et al.* and by Tezel *et al.* that need to be re-examined. Regarding the work of Tezel *et al.*, the assumptions that will be examined in more detail include assuming that: 1) the porosity is an intrinsic property of the skin membrane, 2) there is an increase in the skin tortuosity with a corresponding increase in skin perturbation due to the application of ultrasound, and 3) the tortuosity of the aqueous pore pathways depends on the size of the hydrophilic permeant. This examination of previous model assumptions (see Section 2.2.4 for details) provides the motivation for revising the techniques used to analyze experimental permeation data of hydrophobic compounds in the context of the aqueous pore pathway hypothesis.

With all of the above in mind, in this chapter, I present a novel technique to analyze the experimental permeation data of hydrophilic compounds in the context of the aqueous pore pathway hypothesis. This technique allows one to evaluate the porosity, the tortuosity, and the radii of the aqueous pore channels, while circumventing the need to make potentially problematic assumptions about the structure of the hypothesized aqueous pores in the skin. Specifically, in Section 2.3, I propose a novel method to analyze skin permeation data of hydrophilic compounds in the context of the aqueous pore pathway hypothesis, which requires the application of this hypothesis to both the transient and the steady-state diffusion domains of permeation experiments involving dual radiolabeled hydrophilic compounds. In Section 2.4, the methods and materials required to perform permeation experiments involving dual radiolabeled hydrophilic compounds in untreated and in ultrasound-treated human full-thickness skin samples are described. Finally, in Section 2.5, the data from the diffusion experiments are presented

and analyzed using both previously-used steady-state methods and the novel method developed in Section 2.3, which allows the determination of the porosity, the tortuosity, and the radii of the aqueous pore channels, which are hypothesized to exist in the skin.

2.2 Review of Previous Models for the Transdermal Transport of Hydrophilic Permeants Based on the Aqueous Pore Pathway Hypothesis

In this section, three transdermal transport models for hydrophilic permeants, which are based on the aqueous pore pathway hypothesis, are reviewed, followed by motivating the need to further improve these models.

2.2.1 Evaluation of the Aqueous Pore Radius in the Skin using Dual Radiolabeled Transdermal Permeation Experiments

The steady-state permeability, P, of hydrophilic permeants through the aqueous pore pathways in the skin can be described by the following equation:[9]

$$P = \frac{\varepsilon_p D_p^{\infty} H(\lambda_p)}{\tau_p L} \tag{2.1}$$

where ε_p is the total area fraction of the skin available for transport (i.e. the porosity), D_p^{∞} is the diffusion coefficient of the permeant (p) in the bulk solution at infinite dilution, L is the thickness of the skin membrane, τ_P is the tortuosity factor, and $H(\lambda_p)$ is the hindrance factor. For $\lambda_p < 0.4$, $H(\lambda_p)$ is defined by the following equation:[12]

$$H(\lambda_p) = (1-\lambda_p)^2\left[1 - 2.104\lambda_p + 2.09\lambda_p^3 - 0.95\lambda_p^5\right] \tag{2.2}$$

where λ_p is defined as follows:[12]

$$\lambda_p = \frac{r_p}{r_{pore}} \tag{2.3}$$

where r_p is the radius of the permeant and r_{pore} is the radius of the aqueous pore channels, which are assumed to have a *single average radius*. Equation (2.1) was used by Peck *et al.* to determine the average radius of the aqueous pore pathways in both untreated and in ethanol-treated human epidermal membranes.[9] Since ε_p, τ_p, and r_{pore} are unknowns, experiments were designed to eliminate ε_p and τ_p in order to evaluate r_{pore}. This was accomplished by delivering two permeants simultaneously through the same skin sample. For this case, the ratio of the expressions for the permeabilities of permeants 1 and 2 can be expressed as follows:

$$\frac{P_1}{P_2} = \frac{(\varepsilon/\tau)_1 D_1^\infty H(\lambda_1)}{(\varepsilon/\tau)_2 D_2^\infty H(\lambda_2)} \tag{2.4a}$$

It is useful to express Eq. (2.4a) in logarithmic form as follows:

$$\log P_1 = \log\frac{D_1^\infty}{D_2^\infty} + \log\frac{H(\lambda_1)}{H(\lambda_2)} + \log\frac{\varepsilon_1}{\varepsilon_2} + \log\frac{\tau_2}{\tau_1} + \log P_2 \tag{2.4b}$$

If one assumes that the porosity and the tortuosity are not dependent on the size of the permeant, such that the values are identical for the two permeants, then, ε and τ (as well as L) may be eliminated from Eqs. (2.4a) or (2.4b).[9] This assumption also implies that *the two permeants traverse the skin using the same aqueous pore pathways*. Once the permeability of each of the permeants is measured experimentally, Eqs. (2.4a) or (2.4b), in conjunction with Eqs. (2.2 and (2.3), can be used to determine the value of r_{pore}, the remaining unknown.

2.2.2 Evaluation of the Aqueous Pore Radius in the Skin using Electrical Resistance Measurements and Transdermal Permeation Experiments

Tang *et al.* examined a specific application of the aqueous pore pathway hypothesis where the second hydrophilic permeant is a current-carrying ion.[10] The assumption of this specific application was similar to the assumption of Peck *et al.*, i.e. *current-carrying ions accessed the same aqueous pore channels as the model hydrophilic permeant.* From this assumption, it follows that the values of ε and τ are independent of the size of the permeant and the current-carrying ion. For this case (where $\varepsilon_{ion} = \varepsilon_p$ and $\tau_{ion} = \tau_p$), Eq. (2.4b) can be rewritten as follows:[10]

$$\log P_p = \log \frac{D_p^\infty}{D_{ion}^\infty} + \log \frac{H(\lambda_p)}{H(\lambda_{ion})} + \log P_{ion} \tag{2.5}$$

where P_{ion} is the permeability of the current-carrying ions, D_{ion}^∞ is the diffusion coefficient of the ion in the bulk solution at infinite dilution, and $H(\lambda_{ion})$ is the hindrance factor of the ion (see Eqs (2.2) and (2.3) with "p" replaced by "ion"). Using principles from electrochemistry, Tang *et al.* were able to derive the following equation relating the permeability of the ions through a membrane to the electrical resistance measured across the same membrane:[10]

$$P_{ion} = \frac{kT}{2z^2 F c_{ion} e_0} \frac{1}{RA} \tag{2.6}$$

where k is the Boltzmann constant, T is the temperature (in degrees Kelvin), z is the electrolyte valence, F is the Faraday constant, R is the resistance measured across the skin, A is the area of the skin available for transport, and c_{ion} is the electrolyte molar

concentration in the skin membrane (assumed to be the bulk ion concentration). Substituting Eq. (2.6) in Eq. (2.5) yields:[10]

$$\log P_p = \log \frac{kT}{2z^2 F c_{ion} e_0} + \log \frac{D_p^\infty}{D_{ion}^\infty} + \log \frac{H(\lambda_p)}{H(\lambda_{ion})} - \log RA \tag{2.7}$$

Equation (2.7), then, relates the permeability of a model hydrophilic permeant to the electrical resistance of the skin through which the model hydrophilic permeant is being delivered. Equation (2.7), in conjunction with Eqs. (2.2) and (2.3), can then be used to estimate the permeability of a desired hydrophilic permeant through a membrane using electrical resistance measurements, if the aqueous pore radius, r_{pore}, as well as the radii of the permeant, r_p, and of the current-carrying ions, r_{ion}, are known.

Interestingly, even if the aqueous pore radius is unknown, as in human skin samples, Eq. (2.7) can nevertheless be used to determine the aqueous pore radius using both skin electrical resistance measurements and hydrophilic permeability measurements. On a log P vs. log RA plot, Eq. (2.7) predicts that a slope of -1 passes through the experimental data. The first three terms on the RHS of Eq. (2.7) contribute to the value of the y-intercept in the log P vs. log RA plot. From the experimental value of the y-intercept, the radius of the aqueous pores in the membrane (found in $H(\lambda_p)$ and $H(\lambda_{ion})$) can then be determined. Tang *et al.* used this technique, with mannitol and sucrose as the model hydrophilic permeants, to determine the average available pore radius in both untreated and in ultrasound-treated skin samples.[10] Their results indicated that the average available pore radius in the skin was similar for both model permeants, and was also similar for the untreated and the ultrasound-treated full-thickness pig skin samples.[10] These results led Tang *et al.* to the conclusion that ultrasound enhancement of the skin

results in the creation of additional aqueous pores which *have radii that are similar* to those of the aqueous pores present in the untreated skin samples.[10]

2.2.3 Modification of the Aqueous Pore Pathway Hypothesis to Account for the Presence of a Distribution of Aqueous Pore Radii in the Skin

The next advance in the development of the porous pathway model came as a result of an experimental analysis conducted by Tezel *et al.*[11] In their experiments, Tezel *et al.* repeated the experiments of Tang *et al.* using a broader range of permeant radii. The previous work done by both Peck *et al.* and by Tang *et al.* used similarly sized permeants, ranging from 2.2 Å to 6.6 Å in radius. The work of Tezel *et al.* compared the transdermal permeability of four permeants (mannitol – r_p = 4.4 Å, luteinizing hormone relasing hormone (LHRH) – r_p = 8 Å, inulin – r_p = 12 Å, and dextran – r_p = 26 Å) to skin electrical resistance measurements for both untreated and ultrasound-treated skin samples.[11] Tezel *et al.* observed that the slope of the experimental data for these four permeants significantly deviated from the slope of -1 predicted by the model of Tang *et al.*,[10] and that the experimental data could be fit to the following empirical expression:[11]

$$\log P = \log C - (1-\alpha)\log RA \tag{2.8}$$

where log C is the y-intercept value from the log P vs. log RA plot, and α is an empirical modifier to the -1 slope. Furthermore, the value of α was found to increase as the radius of the permeant increased.

The experimental observation made by Tezel *et al.*[11] required a revision of three key assumptions in the aqueous pore pathway model proposed by Tang *et al.*[10] to account for the fact that the slope in the log P vs. log RA plot was observed to be greater than -1,

as well as to increase with the permeant radius. First, Tezel *et al.* revised the calculation of the hindrance parameter by proposing a distribution of pore radii, $\gamma(r_{pore})$, and, then, integrating the product of $\gamma(r_{pore})*H(\lambda)$ over all values of r_{pore} larger than the radius of the permeant, r_p, as shown in the following expression:[11]

$$H(\lambda_p) = \int_{r_p}^{\infty} \gamma(r_{pore}) H(\lambda) dr_{pore} \tag{2.9}$$

Second, they proposed that the smaller permeants would access more tortuous aqueous pore channels within the skin than the larger permeants, resulting in the smaller permeants having a larger τ value than the larger permeants.[11] Finally, they also proposed that the tortuosity in the dermis would be larger than in untreated skin due to the increased amount of aqueous pore connectivity in the dermis.[11] If ultrasound enhances the connectivity of the aqueous pores, as proposed by Tezel *et al.*,[11] then, it also follows that the tortuosity of the skin should increase as the skin is treated with ultrasound until it reaches the tortuosity value of the dermis. To account for the third model proposition, the following empirical power law relations were proposed for the hydrophilic permeant and the current-carrying ions:[11]

$$\frac{\tau_p}{\tau_p^{dermis}} = \left(\frac{RA_{dermis}}{RA} \right)^m \tag{2.10a}$$

and

$$\frac{\tau_{ion}}{\tau_{ion}^{dermis}} = \left(\frac{RA_{dermis}}{RA} \right)^n \tag{2.10b}$$

Combining Eq. (2.4b) (with 1 = p and 2 = ion) with Eq. (2.6), the following general expression can be written which relates the permeability of a model hydrophilic permeant (p) to the skin electrical resistance:[11]

$$\log P_p = \log \frac{kT}{2z^2 F c_{ion} e_0} + \log \frac{D_p^\infty}{D_{ion}^\infty} + \log \frac{H(\lambda_p)}{H(\lambda_{ion})} + \log \frac{\varepsilon_p}{\varepsilon_{ion}} + \log \frac{\tau_{ion}}{\tau_p} - \log RA \qquad (2.11)$$

For the case where ε is assumed to be an intrinsic property of the skin and independent of the radii of the permeant and of the current-carrying ion, such that $\varepsilon_p = \varepsilon_{ion}$, substituting Eqs. (2.9), (2.10a) and (2.10b) in Eq. (2.11) yields:[11]

$$\log P_p = \log \frac{kT}{2z^2 F c_{ion} e_0} + \log \frac{D_p^\infty}{D_{ion}^\infty} + \log \frac{\int_{r_p}^{\infty} \gamma(r_{pore}) H(\lambda) dr_{pore}}{\int_{r_{ion}}^{\infty} \gamma(r_{pore}) H(\lambda) dr_{pore}} - \alpha \log RA_{dermis} - (1-\alpha) \log RA \qquad (2.12)$$

where it was assumed that, in the dermis, $\tau_{ion} = \tau_p$, and that $\alpha = m - n$. The proposed modifications to the aqueous pore pathway model, embodied in Eq. (2.12), allows the slope of the data in the log P vs. log RA plot to deviate from the slope of -1 predicted by Tang *et al.*[10] Equation (2.12) then fits the form of the empirical relationship presented in Eq. (2.8) which describes the experimental data obtained by Tezel *et al.*[11] Using Eq. (2.12) to interpret their experimental data, Tezel *et al.* observed that the *distribution of pore radii does not change as the skin is treated with ultrasound.*[11] Accordingly, ultrasound creates more pores having a distribution of pore radii which is similar to that found in untreated skin. This proposed mechanism of ultrasound enhancement is similar to that proposed by Tang *et al.* (i.e. ultrasound enhancement serves only to augment the number of aqueous pores found in untreated skin),[10] with the key difference that it replaces the single average pore radius used by Tang *et al.* with an entire distribution of pore radii.

In addition, Tezel *et al.* were able to estimate the porosity and the tortuosity of the aqueous pore pathways separately using other equations based on their additional model assumptions. First, Tezel *et al.* proposed the following empirical power law expression for the porosity by assuming that the skin membrane thickness and the ion tortuosity are both functions of the skin resistivity:[11]

$$\varepsilon = \frac{\Psi}{RA^{\kappa}} \tag{2.13}$$

where Ψ and κ are empirical constants. The ratio, (ε/τ_p), can then be expressed using Eqs. (2.10a) and (2.13) as follows:[11]

$$\log\left(\frac{\varepsilon}{\tau_p}\right) = \log\frac{\Psi}{\tau_p^{dermis} RA_{dermis}^{n+\alpha}} + (n+\alpha-\kappa)\log RA \tag{2.14}$$

The values of n, Ψ, and κ are permeant independent, while those of α and τ_p^{dermis} are permeant dependent.[11] By plotting (ε/τ_p) as a function of the skin resistivity, RA, for several permeants, it is possible to determine the values of n, Ψ, κ, and τ_p^{dermis} for each permeant. Once these values have been determined, the skin porosity and the skin tortuosity can be determined for each permeant. Using this method, Tezel *et al.* demonstrated that the skin porosity increased with decreasing skin electrical resistivity, while the skin tortuosity increased with decreasing skin electrical resistivity and decreased with increasing permeant radius.[11]

2.2.4 Reexamination of Previous Aqueous Pore Pathway Model Assumptions

In this section, I reexamine four key model assumptions made by the previous researchers.[9-11] These assumptions include: 1) the two hydrophilic permeants traverse the skin through the same aqueous pore channels, 2) the porosity of the skin is an intrinsic skin property, and therefore, is independent of the permeant radius, 3) the tortuosity decreases as the radius of the permeant increases, and 4) the tortuosity increases as the skin is perturbed with low-frequency ultrasound.

An examination of assumption (1) – that the two permeants being delivered across the skin traverse the exact same aqueous pore pathways, has already been carried out by Tezel *et al.*,[11] and led to their hypothesis that a distribution of aqueous pore radii may exist in the skin. Note that this hypothesis is not at odds with the assumption made by previous researchers[9,10] that the two hydrophilic permeants traverse the skin through the same aqueous pores, in cases where the two permeants delivered transdermally have similar radii. In the works of Peck *et al.* and Tang *et al.*, the radii of the permeants that they utilized ranged from 2.2 Å to 6.6 Å.[9,10] These radii were small compared to the average aqueous pore radii, ~ 20-25 Å,[9,10] thus satisfying this requirement.

However, when the radii of the two permeants delivered transdermally are very different, such that the smaller permeant can access a larger fraction of the aqueous pore pathways than can the larger permeant, additional considerations are needed. First, since the smaller permeant accesses a larger fraction of the aqueous pore pathways than does the larger permeant, it would also appear that the value of the porosity, which is the fraction of the skin surface occupied by the *available* aqueous pore channels,

corresponding to the smaller permeant would be larger than the porosity corresponding to the larger permeant. This observation differs from the assumption made by Tezel *et al.* that the porosity is an intrinsic property of the skin and is independent of the radius of the permeant.[11] By evaluating the porosity of the skin as a function of the radius of the permeant delivered transdermally, it should be possible to determine if there is a dependence of the skin porosity on the radius of the permeant.

Tezel *et al.* also assumed that the tortuosity of the aqueous channels decreases as the radius of the permeant increases. In making this assumption, in effect, Tezel *et al.* claim that the transport process in the skin is similar to the transport process in size-exclusion chromatography.[11] In size-exclusion chromatography, molecules are separated based on molecular radii, where the smaller molecules are able to access the more tortuous channels within the chromatography column when compared to the larger molecules.[21] While Tezel *et al.* do provide some data which is consistent with this assumption, the data does depend on their proposed model equations, which account for their assumption that the tortuosity of the aqueous channels decreases as the radius of the permeant increases. It would be preferable if the tortuosity of the aqueous pore channels in the skin could be evaluated as a function of the radius of the permeant delivered transdermally using model equations that are not based on any prior assumptions about the dependence of the tortuosity of the aqueous pore channels on the radius of the permeant.

Finally, Tezel *et al.* also assumed that the tortuosity of the skin increases as the skin is perturbed with ultrasound. This assumption is problematic, if the equation for the lag time to reach steady-state, given by:[17]

$$t_{lag} = \frac{(\tau_p L)^2}{6 D_p^{\infty} H(\lambda_p)} \tag{2.15}$$

is considered carefully. As part of their analysis, Tezel *et al.* concluded that the distribution of aqueous pore radii in the skin does not change with ultrasound treatment (implying that $H(\lambda_p)$ should be constant).[11] Therefore, under the assumption that the tortuosity of the skin, τ_p, increases as the skin is treated with ultrasound, the lag time to reach steady-state should also increase (see Eq. (2.15)). As an example, using the values reported by Tezel *et al.* for the tortuosity of dextran in untreated skin (RA ~ 100 kΩ*cm^2, $\tau_p \sim 1$) and in ultrasound-treated skin (RA ~ 1 kΩ*cm^2, $\tau_p \sim 11$),[11] and assuming that L, $H(\lambda_p)$, and D_p^{∞} are independent of the extent of skin perturbation induced by ultrasound, Eq. (2.15) can be used to show that there is a 121-fold *increase* in the lag time to reach steady-state in ultrasound-treated skin samples as compared to untreated skin samples for similarly large molecules. Clearly, treating the skin with low-frequency ultrasound would not be an efficacious enhanced transdermal drug delivery method if more time was required for the drug to reach steady-state in ultrasound-treated skin than in untreated skin. By evaluating the tortuosity of the aqueous pore channels in the skin as a function of the extent to which the skin is perturbed due to ultrasound exposure,[22] which can be evaluated quantitatively using skin electrical resistance measurements, it should be possible to determine if there is a dependence of the tortuosity of the aqueous pore channels in the skin on the amount of ultrasound treatment to which the skin was subjected.

In order to evaluate the porosity, the tortuosity, and the radii of the aqueous pore channels in the skin, an improved theoretical analysis method needs to be developed that

does not require *a priori* assumptions about the behavior of the porosity, the tortuosity, and the radii of the aqueous pore channels in the skin as function of the permeant radii or of the extent of skin perturbation, as was done in previous investigations.[9-11] Previous theoretical analysis methods have also relied solely on steady-state permeability measurements, which limits the number of unknowns that can be determined (see Section 2.4.6). In the following section, I extend the aqueous pore pathway model to include the transient domain of the transdermal transport of hydrophilic permeants. Combining the resulting new theoretical equations with the dual radiolabeled experimental technique, I will show that it is possible to evaluate the porosity, the tortuosity, and the radii of the aqueous pore channels in the skin as a function of both the hydrophilic permeant radii and the extent of skin perturbation induced by the ultrasound treatment.

2.3 Theory

2.3.1 Development of Fick's Second Law of Diffusion in the Context of the Aqueous Pore Pathway Hypothesis

Figure 2-2 shows a thin slice of the skin containing the hypothesized aqueous pore channels, which are assumed to have: 1) a uniform pore radius over the length of the aqueous pore channel, 2) a tortuous shape, and 3) no branching of the pore channels in the skin such that there are no parallel diffusion pathways present. Assuming that drug transport is restricted to these hypothesized aqueous pores in the skin slice, the following mass balance can be written on the thin slice of skin shown in Figure 2-2:

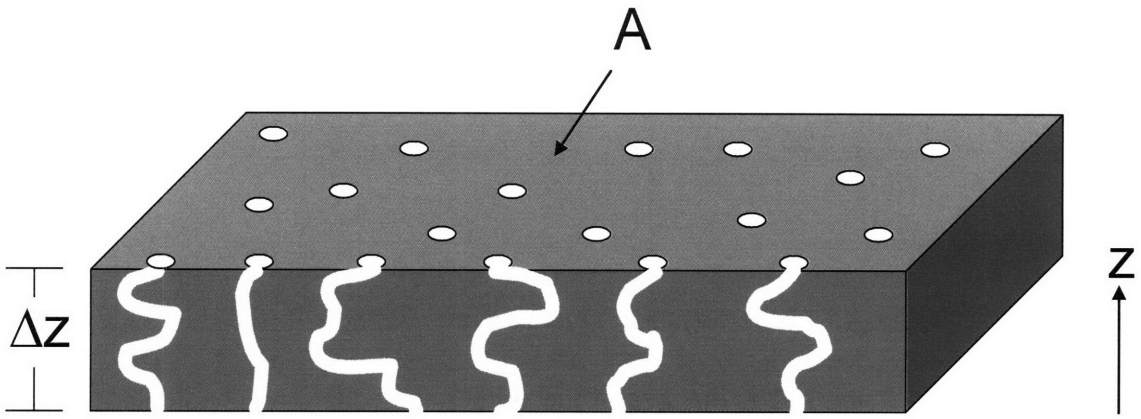

Figure 2-2: Sketch of a thin slice of the skin having cross-sectional area, A, and thickness, Δz, containing the hypothesized aqueous pore channels.

$$\dot{m}_{in} - \dot{m}_{out} = \frac{\partial m}{\partial t} \tag{2.16}$$

where $\dot{m}_{in}$ and $\dot{m}_{out}$ are the drug mass flow rates into, and out of, the hypothesized aqueous pore channels in the skin. The mass, m, which accumulates in the thin slice of the skin can be defined as the product of the volume of the hypothesized aqueous pore channels in the thin slice of skin, V_{pores}, and the drug concentration, C(z,t), where z denotes the direction perpendicular to the thin slice of skin (see Figure 2-2), and t denotes time. Note that, since the length of the hypothesized aqueous pores is much larger than the radius of the hypothesized aqueous pores, diffusion in the pores may be assumed to be 1-D, along the z-direction. Assuming that V_{pores} is independent of time, an assumption which is valid when the skin is not perturbed during diffusive transport, Eq. (2.16) can be rewritten as follows:

$$\dot{m}_{in} - \dot{m}_{out} = V_{pores} \frac{\partial C(z,t)}{\partial t} \tag{2.17}$$

Based on the geometry of the thin slice of skin shown in Figure 2-2, V_{pores} can be defined as follows:

$$V_{pores} = (\varepsilon_p A)(\tau_p \Delta z) \tag{2.18}$$

where $\tau_p \Delta z$ is the length of the tortuous aqueous pore channels in the thin slice of skin shown in Figure 2-2, and $\varepsilon_p A$ is the area of the skin cross-section, perpendicular to the z-direction, occupied by the hypothesized aqueous pore channels. It should be noted that ε_p can be defined, for the case of a single average aqueous pore radius, r_{pore}, in the skin, as follows:

$$\varepsilon_p = \frac{N}{A} \pi r_{pore}^2 \tag{2.19a}$$

or, for the case of a distribution of aqueous pore radii, $\gamma(r_{pore})$, in the skin, as follows:[15]

$$\varepsilon_p = \frac{N}{A} \int_{r_p}^{\infty} \gamma(r_{pore}) \pi r_{pore}^2 \, dr_{pore} \tag{2.19b}$$

where N is the number of hypothesized aqueous pore channels present in a skin sample of area A. Substituting Eq. (2.18) in Eq. (2.17) yields:

$$\dot{m}_{in} - \dot{m}_{out} = \varepsilon_p \tau_p A \Delta z \frac{\partial C(z,t)}{\partial t} \tag{2.20}$$

Dividing Eq. (2.20) by the cross-sectional area of the skin slice, A, and noting that mass per unit area and per unit time is the flux, F, Eq. (2.20) can be rearranged as follows:

$$\frac{1}{\tau_p}\left[\frac{F(z+\Delta z,t) - F(z,t)}{\Delta z}\right] = \varepsilon_p \frac{\partial C(z,t)}{\partial t} \tag{2.21}$$

In the limit when Δz approaches 0, Eq. (2.21) reduces to:

$$\frac{1}{\tau_p}\left[\frac{\partial F(z,t)}{\partial z}\right] = \varepsilon_p \frac{\partial C(z,t)}{\partial t} \tag{2.22}$$

It now remains to evaluate F(z,t) in terms of C(z,t) to obtain a model equation for the partial differential form of Fick's Second Law of diffusion. The mass flow rate of drug delivered through the hypothesized aqueous pores of the thin slice of the skin (see Figure 2-2) can be modeled as follows:[23]

$$\dot{m} = (\varepsilon_p A) D_p^{\infty} H(\lambda_p)\left[\frac{C(z+\Delta z,t) - C(z,t)}{\tau_p \Delta z}\right] \tag{2.23}$$

where $\varepsilon_p A$ is the cross-sectional area of the hypothesized aqueous pore channels available to the drug at the inlet and at the outlet of the skin slice, $\tau_p \Delta z$ is the effective diffusion path length through the hypothesized aqueous pore channels in the thin slice of skin, and $H(\lambda_p)$ is the hindrance factor, which is defined using Eqs. (2.2) and (2.3). Dividing Eq. (2.23), by the cross-sectional area of the thin slice of skin, A, to obtain the flux yields:

$$F = \frac{\dot{m}}{A} = \frac{\varepsilon_p}{\tau_p} D_p^{\infty} H(\lambda_p)\left[\frac{C(z+\Delta z,t) - C(z,t)}{\Delta z}\right] \tag{2.24}$$

As Δz approaches 0, Eq. (2.24) can be further simplified to yield Fick's First Law of diffusion for the hypothesized aqueous pore channels present in the thin slice of skin:

$$F = \frac{\varepsilon_p}{\tau_p}\left[D_p^{\infty} H(\lambda_p)\frac{\partial C(z,t)}{\partial z}\right] \tag{2.25}$$

Substituting Eq. (2.25) in Eq. (2.22) yields the form of Fick's Second Law of diffusion through the hypothesized aqueous pores in the skin:

$$\frac{\partial C}{\partial t} = \frac{D_p^{\infty} H(\lambda_p)}{\tau_p^2}\frac{\partial^2 C}{\partial z^2} \tag{2.26}$$

2.3.2 Obtaining Expressions for the Transient Solution to Fick's Second Law of Diffusion in the Context of the Hypothesized Aqueous Pores in the Skin

Equation (2.26) can be solved for the general case with the following boundary and initial conditions:[23]

$$C(z = L, t) = C_d \tag{2.27a}$$

$$C(z = 0, t) = C_r \tag{2.27b}$$

$$C(z, t = 0) = C_0 \tag{2.27c}$$

where C_d is the bulk concentration of the hydrophilic permeant on the donor side of the skin, C_r is the bulk concentration of the hydrophilic permeant on the receiver side of the skin, and C_0 is the initial concentration of the hydrophilic permeant within the hypothesized aqueous pore channels in the skin. Note that in the z-direction, z = 0 corresponds to the outlet of the skin, rather than to the inlet of the skin, in order to simplify the solution of Eq. (2.26). Following the solution procedure of Fick's Second Law of diffusion through a homogeneous membrane,[23] the solution of Eq. (2.26) with the subject to the initial and boundary conditions given in Eqs. (2.27a) – (2.27c), is given by:

$$\begin{aligned} C(z,t) &= C_r + (C_d - C_r)\frac{z}{L} \\ &+ \frac{2}{\pi}\sum_{n=1}^{\infty}\frac{C_d \cos n\pi - C_r}{n}\sin\left(\frac{n\pi z}{L}\right)\exp\left(-\frac{D_p^{\infty} H(\lambda_p)}{\tau_p^2}\frac{n^2\pi^2 t}{L^2}\right) \\ &+ \frac{4C_0}{\pi}\sum_{m=0}^{\infty}\frac{1}{2m+1}\sin\left(\frac{(2m+1)\pi z}{L}\right)\exp\left(-\frac{D_p^{\infty} H(\lambda_p)}{\tau_p^2}\frac{(2m+1)^2\pi^2 t}{L^2}\right) \end{aligned} \tag{2.28}$$

The total amount of mass of hydrophilic permeant per unit area delivered across the skin, Q(t), is given by a time integral over the flux, that is, by:[23]

$$Q(t) = \int_0^t F(z=0,t)dt = \int_0^t \frac{\varepsilon_p}{\tau_p} D_p^{\infty} H(\lambda_p) \left. \frac{\partial C(z,t)}{\partial z} \right|_{z=0} dt \tag{2.29}$$

where Eq. (2.25) has been used for the definition of the flux of the hydrophilic permeant in the skin. Substituting Eq. (2.28) in Eq. (2.29) and carrying out the integration over time yields:[23]

$$\begin{aligned} Q(t) &= \frac{\varepsilon_p D_p^{\infty} H(\lambda_p) t}{\tau_p L}(C_d - C_r) \\ &+ \frac{2\varepsilon_p \tau_p L}{\pi^2} \sum_{n=1}^{\infty} \left(\frac{C_d \cos n\pi - C_r}{n^2} \right) \left[1 - \exp\left(- \frac{D_p^{\infty} H(\lambda_p)}{(\tau_p L)^2} n^2 \pi^2 t \right) \right] \\ &+ \frac{4\varepsilon_p C_0 \tau_p L}{\pi^2} \sum_{m=0}^{\infty} \left(\frac{C_d \cos n\pi - C_r}{(2m+1)^2} \right) \left[1 - \exp\left(- \frac{D_p^{\infty} H(\lambda_p)}{(\tau_p L)^2} (2m+1)^2 \pi^2 t \right) \right] \end{aligned} \tag{2.30}$$

For the special case when $C_r = C_0 = 0$, which is applicable for most permeation experiments, Eq. (2.30) can be further simplified by noting that $\cos(n\pi) = (-1)^n$ and that $\sum_{n=1}^{\infty} \frac{(-1)^n}{n^2} = -\frac{\pi^2}{12}$.[23] This yields:

$$Q(t) = (\varepsilon_p C_d \tau_p L) \left[\frac{D_p^{\infty} H(\lambda_p) t}{(\tau_p L)^2} - \frac{1}{6} - \frac{2}{\pi^2} \sum_{n=1}^{\infty} \frac{(-1)^n}{n^2} \exp\left(\frac{-D_p^{\infty} H(\lambda_p) n^2 \pi^2 t}{(\tau_p L)^2} \right) \right] \tag{2.31}$$

Equation (2.31) describes the cumulative amount of mass of hydrophilic permeant delivered through the hypothesized aqueous pore channels in the skin, per unit area, at time, t. At steady-state (for large t), Eq. (2.31) simplifies as follows:

$$Q(t) = (\varepsilon_p C_d \tau_p L) \left[\frac{D_p^{\infty} H(\lambda_p)}{(\tau_p L)^2} t - \frac{1}{6} \right] \tag{2.32}$$

From Eq. (2.32), the lag time to reach steady-state for diffusion of the hydrophilic permeant through the hypothesized aqueous pores in the skin can be evaluated by setting Q(t) equal to zero and solving for t_{lag}.[23] This yields:

$$t_{lag} = \frac{(\tau_p L)^2}{6 D_p^{\infty} H(\lambda_p)} \tag{2.33}$$

Finally, the steady-state permeability, P, for the transport of hydrophilic permeants through the hypothesized aqueous pore channels in the skin can be evaluated by dividing Eq. (2.32) by C_d and evaluating the time derivative to obtain:[23]

$$P = \frac{1}{C_d}\frac{\partial Q(t)}{\partial t} = \frac{\varepsilon_p D_p^{\infty} H(\lambda_p)}{\tau_p L} \tag{2.34}$$

which is the expression for the permeability given in Eq. (2.1). Note that for the case of a homogeneous membrane where ε_p and τ_p are equal to 1, Eqs. (2.28) – (2.34) reduce to the equations describing transport through a homogeneous membrane.[23]

2.4 Materials and Methods

2.4.1 Chemicals

Four hydrophilic permeants, ^{14}C-Urea, ^{3}H-Mannitol, ^{3}H-Raffinose, and ^{3}H-Inulin, were obtained from American Radiolabeled Chemicals, Inc. (St. Louis, MO). Phosphate Buffer Saline and Sodium Lauryl Sulfate (SLS) were obtained from Sigma-Aldrich (St. Louis, MO). All these chemicals were used as received.

2.4.2 Skin Preparation

Full-thickness human cadaver skin was obtained from the National Disease Research Institute (Philadelphia, PA) and stored at -80°C until use. Prior to use in the diffusion experiments, the skin was thawed and the subcutaneous fat was removed from the skin using a razor blade. For the experiments with untreated and with ultrasound-treated skin, the skin was sectioned and mounted in vertical Franz diffusion cells (15-mm inner diameter) obtained from Permegear (Bethlehem, PA). For the experiments with human dermis, the skin was heat-stripped to remove the epidermis by submersing the full-thickness skin in 60 °C water for 2 minutes. The epidermis was subsequently removed from the dermis by pulling off the epidermal layer with tweezers.

2.4.3 Skin Electrical Resistance Measurements

Prior to ultrasound pre-treatment, the electrical resistance of the skin mounted on the diffusion cells was measured according to previously published methods,[22] which are summarized next. A 100 mV AC voltage source at 10 Hz was generated using a signal generator (Hewlett-Packard, model HP 33120A) and applied across the skin membrane using two Ag/AgCl electrodes (In Vivo Metrics, Healdsburg, CA) for 5-10 seconds. The skin electrical current was measured using a Fluke Multimeter (Model 139, Fluke Corporation). The skin electrical resistance was obtained from the skin electrical current using Ohm's Law. Since this measurement also includes the resistance of the donor and the receiver cell solutions, a background electrical resistance measurement of just the PBS solution was made separately, and was then subtracted from the electrical resistance of the skin in the diffusion cell to determine the actual skin electrical resistance. The

electrical resistance, R, of all the skin samples was measured and multiplied by the skin area available to ultrasound exposure in the diffusion cell (A = 1.77 cm^2). Any skin sample with an initial RA value of <50 kOhm*cm^2, corresponding to an initial current of 3.3 μAmps, was considered damaged and was discarded, and was subsequently replaced with an intact skin sample.[22]

2.4.4 Ultrasound Pre-Treatment Protocol

Ultrasound, in the presence of a coupling medium containing 1% (w/v) SLS in PBS, was applied to the intact human full-thickness skin samples based on previously published methods.[10,24] Ultrasound (VCX 400, Sonics and Materials, Inc., Newtown, CT) was applied to the skin samples at the following conditions: frequency - 20 kHz, intensity - 7.2 W/cm^2, pulse length - 5 sec on, 5 sec off, and tip displacement - 3 mm,[10,24] until the measured skin electrical current reached values between 25 – 30 μAmps for the low ultrasound-SLS dose and between 250 – 300 μAmps for the high ultrasound-SLS dose. As stated in Section 2.1, these skin electrical current values will enable us to study how the porosity, the tortuosity, and the aqueous pore radii change as the skin structural perturbation is increased due to the ultrasound treatment. After each minute of ultrasound exposure, the coupling medium was changed to minimize the impact of thermal effects on the permeation enhancement of the skin,[10,24] and measurements of the skin electrical current were conducted to determine if the target skin electrical current had been reached. Once the desired skin electrical current was attained, the skin sample was removed from the diffusion cell and was rinsed to remove the excess coupling medium from the skin surface in preparation for the dual radiolabeled diffusion experiments.

2.4.5 Dual Radiolabeled Diffusion Experiments

Dual radiolabeled diffusion experiments were carried out using vertical Franz diffusion cells. In each experiment, urea, which is carbon-14 labeled, was paired with a tritium-labeled permeant – mannitol, raffinose, or inulin. For the untreated skin samples, 2 ml of a solution containing 10 μCi/ml of urea and 10 μCi/ml of one of the three tritium-labeled permeants was placed in the donor chamber, while for the ultrasound-treated skin samples and the dermis samples, 2 ml of a solution containing 1 μCi/ml of urea and 1 μCi/ml of one of the three tritium-labeled permeants was placed in the donor chamber. A higher concentration of the radiolabeled permeants was used in the untreated skin samples relative skin samples treated with ultrasound and SLS and the dermis samples to ensure that enough permeant was delivered through the untreated skin samples to be detected by the scintillation counter. Aliquots (~400 μL) of the receiver chamber were taken at predetermined time points over a period of 48 hours to ensure transition into the steady-state domain for each of the permeants and skin sample types considered. The radioactivity of these aliquot samples was then measured using the dual radiolabeled counting mode in a scintillation counter (Packard, Tri-Carb®, 2200 CA). Plots of Q(t) versus time were then generated from the results of the scintillation counting of the aliquots taken from the receiver cell.

2.4.6 Regression Analysis of the Dual Radiolabeled Diffusion Experimental Data using Eq. (2.31) to Evaluate the Porosity, the Tortuosity, and the Aqueous Pore Radii

In the dual radiolabeled diffusion experiments, a ^{14}C-labeled hydrophilic permeant and a ^{3}H-labeled hydrophilic permeant are *delivered simultaneously using the same skin sample*. This allows Eq. (2.31) to be utilized to model the amounts of ^{14}C-labeled hydrophilic permeant ($Q(t)_{14C}$) and of ^{3}H-labeled hydrophilic permeant ($Q(t)_{3H}$) delivered across the skin, as follows:

$$Q(t)_{14C} = (\varepsilon C_d \tau L)_{14C} \left[\left(\frac{D^{\infty} H(\lambda)}{(\tau L)^2} \right)_{14C} t - \frac{1}{6} - \frac{2}{\pi^2} \sum_{n=1}^{\infty} \frac{(-1)^n}{n^2} \exp\left(- \left(\frac{D^{\infty} H(\lambda)}{(\tau L)^2} \right)_{14C} n^2 \pi^2 t \right) \right] \quad (2.35a)$$

$$Q(t)_{3H} = (\varepsilon C_d \tau L)_{3H} \left[\left(\frac{D^{\infty} H(\lambda)}{(\tau L)^2} \right)_{3H} t - \frac{1}{6} - \frac{2}{\pi^2} \sum_{n=1}^{\infty} \frac{(-1)^n}{n^2} \exp\left(- \left(\frac{D^{\infty} H(\lambda)}{(\tau L)^2} \right)_{3H} n^2 \pi^2 t \right) \right] \quad (2.35b)$$

The quantities, $(\varepsilon C_d \tau L)$ and $[D^{\infty}H(\lambda)/(\tau L)^2]$, in Eqs. (2.35a) and (2.35b) can be evaluated for both the ^{14}C-labeled hydrophilic permeant and the ^{3}H-labeled hydrophilic permeant from the experimental data using non-linear regression methods. Specifically, non-linear regression was conducted with DataFit 8.1 (Oakdale Engineering) with $(\varepsilon C_d \tau L)$ and $[D^{\infty}H(\lambda)/(\tau L)^2]$ for both the ^{14}C-labeled and the ^{3}H-labeled hydrophilic permeants selected as the regression parameters. DataFit 8.1 uses the Levenberg-Marquardt method as the algorithm to adjust the values of the initial estimates of the regression parameters to improve the fit of the nonlinear regression model. This regression analysis yields the following four equations:

$$\left(\varepsilon C_d \tau L\right)_{14C} = R_1 \tag{2.36a}$$

$$\left(\frac{D^{\infty} H(\lambda)}{(\tau L)^2}\right)_{14C} = R_2 \tag{2.36b}$$

$$\left(\varepsilon C_d \tau L\right)_{3H} = R_3 \tag{2.36c}$$

$$\left(\frac{D^{\infty} H(\lambda)}{(\tau L)^2}\right)_{3H} = R_4 \tag{2.36d}$$

where R_1, R_2, R_3, and R_4 are the values of the four expressions above obtained from the non-linear regression analysis. For both the ^{14}C-labeled hydrophilic permeant and the ^{3}H-labeled hydrophilic permeant, the donor concentration, C_d, and the bulk diffusion coefficient, D_p^{∞}, are known. In addition, the thickness of the skin, L, is also known. Therefore, Eqs. (2.36a) – (2.36d) can be simplified as follows:

$$\left(\varepsilon\tau\right)_{14C} = \frac{R_1}{C_{d,14C} L} = a \tag{2.36a}$$

$$\left(\frac{H(\lambda)}{\tau^2}\right)_{14C} = \frac{R_2 L^2}{D_{14C}^{\infty}} = b \tag{2.36b}$$

$$\left(\varepsilon\tau\right)_{3H} = \frac{R_3}{C_{d,3H} L} = c \tag{2.36c}$$

$$\left(\frac{H(\lambda)}{\tau^2}\right)_{3H} = \frac{R_4 L^2}{D_{3H}^{\infty}} = d \tag{2.36d}$$

where a, b, c, and d are known quantities, as defined in Eqs. (2.36a) – (2.36d). The tortuosity for both the ^{14}C-labeled hydrophilic permeant and the ^{3}H-labeled hydrophilic permeant may be eliminated from Eqs. (2.36a) – (2.36d) as follows:

$$\left(\varepsilon\tau\right)_{14C}^2 \left(\frac{H(\lambda)}{\tau^2}\right)_{14C} = \left(\varepsilon^2 H(\lambda)\right)_{14C} = a^2 b \tag{2.37a}$$

$$(\varepsilon\tau)_{3H}^2\left(\frac{H(\lambda)}{\tau^2}\right)_{3H} = \left(\varepsilon^2 H(\lambda)\right)_{3H} = c^2 d \tag{2.37b}$$

At first glance, Eqs. (2.37a) and (2.37b) appear as if there are now two equations for the four unknowns – ε_{14C}, $H(\lambda)_{14C}$, ε_{3H}, and $H(\lambda)_{3H}$. However, for the case of a *single average aqueous pore radius*, as implemented by Peck *et al.*[9] and by Tang *et al.*,[10] Eqs. (2.2) and (2.3) show that $H(\lambda)$ is a function of r_{pore}, while Eq. (2.19a) shows that ε is also a function of r_{pore}, as well as of the total number of aqueous pore channels in the skin, N. Therefore, there are two equations and two unknowns (r_{pore} and N), indicating that a unique solution is possible. Furthermore, for the case of a single average pore radius, the porosity of the skin for the ^{14}C-labeled permeant (ε_{14C}) is equal to the porosity of the skin for the ^{3}H-labeled permeant (ε_{3H}). Therefore, Eqs. (2.37a) and (2.37b) can be combined as follows:

$$\frac{H(\lambda)_{3H}}{H(\lambda)_{14C}} = \frac{c^2 d}{a^2 b} \tag{2.38}$$

Equation (2.38) can then be solved for r_{pore}, the *average aqueous pore radius* (see Eqs. (2.2) and (2.3)). The porosity of the skin, $\varepsilon_{14C} = \varepsilon_{3H} = \varepsilon$, can then be determined using either Eqs. (2.37a) or (2.37b). Finally, the tortuosity of the aqueous pore channels for the ^{14}C-labeled hydrophilic permeant (τ_{14C}) and for the ^{3}H-labeled hydrophilic permeant (τ_{3H}) can be determined using Eqs. (2.36a) or (2.36b) and Eqs. (2.36c) or (2.36d), respectively.

For the case of a distribution of aqueous pore radii in the skin, as proposed by Tezel *et al.*,[11] Eqs. (2.37a) and (2.37b) can again be reduced to a system of two equations with two unknowns. Specifically, if Eqs. (2.9) and (2.19b) are used to define the hindrance factor, $H(\lambda_p)$, and the porosity, ε_p, respectively, characterizing the distribution

of aqueous pore channels in the skin, two unknowns remain, N and $\gamma(r_{pore})$. Once again, this results in a system of two equations for the two unknowns, N and $\gamma(r_{pore})$, which can be solved by substituting Eqs. (2.9) and (2.19b) in Eqs. (2.37a) and (2.37b), and subsequently taking the ratio to eliminate the total number of aqueous pore channels present in the skin, N, to obtain:

$$\left(\frac{\int_{r_{3H}}^{\infty}\gamma(r_{pore})\pi r^2\,dr_{pore}}{\int_{r_{14C}}^{\infty}\gamma(r_{pore})\pi r^2\,dr_{pore}}\right)\left(\frac{\int_{r_{3H}}^{\infty}\gamma(r_{pore})H(\lambda)\,dr_{pore}}{\int_{r_{14C}}^{\infty}\gamma(r_{pore})H(\lambda)dr_{pore}}\right)=\frac{c^2d}{a^2b} \tag{2.39}$$

If a normalized distribution function of the form:[11]

$$\gamma(r_{pore})=\frac{2}{\sigma\sqrt{2\pi}}\exp\left(-\frac{r_{pore}^2}{2\sigma^2}\right) \tag{2.40}$$

is used for $\gamma(r_{pore})$, as proposed by Tezel *et al.*,[11] there is only one unknown parameter, σ, the standard deviation of the normalized distribution function, to solve for in Eq. (2.39), which can done numerically. Once σ is determined in this manner, Eq. (2.9) can then be used to determine $H(\lambda)$ for both the ^{14}C-labeled hydrophilic permeant and for the ^{3}H-labeled hydrophilic permeant. With $H(\lambda)$ evaluated in this manner, the porosities of the ^{14}C-labeled and the ^{3}H-labeled hydrophilic permeants, ε_{14C} and ε_{3H}, can then be determined using Eqs. (2.37a) and (2.37b), respectively. Finally, the tortuosity corresponding to the ^{14}C-labeled hydrophilic permeant, τ_{14C}, can be evaluated using either Eqs. (2.36a) or (2.36b), and the tortuosity corresponding to the ^{3}H-labeled hydrophilic permeant, τ_{3H}, can be evaluated using either Eqs. (2.36c) or (2.36d).

In addition, the steady-state permeability of both the ^{14}C-labeled and the ^{3}H-labeled hydrophilic permeants can be calculated from the two regression parameters, $(\varepsilon C_d \tau L)$ and $[D^{\infty}H(\lambda)/(\tau L)^2]$, using the following equation:

$$P = \frac{1}{C_d}(\varepsilon C_d \tau L)\left[\frac{D^{\infty}H(\lambda)}{(\tau L)^2}\right] \tag{2.41}$$

which, upon simplification, is equal to Eq. (2.1).

2.5 Results and Discussion

2.5.1 Dual Radiolabeled Diffusion Experimental Data

Figure 2-3 shows the cumulative amount of radiolabeled permeant delivered across the skin, Q(t), as a function of time for each of the four hydrophilic permeants used in the diffusion experiments (Figure 2-3a: mannitol, Figure 2-3b: raffinose, Figure 2-3c: inulin, and Figure 2-3d: urea). In each of the plots, the black diamonds correspond to data obtained using the dermis as the model skin membrane, the open squares correspond to data obtained using full-thickness skin treated with a high dose of low-frequency ultrasound, the open triangles correspond to data obtained using full-thickness skin treated with a low dose of low-frequency ultrasound, and the grey diamonds correspond to data obtained using untreated full-thickness skin. Each data point represents an average of 3 – 6 skin samples. Representative error bars, corresponding to $\pm$ 1 S.D., have been included to provide an estimate of the error in the average value (note that in Figure 2-3d for the delivery of urea, the error bars have been omitted for clarity). For data corresponding to delivery in skin treated with low-frequency ultrasound, multiple data points are presented because there was a difference in sampling times between the

experimental runs. In Figure 2-3d, the shaded regions for data corresponding to the delivery in skin treated with a high dose of ultrasound and SLS, with a low dose of ultrasound and SLS, and in untreated skin have been included to increase clarity.

Several trends may be observed from an examination of Figures 2-3a through 2-3d. In each of the figures, in the period from 0 to 20 hours, the amount of permeant delivered through each of the skin samples follows the expected permeability trend – the dermis (black diamonds) is the most permeable, followed by full-thickness skin treated with a high US-SLS dose (open squares), then by full-thickness skin treated with a low US-SLS dose (open triangles), and finally by untreated full-thickness skin (grey diamonds). Also, for each skin type (dermis, a high US-SLS dose, a low US-SLS dose, and untreated), the amount of hydrophilic permeant delivered across the skin decreases as the radius of the permeant increases (urea < mannitol < raffinose < inulin). However, by 48 hours, the results presented in Figures 2-3a through 2-3d indicate that the total amount of permeant delivered, Q(t), in the untreated skin (grey diamonds) is greater than in some of the skin samples treated with a low dose of ultrasound and SLS (open triangles). There is some speculation that the observed increase in the permeability of untreated skin after exposure to an aqueous solution for a long time may be attributed to a skin hydration effect,[25] in which water acts as a chemical enhancer to perturb the structure of the skin. According to the aqueous pore pathway models proposed by Tang *et al.*[10] and by Tezel *et al.*[11], since the permeability of the untreated skin increases after 20 hours of exposure to an aqueous solution, it should also follow that there would be a corresponding increase in the skin electrical current.[10,11] However, in the untreated skin samples used in these experiments, no large increase in the skin electrical current was

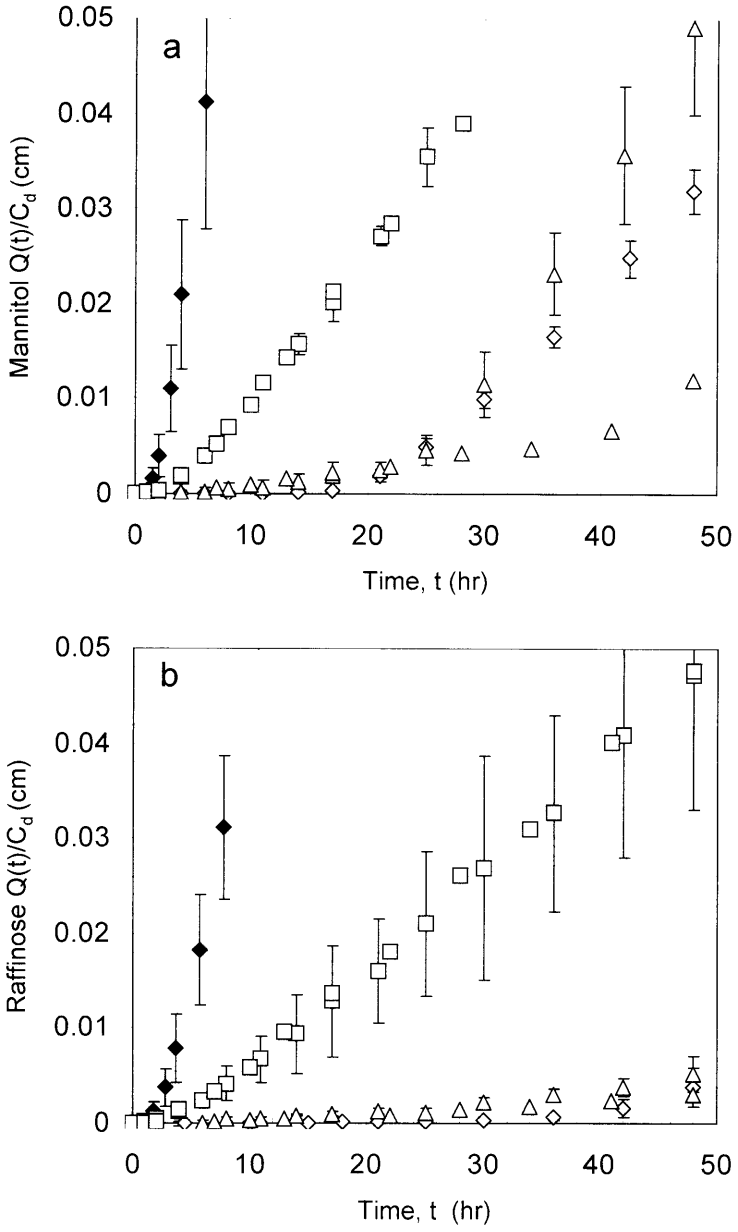

Figure 2-3: Plots of the cumulative amount of hydrophilic permeant, Q(t), delivered through the skin as a function of time, t, normalized by the initial donor concentration, C_d. (a) mannitol, (b) raffinose, (c) inulin, and (d) urea. Key: Untreated skin – grey diamonds, low dose of US-SLS treatment – open triangles, high dose of US-SLS treatment – open squares, dermis – black diamonds. Sample error bars correspond to $\pm$ 1 S.D.

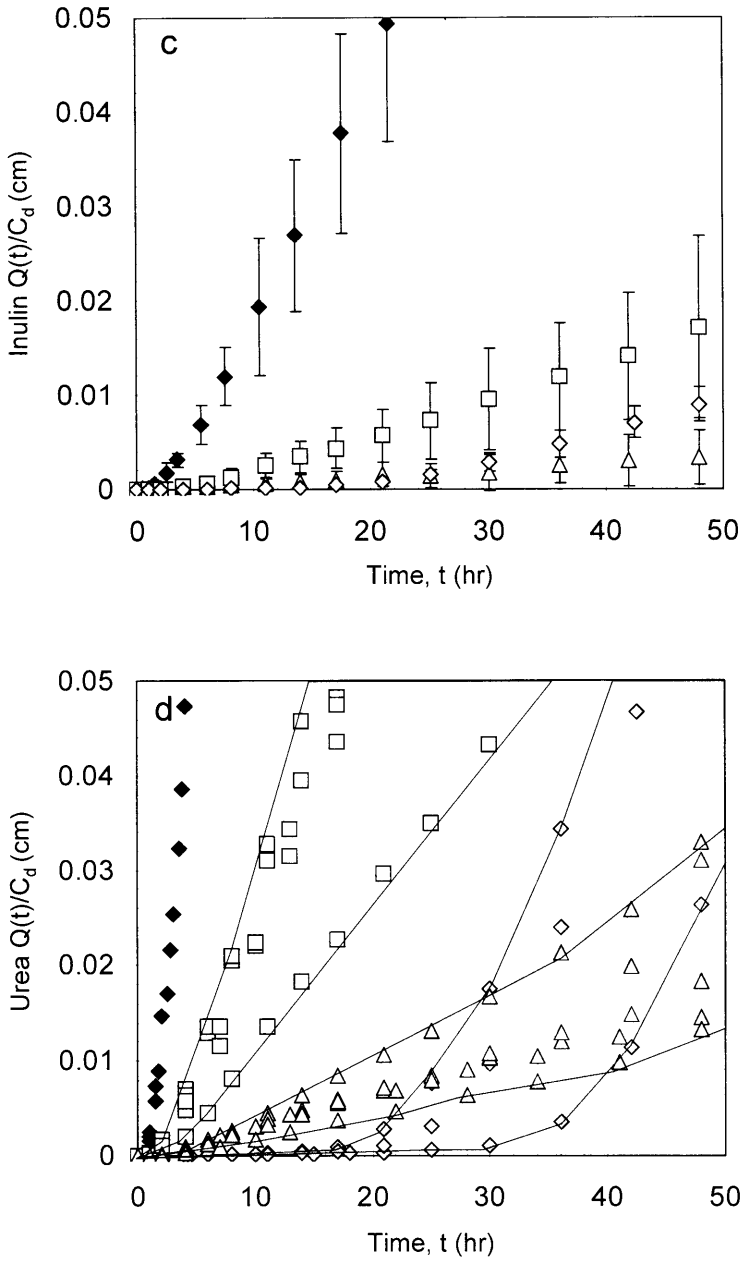

Figure 2-3 (continued): In (d), the error bars have been replaced with shaded regions to aid the reader in identifying the domains for the delivery of urea through untreated skin, through skin treated with a low dose of ultrasound, and through skin treated with a high dose of ultrasound.

observed during the 48 hour experiment, suggesting that the increased perturbation in the skin due to the exposure to water for more than 20 hours cannot account for the increased permeation observed in the untreated skin case.

Another possible explanation of the untreated skin data presented in Figures 2-3a and 2-3d is that the untreated skin may possess a large amount of diffusion sinks, such as binding sites in the skin,[1] a branched network of aqueous pore channels in the skin,[15] or diffusion into the skin cells themselves.[1] These diffusion sinks would initially decrease the rate of delivery of the hydrophilic permeants through the skin, due to the hydrophilic permeants being retained in the skin. Once the diffusion sinks have reached equilibrium, such that they are no longer sinks to the diffusive transport process, the hydrophilic permeants are then free to diffuse through the skin, resulting in a rapid increase in the observed amount of hydrophilic permeant delivered through the skin and in the observed onset of steady-state diffusion. The application of ultrasound and SLS appears to reduce the impact of these diffusion sinks on the overall transport process, since there is no corresponding increase in the permeability in skin samples treated with a high dose of ultrasound and SLS in Figures 2-3a – 2-3d. For example, if the aqueous channels exist as a branched network of interconnected channels, rather than the unbranched channels assumed for the transport model presented in this paper (see Figure 2-2), ultrasound and SLS may make these channels less branched. This would then provide a more direct route of transport through the skin membrane (i.e. decrease τ_p).

The data in Figures 2-3a through 2-3d also suggest that the lag time to reach steady-state delivery of the hydrophilic molecules decreases as the stratum corneum is physically perturbed. Using the regression analysis of the diffusion data described in

Table 2-1: Values of the Lag Time to Reach Steady-State, t_{lag}, Calculated using Eq. (2.33) and the Data Presented in Figures 2-3a through 2-3d.[a,b,c]

Skin Type	Urea	Mannitol	Raffinose	Inulin
Untreated	63.4 ± 5.4	37.3 ± 1.7	70.9 ± 10.2	33.3 ± 1.0
Low US-SLS Dose	2.45 ± 0.04	7.90 ± 3.47	15.2 ± 2.9	2.36 ± 0.93
High US-SLS Dose	1.75 ± 0.15	4.23 ± 0.22	5.48 ± 0.37	6.00 ± 0.42
Dermis	1.41 ± 0.10	2.07 ± 0.05	3.17 ± 0.13	3.73 ± 0.20

a – Errors are presented as ± 1 S.D.
b – The reported values have units of hours.
c – US stands for ultrasound.

Section 2.4.6, it was possible to evaluate the parameter, $[D_p^{\infty} H(\lambda_p)/(\tau_p L)^2]$, for each hydrophilic permeant in each of the skin samples used in the dual radiolabeled diffusion experiments. By substituting the values of $[D_p^{\infty} H(\lambda_p)/(\tau_p L)^2]$ in Eq. (2.33), it was possible to determine the lag time to reach steady-state, t_{lag}, for each permeant and skin type used in this investigation. These values are reported in Table 2-1. As Table 2-1 shows, t_{lag} *decreases* in skin which is physically perturbed by ultrasound, or by heat-stripping, relative to t_{lag} in untreated skin for each hydrophilic permeant examined. These results for t_{lag} differ from those Tezel *et al.*, which suggested that the tortuosity of the aqueous pore channels in the skin, τ, and, therefore, through Eq. (2.33), that the lag time to reach steady-state, t_{lag}, *both increase* with an increase in the skin perturbation induced by ultrasound.[11]

2.5.2 Evaluation of the Average Aqueous Pore Radii from an Analysis of Log P_{3H} vs. Log P_{Urea} Plots using Steady-State Analysis Methods

Figure 2-4 shows plots of the permeability data from the three dual radiolabeled systems examined in this experimental study. The ^{3}H-mannitol – ^{14}C-urea permeability data is presented in Figure 2-4a, the ^{3}H-raffinose – ^{14}C-urea permeability data is presented in Figure 2-4b, and the ^{3}H-inulin – ^{14}C-urea permeability data is presented in Figure 2-4c. Note that each data point in Figures 2-4a through 2-4c represents a single diffusion experiment. The values of the permeability for both the tritium-labeled permeant and urea were calculated from the regression parameters, $(\varepsilon_p C_d \tau_p L)$ and $[D_p^{\infty} H(\lambda_p)/(\tau_p L)^2]$, by using Eq. (2.41) in the time interval from 0 – 20 hours to avoid any contribution from the "hydration effect" which was observed for untreated skin in Figures 2-3a through 2-3d. Note that for the cases corresponding to the delivery of mannitol-urea and to the delivery of inulin-urea in untreated skin, the values of the regression parameters were not significantly different from zero, and, therefore, according to Eq. (2.41), the permeability was also not different from zero. Consequently, no permeability values for the mannitol-urea and for the inulin-urea delivery systems using untreated skin have been reported in Figures 2-4a through 2-4c.

The permeability data were then linearly regressed using Eq. (2.4b) to determine if a slope of 1 passed through the permeability data presented in Figures 2-4a through 2-4c. For the mannitol-urea data, the regressed value of the slope was 1.06 ± 0.06, with an R^2 value of 0.99. For the raffinose-urea data, the regressed value of the slope was 1.00 ± 0.08, with an R^2 value of 0.97. For the inulin-urea data, the regressed value of the slope was 1.03 ± 0.09, with an R^2 value of 0.98. In Figures 2-4a through 2-4c, then, the solid

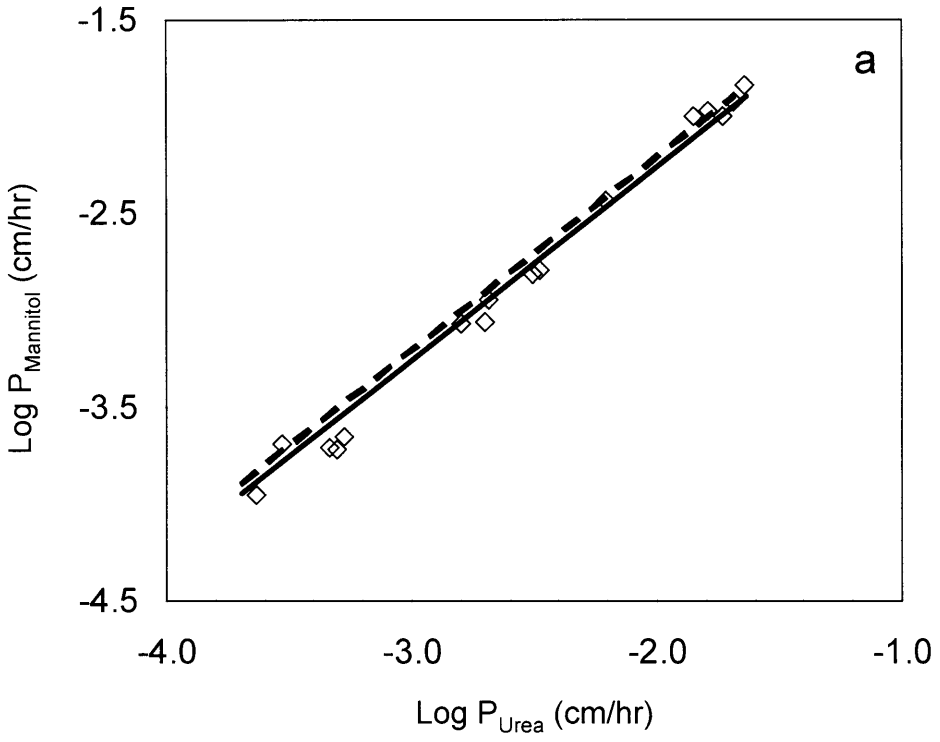

Figure 2-4: Log P of the tritium-labeled permeants plotted against log P of urea, the carbon-14 labeled permeant. (a) Mannitol-Urea, (b) Raffinose-Urea, and (c) Inulin-Urea. Key: data points – open diamonds, ideal slope of 1 – solid line, and limiting case of infinitely large aqueous pore channels – dashed line.

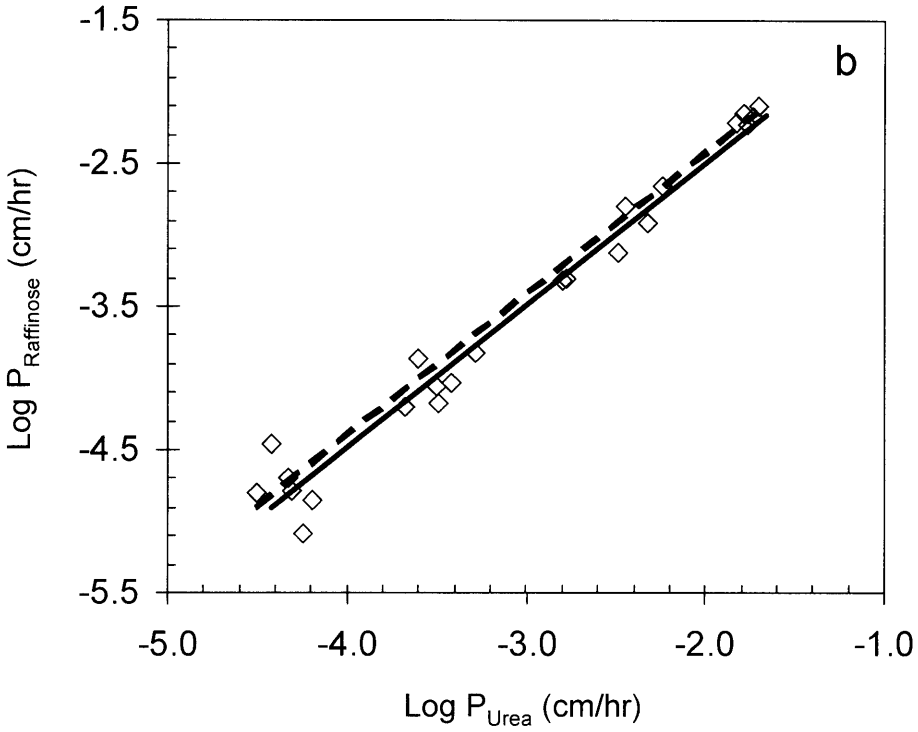
b
-1.5
-2.5
-3.5
-4.5
-5.5
-5.0
-4.0
-3.0
-2.0
-1.0
Log $P_{Raffinose}$ (cm/hr)
Log P_{Urea} (cm/hr)

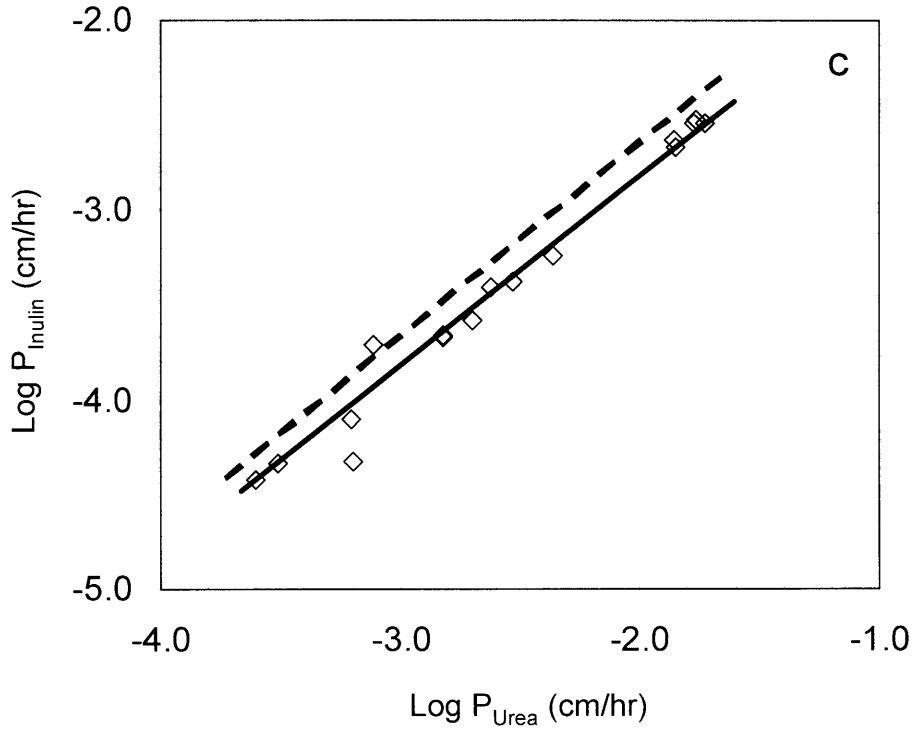
c
-2.0
-3.0
-4.0
-5.0
-4.0
-3.0
-2.0
-1.0
Log P_{Inulin} (cm/hr)
Log P_{Urea} (cm/hr)

lines, corresponding to the ideal slope of 1 through the data, have been added to demonstrate that the data are indeed in agreement with the expression in Eq. (2.4b).

In addition to the solid lines corresponding to the ideal slope of 1 through the data, dashed lines have also been added to Figures 2-4a through 2-4c, which represent a limiting case where: 1) the aqueous pores in the skin are infinitely large, such that the ratio of the hindrance factors for the tritium-labeled permeant and urea is equal to unity, and 2) the porosity and the tortuosity values are not permeant dependent, such that the porosity and the tortuosity ratios are also equal to unity. When (1) and (2) are satisfied, Eq. (2.4b) reduces to:

$$\log P_{3H} = \log \frac{D_{3H}^{\infty}}{D_{Urea}^{\infty}} + \log P_{Urea} \tag{2.42}$$

As can be seen from a comparison of the position of the data points in Figures 2-4a through 2-4c relative to the dashed line representing Eq. (2.42), it would seem that the radii of the aqueous pore channels in the human skin samples used in these studies may be considered infinitely large, since many of the data points lie near or above the dashed line, which represents the limiting case of infinitely large aqueous pore channels. This observation may be confirmed from an evaluation of the average aqueous pore radii in each type of skin sample used for the three dual permeant delivery systems. If it is assumed that the porosity and the tortuosity ratios are unity (as was done by Peck *et al.*, and by Tang *et al.*),[9,10] it is then possible to determine the value of the hindrance factor ratio using Eq. (2.4b), from which the average available pore radii, r_{pore}, may be determined. The values of the hindrance factor ratio and of the average available pore radii are reported in Tables 2-2 through 2-4 for the mannitol-urea system, for the raffinose-urea system, and for the inulin-urea system, respectively.

Table 2-2: Values of the Hindrance Factor Ratio and of the Average Available Pore Radii Calculated from the Permeability Data Obtained from the Mannitol-Urea Delivery System.

Skin Type	Hindrance Factor Ratio[a] $[H(\lambda)_{mannitol}/ H(\lambda)_{urea}]$	Average Available Pore Radii[b] (Å)		
		Low	Average	High
Low US-SLS Dose	0.78 ± 0.20	21	41	450
High US-SLS Dose	0.84 ± 0.09	36	57	130
Dermis	1.01 ± 0.11	91	∞	∞

a – Errors correspond to $\pm$ 1 S.D.
b – The high and the low values reported correspond to 1 standard deviation from the average value of the aqueous pore radii.

An examination of the values of the hindrance factor ratios in Tables 2-2 through 2-4 reveals that these are very close to unity (for example, see the low US-SLS dose skin and the high US-SLS dose skin values in Table 2-2), or are not significantly different from unity (for example, see all the skin types in Table 2-3). Using Eqs. (2.2) and (2.3), these high values of the hindrance factor ratios lead to the prediction of very large values of the average available pore radii. The range of average values of the aqueous pore radii reported in Tables 2-2 through 2-4 (41 Å - infinitely large pores) are also much larger than the values reported by Peck *et al.* (20 ± 5 Å)[9] or by Tang *et al.* (25 ± 20 Å)[10] for similarly-sized permeants. This result suggests, physically, that the particular *human full-thickness* skin samples used in these skin permeation studies possessed much larger aqueous pore channels than those present in those present in the *pig full-thickness* skin samples used by Peck *et al.* and by Tang *et al.* In addition, due to the amount of scatter in the permeation data reported in Figures 2-4a through 2-4c, several of the average values of the hindrance factor ratios reported in Tables 2-2 through 2-4 have very large

Table 2-3: Values of the Hindrance Factor Ratio and of the Average Available Pore Radii Calculated from the Permeability Data Obtained from the Raffinose-Urea Delivery System.

Skin Type	Hindrance Factor Ratio[a] $[H(\lambda)_{raffinose}/ H(\lambda)_{urea}]$	Average Available Pore Radii[b] (Å)		
		Low	Average	High
Untreated	1.09 ± 0.70	25	∞	∞
Low US-SLS Dose	0.80 ± 0.31	32	88	∞
High US-SLS Dose	0.82 ± 0.21	43	98	∞
Dermis	1.01 ± 0.09	225	∞	∞

a – Errors correspond to $\pm$ 1 S.D.
b – The high and the low values reported correspond to 1 standard deviation from the average value of the aqueous pore radii.

Table 2-4: Values of the Hindrance Factor Ratio and of the Average Available Pore Radii Calculated from the Permeability Data Obtained from the Inulin-Urea Delivery System.

Skin Type	Hindrance Factor Ratio[a] $[H(\lambda)_{inulin}/ H(\lambda)_{urea}]$	Average Available Pore Radii[b] (Å)		
		Low	Average	High
Low US-SLS Dose	0.67 ± 0.28	48	111	800
High US-SLS Dose	0.62 ± 0.05	82	95	111
Dermis	0.71 ± 0.04	111	128	151

a – Errors correspond to $\pm$ 1 S.D.
b – The high and the low values reported correspond to 1 standard deviation from the average value of the aqueous pore radii.

standard deviation values. This results in several of the values of the hindrance factor ratios being insignificantly different from unity (i.e. the error bars include unity). This, in turn, leads to infinitely large aqueous pores being included in the range of values for the average available pore radii (see Tables 2-2 and 2-3), which suggests that hindrance may not have contributed significantly to the transport of hydrophilic permeants in the skin samples used in this study. The large standard deviations in the average values of the hindrance factor ratios also leads to the conclusion that there is no significant increase, or decrease, in the hindrance factor ratio as a function of skin perturbation, reconfirming that, based on *the steady-state analysis methods* used here, the radius of the aqueous pore channels in the skin samples utilized in these studies does not increase with ultrasound treatment of the skin. This result further confirms the results of Tang *et al.* and of Tezel *et al.* that ultrasound treatment likely creates new aqueous pore channels which are similar in radius to the aqueous pore channels present in untreated skin.[10,11]

It should be noted that while there was no significant change in the slope of the best-fit line through the data in Figures 2-4a through 2-4c from the predicted value of 1 as a function of permeant size, this does not imply that the conventional porous pathway hypothesis proposed by Peck *et al.* (for two uncharged hydrophilic permeants)[9] and by Tang *et al.* (for one uncharged hydrophilic permeant and one charged hydrophilic permeant)[10] performs better than the modified porous pathway model proposed by Tezel *et al.* (which incorporates the possible existence of a distribution of pore radii).[11] In their study, Tezel *et al.* were able to observe a significant increase in the slope of -1, predicted by the conventional porous pathway hypothesis (see Eq. (2.7)), using hydrophilic permeants which ranged in radius from (4.4 Å – 26 Å) combined with skin electrical

current measurements.[11] Because of the large average radius of the aqueous pore channels in these skin samples (see Tables 2-2 through 2-4), the range of permeant radii used in this investigation (2.6 Å – 12 Å) may not be sufficiently large to observe a significant decrease in the value of the slope from 1, predicted by Eq. (2.4b), in Figures 2-4a through 2-4c as the radius of the hydrophilic permeant was increased. In order to evaluate the distribution of aqueous pore channels in the skin samples used in this investigation, in the following section, I utilize the theoretical techniques presented in Section 2.3.3 to evaluate the standard deviation in the hypothesized distribution of pore radii, as well as the porosity and the tortuosity, as a function of both the radius of the hydrophilic permeant and the extent of skin perturbation induced by ultrasound and by heat-stripping of the stratum corneum.

2.5.3 Evaluation of the Distribution of Pore Radii, the Porosity, and the Tortuosity as a Function of Both the Radius of the Hydrophilic Permeant and the Extent of Perturbation Induced in the Skin

The average values of the hindrance factor, the porosity, and the tortuosity are presented as a function of the skin electrical resistivity, a quantitative measure of the extent of skin perturbation, in Figures 2-5a through 2-5c, respectively. In each figure, the black diamonds correspond to the data for urea, the open squares correspond to the data for mannitol, the open triangles correspond to the data for raffinose, and the open circles correspond to the data for inulin. Error bars represent $\pm$ 1 standard deviation corresponding to the average of 5 or 6 six diffusion experiments.

Due the large size of the error bars associated with the values of the hindrance factor reported in Figure 2-5a, the hindrance factor does not significantly depend on the extent of perturbation induced in the skin by ultrasound. Since the hindrance factor does not vary significantly with ultrasound treatment, one may conclude that the average available pore channel radius also does not vary significantly with ultrasound treatment. However, there is evidence that the value of the hindrance factor corresponding to the larger hydrophilic permeants, raffinose and inulin, is significantly increased ($p<0.05$, using the t-statistic for the difference in the two means[26]) when the epidermis is removed from the skin, suggesting that the average radii of the aqueous pore channels in the dermis may be larger than the average radii of the aqueous pore channels in the epidermis.

Figure 2-5a also demonstrates that there is a significant dependence of the hindrance factor on the radius of the permeant, as expected from Eqs. (2.2) and (2.3). Specifically, the values of the hindrance factor for inulin are significantly lower ($p<0.05$) than the values of the hindrance factor for urea and mannitol. Figure 2-5a also shows that the average value of the hindrance factor of raffinose is lower than that of urea and mannitol and higher than that of inulin, but, due the large values of the standard deviations (see the error bars in Figure 2-5a) the observed differences cannot be viewed as being significant. However, because of the small difference in the radii of urea (2.6 Å) and mannitol (4.4 Å), there is no significant difference in the values of the hindrance factors of urea and mannitol. Therefore, based on the data presented in Figure 2-5a, the following trend is observed in values of the hindrance factor as a function of the radius of the permeant: urea and mannitol > raffinose > inulin.

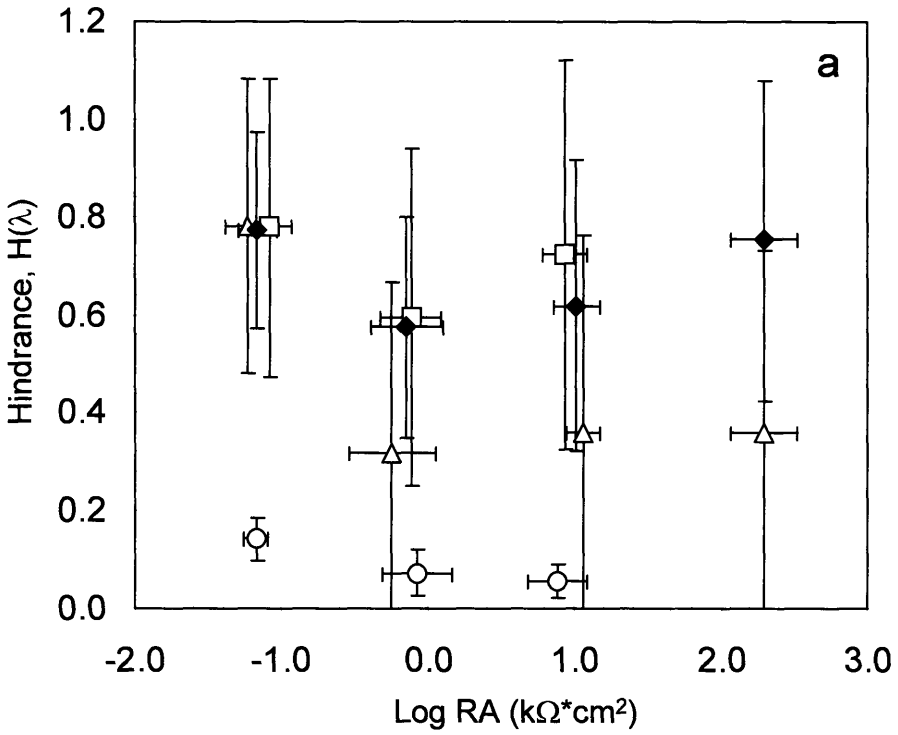

Figure 2-5: Plots of (a) the hindrance factor, H(λ), (b) the porosity, ε, and (c) the tortuosity, τ, as a function of skin perturbation as quantified by the skin electrical resistivity, RA, measurements. Key: urea – black diamonds, mannitol – open squares, raffinose – open triangles, and inulin – open circles. Error bars correspond to $\pm$ 1 standard deviation. A dashed line has been added in (c) to indicate the location of the lower bound value of $\tau = 1$.

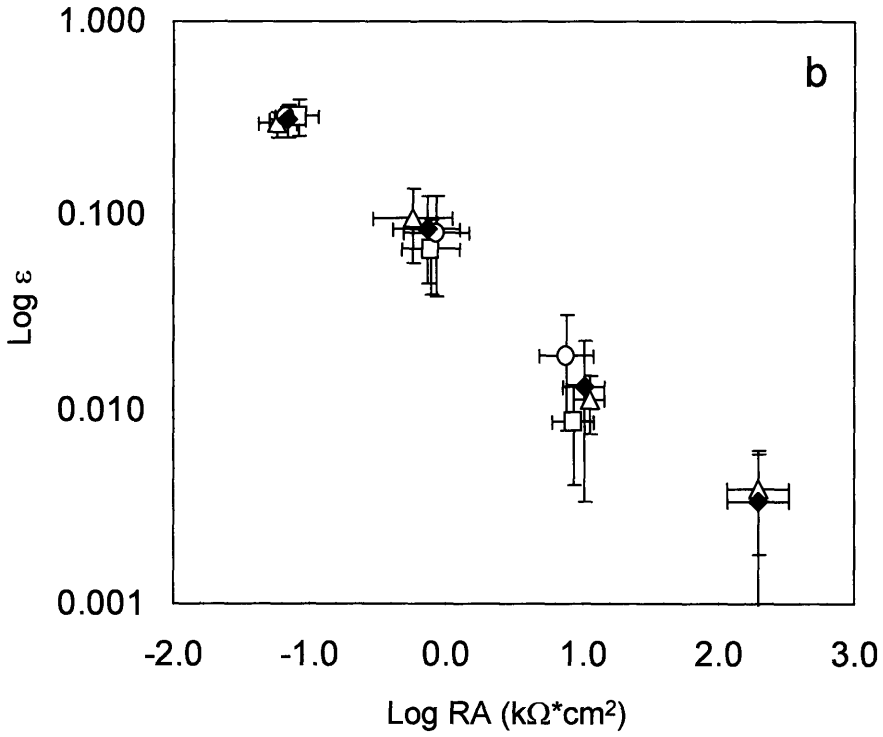
b
1.000
0.100
0.010
0.001
Log ε
-2.0
-1.0
0.0
1.0
2.0
3.0
Log RA (kΩ*cm²)

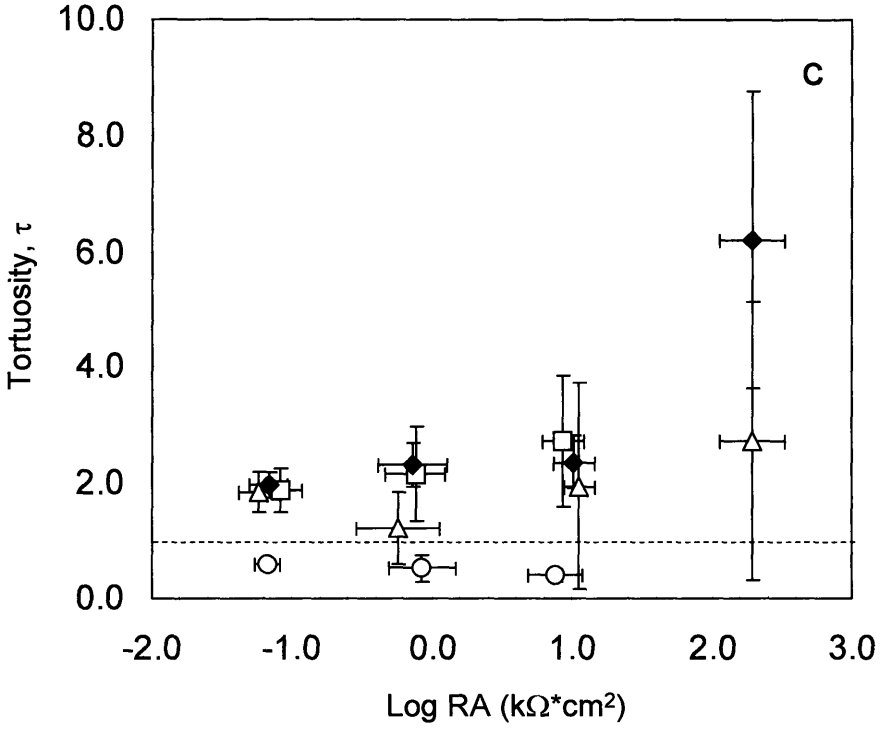
c
10.0
8.0
6.0
4.0
2.0
0.0
Tortuosity, τ
-2.0
-1.0
0.0
1.0
2.0
3.0
Log RA (kΩ*cm²)

Figure 2-5b shows that the porosity of the skin increases as the extent of skin perturbation increases, as quantified by the decreasing values of the skin electrical resistivity, RA. This observation suggests that increased perturbation of the skin due to ultrasound treatment, or due to heat-stripping, of the skin results in an increase of the fraction of the skin surface area occupied by the aqueous pore channels. According to Eqs. (2.19a) and (2.19b), this increase in the porosity may result from: (i) an increase in the average available aqueous pore radii (either through an increase in r_{pore} or an increase in σ for a distribution of pore radii (see Eq. 2.40)), (ii) from an increase in the number of aqueous pore channels, N, or (iii) from both. However, based on an examination of Figure 2-5, it was just concluded that there is no significant increase in the hindrance factor, and, therefore, in the average available aqueous pore radius, as a function of increased perturbation of the skin due to ultrasound treatment. Accordingly, the increase in the porosity of each of the four permeants observed in Figure 2-5b must be due to the formation of additional aqueous pore channels having similar radii to the aqueous pore channels present in untreated skin.

In addition, at each level of skin perturbation, or RA value, there is no significant difference in the values of the porosities reported in Figure 2-5b for the four permeants considered, indicating that the value of the porosity is independent of the radius of the permeant over the range of permeant radii considered. This result suggests that the porosity may be properly modeled as a physical property of the skin membrane rather than as a permeant-dependent property, over the range of permeant radii considered here, as suggested previously by Tezel *et al.*[11] It should also be noted that the values of the porosity in untreated skin are similar to the fractional area of the skin occupied by hair

follicles and by sebaceous glands ($2\text{-}3*10^{-3}$).[1] While this observation does not imply that the aqueous pore channels in untreated skin may be represented by the hair follicles and by the sebaceous glands, it does imply that the fraction of the skin surface occupied by the aqueous pore channels in ultrasound-treated skin, both at a low dose and at a high dose, is much larger than the fraction of the skin surface occupied by hair follicles and sebaceous glands, further suggesting that new aqueous pore channels are formed in the skin as a result of the ultrasound treatment.

In Figure 2-5c, values of the tortuosity of the aqueous pore channels are presented as a function of the skin electrical resistivity for each of the four permeants considered. A dashed line corresponding to $\tau = 1$ has been included in Figure 2-5c to mark the lower bound for the physically realizable value of the tortuosity. As can be seen, in most cases, the tortuosity of the aqueous pore channels does not depend on the extent of skin perturbation, as quantified by the RA values. One notable exception is the tortuosity of the aqueous pore channels for the delivery of urea (see the black diamonds in Figure 2-5c) in untreated skin relative to the dermis and to skin treated with a low and a high dose of ultrasound, which may suggest that ultrasound treatment may reduce the tortuosity of the aqueous pore channels present in the skin for small hydrophilic permeants like urea. In addition, the results presented in Figure 2-5c do demonstrate that the tortuosity does not *increase* as the skin electrical resistivity *decreases*, as suggested previously by Tezel *et al.*[11]

Similar to the results for the hindrance factor presented in Figure 2-5a, the data reported in Figure 2-5c does show that there is some dependence of the tortuosity on the radius of the hydrophilic permeants. Specifically, the values of the tortuosity of inulin

are significantly lower ($p<0.05$) than the values of the tortuosities of urea, mannitol, and raffinose. In addition, the value of the tortuosity of raffinose is also significantly lower ($p<0.05$) than the values of the tortuosities of urea and mannitol in untreated skin and in skin treated with a high dose of ultrasound. These results would seem to confirm the assumption of Tezel *et al.* that the tortuosity of the aqueous pore channels in the skin may decrease as the radius of the permeant increases.[11]

However, there is some concern about the inulin tortuosity values reported in Figure 2-5c, since the calculated values of the tortuosity of inulin obtained using the methods presented in Section 2.3.3 are all statistically significantly lower than unity (see the upper range of the error bars corresponding to the open circles does not include unity). Tortuosity values lower than unity, in the context of the aqueous pore pathway hypothesis, are not physically realizable, since this result suggests that inulin diffuses across the skin barrier along a diffusion path that is shorter than the measured skin thickness. Examining the term, $[H(\lambda)/\tau^2]$ in Eqs. (2.36b) or (2.36d), the tortuosity may be increased if the hindrance factor is increased, such that the value of $[H(\lambda)/\tau^2]$ remains constant. Since the values of the average available pore radius determined from the steady-state analysis (see Section 2.5.2) were very large for each of the three permeant pairs studied (i.e. urea-mannitol, urea-raffinose, and urea-inulin) such that the value of the hindrance factor was close to unity, it is instructive to evaluate the porosity and the tortuosity of the aqueous pore channels as a function of the extent of skin perturbation and of the permeant radii for the limiting case of infinitely large pores, for which $r_{pore} \rightarrow \infty$, and $H(\lambda) = 1$ (see Eqs. (2.2) and (2.3)).

2.5.4 Evaluation of the Porosity and the Tortuosity as a Function of Both the Radius of the Hydrophilic Permeant and the Extent of Skin Perturbation for the Limiting Case of Infinitely Large Aqueous Pores

Figure 2-6 presents the values of the porosity (Figure 2-6a) and the tortuosity (Figure 2-6b) as a function of the extent of skin perturbation for each of the four permeants considered for the case where $r_{pore} \rightarrow \infty$ and $H(\lambda) = 1$. In each figure, the black diamonds correspond to the data for urea, the open squares correspond to the data for mannitol, the open triangles correspond to the data for raffinose, and the open circles correspond to the data for inulin. Error bars represent $\pm$ 1 standard deviation corresponding to the average of 5 or 6 six diffusion experiments.

Similar to the case corresponding to a distribution of pore sizes (see Figure 2-5b), Figure 2-6a reveals that the skin porosity increases as the extent of skin perturbation increases, as quantified by decreasing values of the skin electrical resistivity, RA, for each of the four permeants considered. This observation suggests that increased skin perturbation due to ultrasound treatment, or due to heat-stripping, results in an increase of the fraction of the skin surface area occupied by the aqueous pore channels. Since it has been assumed that $H(\lambda) = 1$, the observed increase can be attained by an increase in the number of aqueous pore channels. However, there seems to be a slight dependence of the porosity on the radius of the permeants considered for the case where $H(\lambda) = 1$. Specifically, the values of the porosities corresponding to inulin (open circles) are significantly lower ($p<0.05$) than the values of the porosities corresponding to urea (black diamonds), mannitol (open squares), and raffinose (open triangles) in the dermis, and also

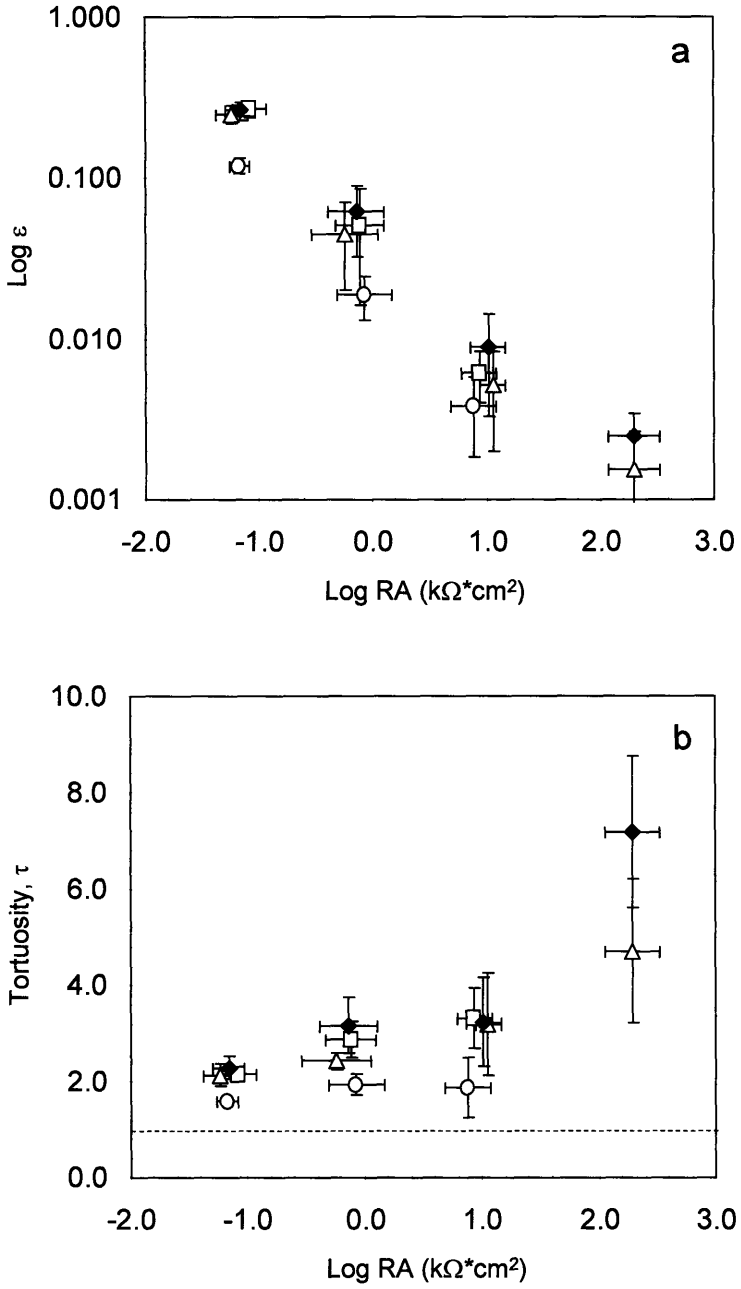

Figure 2-6: Plots of (a) the porosity, ε, and (b) the tortuosity, τ, as a function of the extent of skin perturbation quantified by the skin electrical resistivity, RA, values, for the limiting case where $r_{pore} \rightarrow \infty$ and $H(\lambda) = 1$. Key: urea – black diamonds, mannitol – open squares, raffinose – open triangles, and inulin – open circles. Error bars represent $\pm$ 1 standard deviation. A dashed line has been added in (b) to indicate the value of $\tau = 1$.

significantly lower ($p<0.05$) than the values of the porosities corresponding to urea (black diamonds) and raffinose (open triangles) in skin treated with a high dose of ultrasound.

In Figure 2-6b, in the absence of hindered transport ($H(\lambda) = 1$), the values of the tortuosity exhibit some dependence on both the size of the permeant and on the extent of skin perturbation. Similar to the case corresponding to a distribution of pore radii (see Figure 2-5c), the tortuosities of inulin (open circles) are significantly lower ($p<0.05$) than the tortuosities of urea (black diamonds), mannitol (open squares), and raffinose (open triangles) for the case where $H(\lambda) = 1$. In addition, the values of the tortuosities of inulin are now larger than unity, the lower bound for a physically realizable value of the tortuosity. Furthermore, similar to the case corresponding to a distribution of pore radii in the skin, the values of the tortuosities of raffinose (open triangles) are significantly lower than those of urea (black diamonds) and mannitol (open squares) for untreated skin and for skin treated with a high dose of ultrasound. These results again would seem to confirm the assumption made by Tezel *et al.* that the tortuosity of the aqueous pore channels in the skin may decrease as the radius of the permeant increases.[11] Contrary to the case corresponding to a distribution of pore radii in the skin, when hindered transport is neglected, there is an observable decrease in the values of the tortuosities of each permeant as the extent of skin perturbation is increased. Specifically, for urea (black diamonds), the value of the tortuosity in untreated skin is significantly larger ($p<0.05$) than in ultrasound-treated skin, which is also significantly larger ($p<0.05$) than the tortuosity in the dermis. For raffinose (open triangles), the value of the tortuosity in untreated skin is significantly larger ($p<0.05$) than in skin treated with a high dose of ultrasound, which is also significantly larger ($p<0.05$) than the tortuosity in the dermis.

For mannitol (open squares) and inulin (open circles), the values of the tortuosities in ultrasound-treated skin are significantly larger ($p<0.05$) than the values of the tortuosities in the dermis.

The results of this analysis, where it has been assumed that the aqueous pore channels are infinitely large, suggest that as the extent of skin perturbation increases, new aqueous pore channels, possessing a lower tortuosity than those present in untreated skin, are formed in the skin. For urea, mannitol, and inulin, based on the data in Figure 2-6a, one may also conclude that the porosity can be modeled as an intrinsic property of the skin membrane, similar to the case corresponding to a distribution of pore radii. However, the decreased value of the porosity of inulin relative to those of the other three permeants appears to imply that there are some aqueous pore channels present in the skin which inulin, due to its larger radius, cannot access. This result would seem to contradict the assumption made in the analysis presented in this section, that the aqueous pore channels in the skin are infinitely large, such that $H(\lambda) = 1$. Since the transdermal transport of inulin is not well explained for the case where $H(\lambda) = 1$, or for the case corresponding to a distribution of pore radii of the form given by Eq. (2.40), additional studies are required to better understand the transdermal transport of large molecular weight hydrophilic permeants, such as inulin, in the context of the aqueous pore pathway hypothesis. As a first step, future studies may focus on a more realistic distribution of pore radii, rather than the simple distribution given by Eq. (2.40).

2.6 Conclusions

In this chapter, the aqueous pore pathway hypothesis was extended to model the transient domain of the transdermal transport of hydrophilic permeants, in addition to the previously-investigated steady-state domain, to verify assumptions regarding the behavior of the hindrance factor, the tortuosity, and the porosity as a function of both permeant radius and the extent of skin perturbation. Diffusion experiments were conducted with ^{14}C-urea combined with tritium-labeled mannitol, tritium-labeled raffinose, or tritium-labeled inulin as the model permeants. An analysis of the cumulative amount of the permeant delivered per unit area, Q(t), showed that the lag time to reach steady-state was 10- to 40-fold lower in the dermis than in untreated full-thickness skin, indicating that the tortuosity of the aqueous pore channels does not increase with increasing skin perturbation, contrary to a suggestion made previously by Tezel *et al.*[11]

Analysis of the steady-state permeability data by linear regression revealed that the slope of the best-fit through the steady-state permeability data was statistically similar to the predicted slope of 1 over the range of permeant radii investigated in this study (r_p = 2.6 Å – 12 Å). Using steady-state analysis methods, I determined that the average available aqueous pore radius ranged in size from 41 Å to infinity. Given the large range of values for the average available aqueous pore radius, as well as the large size of the standard deviation in the average available pore radius (in some cases varying from 21 Å to infinity), it is questionable whether the inclusion of a hindrance factor improves the overall modeling of transdermal transport of hydrophilic permeants.

To further investigate the need to include the hindrance factor, as well as to investigate how the porosity and the tortuosity vary as a function of the permeant radius and the extent of skin perturbation, the Q(t) data were analyzed with the proposed model equations describing the transdermal transport of hydrophilic permeants in the transient and the steady-state domains. For the case where a distribution of pore radii exists in the skin, as proposed by Tezel *et al.*,[11] my results indicated that: 1) the value of the hindrance factor depends on the radius of the permeant delivered through the skin, while there is little change in the value of the hindrance factor as a function of the extent of skin perturbation, 2) the value of the porosity does not depend on the radius of the permeant delivered, while the value of the porosity increases as the extent of skin perturbation increases, and 3) the value of the tortuosity decreases as the radius of the permeant increases, while there is little evidence that the tortuosity depends on the extent of skin perturbation. These trends would seem to suggest that ultrasound treatment of the skin results in the formation of aqueous pore channels that are structurally similar to those found in untreated skin.

Because the tortuosity values of inulin were found to be statistically significantly lower than unity, and because of the large standard deviations in the hindrance factor values of urea, mannitol, and raffinose, the values of the porosity and the tortuosity were also evaluated in the limiting case of infinitely large aqueous pores ($r_{pore} \rightarrow \infty$). This analysis showed that, similar to the previous case where a distribution of aqueous pore channels was assumed to exist in the skin, the tortuosity exhibited some dependence on the radius of the permeant, while the porosity of urea, mannitol, and raffinose were found to be statistically similar. In addition, a significant decrease in the tortuosity of each

permeant was observed as a function of the extent of skin perturbation. While the use of infinitely large pores resulted in tortuosity values of inulin which were greater than unity, the value of the porosity for inulin was found to be significantly lower than those of the other three permeants considered, suggesting that there were some aqueous pore channels which could not be accessed by inulin due to its larger radius. These results indicate that additional studies are needed to improve the model for the distribution of the aqueous pore radii in the skin to better understand the transdermal transport of inulin, and other large hydrophilic permeants, in the context of the aqueous pore pathway hypothesis.

Having developed a new theoretical analysis technique to further investigate the transport of hydrophilic permeants across the skin, it is next appropriate to further investigate the transport of *hydrophobic* permeants through the skin. With this in mind, in the next chapter, then, a novel, first-principles model describing transdermal transport of hydrophobic permeants through the intercellular regions of the stratum corneum is derived for the purpose of providing a simpler and more accurate method of evaluating the vehicle-bilayer partition coefficient, K_b, and the bilayer diffusion coefficient, D_b, for hydrophobic permeants solely using transdermal permeability experiments. The transport model proposed for hydrophobic permeants in the next chapter will also be applicable in both the transient and the steady-state domains, similar to the model developed in this chapter for the transport of hydrophilic permeants. A major challenge that will be encountered in the development of a model to describe the transdermal transport of hydrophobic permeants involves the modeling of branched, parallel transport pathways. As will be shown in the next chapter, this additional feature associated with the transdermal transport of hydrophobic permeants will require the introduction of two

tortuosity factors in the model equations, one to account for the total volume of the hydrophobic transport pathways and the second to account for the flux of the hydrophobic permeants through these pathways. Since the hydrophilic permeants considered in this chapter were assumed to traverse the skin solely across unbranched transport pathways, only a single tortuosity factor was needed in the model equations developed in this chapter to account for: (i) the total volume of the hydrophilic transport pathways, and (ii) the flux of hydrophilic permeants through these pathways.

2.7 References

1. Walters KA and Roberts MS. 2002. The structure and function of the skin. Drugs and the Pharmaceutical Sciences: Dermatological and Transdermal Formulations. 119:1-39.
2. Michaels AS, Chandraskeran SK, Shaw JE. 1975. Drug permeation through human skin: theory and in vitro experimental measurement. Am Inst Chem Eng J 21:985-996.
3. Cussler E, Hughes S, Ward W, and Aris R. 1988. Barrier membranes. J Memb Sci 38:161-174.
4. Lange-Lieckfeldt R and Lee G. 1992. Use of a model lipid matrix to demonstrate the dependence of the stratum corneum's barrier properties on its internal geometry. J Cont Rel 20:183-194.
5. Edwards DA and Langer R. 1994. A linear theory of transdermal transport phenomena. J Pharm Sci 83:1315-1334.
6. Frasch HF and Barbero AM. 2003. Steady-state flux and lag time in the stratum corneum lipoid pathway: Results from finite element models. J Pharm Sci 92: 2196-2207.
7. Bodde HE, van der Brink I, Koerten HK, and de Haan FHN. 1991. Visualization of in vitro percutaneous penetration of mercuric chloride; transport through intercellular space versus cellular uptake through desmosomes. J Cont Rel 15:227-236.

8. Sznitowska M, Janciki S, and Williams AC. 1998. Intracellular of Intercellular Localization of the Polar Pathway across Stratum Corneum. J Pharm Sci 87:1109-1114.

9. Peck KD, Ghanem AH, and Higuchi WI. 1994. Hindered diffusion of polar molecules through and effective pore radii estimates of intact and ethanol treated human epidermal membrane. Pharm Res 11:1306-1314.

10. Tang H, Mitragotri S, Blankschtein D, Langer RS. 2001. Theoretical description of transdermal transport of hydrophilic permeants: Application to low-frequency sonophoresis. J Pharm Sci 90:545-568.

11. Tezel A, Sens A, and Mitragotri S. 2003. Description of transdermal transport of hydrophilic solutes during low-frequency sonophoresis based on a modified porous pathway model. J Pharm Sci. 92: 381-393.

12. Deen WM. 1987. Hindered transport of large molecules in liquid-filled pores. AIChE J 33:1409-1425.

13. Hou SYE, Mitra AK, White SH, Menon GK, Ghadially R, and Elias PM. 1991. Membrane structures in normal and essential fatty acid deficient stratum corneum: characterization by ruthenium tetroxide staining and X-ray diffraction. J Invest Dermatol 96:215-223.

14. Paliwal S, Menon GK, Mitragotri S. 2006. Low-frequency sonophoresis: Ultrastructural basis for stratum corneum permeability assessed using quantum dots. J Invest Dermatol 126:1095-1101.

15. Tezel A, Mitragotri S. 2003. On the origin of size-dependent tortuosity for permeation of hydrophilic solutes across the stratum corneum. J Cont Rel 86:183-186.

16. Li SK, Suh W, Parikh HH, Ghanem AH, Mehta SC, Peck KD, and Higuchi WI. 1998. Lag time data for characterizing the pore pathway of intact and chemically pretreated human epidermal membrane. Int J Pharm. 170: 93-108.

17. Song Y, Li SK, Peck KD, Zhu HG, Ghanem AH, and Higuchi WI. 2002. Human epidermal membrane constant conductance iontophoresis: Alternating current to obtain reproducible enhanced permeation and reduced lag times of a nonionic polar permeant. Int J Pharm 232: 45-57.

18. Hatanaka T, Manabe E, Sugibayashi K, Morimoto Y. 1994. An application of the hydrodynamic pore theory to percutaneous absorption of drugs. Pharm Res 11:654-658.

19. Menon GK, Bommannan DB, Elias PM. 1994. High-frequency sonophoresis: Permeation pathways and structural basis for enhanced permeability. Skin Pharmacol 7:130-139.

20. Menon GK and PM Elias. 1997. Morphological basis for a pore-pathway in mammalian stratum corneum. Skin Pharmacol 10:235-246.

21. Mori S, Barth HG. 1999. Size Exclusion Chromatography. Springer: New York. Pp. 11-12.

22. Tang H, Blankschtein D, Langer R. 2002. Effects of low-frequency ultrasound on the transdermal permeation of mannitol: Comparative studies with in vivo and in vitro skin. J Pharm Sci 91:1776-1794.

23. Crank J. 1964. The Mathematics of Diffusion. Oxford University Press, London. Pp. 47-48.

24. Tezel A, Sens A, Tuchscherer J, Mitragotri S. 2002. Synergistic effect of low-frequency ultrasound and surfactants on skin permeability. J Pharm Sci 91:91-100.

25. Tang H, Blankschtein D, and Langer RS. 2002. Prediction of steady-state skin permeabilities of polar and nonpolar permeants across excised pig skin based on measurements of transient diffusion: Characterization of hydration effects on the skin porous pathway. J Pharm Sci 91:1891-1907.

26. Montgomery DC, Runger GC, Hubele NF. 1998. Engineering Statistics. John Wiley & Sons, Inc. New York.

Chapter 3

Fundamental Structure-Based Modeling of Drug Transport through the Intercellular Regions of the Stratum Corneum

3.1 Introduction

The development of skin permeation models is an important area of continuing research in the field of transdermal drug delivery. A major portion of this research is focused on modeling the transport of drugs through the outermost layer of the skin, the stratum corneum (SC). As discussed in Chapter 1, the SC provides the major resistance barrier to transdermal drug delivery,[1] even though it is the thinnest layer of the skin (~10-20 μm thick). The SC derives its high resistance to drug transport from a highly organized brick-and-mortar structure of highly impermeable corneocyte cells (the bricks) and intercellular lipid lamellar bilayers (the mortar).[2] Due to the highly impermeable nature of the corneocyte cells of the SC, researchers have shown that passive drug permeation in the SC, especially for lipophilic drugs, occurs through the intercellular lipid lamellar bilayers.[3-7]

Over the past thirty years, several researchers have proposed permeation models for the transport of drugs solely through the intercellular regions of the SC which are heavily based on the structure and the geometric parameters of the SC.[8-12] The general form of the intercellular permeation model, for the steady-state transport phase, can be represented by Eq. (3.1):

$$P = \left(\frac{\varepsilon}{\tau}\right)\frac{K_b D_b}{L} \tag{3.1}$$

where P is the steady-state permeability, K_b is the permeant vehicle-bilayer partition coefficient, D_b is the bilayer diffusion coefficient of the permeant, and L is the SC thickness. The porosity, ε, and the tortuosity, τ, are transport parameters that can be evaluated from the structural parameters of the SC (see section 3.2 for definitions). These structural parameters include (see Figure 3-1): 1) the number of corneocyte layers in the SC (N), 2) the diameter (d) of the corneocytes, 3) the height (h) of the corneocytes, 4) the length of the intercellular gap between the corneocyte cells (g), and 5) the corneocyte offset (ω), defined as the longer lateral diffusion path, d_L, divided by the shorter lateral diffusion path, d_S, that is, $\omega = d_L/ds$. Michaels *et al.* proposed the first model for the SC geometry (see Figure 3-1a) using symmetrically offset ($\omega = d_L/d_S = 1$) square corneocyte bricks and the physical path length of a molecule through the SC to estimate of the tortuosity factor.[8] Subsequent refinements to the SC geometry in the context of modeling intercellular transport incorporated: i) infinitely long corneocytes (see Figure 3-1b),[9] ii) circular corneocytes (see Figure 3-1c),[10] iii) separate regions for the hydrophobic and the hydrophilic regions within the lipid lamellar bilayers with infinitely long corneocytes (similar to Figure 3-1b),[11] and iv) asymmetrically offset corneocytes

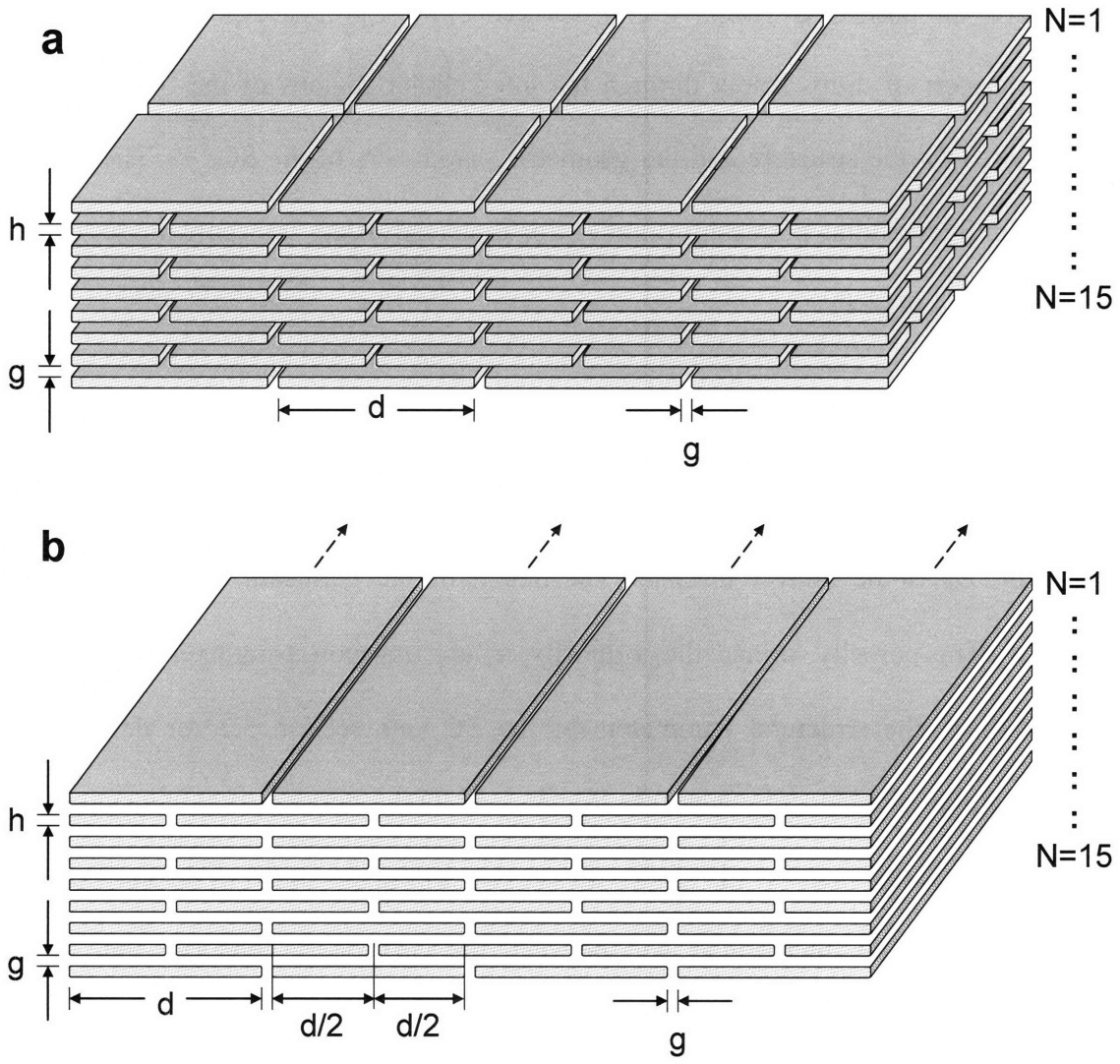

Figure 3-1: Previously-proposed brick-and-mortar models of the stratum corneum: (a) model of Michaels *et al.* (symmetrically offset square corneocytes), (b) models of Cussler *et al.* and of Edwards and Langer (symmetrically offset semi-infinite corneocytes),[8,9,11] where N – number of corneocyte layers, d – corneocyte characteristic length, h – corneocyte thickness, g – intercellular space thickness (occupied by the lamellar lipid bilayers), and d_S and d_L – short and long corneocyte diffusion path lengths, respectively. The dashed arrows in (b) and (d) indicate that the corneocytes are modeled as being infinite in the direction of the arrows.

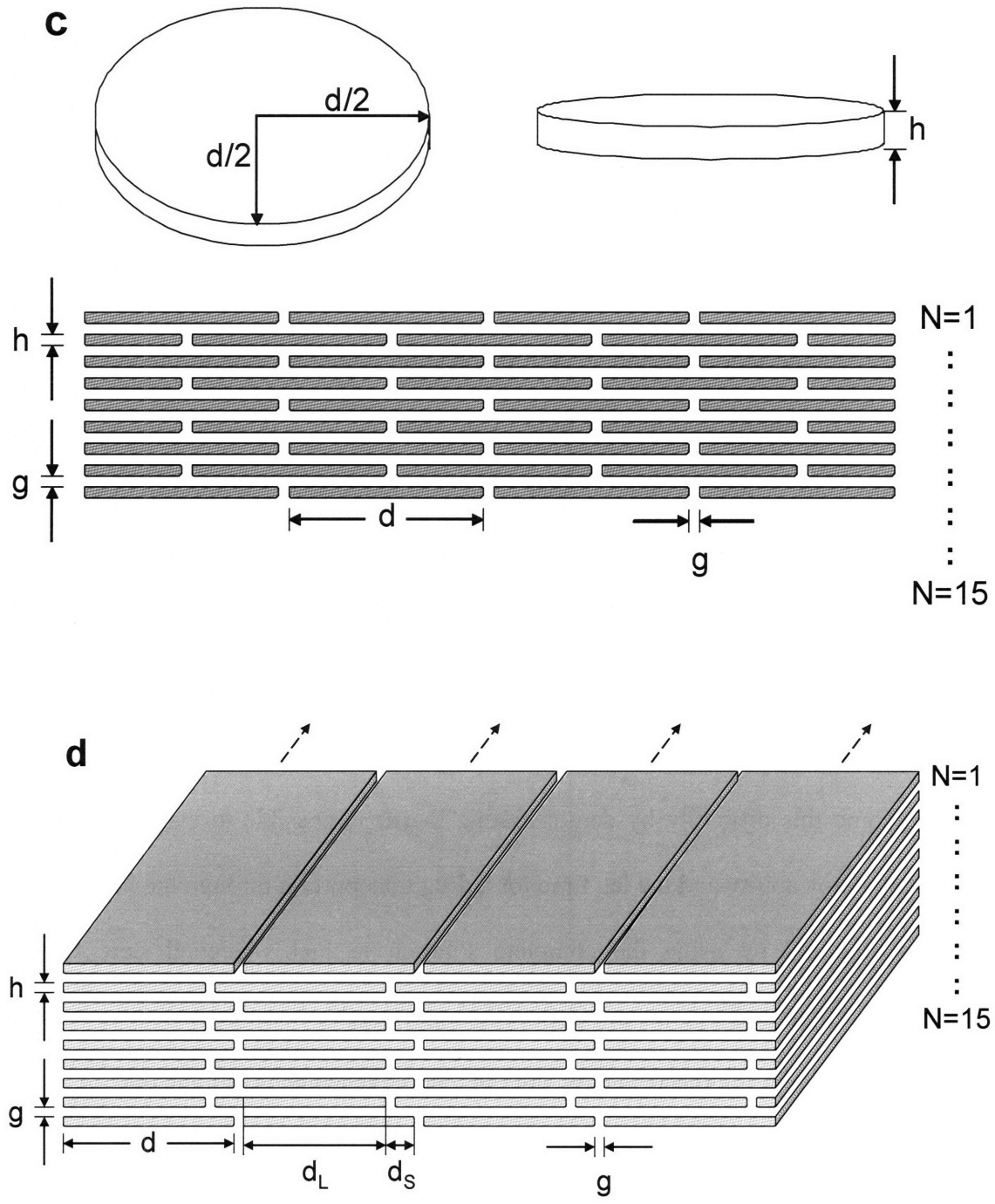

Figure 3-1 (continued): (c) model of Lange-Lieckfeldt and Lee (symmetrically offset circular corneocytes), and (d) model of Johnson *et al.* (asymmetrically offset semi-infinite corneocytes).[10,12]

(see Figure 3-1d).[12] Currently, the model presented by Johnson *et al.* (see Figure 3-1d) is the most widely accepted representation of the 2D structure of the SC. Also, due to the presence of the parallel lateral diffusion paths in the SC geometry, Cussler *et al.* introduced the concept of an effective lateral diffusion path length, modeled analogously to electrical resistors in parallel, which has been used by subsequent researchers,[12] for the evaluation of the tortuosity factor.[9]

It is essential that an adequate skin permeation model be able to predict both the steady-state permeability and the lag time to steady-state for a desired drug, as both of these quantities are critical to attain proper clinical drug delivery. While Eq. (3.1) is able to acceptably describe the steady-state permeability of a lipophilic drug through the intercellular regions of the SC, attempts to predict the lag time required to reach steady-state, ($t_{lag} = (\tau L)^2/6D_b$), based on the values of D_b, L, and τ used in Eq. (3.1), have been less successful for a broad class of lipophilic permeants.[12] Recently, Frasch and Barbero have overcome this difficulty by demonstrating that it is possible to evaluate both the steady-state permeability and the lag time for a drug transporting through the intercellular regions of the SC by using the complete solution to Fick's Second Law for the accumulation of mass of a permeant, Q(t), diffusing through a homogeneous membrane.[13] Since the intercellular regions of the SC are not a homogeneous membrane due the brick-and-mortar structure of the SC, Frasch and Barbero introduced parameters for the effective diffusion coefficient, D*, and for the effective membrane thickness (or the effective diffusion path length), L*, as shown in Eq. (3.2):[13]

$$Q(t) = K_b C L^* \left[\frac{D^* t}{L^{*2}} - \frac{1}{6} - \frac{2}{\pi^2} \sum_{n=1}^{\infty} \frac{(-1)^n}{n^2} \exp\left(\frac{-D^* t}{L^{*2}} n^2 \pi^2 \right) \right] \tag{3.2}$$

where C is the concentration difference across the membrane and K_b was assumed to be 1 for simplicity. Frasch and Barbero obtained estimates of D* and L* by regressing data obtained from finite element method (FEM) simulations of drug permeation through model SC geometries using Eq. (3.2).[13] Having obtained R^2 values in excess of 0.999 for a wide range of SC geometries, Eq. (3.2) seems to have the proper form for describing the transport of drugs through the complex SC intercellular geometry.[13]

However, the dependence of Eq. (3.2) on the effective values of D and L, and not on the intrinsic values of both the diffusion coefficient and the membrane thickness, provides an excellent opportunity for further model refinement. In Section 3.2, I will analyze five previous structure-based models for the purpose of: 1) highlighting the subtle differences between the five previous models, and 2) using the results of the analysis of the previous structure-based models to guide the proposed refinements to model the barrier properties of the skin. In Section 3.3, I will derive, from first principles, a new 2D model for the diffusion of a drug through the intercellular regions of the SC. The new model will use the *intrinsic* values of the diffusion coefficient and the membrane thickness, rather than the *effective* values, by explicitly incorporating the structure and geometry of the intercellular regions of the SC into the model equations. In Section 3.5, I will then demonstrate how predictions using the new model compare with finite element simulations of drug transport through the SC over a wide range of SC geometric parameter values both in the transient and in the steady-state transport phases.

Finally, I will use the new 2D model to evaluate, for the first time, both the SC lipid bilayer diffusion and partition coefficients, D_b and K_b, for two hydrophobic permeants directly from permeation experiments (see Section 3.5 for details). Currently,

K_b can be determined indirectly from octanol-water partitioning experiments using the Potts and Guy correlation, $K_b = K_{o/w}^{0.71}$,[14] of the Flynn permeation database,[15] where $K_{o/w}$ is the permeant octanol-water partition coefficient. Once K_b has been evaluated, Eq. (3.1) can be utilized to estimate D_b from permeability experiments. However, to evaluate K_b and D_b for an unknown drug, this approach requires both an octanol-water partition experiment and a skin permeation experiment. Another potential drawback to this method is that the value of D_b obtained from Eq. (3.1) is directly based on the value of K_b obtained *indirectly* from octanol-water partition experiments. Any inaccuracies in the experimental value of K_b would then be added directly to inaccuracies in the deduced value of D_b through the use of Eq. (3.1). Another approach for evaluating K_b and D_b using both permeation experiments and solute release experiments was demonstrated by Mitragotri.[16] While this approach deduces the values of K_b and D_b directly from the SC, it still requires two sets of experiments. Using the new 2D model, I will demonstrate that both K_b and D_b can be evaluated directly *solely* from skin permeation experiments, thereby greatly simplifying the experimental procedure, and providing a more direct measure to deduce these critical drug transport parameters.

3.2 Review of Previously Developed Structure-Based Models Describing Transport in the Intercellular Regions of the Stratum Corneum

In this section, the five models discussed in the previous section will be analyzed for the purpose of: 1) highlighting the subtle differences between the five previous models,

illustrating how the modeling of the skin structure for the purpose of estimating transdermal drug permeabilities has evolved over the past thirty years, and 2) using the above information to guide the proposed refinements to model the barrier properties of the skin. Before carrying out an analysis of the previously-developed models, it is useful to derive some simple expressions for ε and τ based on the geometric structure of the stratum corneum for comparison with the expressions for ε and τ used in each of the five previously-developed models. This comparison will provide some insight into the model assumptions and techniques used by the previous researchers, as well as allow a determination of which of these assumptions and techniques should be employed in the newly-proposed model. Regarding the porosity of the stratum corneum, which is a measure of the lipid bilayer fraction at the stratum corneum surface, both 2-D and 1-D expressions can be derived as follows:

$$\varepsilon = \frac{A_{lipids}}{A_{corneocytes} + A_{lipids}} \qquad \text{(2-D)} \tag{3.3}$$

$$\varepsilon = \frac{L_{lipids}}{L_{corneocytes} + L_{lipids}} \qquad \text{(1-D)} \tag{3.4}$$

where A_{lipids} and $A_{corneocytes}$ are the areas of the lipids and the corneocytes at the stratum corneum surface, respectively, used in the 2-D model for the porosity, and L_{lipids} and $L_{corneocytes}$ are the lengths of the intercellular lipid region and the corneocytes, respectively, used in the 1-D model for the porosity. Note that Eqs. (3.3) and (3.4) are necessarily valid whether one considers a single corneocyte surrounded by a half-width of lamellar lipid bilayers or the total areas (or lengths in the 1-D case) of the corneocytes and the lamellar lipid regions at the stratum corneum surface.

The tortuosity, τ, is generally defined as follows:[18]

$$\tau = \frac{\text{Total diffusion distance traveled by the permeant molecule}}{\text{Stratum corneum membrane thickness}} \tag{3.5}$$

For a stratum corneum membrane sample of thickness, h, containing N layers of corneocytes, Eq. (3.5) can be rewritten as follows (see Figure 3-1, a – d):

$$\tau = \frac{Nh + (N-1)g + (N-1)d_{lat}}{L} \tag{3.6}$$

where h is the thickness of the corneocyte cells, g is the thickness of the lipid bilayers between the layers of corneocytes in the stratum corneum (which is equal in both the horizontal and the vertical directions[19]), and d_{lat} is the distance traveled by the permeant molecules laterally in a given layer of the stratum corneum before descending to the next stratum corneum layer, which can be evaluated from the SC structural parameters shown in Figure 3-1. While h and g are physical dimensions of the stratum corneum that can be measured,[16,19] the calculation of d_{lat} is as yet unresolved, as the following comparative analysis of the five previous models available in the literature will highlight. By examining Figure 3-1, it is noteworthy that the term Nh + (N-1)g is equivalent to the stratum corneum thickness, L. Therefore, the value of the tortuosity is very sensitive to the value of d_{lat} (see Eq. (3.1)), stressing the need for the availability of an accurate model equation, based on the structural parameters of the skin, to evaluate d_{lat}. Having derived Eqs. (3.3), (3.4), and (3.6) for ε and τ, it is now possible to effectively analyze the five previously-developed models.

3.2.1 Model of Michaels et al.

In the model of Michaels *et al.* (based on symmetrically offset, impermeable, square-shaped corneocyte bricks, see Figure 3-1a), the equation for the permeability through the intercellular regions of the stratum corneum is given by:[12]

$$P = \frac{\left(\frac{2g}{d}\right)}{\left(1+\frac{\frac{d}{h}+\frac{g}{h}}{2\left(1+\frac{g}{h}\right)}\right)}\frac{K_b D_b}{L} \tag{3.7}$$

Comparing Eq. (3.7) with Eq. (3.1), it follows that the porosity and the tortuosity of the intercellular lipid bilayer regions of the stratum corneum in the model of Michaels *et al.* are given by:

$$\varepsilon = \frac{2g}{d} \tag{3.8a}$$

and

$$\tau = 1+\frac{\frac{d}{h}+\frac{g}{h}}{2\left(1+\frac{g}{h}\right)} \tag{3.8b}$$

Equation (3.8a) for ε can be derived by using Eq. (3.3) for the two-dimensional geometry of a square corneocyte as follows (see Figure 3-1a):

$$\varepsilon = \frac{(d+g)^2 - d^2}{(d+g)^2} = \frac{2gd+g^2}{(d+g)^2} \tag{3.9}$$

If it is assumed that d>>g, which is valid for typical dimensions of the corneocytes and the intercellular lipid bilayers in the stratum corneum, [16,19-23] Eq. (3.9) reduces to Eq.

(3.8a). To effectively compare Eq. (3.8b) with Eq. (3.6), Eq. (3.8b) needs to be rearranged to yield a form similar to Eq. (3.6), as shown below:

$$\tau = \frac{(h+g)+\left(\frac{d+g}{2}\right)}{h+g} \tag{3.10}$$

Then, multiplying the right-hand side of Eq. (3.10) by N/N yields:

$$\tau = \frac{Nh+Ng+N\left(\frac{d+g}{2}\right)}{N(h+g)} \tag{3.11}$$

Comparing Eq. (3.11) with Eq. (3.6) allows one to make several observations about the assumptions made by Michaels *et al.* in the development of their model for τ. First, these authors made the assumption that for sufficiently large values of N, (N-1) in Eq. 3.6 can be replaced by N without significantly affecting the value of τ. While this is a good approximation for the (N-1)g term in Eq. (3.6) and for the stratum corneum thickness, L, since h>>g, it is not a good approximation for the $(N-1)d_{lat}$ term in Eq. (3.6), since typically, (d+g)/2>>h, which could introduce a significant overestimation of τ calculated using Eq. (3.11). Second, a comparison of Eqs. (3.6) and (3.11) shows that $d_{lat} = (d+g)/2$ in Eq. (3.11). An examination of Figure 3-1a reveals that this d_{lat} value corresponds to the *physical diffusion path length* that a solute must travel along a corneocyte to reach the center of the next intercellular gap. In summary, the model of Michaels *et al.*, which is based on symmetrically offset, impermeable, square-shaped corneocyte bricks (see Figure 3-1a), uses a 2-D calculation to determine ε and the *physical path length* to calculate d_{lat} in the expression for τ.

3.2.2 Model of Cussler et al.

In the model of Cussler *et al.* (based on symmetrically offset, impermeable, semi-infinite corneocyte bricks, see Figure 3-1b), the equation for the permeability through the membrane is given by:[13]

$$P = \frac{K_h D_h}{L\tau^*} \tag{3.12}$$

where τ^* is given by:[13]

$$\tau^* = 1 + \frac{2g}{L}\ln\left(\frac{d+g}{2g}\right) + \frac{N(d+g)h}{gL} + (N-1)\frac{\left(\frac{d+g}{2}\right)^2}{gL} \tag{3.13}$$

The four terms on the right-hand side of Eq. (3.13) describe the resistance of a membrane without bricks, the resistance due to the constriction of the slit opening at the top and at the bottom of the membrane, the resistance due to transport through the intercellular spaces themselves, and the resistance due to the tortuous nature of the intercellular spaces, respectively.[13] Comparing Eq. (3.12) with Eq. (3.1), it follows that $1/\tau^*$ in Eq. (3.12) must be equivalent to (ε/τ) in Eq. (3.1), although the equivalence is not readily apparent if Eq. (3.13) is compared directly with Eqs. (3.3), (3.4), and (3.6). However, by substituting typical values of the physical parameters of the stratum corneum in Eq. (3.13),[16,19-23] one can show that the third and fourth terms are orders of magnitude larger than the first and second terms, such that Eq. (3.13) can be approximated well as follows:

$$\tau^* = \frac{N(d+g)h}{gL} + (N-1)\frac{\left(\frac{d+g}{2}\right)^2}{gL} \tag{3.14}$$

Noting that the term, (d+g)/g, can be factored out from both terms in Eq. (3.14), the following further simplification of Eq. (3.14) can be made:

$$\tau^* = \left(\frac{d+g}{g}\right)\left(\frac{Nh+(N-1)\frac{1}{2}\left(\frac{d+g}{2}\right)}{L}\right) \tag{3.15}$$

By comparing Eq. (3.15) with Eqs. (3.4) and (3.6), one can identify the (d+g)/g term in Eq. (3.15) as being equivalent to 1/ε, and the second term as being similar in form to the expression for τ in Eq. (3.6). Therefore, τ^* in Eq. (3.12) is actually equal to (τ/ε), and Eq. (3.12) has the same form as Eq. (3.1). It is now possible to make several observations about the assumptions made by Cussler *et al.* in the development of their model. First, ε = g/(d+g) is calculated in Eq. (3.15) using the one-dimensional model given in Eq. (3.4). This observation is confirmed by examining Figure 3-1b, which shows that the model of Cussler *et al.* is a 1-D model. This is different from the model of Michaels *et al.* who used a 2-D model for square corneocyte bricks. Second, a comparison of Eqs. (3.15) and (3.6) shows that the diffusion distance contribution of the intercellular lipids between the layers of the corneocytes (given by (N-1)g) has been neglected in Eq. (3.15), which, based on the physical parameters of the stratum corneum, could lead to an underestimation of τ calculated using Eq. (3.15). Finally, d_{lat} = (d+g)/4 in Eq. (3.15), which is a factor of 2 smaller than the result of Michaels *et al.* for d_{lat}. The extra factor of ½ in the calculation of d_{lat} reflects the use of an *effective diffusion path length.* Cussler *et al.* argue that a diffusing molecule has two parallel paths by which it may travel laterally to diffuse around an impermeable corneocyte.[13] Modeling the parallel diffusion paths using the analogy of current flow through electrical resistors in parallel, the expression for d_{lat} used in Eq. (3.15) is obtained as follows (see Figure 3-1b):

$$\frac{1}{d_{lat}} = \frac{1}{\left(\frac{d+g}{2}\right)} + \frac{1}{\left(\frac{d+g}{2}\right)} = 2\left(\frac{2}{d+g}\right) \tag{3.16}$$

Equation (3.16) clearly shows that the use of an effective diffusion path length, modeled in terms of electrical resistors in parallel, will always result in a diffusion path length that is smaller than the actual diffusion path lengths associated with either path.

3.2.3 Model of Lange-Lieckfeldt and Lee

In the model of Lange-Lieckfeldt and Lee (based on symmetrically offset, impermeable, circular-shaped corneocyte bricks, see Figure 3-1c), the permeability equation for permeation solely through the intercellular regions of the stratum corneum is given by:[14]

$$P = \left(\frac{L}{L^*}\right)\left(\frac{A^*}{A}\right)\frac{K_h D_h}{L} \tag{3.17}$$

where the terms (L^*/L) and (A/A^*) are given by:[14]

$$\left(\frac{L^*}{L}\right) = \frac{L + (N-1)\left(\frac{d+g}{2}\right)}{L} \tag{3.18a}$$

and

$$\left(\frac{A^*}{A}\right) = \frac{\left[\left(\frac{d+g}{2}\right)^2 - \left(\frac{d}{2}\right)^2\right]}{\left(\frac{d}{2}\right)^2} \tag{3.18b}$$

Comparing Eq. (3.18a) with Eq. (3.6), and recalling that L = Nh + (N-1)g, it follows that (L^*/L) is equivalent to τ, and that it matches Eq. (3.6) exactly, for $d_{lat} = (d+g)/2$, which corresponds to the *physical diffusion path length* of a permeant traversing a circular

corneocyte, originating from the center of the corneocyte (see Figure 3-1c). Comparing Eq. (3-18b) with Eq. (3.3), it follows that (A^*/A) is equivalent to ε, with $A_{lipids} = \pi((d+g)/2)^2 - \pi(d/2)^2$ and $A_{corneocyte} = \pi(d/2)^2$ for the two-dimensional geometry corresponding to a circular corneocyte of radius (d/2) surrounded by a half-width of the lipid bilayers of thickness (g/2) (see Figure 3-1c). In addition, it was assumed that $A_{corneocytes} >> A_{bilayers}$ in the denominator of Eq. (3.18b), since d>>g. This should only introduce a minor overestimation when ε is calculated according to Eq. (3.18b).

3.2.4 Model of Edwards and Langer

In the model of Edwards and Langer (which is similar to the model corresponding to Figure 3-1b), the permeability equation for the permeation of small hydrophobic solutes through the intercellular regions of the stratum corneum is given by:[15]

$$P = \left(\frac{g}{d+g}\right)\left(\frac{l_o}{l_w + l_o}\right)\left(\frac{h}{h+d}\right)\frac{K_h D_h}{L} \tag{3.19}$$

where l_o and l_w are the fractions of the intercellular lipid bilayer regions that are hydrophobic and hydrophilic in nature, respectively. A comparison of Eq. (3.19) with Eq. (3.1), keeping in mind Eq. (3.4) for this one-dimensional model of the stratum corneum, shows that the term [g/(d+g)] on the right-hand side of Eq. (3.19) is equivalent to ε given in Eq. (3.4). The term $[l_o/(l_w+l_o)]$, from a structural standpoint, is a further refinement to estimate ε, where the actual fraction of the intercellular regions which are hydrophobic is accounted for explicitly. Therefore, in the model of Edwards and Langer, ε is equal to the product of the first two terms on the right-hand side of Eq. (3.19).

As part of the derivation of Eq. (3.19), in their work, Edwards and Langer identified the tortuosity of the intercellular regions of the stratum corneum as given by the third term on the right-hand side of Eq. (3.19), that is, they take $\tau = (h+d)/h$.[15] The third term can be manipulated in the following manner to derive an expression similar in form to that in Eq. (3.6):

$$\tau = \frac{h+d}{h} = \frac{Nh+Nd}{Nh} \tag{3.20}$$

Comparing Eq. (3.20) with Eq. (3.6), the following three observations can be made. First, the thickness of the intercellular regions between the corneocyte layers, reflected in the (N-1)g term in Eq. (3.6), has been neglected in the calculation of τ according to Eq. (3.20). Second, N layers are used for the contribution of the lateral diffusion path length, d_{lat}, to the total diffusion path length of a solute permeating across the stratum corneum in Eq. (3.20), instead of the (N-1) layers used in Eq. (3.6). Finally, d_{lat} is given by d, the characteristic length of a corneocyte. This value of d_{lat} is different from that used in the three previous models considered above and, physically, it appears less probable. While the first two approximations may lead to a slight overestimation of τ calculated using Eq. (3.20), taking $d_{lat} = d$ will overestimate τ calculated according to Eq. (3.20) by two-fold as compared to the τ values predicted by the models of Michaels *et al.* and of Lange-Lieckfeldt and Lee, which use $d_{lat} = (d+g)/2$, and by four-fold as compared to the τ value predicted by the model of Cussler *et al.*, which uses $d_{lat} = (d+g)/4$.

3.2.5 Model of Johnson et al.

In the model of Johnson *et al.* (see Figure 3-1d), the permeability equation for the diffusion of a hydrophobic solute through the intercellular regions of the stratum corneum is also given by Eq. (3.12),[16] corresponding to the model of Cussler *et al.*[13] In their model, however, Johnson *et al.* incorporated an asymmetric offset of the corneocyte layers, which leads to the following modification of Eq. (3.13) for τ^*:[16]

$$\tau^* = 1 + \frac{2g}{L}\ln\left(\frac{d+g}{2g}\right) + \frac{N(d+g)h}{gL} + (N-1)\frac{w}{(1+w)^2}\frac{d^2}{gL} \tag{3.21}$$

where w is the offset ratio which is defined as (see Figure 3-1d):[16]

$$w = \frac{d_L}{d_S} \tag{3.22}$$

where d_L and d_S are the longer and shorter diffusion path lengths, respectively. As was done with the model of Cussler *et al.*, Eq. (3.21) can be simplified as follows:

$$\tau^* = \frac{N(d+g)h}{gL} + (N-1)\frac{w}{(1+w)^2}\frac{d^2}{gL} \tag{3.23}$$

Since d>>g, Eq. (3.23) can be further simplified as follows:

$$\tau^* = \left(\frac{d+g}{g}\right)\left(\frac{Nh + (N-1)\left(\frac{w}{(1+w)^2}\right)d}{L}\right) \tag{3.24}$$

As we already saw in the case of the model of Cussler *et al.*, the first term on the right-hand side of Eq. (3.24) corresponds to the expression for $1/\varepsilon$ in the case of a one-dimensional model of the stratum corneum (see Eq. (3.4)). The second term corresponds to an expression for τ, where the contribution of the thickness of the lipid bilayers

between the layers of corneocytes (reflected in the (N-1)g term in Eq. (3.6)) is again neglected. For the model of Johnson *et al.*, d_{lat} is now given by:

$$d_{lat} = d\left[\frac{w}{(1+w)^2}\right] \tag{3.25}$$

For the case of a symmetric offset corresponding to w = 1, d_{lat} = d/4, which is equal to the value of d_{lat} in the model of Cussler *et al.* [(d+g)/4], when d>>g. Therefore, the model of Johnson *et al.* also utilizes the concept of an *effective diffusion path length*, introduced originally by Cussler *et al.*, while making a significant contribution to the literature by considering the observed asymmetric offset of the corneocyte layers in the stratum corneum.

3.2.6 Summary of Key Aspects of the Previous Structure-Based Models Aimed at Developing a First-Principles Intercellular Transport Model

In the next section, the derivation of a model for drug transport through the intercellular regions of the stratum corneum, which utilizes the structural parameters of the skin to determine the values of the porosity and the tortuosity, is presented. From the review of the previous structure-based models presented in Sections 3.2.1 – 3.2.5, several key ideas were incorporated into the derivation of this first principles transport model, including: 1) the use of a model of the stratum corneum that best represents the observed physical cross-section of the stratum corneum, in the direction of permeant flux through the stratum corneum, 2) the use of the same model of the stratum corneum for the evaluation of the porosity and the tortuosity factors, and 3) the realization that the use of an *effective diffusion path length* to model diffusive flux through the parallel intercellular diffusion

pathways in the stratum corneum always underestimates the total amount of intercellular space present in the stratum corneum. From microscopic imaging of the stratum corneum, the model of Johnson *et al.* (see Figure 3-1d), which incorporates the existence of asymmetrically offset corneocytes, seems to be the most accurate representation of the cross-section of the stratum corneum, in the direction of permeant flux. In addition, it is necessary to maintain consistency of the stratum corneum model in the evaluation of the porosity and the tortuosity factors. While it is possible to evaluate the porosity of the stratum corneum surface in two dimensions using hexagonal-shaped corneocytes, it is not currently possible to analytically evaluate the tortuosity in a three-dimensional section of the stratum corneum, since it is not clear how the parallel diffusion pathways should be treated in three-dimensions. (At first glance, it appears that there exist an infinite number of paths a molecule can choose to travel along the surface of a corneocyte to move from the center of the corneocyte to the edge of the corneocyte. Following the analogy with electrical circuits, the effective diffusion path length for an infinite number of finite diffusion paths would be zero, indicating that the stratum corneum would provide no resistance to transdermal diffusion. Clearly, this conclusion does not agree with experimental data, requiring more in depth study of parallel diffusion pathways in three dimensions.) For the purpose of the derivation presented in Section 3.3, therefore, a two-dimensional cross-section of the stratum corneum, oriented in the direction of permeant flux, was used to evaluate the tortuosity, while the porosity was evaluated from the one-dimensional "surface" corresponding to the two-dimension model of the stratum corneum cross-section. Finally, the review of the previous models has revealed that either the physical diffusion path length or the effective diffusion path length, modeled analogously

to electrical resistors in parallel, has been used in the past to estimate the tortuosity of the intercellular regions of the stratum corneum. It has been shown that the use of the effective diffusion path length in the expression for the tortuosity represents the best model to describe the flux of material through the intercellular region of the stratum corneum.[12,13] However, the use of the effective diffusion path length model always underestimates the total amount of space occupied by the intercellular regions of the stratum corneum, which could significantly underestimate the time required to reach steady-state diffusion in the stratum corneum. On the other hand, the actual physical space occupied by the intercellular regions of the stratum corneum can be well represented when the physical diffusion path length is used in the expression for the tortuosity of the intercellular diffusion pathways. However, use of the physical diffusion path length will lead to some underestimation of the steady-state diffusive flux. As the theoretical derivation presented next demonstrates, these modeling difficulties can be overcome if *two unique tortuosity factors*, one accounting for the *physical space occupied by the intercellular regions of the stratum corneum* and the second accounting for *the diffusive flux through the intercellular regions of the stratum corneum*, rather than a *single tortuosity factor*, are used to model the transport of drugs through the intercellular regions of the stratum corneum.

3.3 Theory

3.3.1 Derivation of Fick's Second Law for the Intercellular Regions of the Stratum Corneum

Figure 3-2 represents a horizontal repeating slice of the SC. Assuming that drug transport is restricted to the intercellular region of the SC, the following mass balance can be written on the thin slice of SC shown in Figure 3-2:

$$\dot{m}_{in} - \dot{m}_{out} = \frac{\partial m}{\partial t} \tag{3.26}$$

where $\dot{m}_{in}$ and $\dot{m}_{out}$ are the drug mass flow rates into, and out of, the thin slice of SC. The mass, m, which accumulates in the intercellular region of the SC can be defined as the product of the intercellular volume, V_{lipids}, and the drug concentration, C(z,t), where z denotes the direction perpendicular to the SC slice (see Figure 3-2). In the absence of hydration (swelling) effects in the SC during the course of a permeation experiment, V_{lipids} is constant with time, and Eq. (3.26) can be rewritten as follows:

$$\dot{m}_{in} - \dot{m}_{out} = V_{lipids} \frac{\partial C(z,t)}{\partial t} \tag{3.27}$$

Based on the geometry of the SC in Figure 3-2, V_{lipids} can be defined as follows:

$$V_{lipids} = Wg(h+g+d) \tag{3.28}$$

The volume of the entire SC slice is given by:

$$V_{SC} = W(d+g)(h+g) \tag{3.29}$$

The ratio of V_{lipids} to V_{SC} is then given by:

$$\frac{V_{lipids}}{V_{SC}} = \left(\frac{g}{d+g}\right)\left(\frac{h+g+d}{h+g}\right) = \varepsilon\tau_{volume} \tag{3.30}$$

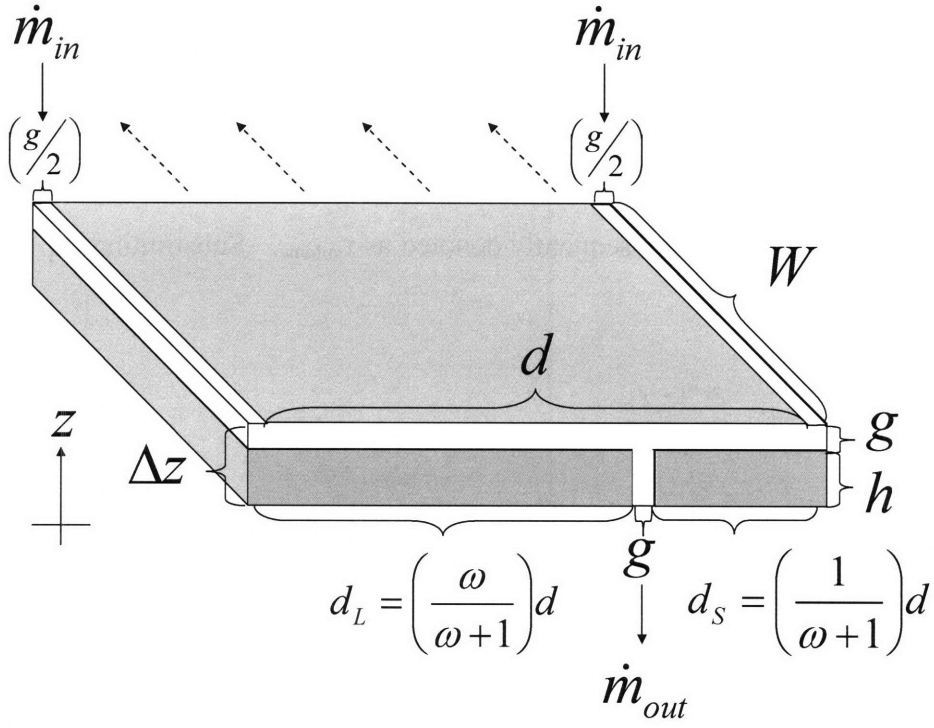

Figure 3-2: Repeating lateral slice of the stratum corneum, corresponding to the model of Johnson *et al.* (see Figure 3-1d), used for the derivation of Fick's Second Law of diffusion through the intercellular regions of the stratum corneum. The grey regions represent the impermeable corneocytes and the white regions represent the intercellular lipid lamellar regions. The dashed arrows indicate that the corneocytes are modeled as being infinite in the direction of the arrows. Note that the two intercellular regions at the inlet of the slice are each half of the intercellular gap width, (g/2), to maintain equality with the width of the intercellular region at the outlet of the slice.

Comparing the first term in parentheses in Eq. (3.30) to Eq. (3.4), it follows that it corresponds to the porosity, ε, in 1-D. Comparing the second term in parentheses in Eq. (3.30) to Eq. (3.6), it follows that Eq. (3.30) has a form similar to the expression for the tortuosity, τ, for the case of a single corneocyte and a single intercellular region, where d_{lat} is given by d. Since this tortuosity factor in Eq. (3.30) accounts for the total amount of lipids in the SC slice, it is subsequently denoted as τ_{volume}. Substituting Eq. (3.30) into Eq. (3.27) yields:

$$\dot{m}_{in} - \dot{m}_{out} = \varepsilon \tau_{volume} V_{SC} \frac{\partial C(z,t)}{\partial t} \tag{3.31}$$

Dividing Eq. (3.31) by the cross-sectional area of the SC slice, W(d+g), and using Eq. (3.29) for V_{SC} yields:

$$\frac{\dot{m}_{in}}{W(d+g)} - \frac{\dot{m}_{out}}{W(d+g)} = \varepsilon \tau_{volume} (h+g) \frac{\partial C(z,t)}{\partial t} \tag{3.32}$$

Noting that mass per unit area and per unit time is the flux, F, and that (h+g) = Δz (see Figure 3-2), Eq. (3.32) can be rearranged as follows:

$$\frac{1}{\tau_{volume}} \left[\frac{F(z+\Delta z,t) - F(z,t)}{\Delta z} \right] = \varepsilon \frac{\partial C(z,t)}{\partial t} \tag{3.33}$$

For the SC that has many layers of corneocytes, Δz can be assumed to be small compared to the entire SC thickness. In that case, the square-bracketed term in Eq. (3.33) corresponds to a derivative, and Eq. (3.33) reduces to:

$$\frac{1}{\tau_{volume}} \left[\frac{\partial F(z,t)}{\partial z} \right] = \varepsilon \frac{\partial C(z,t)}{\partial t} \tag{3.34}$$

It now remains to evaluate F(z,t) in terms of C(z,t) to obtain a model equation for the partial differential form of Fick's Second Law of diffusion. The mass flow rate of

drug delivered through the intercellular regions of the thin slice of the SC (see Figure 3-2) can be modeled as follows:

$$\dot{m}_{lipids} = D_b(Wg)\frac{C(z+\Delta z,t)-C(z,t)}{h+g+d_{lat}} \tag{3.35}$$

where (Wg) is the cross-sectional area of the lipids available to the drug at the inlet and the outlet of the SC slice, and ($h+g+d_{lat}$) is the effective intercellular diffusion path length through the thin slice of SC. Since there are two parallel lateral diffusion pathways, d_L and d_S, that the diffusing molecule may chose, d_{lat} may be evaluated using the techniques of Cussler *et al.* and of Johnson *et al.*, as follows:

$$\frac{1}{d_{lat}} = \frac{1}{d_L} + \frac{1}{d_S} \tag{3.36}$$

where d_L and d_S represent the long and the short diffusion paths (see Figure 3-2 for the corresponding expressions, and recall that $\omega = d_L/d_S$). The expressions for d_L and d_S represent the average physical diffusion path lengths for the long and the short parallel diffusion pathways, respectively. Substituting the expressions for d_L and d_S given in Figure 3-2 into Eq. (3.36) and simplifying yields:

$$d_{lat} = \frac{\omega}{(1+\omega)^2}d \tag{3.37}$$

The mass flow rate through a *homogeneous lipid membrane* that has the same thickness, (h+g), and cross-sectional area, W(d+g), as the slice of SC shown in Figure 3-2 can be expressed as follows:

$$\dot{m}_{SC} = D_b[W(d+g)]\frac{C(z+\Delta z,t)-C(z,t)}{h+g} \tag{3.38}$$

Taking the ratio of Eqs. (3.35) and (3.38) yields:

$$\frac{\dot{m}_{lipids}}{\dot{m}_{SC}} = \left(\frac{g}{d+g}\right)\frac{1}{\left(\dfrac{h+g+\dfrac{\omega}{(1+\omega)^2}d}{h+g}\right)} = \frac{\varepsilon}{\tau_{flux}} \tag{3.39}$$

As in Eq. (3.30), the first term in parentheses in Eq. (3.39) corresponds to the porosity, ε, in 1-D, and the second term in parentheses in Eq. (3.39) is similar to the expression for the tortuosity, τ, where d_{lat} is given by $[\omega/(1+\omega)^2]d$. Since this tortuosity factor in Eq. (3.30) accounts for the effect of the parallel, intercellular lateral diffusion pathways shown in Figure 3-2 on the *flux of material through the slice of SC*, it is subsequently denoted as τ_{flux}. Substituting Eq. (3.38) into Eq. (3.39) and dividing by the cross-sectional area of the SC to obtain the flux yields:

$$F = \frac{\dot{m}_{lipids}}{[W(d+g)]} = \frac{\varepsilon}{\tau_{flux}} D_h \frac{C(z+\Delta z,t)-C(z,t)}{h+g} \tag{3.40}$$

Noting again that (h+g) = Δz, where Δz represents a thin slice of the SC, Eq. (3.40) can be further simplified to yield Fick's First Law of diffusion for the intercellular regions of the SC:

$$F = \frac{\varepsilon}{\tau_{flux}}\left[D_h \frac{\partial C(z,t)}{\partial z}\right] \tag{3.41}$$

Substituting Eq. (3.41) into Eq. (3.34) yields the form of Fick's Second Law of diffusion through the intercellular regions of the SC.

$$\frac{\partial C}{\partial t} = \frac{D_h}{\tau_{flux}\tau_{volume}}\frac{\partial^2 C}{\partial z^2} \tag{3.42}$$

3.3.2 Obtaining Expressions for the Lag Time and for the Steady-State Permeability Corresponding to the Intercellular Regions of the Stratum Corneum

Equation (3.42) can be solved for the general case with the following boundary and initial conditions:

$$C(z = L,t) = K_{b,in}C_2 \tag{3.43a}$$

$$C(z = 0,t) = K_{b,out}C_1 \tag{3.43b}$$

$$C(z,t = 0) = C_0 \tag{3.43c}$$

where K_b is the vehicle/lipid bilayer partition coefficient, C_2 is the bulk concentration on the donor side of the SC, C_1 is the bulk concentration on the receiver side of the SC, and C_0 is the initial concentration of the drug within the intercellular lipids of the SC. Note that in the z-direction, z = 0 corresponds to the outlet of the stratum corneum, rather than to the inlet of the stratum corneum, in order to simplify the solution of Eq. (3.42). Following the solution procedure of Fick's Second Law of diffusion through a homogeneous membrane,[20] the solution to Eq. (3.42) with the above initial and boundary conditions, is given by:

$$\begin{aligned} C(z,t) &= K_{b,out}C_1 + \left(K_{b,in}C_2 - K_{b,out}C_1\right)\frac{z}{L} \\ &+ \frac{2}{\pi}\sum_{n=1}^{\infty}\frac{K_{b,in}C_2\cos n\pi - K_{b,out}C_1}{n}\sin\left(\frac{n\pi z}{L}\right)\exp\left(-\frac{D_b}{\tau_{flux}\tau_{volume}}\frac{n^2\pi^2 t}{L^2}\right) \\ &+ \frac{4C_0}{\pi}\sum_{m=0}^{\infty}\frac{1}{2m+1}\sin\left(\frac{(2m+1)\pi z}{L}\right)\exp\left(-\frac{D_b}{\tau_{flux}\tau_{volume}}\frac{(2m+1)^2\pi^2 t}{L^2}\right) \end{aligned} \tag{3.44}$$

The total amount of mass per unit area delivered across the SC, Q(t), is given by a time integral over the flux, that is, by:

$$Q(t) = \int_0^t F(z=0,t)dt = \int_0^t \frac{\varepsilon}{\tau_{flux}} D_h \left.\frac{\partial C(z,t)}{\partial z}\right|_{z=0} dt \tag{3.45}$$

where Eq. (3.41) has been used for the definition of the flux in the SC. Substituting Eq. (3.44) into Eq. (3.45) and carrying out the integration over time yields:

$$\begin{aligned} Q(t) &= \frac{\varepsilon D_h t}{\tau_{flux} L}\left(K_{h,in}C_2 - K_{h,out}C_1\right) \\ &+ \frac{2\varepsilon\tau_{volume}L}{\pi^2}\sum_{n=1}^{\infty}\left(\frac{K_{h,in}C_2\cos n\pi - K_{h,out}C_1}{n^2}\right)\left[1-\exp\left(\frac{-D_h n^2\pi^2 t}{\tau_{flux}\tau_{volume}L^2}\right)\right] \\ &+ \frac{4\varepsilon C_0\tau_{volume}L}{\pi^2}\sum_{m=0}^{\infty}\left(\frac{K_{h,in}C_2\cos n\pi - K_{h,out}C_1}{(2m+1)^2}\right)\left[1-\exp\left(\frac{-D_h(2m+1)^2\pi^2 t}{\tau_{flux}\tau_{volume}L^2}\right)\right] \end{aligned} \tag{3.46}$$

For the special case when $C_1 = C_0 = 0$, which is applicable for most permeation experiments, Eq. (3.46) can be further simplified by noting that $\cos(n\pi) = (-1)^n$ and that $\sum_{n=1}^{\infty}\frac{(-1)^n}{n^2} = -\frac{\pi^2}{12}$. This yields:

$$Q(t) = \left(\varepsilon K_{h,in}C_2\tau_{volume}L\right)\left[\frac{D_h t}{\tau_{flux}\tau_{volume}L^2} - \frac{1}{6} - \frac{2}{\pi^2}\sum_{n=1}^{\infty}\frac{(-1)^n}{n^2}\exp\left(\frac{-D_h n^2\pi^2 t}{\tau_{flux}\tau_{volume}L^2}\right)\right] \tag{3.47}$$

Equation (3.47) describes the cumulative amount of mass delivered through the intercellular regions of the SC at time, t, while using both the intrinsic values of the drug vehicle/lipid bilayer partition coefficient and the diffusion coefficient. At steady-state (for large t), Eq. (3.47) simplifies as follows:

$$Q(t) = \left(\varepsilon K_{h,in}C_2\tau_{volume}L\right)\left[\frac{D_h t}{\tau_{flux}\tau_{volume}L^2} - \frac{1}{6}\right] \tag{3.48}$$

From Eq. (3.48), the lag time for diffusion through the intercellular regions of the SC can be evaluated by setting Q(t) in Eq. (3.48) equal to zero and solving for t_{lag},[20] which yields:

$$t_{lag} = \frac{\tau_{flux}\tau_{volume}L^2}{6D_b} \tag{3.49}$$

Equation (3.49), which describes the lag time to steady-state in the intercellular regions of the stratum corneum, has *two* unique tortuosity factors, rather than the *single* tortuosity factor present in the expression for the lag time, ($t_{lag} = (\tau L)^2/6D_b$), presented in Section 3.1. Finally, the steady-state permeability, P, for drug transport through the intercellular regions of the SC can be evaluated by dividing Eq. (3.48) by C_2 and evaluating the time derivative to obtain:

$$P = \frac{1}{C_2}\frac{\partial Q(t)}{\partial t} = \left(\frac{\varepsilon}{\tau_{flux}}\right)\frac{K_{b,in}D_b}{L} \tag{3.50}$$

Equation (3.50) has a form similar to Eq. (3.1), where τ and K_b in Eq. (3.1) are now given by τ_{flux} and $K_{b,in}$, respectively, for steady-state diffusion through the intercellular regions of the stratum corneum. Note that for the case of a homogeneous membrane where ε, τ_{volume}, and τ_{flux} are equal to 1, Eqs. (3.44) – (3.50) reduce to the equations describing transport through a homogeneous membrane.[20]

Application of Eqs (3.47) – (3.50) to human SC samples of the type shown in Figure 3-1d requires slight modifications to the expressions used for τ_{volume} and τ_{flux} to account for the presence of N corneocyte layers and (N-1) intercellular lateral lipid layers in the SC model presented in Figure 3-1d. The expressions for τ_{volume} and τ_{flux} corresponding to this case are:

$$\tau_{volume} = \frac{Nh + (N-1)g + (N-1)d}{Nh + (N-1)g} \tag{3.51a}$$

and

$$\tau_{flux} = \frac{Nh + (N-1)g + (N-1)\dfrac{\omega}{(1+\omega)^2}d}{Nh + (N-1)g} \tag{3.51b}$$

Equations (3.51a) and (3.51b) have the same general form as the expression for the tortuosity given in Eq. (3.6), which accounts for the actual number of layers of corneocytes (N) and intercellular lateral lipid bilayers (N-1), where d_{lat} is equal to d for τ_{volume} and equal to $[\omega/(1+\omega)^2]d$ for τ_{flux}, and L = Nh+(N–1)g. By including these two tortuosity factors in the model equations, it is now possible to separate the effect of the volume of the stratum corneum intercellular domain on the time required to reach steady-state in the intercellular domain and the effect of the parallel pathways in the intercellular domain on the diffusive flux of hydrophobic molecules through the stratum corneum. Previous structure based models, restricted by the use of a single tortuosity factor, were unable to distinguish these separate effects on diffusive transport that arise from the physical arrangement of the stratum corneum intercellular domain.

3.4 Theoretical and Experimental Methods and Materials

3.4.1 Finite Element Method Simulations

Finite Element Method simulations were conducted using FEMLAB 3.0a (Comsol, Inc.). 2D geometric models of the SC, similar to the one presented in Figure 3-1d, were generated in FEMLAB. The assumptions built into the model included: 1) no diffusive flux into or out of the corneocytes, 2) zero concentration of the permeant on the receiver side of the SC (note that while permeant does accumulate in the receiver chamber in an actual permeability experiment, if the concentration of the permeant in the receiver chamber is much lower than that in the donor chamber, one can safely assume that the

permeant concentration in the receiver chamber is zero, relative to that in the donor chamber), 3) a non-zero value of the bulk concentration, C_0, on the donor side of the SC (a value of 0.1 g/L was used in the simulations), and 4) periodic boundary conditions equating the values of the permeant concentrations on the left edge and on the right edge of the intercellular regions within the SC. Values of 1 and $1*10^{-9}$ m^2/s were chosen as inputs in the simulations for K_b and D_b, respectively. The following SC geometric parameters were varied (over the listed range of values): the corneocyte diameter, d (20, 30, **40**, 50 and 60 μm); the ratio, g/h, which measures the amount of intercellular space in the SC relative to the amount of space in the SC occupied by the corneocytes (0.02, **0.1**, 0.5); and the corneocyte layer offset, ω (1, **3**, **8**, 19, 37, and infinity).[13] These values were selected to examine the robustness of Eq. (3.47) over a range of SC structural parameters, centered around the structural parameter values corresponding to native SC, listed in bold above.[12,13] The chosen values of g/h vary from the case of swollen corneocytes (g/h = 0.02) to the case of a swollen intercellular region (g/h = 0.5), while the native SC structure is represented by g/h = 0.1. In each of the above cases, the volume of the intercellular region was assumed to be constant during the simulation of each permeation experiment, even though the volume of the intercellular region did vary between each case examined. The values of ω were varied from the case corresponding to symmetrically offset corneocyte layers (ω = 1) to the case corresponding to aligned corneocyte layers which have no offset (ω = infinity). Each simulation was run for 100 seconds of simulation time to ensure that the FEMLAB simulations reached the steady-state diffusion phase. Time steps were taken every 0.4 seconds to minimize numerical errors, while keeping the simulation solution time on the order of minutes. Plots of Q(t)

vs. time were generated by exporting the flux vs. time data corresponding to the lipid bilayer edge located on the receiver side of the SC model generated in FEMLAB into an Excel spreadsheet, and then performing the numerical integration required by Eq. (3.45) to obtain Q(t). Note that increases, or decreases, in the values of K_b and C_0 used in the FEMLAB simulations relative to the values reported above result directly in proportional increases, or in decreases, of Q(t), and, thus, will have no impact on the calculated values for % error in the regressed values of K_b and D_b. In addition, decreases in the values of D_b used in the FEMLAB simulations can impact whether the FEMLAB simulation reaches the steady-state regime, but this can easily be addressed by increasing the simulation time, such that the term, D_bt, remains constant.

3.4.2 Permeability Experiments with Human SC Membranes

Two radiolabeled *hydrophobic* permeants – Naphthol (MW = 144.2 Da, log $K_{o/w}$ = 2.84) and Testosterone (MW = 288.4, log $K_{o/w}$ = 3.31) – were selected to demonstrate how Eq. (3.47) can be used to *simultaneously evaluate* K_b and D_b from the permeability experiments. Both permeants were selected because of their previous use as model hydrophobic permeants.[12,16] These chemicals were obtained from American Radiolabeled Chemicals, Inc. (St. Louis, MO). Phosphate Buffer Saline was obtained from Fluka Chemical (St. Louis, MO).

Full-thickness human cadaver skin was obtained from the National Disease Research Institute (Philadelphia, PA) and stored at -80°C until use. The full-thickness human skin was submersed in 60°C water for 2 minutes to heat strip the epidermis from the dermis.[17] The heat-stripped epidermis was then placed, with the stratum corneum

side up, in a phosphate buffer saline (PBS) solution containing 0.1% (w/v) trypsin (Sigma Chemical, St. Louis, MO) for 24 hours at 25 °C to remove the epidermis. The SC was rinsed in PBS and any residual epidermis was gently scrapped from the SC. The SC was then transferred to a nylon mesh for support and stored at 4°C, 95 % humidity for up to 14 days prior to use.[18]

Diffusion experiments were carried out using side-by-side diffusion cells. The structural integrity of the SC samples was tested using electrical resistivity measurements according to previously published methods.[19] Any SC sample with an initial electrical resistivity below 30 kOhm*cm^2 was considered damaged and was replaced with a new SC sample. The hydrophobic permeants were rotary evaporated to remove the solvent, and were subsequently redissolved in PBS to obtain a donor solution concentration of 1 μCi/ml. Aliquots of the receiver chamber were taken at predetermined time points, and their radioactivity was measured using a scintillation counter (Packard, Tri-Carb®, 2200 CA). Permeability experiments were conducted for 2 hours for naphthol, and for 8 hours for testosterone to ensure transition into the steady-state regime for the two hydrophobic permeants considered. Note that more time was required for testosterone to reach steady-state, because testosterone has a larger molecular weight than naphthol (see Figure 3-4). Plots of Q(t) versus time were then generated from the results of the scintillation counting of the aliquots taken from the receiver cell.

3.4.3 Regression Analysis of FEMLAB and of the Experimental Diffusion Data using Eq. (3.47) to evaluate K_b and D_b

The Q(t) versus time data generated from the FEMLAB simulations and from the human SC diffusion experiments were analyzed using DataFit 8.1 (Oakdale Engineering). Equation (3.47) was used as the model equation for the nonlinear regression analysis, and K_b and D_b were selected as the regression parameters for analysis of both data sets. DataFit 8.1 uses the Levenberg-Marquardt method as the algorithm for adjusting the values of the initial estimates of the regression parameters to improve the fit of the nonlinear regression model. For the FEMLAB data, the initial values of K_b and D_b for the regression analysis were set at 1 and $1*10^{-9}$ m^2/s, respectively, which were the chosen input values of K_b and D_b used in the FEMLAB simulations. For the human SC diffusion experimental data, the initial values of K_b and D_b for the regression analysis were 100 and $1*10^{-8}$ cm^2/s, respectively. These initial values of K_b and D_b were selected as representative values of K_b and D_b for hydrophobic permeants based on previously published data.[12,16]

3.5 Results and Discussion

3.5.1 Comparison of the K_b and D_b Inputs for the FEMLAB Simulations with the Values of K_b and D_b Obtained from the Regression Analysis of the FEMLAB Data Using Eq. (3.47)

Figures 3-3a and 3-3b present the absolute % error in the regressed values of D_b and K_b, respectively, compared to the FEMLAB input values of D_b ($1*10^{-9}$ m^2/s) and K_b (1) over

the range of SC geometric parameters studied. Note that the R^2 values for all the regressions of the FEMLAB data using Eq. (3.47) exceeded 0.9999. In both figures, the white blocks correspond to the swollen corneocyte case (g/h = 0.02), the light grey blocks correspond to the native SC case (g/h = 0.1), and the dark grey blocks correspond to the swollen intercellular region case (g/h = 0.5). For each individual case, the data are plotted by decreasing corneocyte length, d, on the x-axis and by increasing corneocyte offset, ω, on the y-axis (recall that for ω = 1, the corneocytes are symmetrically offset, while for ω = infinity, the corneocytes are aligned such that there is no offset). Absolute % error values in D_b and K_b for SC models similar to the native SC skin structure (d = 40 μm, h = 1 μm, g = 0.1 μm, w = 3 – 8) are denoted by the asterisks (*).

Based on the results in Figures 3-3a and 3-3b, it appears that Eq. (3.47) performs better (i.e. the absolute % error decreases) as: 1) the ratio, g/h, approaches zero, 2) the corneocyte length, d, increases, and 3) the corneocyte offset, ω, approaches 1. Therefore, one may conclude, based on comparisons with the finite-element data generated by FEMLAB, that Eq. (3.47) approaches the exact solution describing transient diffusion through the intercellular regions of the SC membrane as the intercellular regions of the SC become infinitely thin (g/h approaches 0), and when the corneocytes are symmetrically offset (ω approaches 1). While Eq. (3.47) compares very well to the FEMLAB data at these idealized conditions, Eq. (3.47) also performs very well over the wide range of SC geometries that were analyzed. In Figures 3-3a and 3-3b, absolute % errors greater than 5% correspond to the highlighted blocks. In Figure 3-3a, Eq. (3.47) was able to reproduce the value of D_b to within less than 5% of the FEMLAB input value for over two-thirds of the SC geometries sampled. In addition, in Figure 3-3b, Eq. (3.47)

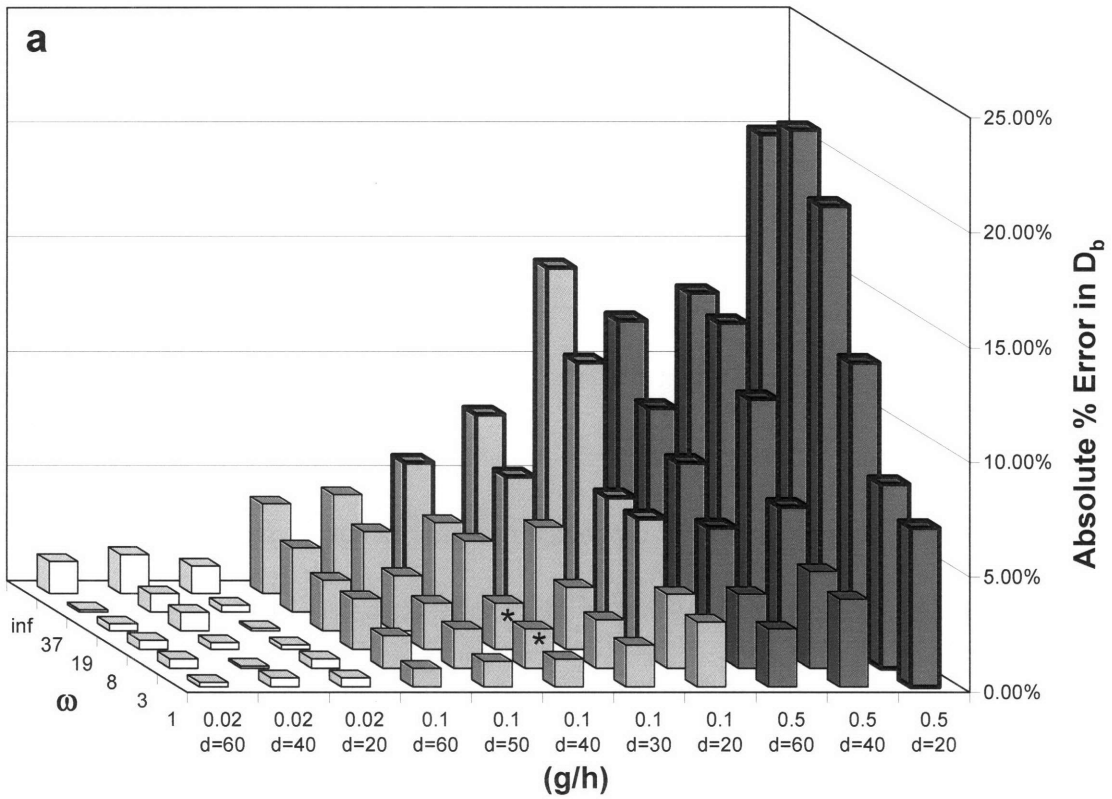

Figure 3-3: Absolute % errors in the values of (a) D_b and (b) K_b from the FEMLAB simulations regressed using Eq. (3.47). The white bars correspond to a (g/h) ratio of 0.02, the light grey bars correspond to a (g/h) ratio of 0.1, and the dark grey bars correspond to a (g/h) ratio of 0.5, where g/h is the ratio of the intercellular region in the SC to the corneocyte region in the SC. Values of ω vary from 1, corresponding to the case of symmetrically offset corneocyte layers, to infinity, corresponding to the case where the corneocyte layers have no offset. Values of the corneocyte diameter, d, vary from 20 μm to 60 μm. The asterisks (*) correspond to stratum corneum geometries found in native human stratum corneum samples. Columns having values larger than 5% are highlighted in bold.

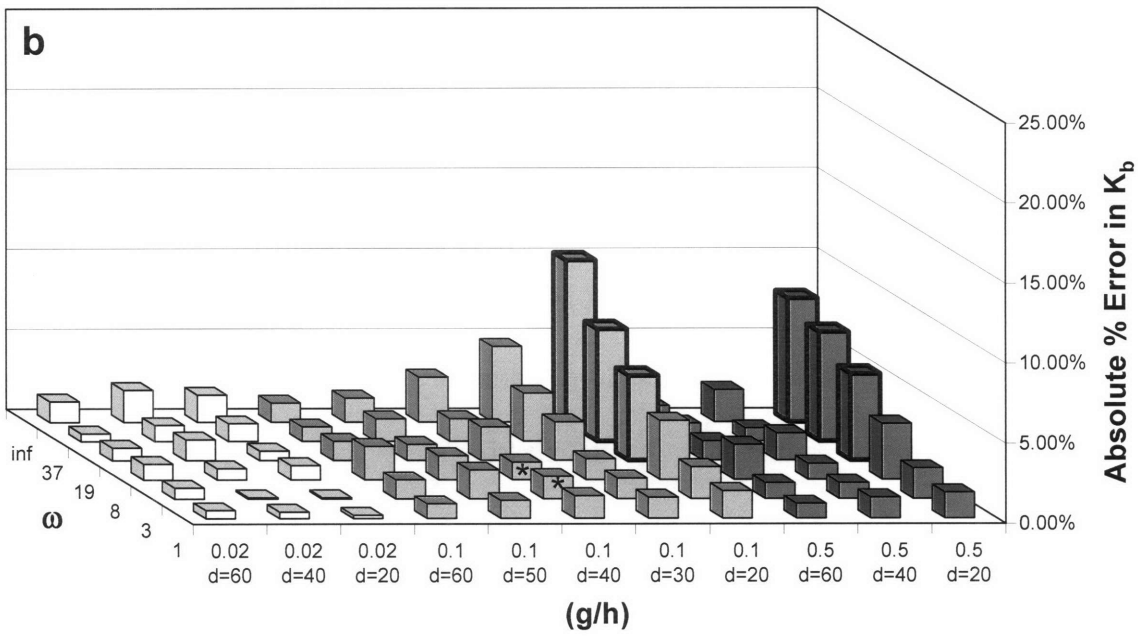
b
25.00%
20.00%
15.00%
10.00%
5.00%
0.00%
Absolute % Error in K_b
inf
37
19
8
3
ω
1
0.02 d=60
0.02 d=40
0.02 d=20
0.1 d=60
0.1 d=50
0.1 d=40
0.1 d=30
0.1 d=20
0.5 d=60
0.5 d=40
0.5 d=20
(g/h)

was able to reproduce the value of K_b to within less than 5% of the FEMLAB input value for over 90% of the SC geometries sampled. Most importantly, perhaps, Figures 3-3a and 3-3b indicate that Eq. (3.47) can be used to obtain values of K_b and D_b to within approximately 2-3% of the actual value of these parameters for a drug permeating through the intercellular regions of a native human SC sample (see the asterisked columns).

One source for the observed errors between the regressed values of K_b and D_b and the FEMLAB input values of K_b and D_b is the inability of the current model to predict the initial exit of permeant from the SC. Equation (3.47) assumes that all permeants will travel along a diffusion path which is proportional to the effective lateral diffusion path, d_{lat}. However, in the FEMLAB simulations, permeants that physically travel along the shorter lateral diffusion path length, d_s, will exit from the SC earlier than predicted by Eq. (3.47), which results in decreased diffusion lag times. As ω approaches infinity and d_s approaches 0, this error in the diffusion lag times increases. Since L, τ_{flux}, and τ_{volume} are fixed quantities in Eq. (3.47), the decrease in the lag time is compensated for by increasing the value of D_b. This increase in D_b is then coupled with a corresponding decrease in K_b to increase the goodness of the fit corresponding to the steady-state regime. This may explain why the errors in K_b and D_b increase as ω increases and as d decreases (see Figures 3-3a and 3-3b), since both result in a decrease of the value of d_s. A second source of error may be attributed to the presence of increased 2-D diffusion as the ratio, g/h, increases. As g/h approaches zero, the intercellular region becomes infinitely thin and diffusion in the intercellular region can adequately be modeled as 1-D diffusion. As g/h increases, the thickness of the intercellular regions increases, which

may cause 2-D diffusion to become significant. This may explain why the errors in D_b when g/h = 0.5 are much larger than the errors in D_b when of g/h = 0.1 and 0.02, without a corresponding increase in the errors in K_b over the same range of g/h values (see the d = 40 and the d = 60 columns in Figure 3-3a and 3-3b). When d = 20, corresponding to the largest errors in D_b and K_b, both sources of error discussed here are likely to contribute to the observed errors in D_b and K_b.

The errors in D_b and K_b reported here between the regressed values of D_b and K_b using Eq. (3.47) and the values of D_b and K_b used in the FEMLAB simulation are still small when compared to the values of D_b and K_b regressed from the five previous structure-based SC permeability models discussed in Section 3.2 that utilize the intrinsic values of D_b and K_b in the model equations. Table 3-1 summarizes the expressions for the porosity and the tortuosity used in these five models, which were presented in Section 3.2. These expressions for the porosity and the tortuosity can be used in the following equation:

$$Q(t) = \varepsilon K_b C \tau L \left[\frac{D_b t}{(\tau L)^2} - \frac{1}{6} - \frac{2}{\pi^2} \sum_{n=1}^{\infty} \frac{(-1)^n}{n^2} \exp\left(-\frac{D_b t}{(\tau L)^2} n^2 \pi^2 \right) \right] \tag{3.52}$$

Equation (3.52) was derived using the methods presented in Section 3.3.2, but where Eq. (3.42) would have a single tortuosity factor for the flux and the volume of intercellular space in the SC, rather than separate tortuosity factors for the flux and the volume of intercellular space in the SC. Equation (3.52) can be used in place of Eq. (3.47) as the regression equation, with D_b and K_b as the regression parameters, to compare with the FEMLAB Q(t) vs. time data. The results of this analysis for three SC geometries are presented in Table 3-2. The SC geometries selected include: 1) symmetrically offset,

Table 3-1: Expressions for the Porosity, ε, and the Tortuosity, τ, from the Five Previously Published Structure-Based Models for Transport through the Intercellular Regions of the Stratum Corneum.

Model	Porosity, ε	Tortuosity, τ
Michaels *et al.*[8]	$\frac{2g}{d}$	$1+\frac{\frac{d}{h}+\frac{g}{h}}{2\left(1+\frac{g}{h}\right)}$
Cussler *et al.*[9]	$\frac{g}{d+g}$	$\frac{Nh+(N-1)\left(\frac{d+g}{4}\right)}{L}$
Lange-Lieckfeldt and Lee[10]	$\frac{\left[\left(\frac{d+g}{2}\right)^2-\left(\frac{d}{2}\right)^2\right]}{\left(\frac{d}{2}\right)^2}$	$\frac{L+(N-1)\left(\frac{d+g}{2}\right)}{L}$
Edwards and Langer[11]	$\left(\frac{g}{d+g}\right)\left(\frac{l_o}{l_o+l_w}\right)$	$\frac{d+h}{h}$
Johnson *et al.*[12]	$\frac{g}{d+g}$	$\frac{Nh+(N-1)\left(\frac{\omega}{(1+\omega)^2}\right)d}{L}$

swollen corneocytes (d = 60, h = 5, g = 0.1, and ω = 1), 2) native SC structure (d = 40, h = 1, g = 0.1, and ω = 3), and 3) asymmetrically offset corneocytes with swollen lipids (d = 20, h = 1, g = 0.5, and ω = 37). These three SC geometries were selected as examples of a native SC geometry and extreme cases of the SC geometries considered for the

Table 3-2: Comparison of the Regressed Values of K_b and D_b from the FEMLAB Q(t) versus Time Data Using Eq. (3.47) (the Two-Tortuosity Model) and Eq. (3.52) (the five models presented in Section 3.2, each having a single tortuosity factor).[a]

	d = 60, h = 5, g = 0.1, ω = 1		d = 40, h = 1, g = 0.1, ω = 3		d = 20, h = 1, g = 0.5, ω = 37	
Model	K_b	D_b*10^9	K_b	D_b*10^9	K_b	D_b*10^9
Two-Tortuosity Model	0.995	1.002	0.986	1.017	0.932	1.210
Michaels *et al.*	4.086	0.048	0.913	1.419	1.085	2.489
Cussler *et al.*	14.91	0.014	3.661	0.351	4.381	0.642
Lange-Lieckfeldt and Lee	4.261	0.044	0.953	1.286	1.104	2.344
Edwards and Langer	40.30	0.017	7.967	6.390	7.709	17.89
Johnson *et al.*	14.93	0.014	4.742	0.209	4.807	0.145

[a] = The chosen input values of K_b and D_b for the FEMLAB simulations were 1 and $1*10^{-9}$ m^2/s, respectively.

FEMLAB experiments. As can be seen from Table 3-2, the values of K_b and D_b obtained with Eq. (3.47) for these three SC geometries are closer to the FEMLAB input values (K_b = 1, $D_b = 1*10^{-9}$ m^2/s) than the values of K_b and D_b obtained using any of the other five structure-based SC permeability models considered here. The observed improvement is due to accounting for the impact of the volume of the SC intercellular region on intercellular transport through the SC in Eq. (3.47), captured in the term, τ_{volume}. As discussed in Section 3.3, this tortuosity term was obtained directly from first-principles by using a mass balance to describe the accumulation of the drug within the intercellular regions of the SC.

It is noteworthy that the expression for the ratio of the lag time from the Two-Tortuosity Model (see Eq. (3.49)) to the lag time for a similar sized homogeneous membrane ($t_{lag0} = L^2/6D_b$), given by:

$$\frac{t_{lag}}{t_{lag0}} = \tau_{volume}\tau_{flux} = \left(1 + \frac{(N-1)d}{Nh + (N-1)g}\right)\left(1 + \frac{(N-1)\dfrac{\omega}{(1+\omega)^2}d}{Nh + (N-1)g}\right) \tag{3.53}$$

is very similar, assuming that N ~ (N-1), to the expression for the ratio of the lag time through the SC membrane to the lag time of a similar sized homogeneous membrane presented by Frasch and Barbero:[13]

$$\frac{t_{lag}}{t_{lag0}} = \left(1 + \frac{d}{h+g}\right)\left(1 + \frac{\dfrac{\omega}{(1+\omega)^2}d}{h+g}\right) \tag{3.54}$$

where t_{lag} is the lag time through the SC, t_{lag0} is the lag time through a similar sized homogeneous membrane. While the first-principles derivation of Eq. (3.47) presented in this chapter yields similar expressions for the lag time ratio to those presented by Frasch and Barbero, the model equation described in Eq. (3.47) utilizes the *intrinsic* values of the SC membrane thickness, L, the intercellular lipid diffusion coefficient, D_b, and the vehicle/lipid bilayer partition coefficient, K_b. By including a second tortuosity factor into the diffusion model equation, Eq. (3.47) properly accounts for the geometric factors influencing the SC tortuosity, which, in turn, allows for the use of the *intrinsic* values of L, D_b, and K_b in the model equation. When only one tortuosity factor is used to describe the SC diffusion length, as in Eq. (3.2), it then becomes necessary to use the *effective* values of L and D_b to describe permeation data through the SC, as stated by Frasch and Barbero.[13] Having demonstrated the ability of Eq. (3.47) to extract values of D_b and K_b from FEMLAB SC permeability simulations for SC structures similar to native human SC structures to within 2-3% of the *intrinsic* values of K_b and D_b, Eq. (3.47) can now be

used as a tool to simultaneously deduce the *intrinsic* values of K_b and D_b for hydrophobic permeants directly from permeability experiments.

3.5.2 Simultaneous Evaluation of K_b and D_b for Hydrophobic Permeants from SC Permeability Experiments with Hydrophilic Molecules Using Eq. (3.47)

The delivery of the hydrophobic permeants – naphthol and testosterone – through human SC as a function of time is presented in Figure 3-4a and Figure 3-4b, respectively. The experimental data, as shown by the black circles, in Figure 3-4 represents the average of 5 experiments. The error bars represent the standard deviation of the experimental data for the 5 experiments conducted. For naphthol (Figure 3-4a), the solid line represents the best-fit curve (R^2 = 0.9975) of the experimental data using Eq. (3.47). The intrinsic values of K_b and D_b obtained from the regression analysis are 233 ($\pm$44) and $1.6*10^{-7}$ ($\pm 0.3*10^{-7}$) cm^2/s, respectively. For testosterone (Figure 3-4b), the solid line represents the best-fit curve (R^2 = 0.998) of the experimental data using Eq. (3.47). The intrinsic values of K_b and D_b obtained from the regression analysis are 100 ($\pm$14) and $1.8*10^{-8}$ ($\pm 0.2*10^{-8}$) cm^2/s, respectively. These values for K_b and D_b for naphthol and testosterone compare well with the values of K_b and D_b obtained using permeation experiments combined with octanol-water partition experiments,[12] as well as using permeation experiments combined with solute release experiments,[16] as shown in Table 3-3. Again, the great practical advantage of the new method to obtain K_b and D_b is that it requires *only* permeability experiments to evaluate these parameters, while all the previous methods require *two types* of experimental measurements.

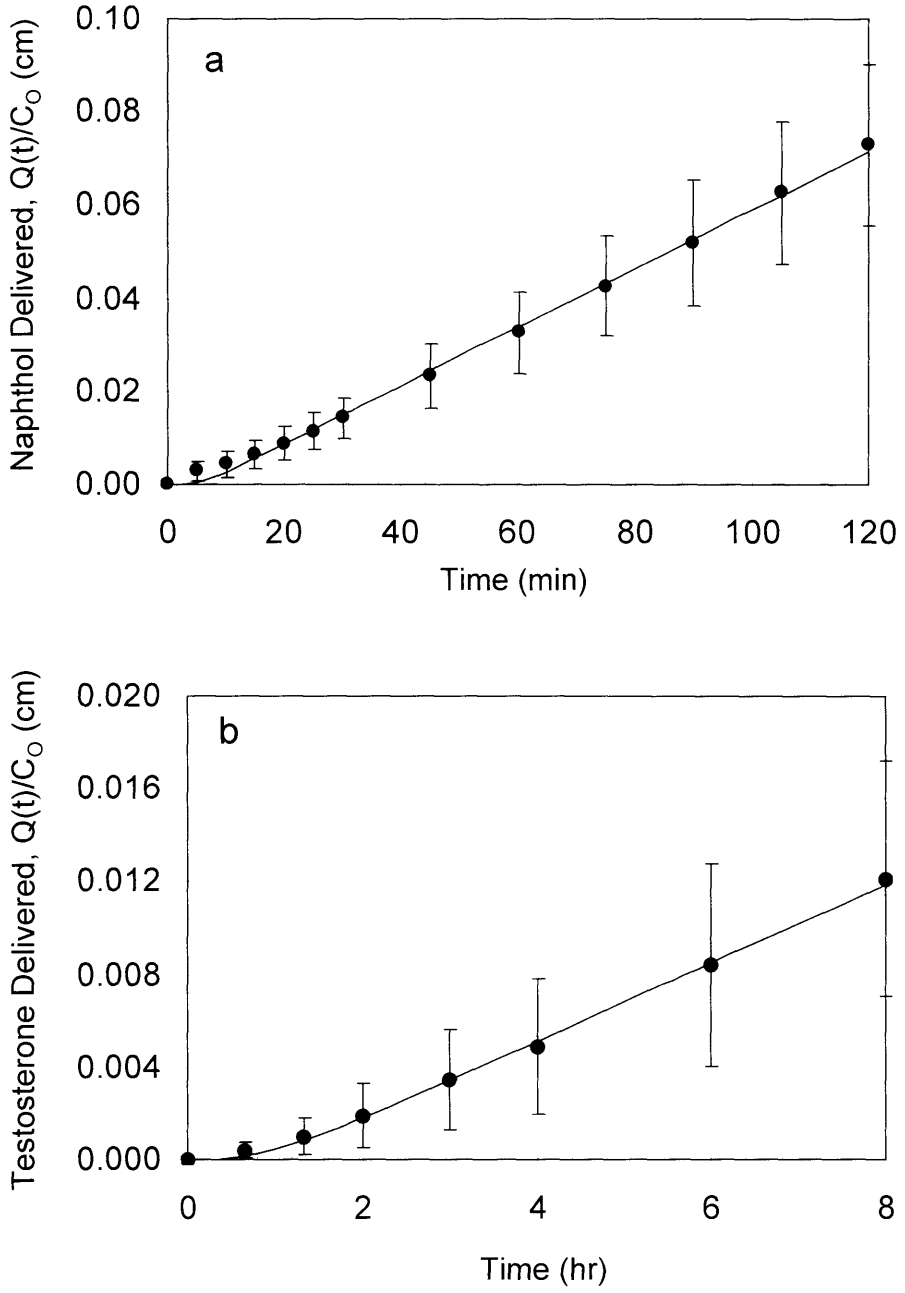

Figure 3-4: Delivery of hydrophobic permeants through human SC: (a) Naphthol, (b) Testosterone. Key: Black circles – experimental data (n = 5), solid lines – best-fit curve of the experimental data using Eq. (3.47). Error bars: $\pm$ 1 S.D.

Table 3-3: Comparison of K_b and D_b Values Obtained using the Two-Tortuosity Model with Values of K_b and D_b Obtained Using Previously Published Techniques.

	Naphthol		Testosterone	
	K_b	D_b (cm^2/s)	K_b	D_b (cm^2/s)
Two-Tortuosity Model (*ONLY* permeation experiments)	233 ($\pm$44)	$1.6*10^{-7}$ ($\pm 0.3*10^{-7}$)	100 ($\pm$14)	$1.8*10^{-8}$ ($\pm 0.2*10^{-8}$)
Permeation experiments *AND* octanol-water partition experiments[12]	144	$1.9*10^{-7}$	328	$1.6*10^{-8}$
Permeation experiments *AND* solute release experiments[16]	519	$0.5*10^{-7}$	108	$2.0*10^{-8}$

The value of D_b for testosterone obtained with the Two-Tortuosity Model was also in good agreement with the expected value of D_b based on FRAP (fluorescence recovery after photobleaching) measurements in extracted human stratum corneum lipids. Johnson *et al.* measured the value of the lateral diffusion coefficient for permeants having a molecular weight in the range of 223 to 854 Da in three model membranes, dimyristoylphosphatidylcholine (DMPC), DMPC/cholesterol (40% mol), and human stratum corneum lipids extracted with chloroform/methanol (2:1).[21] Based on the results of Johnson *et al.*, the expected values for testosterone in DMPC, DMPC/cholesterol, and extracted stratum corneum are $12.5*10^{-8}$, $3.2*10^{-8}$, and $1.0*10^{-8}$ cm^2/sec.[21] The value of D_b obtained from permeability experiments in the SC with the two-tortuosity model ($1.8*10^{-8}$ cm^2/sec) is closest to the FRAP measurements conducted with extracted human stratum corneum lipids. The difference in the values of D_b for testosterone with the two-tortuosity model and the expected value in extracted human stratum corneum could be due to the lipid extraction and bilayers formation processes. The extraction and

deposition of the stratum corneum lipids could result in a bilayer structure that is different from what is found in native human SC samples. Still, comparison of the value of D_b from the two-tortuosity model and the value expected in with FRAP does support the accuracy of the two-tortuosity method, since, as previously mentioned, the value obtained from permeability experiments in the SC with the two-tortuosity model is closest to the FRAP measurements conducted with extracted human stratum corneum lipids.

In addition to being able to more accurately and more easily determine the values of K_b and D_b associated with drug transport in the intercellular regions of the stratum corneum, the new method of analysis presented in this chapter would allow determination of the enhancement mechanism induced by chemical enhancers. Specifically, by comparing the values of K_b and D_b for a desired drug in untreated and chemically-treated skin, one could determine whether the chemical enhancer increases the partitioning of the drug into the skin (by increasing the value of K_b), or whether it perturbs the highly-ordered structure of the lipid bilayers to increase the permeability of the drug (by increasing the value of D_b), or both.

3.6 Conclusions

From first principles, a new theoretical model that describes Fickian diffusion of hydrophobic permeants which diffuse through the intercellular lipid domains of the stratum corneum has been developed. This new theoretical model utilizes the structural parameters of the stratum corneum to evaluate the porosity and the tortuosity parameters. The new feature of the model is the presence of two tortuosity factors in the model equations, which account for: 1) the total amount of lipid in the SC, and 2) the impact of

parallel diffusion pathways on the diffusive flux through the SC. Based on a regression analysis of the data obtained from the simulated stratum corneum diffusion experiments performed with FEMLAB, the new transport model deduced K_b and D_b to within a 2-3% error for native stratum corneum structures, out-performing all the five previous structure-based transport models considered. The regressed values of $K_b = 233$ ($\pm$44) and $D_b = 1.6*10^{-7}$ ($\pm 0.3*10^{-7}$) cm^2/s for naphthol and $K_b = 100$ ($\pm$14) and $D_b = 1.8*10^{-8}$ ($\pm 0.2*10^{-8}$) cm^2/s for testosterone, obtained using the new transport model, are comparable to the K_b and D_b values obtained using previously published experimental techniques. This result demonstrates that K_b and D_b values for hydrophobic permeants can be evaluated solely from permeation experiments using the new theoretical model, which should greatly simplify the experimental method used to evaluate K_b and D_b for hydrophobic permeants.

In the next chapter, the impact of localized transport regions on the transport of hydrophilic drugs through ultrasound-treated skin is examined. As part of this examination, the results of this chapter are used to establish whether drugs permeate through the LTRs via an intercellular or via a transcellular pathway. Specifically, the equations for $(\varepsilon/\tau_{flux})$ for the intercellular domain of the stratum corneum obtained in this chapter are used to determine a threshold value for the presence of hydrophilic intercellular pathways in the LTRs. If the value of $(\varepsilon/\tau_{flux})$ for the hydrophilic pathways is greater than the threshold value, then this would suggest that transcellular permeation pathways are formed in the LTRs present in the ultrasound-treated skin.

3.7 References

1. Jarrett A, Ed. 1978. The Physiology and Pathology of the Skin. London: Academic.
2. Schaefer H and Redelmeier TE. 1996. Skin Barrier: Principles of Percutaneous Absorption; New York: Karger.
3. Hou SYE, Mitra AK, White SH, Menon GK, Ghadially R, Elias PM. 1991. Membrane structures in normal and essential fatty acid deficient stratum corneum: Characterization by ruthenium tetroxide staining and x-ray diffraction. J Invest Dermatol 96:215-223.
4. Bodde HE, van der Brink I, Koerten HK, de Haan FHN. 1991. Visualization of in vitro percutaneous penetration of mercuric chloride: Transport through intercellular spaces cellular uptake through desmosomes. J Cont Rel 15:227-236.
5. Bommanan D, Menon GK, Okuyama H, Elias PM, Guy RH. 1992. Sonophoresis. II. Examination of the mechanism(s) of ultrasound-enhanced transdermal drug delivery. Pharm Res. 9:1043-1047.
6. Nemanic MK, Elias PM. 1980. In situ precipitation: A novel cytochemical technique for visualization of permeability pathways in mammalian stratum corneum. J Histochem Cytochem 28:573-578.
7. Squier CA, Lesch CA. 1988. Penetration pathways of different compounds through epidermis and oral epithelia. J Oral Pathol 17:512-516.
8. Michaels AS, Chandraskeran SK, Shaw JE. 1975. Drug permeation through human skin: theory and in vitro experimental measurement. Am Inst Chem Eng J 21:985-996.

9. Cussler E, Hughes S, Ward W, and Aris R. 1988. Barrier membranes. J Memb Sci 38:161-174.

10. Lange-Lieckfeldt R and Lee G. 1992. Use of a model lipid matrix to demonstrate the dependence of the stratum corneum's barrier properties on its internal geometry. J Cont Rel 20:183-194.

11. Edwards DA and Langer R. 1994. A linear theory of transdermal transport phenomena. J Pharm Sci 83:1315-1334.

12. Johnson ME, Blankschtein D, and Langer R. 1997. Evaluation of solute permeation through the stratum corneum: Lateral bilayer diffusion as the primary transport mechanism. J Pharm Sci 86:1162-1172.

13. Frasch HF and Barbero AM. 2003. Steady-state flux and lag time in the stratum corneum lipid pathway: Results from finite element models. J Pharm Sci 92: 2196-2207.

14. Potts RO and Guy RH. 1992. Predicting skin permeability. Pharm Res 9:663-669.

15. Flynn GL. 1990. Physicochemical determinants of skin absorption. In Principles of Route to Route Extrapolation for Risk Assessment; Gerrity TR, Henry CJ, eds. Elsevier: New York, pp 93-127.

16. Mitragotri S. 2000. In situ determination of partition and diffusion coefficients in the lipid bilayers of stratum corneum. Pharm Res 17: 1026-1029.

17. Yu B, Kim KH, So PTC, Blankschtein D, Langer R. 2003. Visualization of oleic-acid induced transdermal diffusion pathways using two-photon fluorescence microscopy. J Invest Dermatol. 120:448-455.

18. Chen T, Langer R, Weaver J. 1999. Charged microbeads are not across the human stratum corneum in vitro by short high-voltage pulses. Bioelectrochem. Bioenerg. 48:181-192.

19. Kushner J, Blankschtein D, and Langer R. 2004. Experimental demonstration of highly permeable localized transport regions in low-frequency sonophoresis. J Pharm Sci. 93:2733-2745.

20. Crank J. 1964. The Mathematics of Diffusion. Oxford University Press, London. Pp. 47-48.

21. Johnson ME, Berk DA, Blankschtein D, Golan DE, Jain RK, Langer R. 1996. Lateral diffusion of small compounds in human stratum corneum and model lipid bilayer systems. Biophys J 71:2656-2668.

Chapter 4

Experimental Demonstration of the Existence of Highly Permeable Localized Transport Regions in Low-Frequency Sonophoresis

4.1 Introduction

As discussed in Chapter 1, transdermal drug delivery offers several advantages over traditional methods of drug delivery. However, due to the structure and function of the skin, specifically of the stratum corneum, successful application of transdermal delivery methods has been restricted to a few, small (MW < 400 Da), hydrophobic (positive octanol-water partition coefficients, log $K_{O/W}$) compounds (see Table 1-1 in Chapter 1).[1-4] To deliver larger hydrophobic molecules, as well as hydrophilic compounds of any size, four primary methods have been developed to make the skin more permeable to drug transport – (i) electroporation,[5-10] (ii) iontophoresis,[11-17] (iii) chemical enhancers,[17-22] and (iv) sonophoresis[22-28] (see Chapter 1 for details).

While the mechanistic details associated with methods (i), (ii), and (iv) to enhance transdermal drug delivery are not yet fully understood, there is some evidence that

enhanced transport of model permeants occurs by means of highly permeable, localized pathways. These so-called localized transport regions (LTRs) have been observed in the fields of electroporation and iontophoresis in several studies.[5-8,11] Using heat-stripped human cadaver skin with the hydrophilic, fluorescent probes sulforhodamine B (SRB) and calcein, LTRs (diameter 40-80 μm) were observed in electroporation for applied voltages which were greater than 75 V.[5] In an attempt to deliver DNA antisense oligonucleotides with electroporation, the DNA delivery was localized to 30-μm diameter LTRs.[6] Further work determined that the size of the LTRs was much larger (~1 mm^2) when long pulses (100 – 300 ms) of medium-voltage (>30 V), rather than short pulses (1 ms) of high-voltage (100 V), were applied.[7] However, the total number of LTRs formed on the skin was higher for the short pulse, high-voltage case.[7] All the LTRs observed in electroporation and iontophoresis exhibited a characteristic ring structure, in which the LTR was highlighted by high concentrations of residual fluorescent probe bordering the outer edge of the LTR.[5-8,11]

A recent discovery in the field of sonophoresis, made independently by Tang[29] and by Tezel *et al.*,[23-25] unveiled the possible existence of LTRs on the surface of full-thickness human skin and full-thickness pig skin as a result of exposure to low-frequency ultrasound (20 – 76 kHz). Using the red-colored hydrophilic probe SRB, Tang observed, with the naked eye, a single red spot, indicating the location of the *hypothesized* LTR, at the center of the surface of sonicated (frequency - 20 kHz, intensity – 1.6 W/cm^2, duty cycle - 0.1:0.9 sec, time - 20 hrs, transducer displacement – 0.8 cm) full-thickness human skin.[29] Tezel *et al.*, using both SRB and sodium lauryl sulfate (SLS) (a surfactant used to enhance the effects of sonophoresis), observed, also with the naked eye, a heterogeneous

pattern of red spots on full-thickness pig skin (frequency - 20 kHz, intensity - 7.5 W/cm^2, duty cycle - 5:5 sec, time – 15 min, transducer displacement - 3 mm).[23] Unlike the microscopic ring structure observed in electrophoresis, the hypothesized LTRs observed in low-frequency sonophoresis are more macroscopic structures, on the order of millimeters in diameter.[22-25,29] In addition to these initial observations, some microscopic visualization of the hypothesized LTRs has been attempted by Tang[29] and by Alvarez-Román *et al.*[28] Using SRB as the fluorescent probe, Tang imaged sonicated (frequency - 20 kHz, intensity – 1.6 W/cm^2, duty cycle - 0.1:0.9 sec, time - 20 hrs, transducer displacement – 0.8 cm) full-thickness human skin using two-photon microscopy and observed that a higher concentration of SRB was present within the single observed LTR as compared to that found in the surrounding regions of the skin (the non-LTRs).[29] Using calcein as the fluorescent probe, Alvarez-Román *et al.* imaged sonicated (frequency - 20 kHz, intensity - 15 W/cm^2, duty cycle - 0.1:0.9 sec, time - 2 hrs, transducer displacement – 0.5 cm) full-thickness pig skin using confocal microscopy and observed that a single, discrete region of the SC, located within an area of 1 cm^2 beneath the ultrasound probe, had been perturbed, while the surrounding regions of the SC were less affected by the ultrasound exposure.[28]

While these observations appear to suggest that regions of increased permeability do exist in sonicated skin samples, there has not yet been a direct, quantitative demonstration that the hypothesized LTRs produced by low-frequency sonophoresis are indeed regions of increased transdermal drug permeability. Also, no attempt has yet been made to incorporate the existence of highly permeabilized regions of the skin into current models of transdermal drug permeation to obtain a more accurate estimate of ultrasound

enhancements, a need that has been emphasized recently by Alvarez-Román *et al.*[28] With all of the above in mind, in this chapter, we pursue the following objectives: 1) demonstrating quantitatively that the hypothesized LTRs that are produced in full-thickness pig skin by low-frequency sonophoresis are indeed regions of higher transdermal drug permeability (see Section 4.4), and 2) developing model equations to describe skin samples having two regions with differing transdermal drug permeabilities (see Section 4.3). To accomplish the first objective, we first pre-treat skin samples with ultrasound in the presence of SLS using the constant skin electrical resistivity protocol, which was developed by Tang *et al.*[26] The constant skin electrical resistivity protocol is an excellent technique for ensuring high reproducibility in the transdermal permeability values of hydrophilic permeants delivered across skin samples perturbed by ultrasound. This is because increases in transdermal permeability of hydrophilic solutes across the skin are proportional to decreases in the skin electrical resistivity (or to increases in the skin electrical conductivity, since resistivity and conductivity are inversely related), which are both a result of the increased structural perturbations in the skin induced by the exposure to ultrasound. Using the constant skin electrical resistivity protocol, we prepared three groups of pig full-thickness skin samples that have unique skin electrical resistivity values, and therefore, have unique transdermal permeability values, unique skin electrical conductivity values, and unique structural perturbation levels. Note that three groups with unique structural perturbation levels (and therefore, with unique skin electrical conductivity values) were chosen so that the effect of increasing the structural perturbation levels (and therefore, of increasing the skin electrical conductivity values) on the size and on the transport properties of the LTRs and the non-LTRs could be

examined. After pre-treatment with ultrasound, we conducted a series of diffusion masking experiments, in which skin samples are masked for permeation of a model hydrophilic drug through select portions of the skin (see Section 4.2). Based on the permeability results of these diffusion masking experiments, as well as on skin electrical resistivity measurements, we show that the hypothesized LTRs experience greater structural perturbation than the surrounding non-LTRs due to ultrasound exposure, confirming that the hypothesized LTRs are indeed regions of high localized transport (see Section 4.4). Finally, we address how the results of the proposed experimental analysis may impact our understanding of both the enhancing mechanisms, including the nature of the transdermal transport pathways generated, in ultrasound-mediated transdermal drug delivery (see Section 4.5). To accomplish the second objective, we start with mass balances to develop the equations that relate the permeability of the LTRs and the non-LTRs to the permeability of the entire skin sample (see Section 4.3). These equations are then used to validate the permeability data obtained from the diffusion masking experiments (see Section 4.4).

4.2 Materials and Methods

4.2.1 Chemicals

Phosphate buffer saline (PBS; 0.01 M phosphate, 0.137 M NaCl) was obtained from Fluka Chemical (St. Louis, MO). Sulforhodamine B (SRB) was obtained from Molecular Probes (Eugene, OR). Calcein (absorbance at λ = 494 nm) and Sodium Lauryl Sulfate (SLS) were obtained from Sigma Chemical Company (St. Louis, MO). All these chemicals were used as received.

4.2.2 Skin Preparation

Skin samples were prepared following previously published methods,[30] which are briefly summarized next. Pig full-thickness skin samples were obtained from the back and flank of female Yorkshire pigs. Excess hair was carefully removed from the skin, which was subsequently harvested within 1 hour after the animal was sacrificed. The subcutaneous fat was removed from the skin, which was then sectioned into strips and stored at (-80°C) for up to 12 months. Before use in the permeation experiments, the skin was thawed for an hour prior to being placed in vertical Franz diffusion cells (15-mm inner diameter) obtained from Permegear (Bethlehem, PA) (see Figure 4-1). The receiver cell was filled with PBS, and the donor cell was filled with a solution of PBS containing 0.5 % (w/v) of SRB and 1.0 % (w/v) SLS.

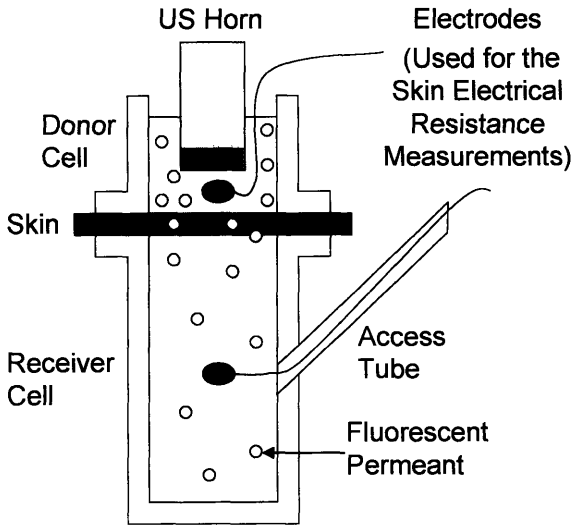

Figure 4-1: Experimental setup of the vertical Franz diffusion cell used in the diffusion masking experiments.

4.2.3 Skin Electrical Resistance Measurements

The electrical resistance of the skin was measured according to previously published methods,[30] which are summarized next. A 100 mV AC voltage source at 10 Hz was generated using a signal generator (Hewlett-Packard, model HP 33120A) and applied across the skin membrane using two Ag/AgCl electrodes (In Vivo Metrics, Healdsburg, CA) for 5-10 seconds. The skin electrical current was measured using a Fluke Multimeter (Model 139, Fluke Corporation). The skin electrical resistance was obtained from the skin electrical current using Ohm's Law. Since this measurement also includes the resistance of the donor and the receiver cell solutions, a background electrical resistance measurement of just the PBS solution was made separately and was then subtracted from the electrical resistance of the skin in the diffusion cell to determine the actual skin electrical resistance.

Prior to ultrasound exposure, the electrical resistance, R, of all the skin samples was measured and multiplied by the skin area available to ultrasound exposure in the diffusion cell (A = 1.77 cm^2). Any skin sample with an initial RA value of <50 kOhm*cm^2 was considered damaged and was discarded, and was subsequently replaced with an intact skin sample.[31]

4.2.4 Ultrasound Pre-Treatment Protocol

Ultrasound was applied to the intact pig full-thickness skin samples following previously published methods.[23,30] Ultrasound (VCX 400, Sonics and Materials, Inc., Newtown, CT) was applied to the skin samples at the following conditions: frequency - 20 kHz, intensity - 7.2 W/cm^2, pulse length - 5 sec on, 5 sec off, and tip displacement - 3 mm,

until the skin electrical current measured reached values of 225, 275, or 325 μAmps. As stated in Section 4.1, these three skin electrical current values will enable us to study the role of the LTRs at three unique transdermal permeability values and three unique structural perturbation levels. Moreover, these three skin electrical current values were selected to ensure visible LTR formation with the naked eye, which is necessary to effectively mask the surface of the skin in order to carry out the masking experiments (see below). The skin electrical resistances corresponding to these three electrical currents are 380, 240, and 150 Ohms, respectively. After each minute of ultrasound exposure, the SRB/SLS/PBS coupling medium was changed to minimize the impact of thermal effects on the permeation enhancement of the skin,[25] and measurements of the skin electrical current were conducted to determine if the target skin electrical current had been reached. Once the desired skin electrical current was attained, the skin sample was removed from the diffusion cell and was rinsed for 15 minutes in PBS to remove all excess coupling medium from the skin surface in preparation for the digital imaging and the analysis of the hypothesized LTRs.

4.2.5 Digital Imaging and Analysis of the LTRs

After the PBS wash, the skin sample was blotted dry and was then imaged using a digital camera (Kodak DC4800, 3.1 Megapixels, F-stop – 2.8, shutter speed – 1/15 second). To correct for any color infidelity of the CCD (charged coupled device) chip of the camera, as well as for any fluctuations in the laboratory lighting, an orange-colored strip of tape was included in the digital image of the skin (see Figure 4-2, image 1). (Note: the color of the strip of tape is not critical. Any color strip of tape could have been used, as long as

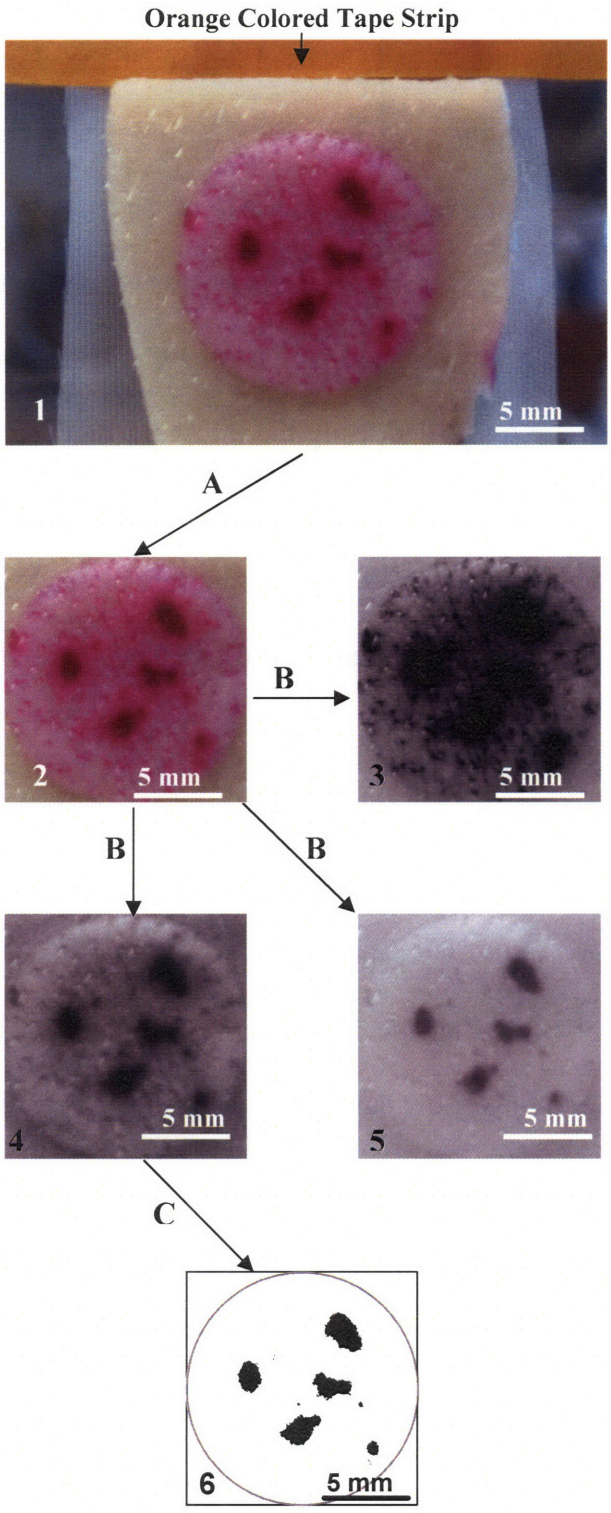

Figure 4-2: Sequence of steps in the method used to analyze the digital skin images. In step A, the original digital image (1) is standardized (to eliminate lighting variations) and

then cropped to isolate the ultrasound exposed region of the skin (2). In step B, the cropped digital image (2) is separated into the green (3), the blue (4), and the red (5) channel images (which are displayed as grayscale images). By examining the three channel images separately, the dark regions in the blue channel image (4) are very close in size to the LTRs in the cropped image (2). In step C, the dark regions (LTRs) in the blue channel image (4) are quantified using the threshold function (threshold = 75 blue pixel count), which counts all pixels with a blue pixel count at, or below, 75 (6). From this information, the area of the LTRs (in cm^2) can then be readily determined (see the text for a detailed explanation). In images (1) – (6), the scale bar represents 5 mm.

the same color tape is used in all the digital images.) Also, three repeat images of each ultrasound-treated skin sample were taken for statistical certainty. The digital skin images were then analyzed using the Corel Photo-Paint 11 Software Package (Corel Corporation) according to the following method, which is outlined in Figure 4-2. (Note: digital color variation is defined by the number of bits used to store different levels of color. In 24-bit color, which is the depth of color used in this analysis, there are 2^{24} levels of color variation that can be described digitally. The 2^{24} shades of color in a single pixel are determined by the combination of the levels of the individual red, green, and blue channels, which each have 2^8 levels of color. Therefore, any 24-bit digital color image can be decomposed into its individual 8-bit red, green, and blue channel digital images.) First, the orange-colored tape strip included in the digital image of the ultrasound-treated skin (see Figure 4-2, image 1) is isolated from the rest of the image to

determine the average blue channel color count (scale from 0 – 255 for 8-bit color, 2^8) of the orange colored tape strip (see the following paragraph for the rationale behind using the blue channel). This average blue channel color level is then compared to the standard average blue channel color level of the orange-colored tape strip, which is 32 for the orange-colored tape strip used in these experiments, obtained from the average blue color levels of 40 digital images of the orange-colored tape strip. The blue channel color levels from the entire ultrasound-treated skin image are then shifted so that the average blue channel color level for the colored tape strip matches the standard average blue channel color level for the colored tape strip. For example, suppose that the colored tape strip in a skin image has an average blue channel color level of 39. In order to match the standard average blue channel color level for the colored tape strip, which is 32 for the orange-colored tape strip, the entire skin image needs to have all the blue channel color levels decreased by 7. This standardization procedure was accomplished with the function named "Contrast Enhancement" in Corel Photo-Paint 11.

After standardization of the ultrasound-treated skin sample digital images, the digital images are cropped down to the diameter of the ultrasound-treated skin region (diameter = 1.5 cm) (see Figure 4-2, step A). To determine the size of the LTRs from the cropped digital image (see Figure 4-2, image 2), the Threshold function in Corel Photo-Paint 11 is used to calculate the number of pixels having a blue channel color level of 75 or less. The blue channel image (see Figure 4-2, image 4) was selected for the determination of the LTR size, since the blue channel image seems to offer a better definition of the LTR region over the red channel image (see Figure 4-2, image 5) or the green channel image (see Figure 4-2, image 3) of the skin sample (see Figure 4-2, step

B). (Note: the red channel, the green channel, and the blue channel images are displayed by Corel Photo-Paint in grayscale.) A blue color level threshold of 75 was selected to define the LTRs of the ultrasound-treated skin since a blue color level threshold of 75 closely matches the dark red regions of the ultrasound-treated skin (compare Figure 4-2, images 2 and 6), indicating that the entire area of the LTRs has been quantified (see Figure 4-2, step C). If the value of the blue color level threshold was higher, or lower, than 75, a larger, or smaller, LTR area would be estimated by this method, which would lead to different values for the estimated area of the LTRs (see the Appendix, Section 4.7). By knowing the number of pixels with a blue color level at, or below, 75, the total number of pixels in the cropped digital image, and the total area of the cropped digital image (2.25 cm^2), it is possible to calculate the area of the hypothesized LTRs formed on the ultrasound-treated skin. The reader should again note that these calculated LTR area values are directly based on the blue pixel threshold value of 75.

4.2.6 Masking Experiments

Following digital imaging of the skin, the ultrasound-treated skin samples were divided into four groups: A) Control, B) non-LTRs, C) LTRs, and D) Total (see Figure 4-3). In the Control group (see Figure 4-3A), we determined the background absorbance of the solution in the receiver cells by masking the entire skin surface with vacuum grease (High Vacuum Grease, Dow Corning, Midland, MI), which prevents calcein permeation across the entire ultrasound-treated skin samples. The effectiveness of the vacuum grease to prevent transdermal permeation of calcein in the Control group was confirmed in two ways: 1) an absorbance spectrum of the contents of the receiver cells after calcein

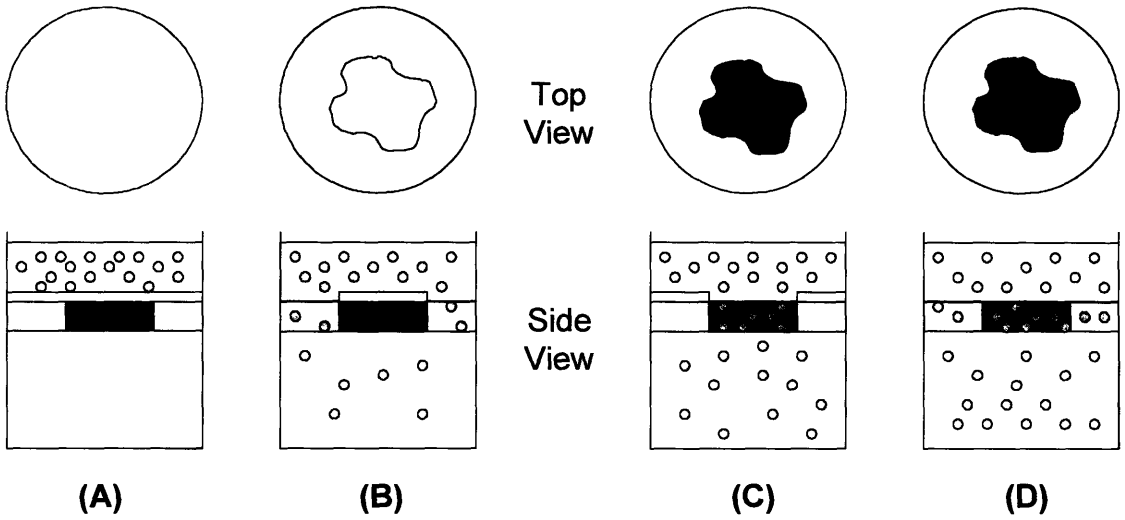

Figure 4-3: Sample setup of the diffusion masking experiments. (A) Control group – no transport of calcein. (B) Non-LTR group – only the non-LTRs are available for calcein transport. (C) LTR group – only the LTRs are available for calcein transport. (D) Total group – the entire skin surface is available for calcein transport. Key: Masking material - (□), LTRs - (■), and non-LTRs (□).

exposure showed no peak at 494 nm (the absorbance peak of calcein; data not shown), and 2) skin electrical resistance measurements revealed that after application of the vacuum grease mask, the RA values were higher than 300 kOhm*cm^2, well above the threshold RA value for the intact skin samples (50 kOhm*cm^2). In the non-LTR group (see Figure 4-3B), we determined the permeability of the non-LTRs in the skin by masking the surface of the LTRs with vacuum grease to prevent calcein permeation through the LTRs. In the LTR group (see Figure 4-3C), we determined the permeability of the LTRs in the skin by masking the surface of the non-LTRs with vacuum grease to prevent calcein permeation through the non-LTRs. (See the Appendix, Section 4.7, for a

brief discussion of the possible experimental errors associated with the mask application for the LTRs and the non-LTRs.) In the Total group (see Figure 4-3D), we determined the permeability of the entire skin sample since no vacuum grease was applied to these ultrasound-treated skin samples. These four sub-groups of ultrasound-treated skin samples were utilized for each of the three current conditions listed above.

After masking, the ultrasound-treated skin samples were placed in another vertical Franz diffusion cell with fresh PBS in the receiver cell and 2 ml of 0.2 % (w/v) calcein in PBS in the donor cell. Passive diffusion through the ultrasound-treated skin samples was conducted for a total of 30 hours to ensure that enough calcein was delivered to obtain an accurate measurement of the absorbance of calcein in the receiver cell solution. Measurements of the skin electrical resistance were made at the beginning and at the conclusion of the 30-hour permeation experiments to determine if there was any significant change in the electrical resistance properties of the skin during the masking experiments (no significant difference was observed). The amount of calcein that diffused through the available regions of the ultrasound-treated skin was determined by measuring the absorbance of a 1-ml aliquot of the receiver cell solution exposed to 494-nm light with a UV-Vis spectrophotometer (Cary, Bio 50). The absorbance measurement of the receiver cell solution was used in conjunction with a standard curve to determine the mass concentration of calcein in the receiver cell. The steady-state skin permeability, P, of calcein was determined using the following equation:[32]

$$P = \frac{V}{AC_o}\frac{\Delta C}{\Delta t} \tag{4.1}$$

where V is the volume of the receiver cell (12 ml), A is the cross-sectional skin area available for transport, C_o is the initial mass concentration of the permeant (calcein) in

the donor cell (2 mg/ml), ΔC is the change in mass concentration of the permeant in the receiver cell, and Δt is the total time allowed for permeant diffusion through full-thickness pig skin minus the lag time (which is approximately 13 hours, see Figure 4-4).

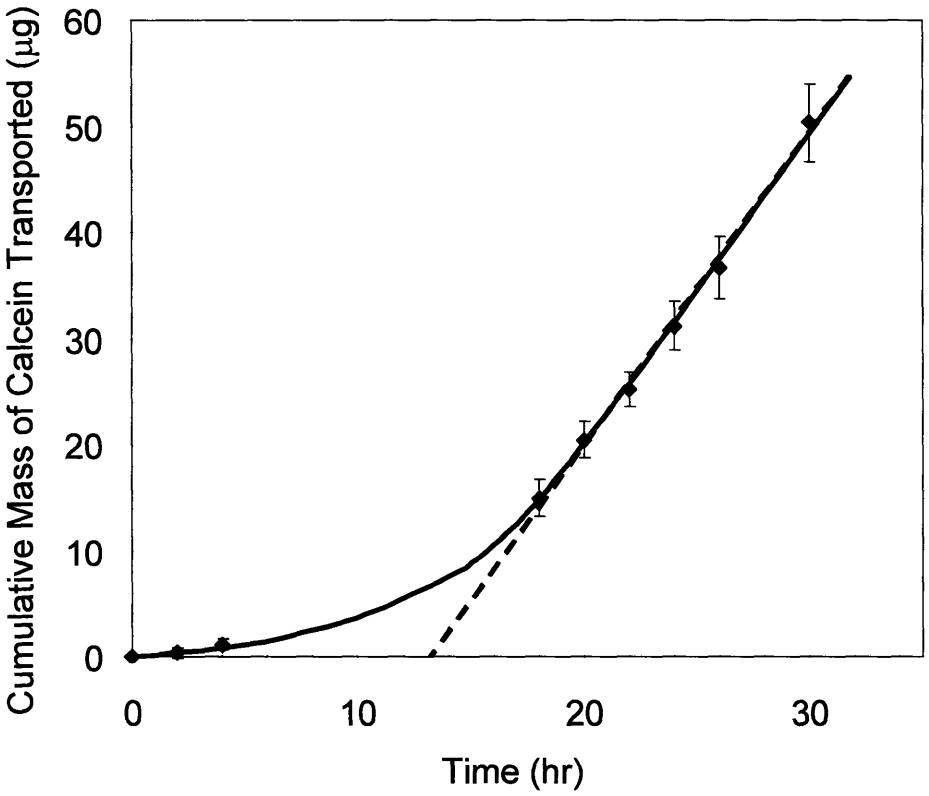

Figure 4-4: Sample plot of the cumulative amount of calcein transported across the skin into the receiver compartment as a function of time. The solid line is shown to guide the eye. The dashed line represents the linear regression of the data points in the steady-state phase (18 - 30 hrs). The lag time is determined from the intercept of the dashed line with the x-axis (n = 3, error bars = $\pm$ 1 S.D.).

4.3 Theory

4.3.1. Relating the Total Skin Permeability to the Permeabilities of the Non-LTR and the LTR Skin Regions

As indicated in Materials and Methods (Section 4.2), Eq. (4.1) can be utilized to calculate transdermal drug permeabilities in a diffusion cell experiment. Equation (4.1) may be applied to the non-LTR, the LTR, and the Total groups of diffusion masking experiments to determine $P_{non\text{-}LTR}$, P_{LTR}, and P_{Total} (which are the permeabilities of the non-LTR, the LTR, and the Total skin regions, respectively), as follows:

$$P_{non-LTR} = \frac{V}{C_o \Delta t} \frac{\Delta C_{non-LTR}}{A_{non-LTR}} \tag{4.2a}$$

$$P_{LTR} = \frac{V}{C_o \Delta t} \frac{\Delta C_{LTR}}{A_{LTR}} \tag{4.2b}$$

$$P_{Total} = \frac{V}{C_o \Delta t} \frac{\Delta C_{Total}}{A_{Total}} \tag{4.2c}$$

where $\Delta C_{non\text{-}LTR}$, ΔC_{LTR}, and ΔC_{Total} are the changes in the mass concentrations of the permeant (calcein) measured in the receiver cell over the duration of the diffusion masking experiments, and $A_{non\text{-}LTR}$, A_{LTR}, and A_{Total} are the measured areas of the skin available for transport for the non-LTR, the LTR, and the Total skin regions, respectively. Noting that the quantity ($V\Delta C$) is equal to the mass of calcein delivered in each diffusion masking experiment, the following mass balance must hold:

$$V\Delta C_{Total} = V\Delta C_{non-LTR} + V\Delta C_{LTR} \tag{4.3}$$

Equation (4.3) states that the mass of calcein delivered across the non-LTR and the LTR skin regions must be equal to the mass of calcein delivered across the Total skin region. Substituting Eqs. (4.2a)-(4.2c) in Eq. (4.3) yields the following result:

$$P_{Total} A_{Total} C_O \Delta t = P_{non-LTR} A_{non-LTR} C_O \Delta t + P_{LTR} A_{LTR} C_O \Delta t \tag{4.4}$$

Since the diffusion masking experiments have been designed such that C_o and Δt are identical for each set of masking experiments, C_o and Δt can be eliminated from Eq. (4.4). By further dividing both sides of Eq. (4.4) by A_{Total}, the following equation is obtained to calculate the total skin permeability, P_{Total}:

$$P_{Total} = P_{non-LTR} \alpha_{non-LTR} + P_{LTR} \alpha_{LTR} \tag{4.5}$$

where $\alpha_{non\text{-}LTR} = A_{non\text{-}LTR}/A_{Total}$ and $\alpha_{LTR} = A_{LTR}/A_{Total}$ are the area fractions of the non-LTR and of the LTR skin regions, respectively.

4.3.2 Evaluating the Skin Electrical Resistivity from the Skin Electrical Resistance Measurements

The electrical resistivity, ρ, of a resistor is defined as follows:

$$\rho = \frac{RA}{\Delta x} \tag{4.6}$$

where R is the electrical resistance, A is the cross-sectional area of the resistor, and Δx is the thickness of the resistor. If the skin is modeled as an electrical resistor, Eq. (6) can be used to determine the skin electrical resistivity for each region of the skin from experimental measurements of the skin electrical resistance (R), the area available for transport (A), and the thickness of the stratum corneum (Δx = 13.1 μm).[2] The skin electrical resistivity is preferred in our analysis over the skin electrical resistance because

the skin electrical resistivity is an intrinsic electrical property of the skin membrane, while the skin electrical resistance is an extensive electrical property of the skin membrane. Consequently, by using the skin electrical resistivity, it will be easier to compare differences in the electrical properties of the sonicated regions of the skin - the LTRs, the non-LTRs, and the Total group – with those of the untreated skin samples. Since the skin electrical resistivity is an almost instantaneous measure of the structural integrity of the skin,[30] a comparison of the skin electrical resistivity within the LTRs and the non-LTRs will shed light on the extent of structural perturbation generated in the LTRs and in the non-LTRs as a result of the exposure to ultrasound, in the presence of SLS.

4.3.3 Evaluating the Structural Parameter, (ε/τ), to Characterize the Transdermal Pathways in the LTR and the non-LTR Regions of the Skin

It is possible to determine the ratio of the fraction of the stratum corneum surface available for transport (*i.e.* the porosity), ε, to the tortuosity, τ, of the hydrophilic transport pathways, within the LTR, the non-LTR, and the Total regions of the skin using the following equation based on the Porous Pathway Theory (which is a theory that has been previously proposed to model the transport of hydrophilic solutes across the SC through aqueous tortuous pathways, see Chapter 2 for details):[30]

$$\left(\frac{\varepsilon}{\tau}\right)_i = \frac{\rho_i}{\sigma_{sol} H(\lambda_{ion})} \tag{4.7}$$

where ρ_i is the measured skin electrical resistivity of the LTR group, the non-LTR group, or the Total group, and σ_{sol} is the electrical conductivity of the PBS coupling medium (0.012 $\Omega^{-1}cm^{-1}$).[30] The hindrance factor for the transport of the principal ions in the solution (in the present case, the sodium ions), $H(\lambda_{ion})$, is defined, for $\lambda<0.4$, as follows:[33]

$$H(\lambda_{ion}) = (1-\lambda_{ion})^2\left(1-2.104\lambda_{ion}+2.09\lambda_{ion}^3-0.95\lambda_{ion}^5\right) \tag{4.8}$$

where λ_{ion} is defined as:[33]

$$\lambda_{ion} = \frac{r_{ion}}{r_{pore}} \tag{4.9}$$

where r_{ion} is the hydrodynamic radius of the solute (2.2 Å for sodium ions)[30] and r_{pore} is the average radius of the aqueous pore pathways available for transport. The value of r_{pore} in each region of the skin may be determined from the transdermal permeability, P, the skin electrical resistance, R, and the area available for transport, A, using the following equation based on the Porous Pathway Theory:[30]

$$PRA = \frac{kT}{2z^2Fc_{ion}e_0}\frac{D_p^{\infty}H(\lambda_p)}{D_{ion}^{\infty}H(\lambda_{ion})} \tag{4.10}$$

where k is the Boltzmann constant (1.38 x 10^{-23} J/K), T is the absolute temperature (298 K), z (= 1) is the valence of the principal ion in the solution, F is the Faraday constant (9.648 x 10^4 C/mol), c_{ion} is the electrolyte molar concentration (0.137 M), e_0 is the electronic charge (1.6 x 10^{-19} C), D_{ion}^{∞} and D_p^{∞} are the diffusion coefficients of the sodium ions (1.33 x 10^{-5} cm^2/s)[31] and of calcein (3.63 x 10^{-6} cm^2/s, estimated using an empirical correlation based on molecular weight), respectively, at infinite dilution, and $H(\lambda_p)$ is the hindrance factor of calcein. Since P, R, and A are experimentally determined, Eq. (4.10) may be used to determine r_{pore} in each region of the skin. Once

r_{pore} is determined, Eq. (4.7) may be used to determine the value of (ε/τ) for each region of the skin from the values of the skin electrical resistivity (ρ) obtained from Eq. (4.6). From knowledge of the values of (ε/τ) for each region of the skin, we can then gain useful insight about the type of transport pathways present in the LTRs and the non-LTRs (see Discussion, Section 4.5).

4.4 Results

4.4.1 Determining the Permeabilities of the LTRs and the Non-LTRs

The amount of calcein transported across the skin and the skin permeability to calcein in the diffusion masking experiments, as determined from measurements of the absorbance of 494-nm light in the receiver cell solution, are presented in Figure 4-5. Figure 4-5A shows the results of the calcein absorbance measurements for each of the four groups of diffusion masking experiments conducted (Control, non-LTR, LTR, and Total skin regions) at each of the three specified skin electrical current conditions (225, 275, and 325 μAmps). Since no peak was observed for calcein in the absorbance spectrum of the Control group, the results of the Control group serve as a measurement of the background absorbance of the receiver cell solution. Therefore, the absorbance values corresponding to the Control group can be subtracted from those corresponding to the non-LTR, the LTR, and the Total groups to obtain the actual amount of calcein transported across the skin in each of these three groups of masking experiments, as shown in Figure 4-5B. As Figure 4-5B reveals, within the experimental uncertainty, the amount of calcein that permeates across the LTRs is comparable to the amount of calcein that permeates across

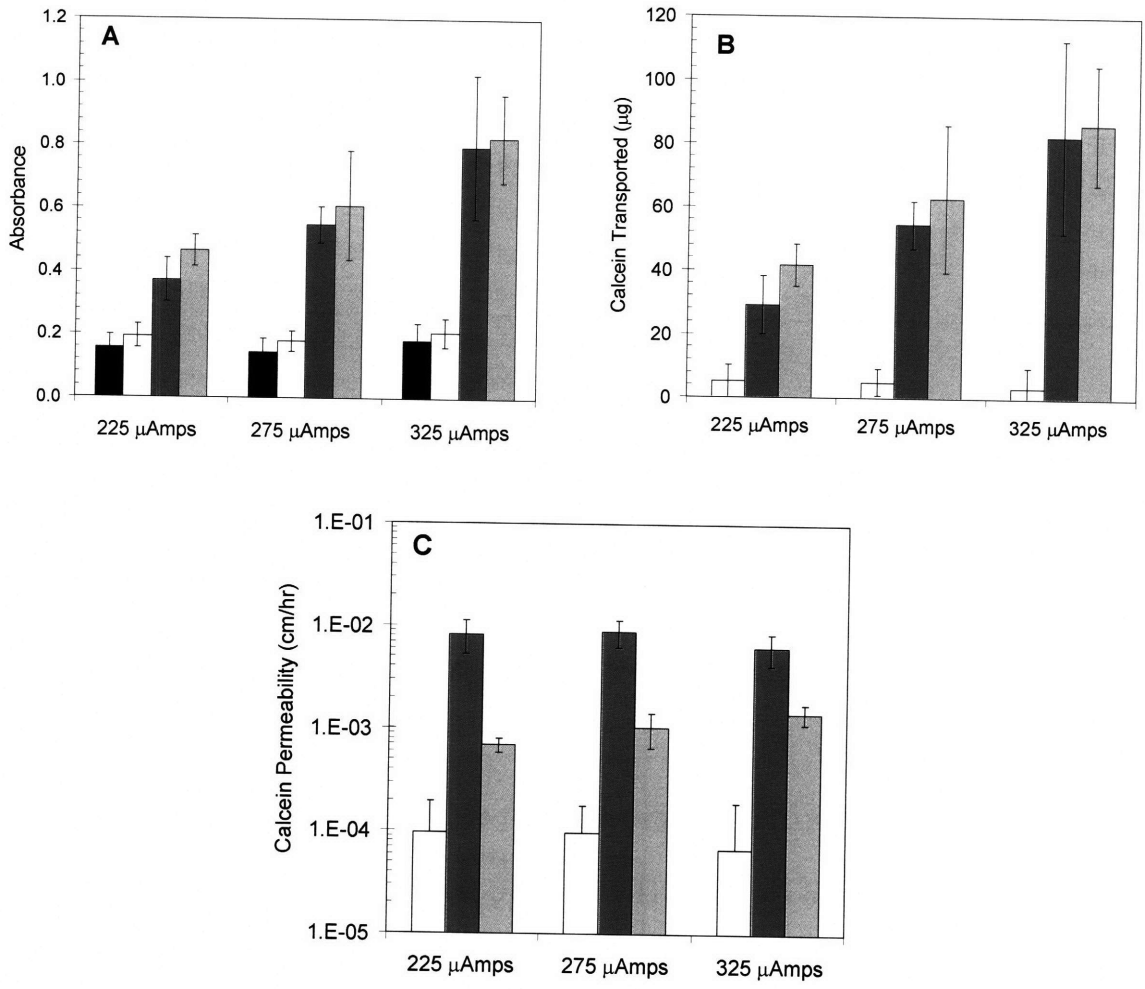

Figure 4-5: Results of the diffusion masking experiments: (A) receiver cell absorbance measurements (at 494 nm), (B) mass of calcein transported across the skin in each masking group, and (C) calcein permeability of each masking group. Key: Control group (■), non-LTR group (□), LTR group (■), Total group (■). Error bars = ± 1 S.D.

Table 4-1: Summary of Experimental Results and Calculated Values from the Diffusion Masking Experiments.[a]

Skin Electrical Current	Diffusion Masking Group	Area Available for Transport, A (mm^2)	Area Fraction, $\alpha_i = A_i/A_{Total}$	Skin Electrical Resistance, R (kOhm)	Calcein Skin Permeability, P ($*10^4$ cm/hr)	Skin Electrical Resistivity, ρ^b (kOhm*cm)	$(\varepsilon/\tau)^c$ ($*10^4$)
225 μAmps	Total	177	1	0.347 ± 0.062	6.89 ± 1.11	469 ± 77	2.47 ± 0.21
	LTR	11.4 ± 4.4	0.064 ± 0.024	0.461 ± 0.083	81.8 ± 29.4	40.1 ± 14.1	29.5 ± 7.64
	Non-LTR	159.6 ± 11.9	0.902 ± 0.067	1.00 ± 0.43	0.97 ± 0.98	1220 ± 520	1.29 ± 0.21
275 μAmps	Total	177	1	0.250 ± 0.041	10.4 ± 3.86	338 ± 55	3.29 ± 0.57
	LTR	19.3 ± 4.6	0.110 ± 0.026	0.244 ± 0.029	87.5 ± 26.3	35.9 ± 9.9	32.2 ± 4.44
	Non-LTR	152.7 ± 10.8	0.863 ± 0.061	1.08 ± 0.58	0.96 ± 0.81	1520 ± 440	1.47 ± 0.23
325 μAmps	Total	177	1	0.216 ± 0.040	14.3 ± 3.1	292 ± 59	3.62 ± 0.56
	LTR	38.9 ± 9.0	0.220 ± 0.051	0.212 ± 0.042	63.0 ± 21.6	63.0 ± 17.0	17.0 ± 4.14
	Non-LTR	143.6 ± 7.2	0.811 ± 0.041	1.39 ± 0.39	0.67 ± 1.25	1520 ± 437	1.02 ± 0.25

[a]Errors in the data ± 1 SD.
[b]Calculated using Eq. (4.6).
[c]Calculated using Eq. (4.7).

the total skin sample (compare the second and third columns), indicating that *most of the calcein permeates through the LTRs.*

Using Eqs. (4.2a)-(4.2c), the experimental data in Figure 4-5B, and the values of the areas corresponding to the non-LTR, the LTR, and the Total regions of the skin (see Table 4-1), we can now calculate the permeability through these three regions of the skin. The results of these calculations are presented in Figure 4-5C, which shows that the *LTRs are almost two orders-of-magnitude more permeable than the non-LTRs* (compare the second and the first columns). In addition, over the range of skin electrical currents examined (225 – 325 μAmps), the permeabilities of the non-LTRs and of the LTRs are almost constant based on a statistical analysis of the data (95% confidence). Based on this finding and Eq. (4.5), it follows that the increase in the total skin permeability, as the skin electrical current increases from 225 μAmps to 325 μAmps, observed in Figure 4-5C

(see the third column), is likely due to the observed increase in the size of the more permeable LTRs (see Table 4-1), as the skin electrical current increases from 225 μAmps to 325 μAmps. It is also worth noting that the Total calcein permeability is less than the LTR calcein permeability, but greater than the non-LTR calcein permeability, at each skin electrical current condition. This is because the Total calcein permeability is a quantitative measure of the combined calcein permeability of both the more permeable LTR and the less permeable non-LTR skin regions. Since the Total calcein permeability combines both the high and the low calcein permeability regions, it is not surprising to find that the Total calcein permeability lies between the calcein permeabilities of the LTR and the non-LTR skin regions.

To ensure that our experimental data set is accurate for the analysis presented above, we verified that the calcein mass balance in Eq. (4.3) is satisfied. The results of this verification are presented in Figure 4-6, where we compared the mass of calcein transported in the Total group (see the first column) with the combined masses of calcein transported separately through the non-LTRs (from the first column of Figure 4-5B) and through the LTRs (from the second column of Figure 4-5B) at the three current conditions examined (see the second column). As Figure 4-6 shows, a mass balance is attained for each of the three electrical current conditions examined (95% confidence). In addition, we can also use the data in Figure 4-5C to determine if Eq. (4.5) is satisfied. These results are presented in Figure 4-7, where we compare the experimentally-obtained value of the calcein permeability corresponding to the Total group (the third column of Figure 4-5C) with the value of the calcein permeability of the entire skin sample, which was predicted using the measured calcein permeabilities of the non-LTR (the first column

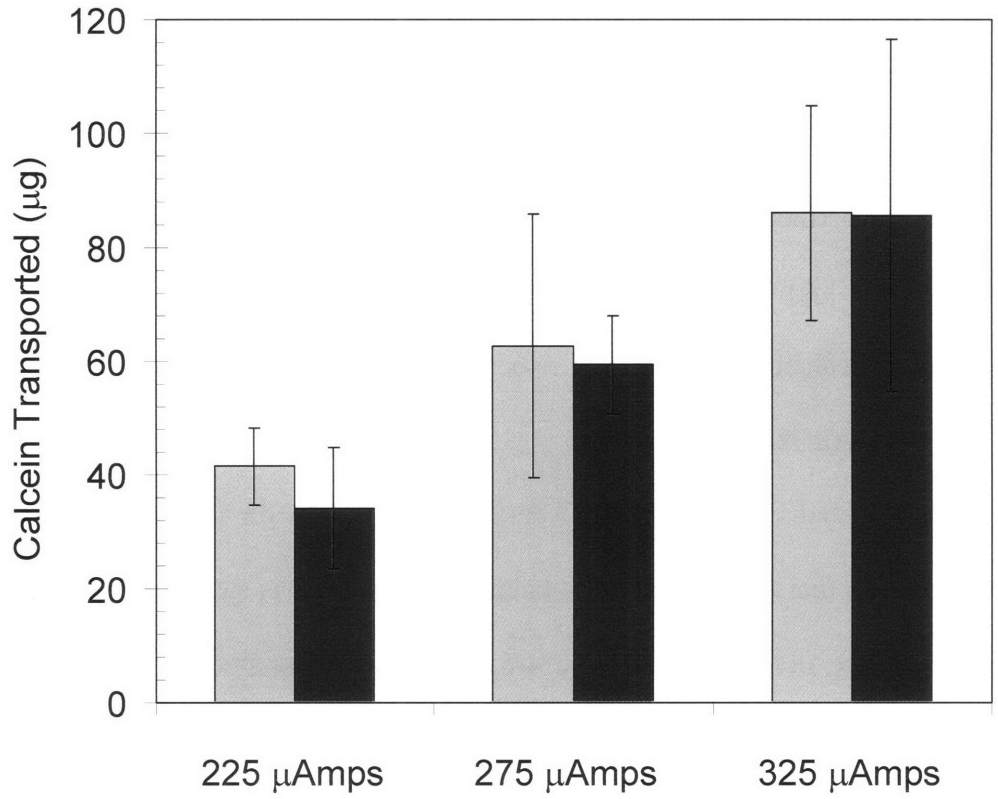

Figure 4-6: Verification that the calcein mass balance in Eq. (4.3) is satisfied at the three skin electrical current conditions studied. Key: Total group (□), non-LTR group + LTR group (■). Error bars = ± 1 S.D.

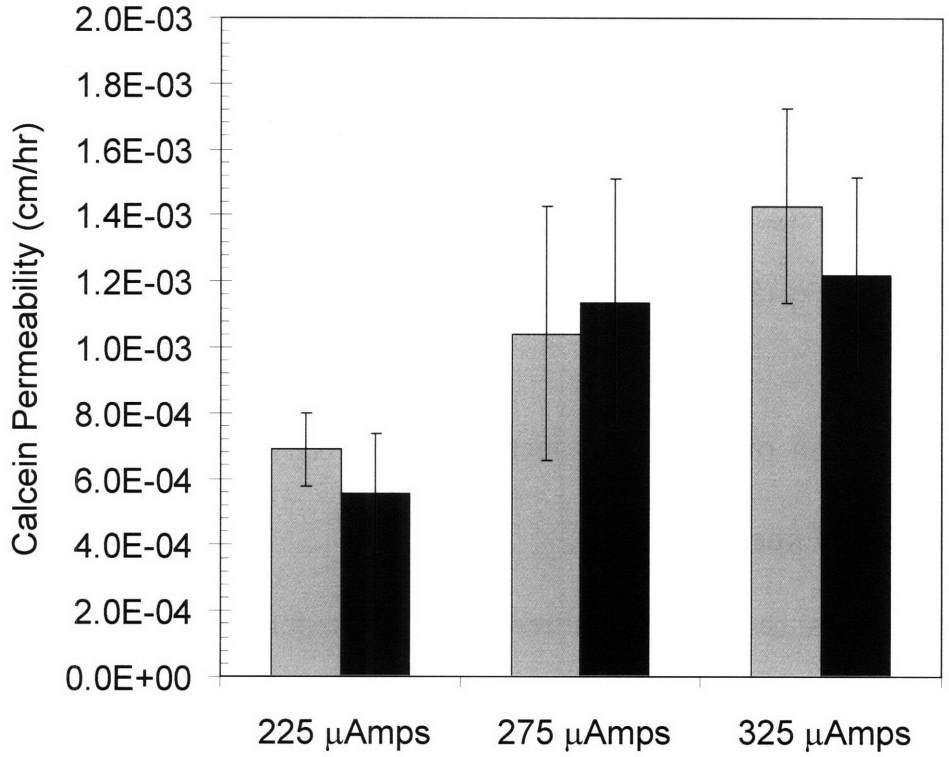

Figure 4-7: Comparison of the experimentally measured Total calcein skin permeability with that predicted from the experimentally measured values of the calcein permeability and the area fraction available for transport of the non-LTRs and the LTRs, as reported in Table 4-1, at the three skin electrical current conditions examined. Key: Total group – experimental measurement (▨), Total group – calculated from Eq. (5) (■). Error bars = $\pm$ 1 S.D.

in Figure 4-5C) and the LTR (the second column in Figure 4-5C) skin regions in conjunction with the measured values of $\alpha_{non\text{-}LTR}$ and α_{LTR} (see Table 4-1) in Eq. (4.5). Similar to the verification of the mass balance shown in Figure 4-6, Figure 4-7 demonstrates that the measured values of the calcein permeabilities of the non-LTR and the LTR skin regions can be utilized in conjunction with the LTR and the non-LTR area fractions (α_{LTR} and $\alpha_{non\text{-}LTR}$, respectively) to predict the calcein permeability of the entire skin sample using Eq. (5) (95% confidence).

4.4.2 Comparison of the Skin Electrical Resistivity (ρ) Data based on the Masking Experiments

Figure 4-8 presents the skin electrical resistivity, ρ, data for the untreated skin samples (the first column, n = 30), the non-LTR group (the second column, n = 10), the LTR group (the third column, n = 10), and the Total group (the fourth column, n = 10) for each of the three current conditions (225, 275, and 325 μAmps) used in the masking experiments. By comparing the columns for the LTRs and the non-LTRs at the three current conditions, it follows that the ρ value corresponding to the LTRs (46.4 kOhm*cm, which is the average of the three Figure 8 values) is approximately 30-fold lower than the ρ value corresponding to the non-LTRs (1330 kOhm*cm, which is the average of the three Figure 4-8 values). Since the ρ data is a quantitative measure of the structural integrity of the skin membrane,[30] the non-LTRs are more structurally intact than the LTRs. Hence, based on the ρ measurements, the non-LTRs are less permeable than the LTRs, thereby confirming the results of the permeability measurements.

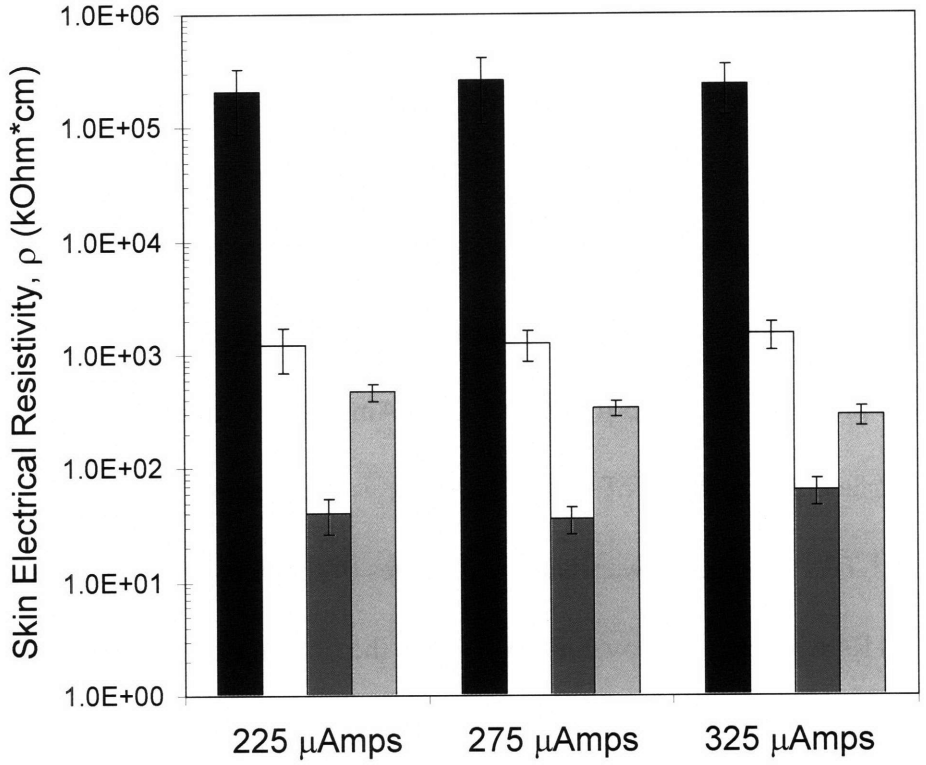

Figure 4-8: Skin electrical resistivity data from the masking experiments. Key: Untreated skin (■), non-LTR group (□), LTR group (■), Total group (□). Error bars = ± 1 S.D. For the untreated skin data, n = 30 samples, while for all the other groups, n = 10 samples.

Figure 4-8 also shows that the ρ values for the Total group decrease as the current increases from 225 μAmps to 325 μAmps (this can also be seen in Table 4-1), and consistently fall between the ρ values for the LTR group and for the non-LTR group. Similar to the nature of the permeability of the Total group, the ρ value for the Total group is a combined measure of regions with high electrical resistance and low current flow (the non-LTRs) and regions with low electrical resistance and high current flow (the LTRs). Therefore, the ρ value for the Total group will always fall between the ρ values of the non-LTRs and the LTRs. The decreasing trend in the ρ values for the Total group as the current increases from 225 μAmps to 325 μAmps can be attributed to the increase in the skin surface area fraction of the LTRs, α_{LTR}, as the current increases. Since the ρ values of the LTRs are much lower than the ρ values of the non-LTRs, an increase in the area of the LTRs will lead to an overall decrease in the ρ values of the entire skin sample, as is observed for the Total group in Figure 4-8. These results are consistent with the observed trends in the permeability data of the Total group presented in Figure 4-5C.

4.4.3 Determining the Structural Parameter, (ε/τ), for the Transdermal Pathways in the LTR and the Non-LTR Regions of the Skin

Finally, using the values of ρ reported in Table 4-1, we can calculate values of (ε/τ) for each of the three skin regions at each of the three current conditions examined using Eq. (4.7). These values are listed in the last column of Table 4-1. An examination of these values shows that the values of (ε/τ) corresponding to the LTR group are approximately 30-fold higher than the values of (ε/τ) corresponding to the non-LTR group at the three

current conditions examined. In addition, the values of (ε/τ) corresponding to the Total group consistently fall in between the values of (ε/τ) corresponding to the LTR group and to the non-LTR group, similar to the behavior exhibited by the permeability data and the skin electrical resistivity data corresponding to the Total skin region relative to the permeabilities and the skin electrical resistivities of the LTR and the non-LTR skin regions. In the Discussion section, we describe how useful conclusions can be reached about the nature of the transport pathways present in the LTRs and in the non-LTRs based on the values of (ε/τ) reported in Table 4-1.

4.5 Discussion

4.5.1 Analysis of the Results of the Diffusion Masking Experiments

As the results presented in Figure 4-5 show, most of the transdermal delivery of calcein occurs through the LTRs. Indeed, Figure 4-5C clearly shows that the permeability of the LTRs to calcein is nearly two orders-of-magnitude greater than the permeability of the non-LTRs to calcein. *These observations provide explicit proof that the red spots observed by previous authors when full-thickness pig skin or full-thickness human skin was treated with ultrasound in the presence of SRB, a red-colored permeant,*[22-25,29] *are, indeed, markers of localized regions of extremely high transdermal permeability.* In fact, the average measured calcein permeability in the LTRs for the three skin electrical currents examined (77 x 10^{-4} cm/hr, see Table 4-1) is of the same order-of-magnitude as the permeability of the dermis for small molecular weight hydrophilic permeants (100 x 10^{-4} cm/hr),[25,30] indicating that the formidable barrier to transdermal transport of small, hydrophilic molecules exhibited by the SC has been successfully bypassed in the LTRs.

Interestingly, the results of the diffusion masking experiments also reveal that the non-LTRs formed on skin sonicated in the presence of SLS also undergo a significant structural perturbation when compared to untreated skin due to the exposure to low-frequency ultrasound and SLS. A comparison of the skin electrical resistivity data in Figure 4-8 and in Table 4-1, which quantifies the structural integrity of the skin, for the non-LTRs (ρ = 1330 kOhm*cm, average of the three Table 4-1 values) and for the LTRs (ρ = 46.4 kOhm*cm, average of the three Table 4-1 values) with the skin electrical resistivity data for all the skin samples prior to ultrasound treatment ($\rho = 2.35 \times 10^5$ kOhm*cm, average of the three Figure 4-8 values) shows that the non-LTR and the LTR skin regions experience a ~170-fold and a ~5000-fold enhancement, respectively, over untreated skin due to the exposure to ultrasound and SLS. This would suggest that the observed enhancement in the skin electrical resistivity of full-thickness pig skin is due to two distinct levels of ultrasound exposure in the presence of SLS. A high level of ultrasound enhancement likely results in the formation of the highly permeable LTRs, while a lower level of ultrasound enhancement results in the formation of the less permeable non-LTRs. While it is known that transient cavitation events near the skin surface, which are triggered by ultrasound exposure, are the primary mechanism responsible for the observed enhancements in the skin electrical resistivity of pig full-thickness skin,[27] further study is required to better understand how this mechanism is responsible for the apparent dual-level of enhancement in the skin electrical resistivity of pig full-thickness skin samples treated with ultrasound in the presence of SLS.

4.5.2 Quantitative Prediction of Intercellular versus Transcellular Transdermal Transport Pathways for Hydrophilic Permeants Using the Calculated (ε/τ) Values

In the field of transdermal drug delivery, it is typically assumed that most hydrophilic permeants diffuse across the SC primarily through the intercellular lipid bilayers. This assumption, based on the results of several visualization studies,[3,4,35-37] has been a key aspect of many previous studies addressing the modeling of both hydrophilic and hydrophobic drug transport through the stratum corneum.[2,38-41] For typical physical dimensions of the stratum corneum,[2,42-44] the threshold value of (ε/τ) corresponding to steady-state transport in the intercellular regions of the stratum corneum was estimated to be $3.6*10^{-4}$ using the equations for porosity, ε, and the tortuosity for the flux, τ_{flux}, obtained in Chapter 3 (see Section 3.3 for details). By comparing this threshold value of (ε/τ) for the intercellular regions of the SC with the calculated values of (ε/τ) presented in Table 4-1, it follows that the values of (ε/τ) for the more permeable LTRs (26.2×10^{-4}, average of the Table 4-1 values) are an order-of-magnitude (~7-fold) higher than this threshold value of (ε/τ) for the intercellular regions of the SC (3.6×10^{-4}). This 7-fold increase in (ε/τ) could be the result of a 7-fold increase in ε, of a 7-fold decrease in τ, or of a combination of an increase in ε and a decrease in τ. Physically, such a 7-fold increase in ε, or a 7-fold decrease in τ, above the threshold value of (ε/τ) for the intercellular regions would require the formation of some *transcellular transdermal pathways*, either in the corneocytes at the SC surface (resulting in an increase in ε) or in the corneocytes within the SC itself (resulting in a decrease in τ). Interestingly, the

presence of transcellular transdermal transport pathways within LTRs has been visualized recently near the SC surface by Tang using two-photon microscopy.[29] Furthermore, Tang observed that, in the non-LTR regions of the SC, intercellular transdermal transport pathways were the dominant pathway.[29] Since the values of (ε/τ) for the non-LTR regions (1.26×10^{-4}, average of the Table 4-1 values) are lower than the threshold value of 3.6×10^{-4}, one may conclude that transcellular transdermal transport regions are not the primary route of transport through the non-LTRs, which is consistent with the results of Tang.[29] Since the previous two-photon microscopy studies examined skin samples sonicated in the absence of SLS, future two-photon microscopy studies will be conducted to confirm whether or not transcellular transdermal transport pathways are present in the more permeable LTRs and in the less permeable non-LTRs of skin samples sonicated in the presence of SLS.

4.6 Conclusions

A series of diffusion masking experiments have been performed for the purpose of demonstrating quantitatively that the patterns of red spots observed on the skin when the red-colored permeant SRB and the chemical enhancer SLS are used in the ultrasound coupling medium are, indeed, markers for localized regions of high transdermal permeability on ultrasound-treated full-thickness pig skin. The results of these experiments, carried out over a range of skin electrical currents, have shown that the transdermal permeability of the LTRs is 80-fold higher, on average, than the transdermal permeability of the less permeable non-LTRs. Although most of the transdermal delivery occurs in the more permeable LTRs, an analysis of the skin electrical resistivity data also

indicates that there is a significant enhancement in both the highly permeable LTRs and in the less permeable non-LTRs when compared to untreated skin (~5000-fold and ~170-fold, respectively). This indicates that the skin may be experiencing two levels of structural perturbation in the ultrasound/SLS system. Finally, an analysis of the (ε/τ) values for the less permeable non-LTRs and the highly permeable LTRs reveals that, while the transdermal transport pathways in the less permeable non-LTRs may be entirely intercellular, the transdermal transport pathways in the more permeable LTRs are likely to be both intercellular and transcellular. Further studies need to be conducted to confirm the presence of transcellular transdermal transport pathways in the more permeable LTRs and to better understand how two levels of structural perturbation may be induced in skin samples treated with low-frequency ultrasound in the presence of SLS.

In the next chapter (Chapter 5), then, two-photon microscopy will be used to: 1) confirm the presence of transcellular permeation pathways in the LTRs as a result of exposure to low frequency ultrasound, and 2) evaluate the enhancements in the partition coefficient and the diffusion gradient in the skin for a model hydrophilic permeant (SRB) and a model hydrophobic permeant (RBHE) diffusing in SLS-treated, ultrasound-treated, and ultrasound/SLS-treated skin samples as compared to untreated skin.

4.7 Appendix

In this appendix, three possible sources of error in the experimental procedure for the diffusion masking experiments are examined: 1) the choice of 75 as the blue color threshold value for determining the LTR area, 2) skin variability, and 3) the placement of the masking material on the skin samples prior to calcein diffusion. To give the reader a

quantitative sense of how the estimated LTR area would vary with changes in the blue color level threshold value, estimates of the LTR area were made at blue color level threshold values of 60, 65, 70, 75, 80, 85, and 90 on a randomly-selected skin sample. The results of this analysis are presented in Table 4-A1. As the table shows, there is approximately a 10% increase in the estimated LTR area for every 5-pixel increase in the value of the blue color level threshold. For the LTR data in Table 4-A1, the relative error in the average LTR area for 10 samples is roughly 20% - 35% over the range of skin electrical currents examined, due solely to the second source of error- the high variability of the skin samples themselves. Comparing these sources of error in the LTR area estimate, we can conclude that the error that arises from skin sample variability (20% - 35%) will have a greater influence on the total error in the deduced average LTR area than the error in the selection of the blue color level threshold value (10% increase per 5 pixel increase).

Table 4-A1: Estimated LTR Area at Different Blue Color Level Threshold Values for a Randomly-Selected Skin Sample.

Blue Color Level Threshold Value	Estimated LTR Area (mm^2)
60	17.65
65	19.23
70	20.82
75	22.67
80	24.64
85	26.97
90	30.23

The third possible source of error in the experimental procedure is the placement of the masking material on the skin prior to calcein diffusion. While the ideal result would be to place the masking material directly on the border between the LTRs and the non-LTRs, this can be difficult in practice. In order to obtain the most accurate results possible, it was initially assumed (correctly, based on our results) that the hypothesized LTRs were regions of very high transport. Therefore, when applying the mask on skin samples that would be used to measure transport through the LTRs, care was taken to not partially cover the LTRs with masking material. This was achieved by including a thin unmasked perimeter of the surrounding non-LTR with the unmasked LTR. Since the non-LTR is a region of low transdermal transport, the inclusion of this perimeter would not impact the results as much as if a fraction of the LTR had been unknowingly covered during mask application. Likewise, for the measurement of the transport in the non-LTRs, a thin perimeter of the non-LTR surrounding the LTRs was covered with masking material along with the LTRs. This was done to ensure that the highly permeable LTRs would be completely masked, and hence would be unable to introduce errors into the measurement of the less permeable non-LTRs.

4.8 References

1. Mitragotri, S. 2001. Effect of bilayer disruption on transdermal transport of low-molecular weight hydrophobic solutes. Pharm Res 18:1018-1023.
2. Johnson ME, Blankschtein D, Langer R. 1997. Evaluation of solute permeation through the stratum corneum: Lateral bilayer diffusion as the primary transport mechanism. J Pharm Sci 86:1162-1172.
3. Hou SYE, Mitra AK, White SH, Menon GK, Ghadially R, Elias PM. 1991. Membrane structures in normal and essential fatty acid deficient stratum corneum: Characterization by ruthenium tetroxide staining and x-ray diffraction. J Invest Dermatol 96:215-223.
4. Bodde HE, van der Brink I, Koerten HK, de Haan FHN. 1991. Visualization of in vitro percutaneous penetration of mercuric chloride: Transport through intercellular spaces cellular uptake through desmosomes. J Cont Rel 15:227-236.
5. Pliquett UF, Zewert TE, Chen T, Langer R, Weaver JC. 1996. Imaging of fluorescent molecule and small ion transport through human stratum corneum during high voltage pulsing: Localized transport regions are involved. Biophys Chem 58:185-204.
6. Zewert TE, Pliquett UF, Langer R, Weaver JC. 1995. Transdermal Transport of DNA Antisense Oligonucleotides by Electroporation. Biochem Biophys Res Co 212:286-292.
7. Vanbever R, Pliquett UF, Preat V, Weaver JC. 1999. Comparison of the effects of short, high-voltage and long, medium-voltage pulses on skin electrical and transport properties. J Cont Rel 60:35-47.

8. Gowrishankar TR, Herdon TO, Vaughan TE, Weaver JC. 1999. Spatially constrained localized transport regions due to skin electroporation. J Cont Rel 60:101-110.

9. Sharma A, Kara M, Smith FR, Krishnan TR. 2000. Transdermal drug delivery using electroporation. I. Factors influencing in vitro delivery of terazosin hydrochloride in hairless rats. J Pharm Sci 89:528-535.

10. Sharma A, Kara M, Smith FR, Krishnan TR. 2000. Transdermal drug delivery using electroporation. II. Factors influencing skin reversibility in electroporative delivery of terazosin hydrochloride in hairless rats. J Pharm Sci 89:536-544.

11. Prausnitz MR, Aura Gimm J, Guy RH, Langer R, Weaver JC, Cullander C. 1996. Imaging regions of transport across human stratum corneum during high-voltage and low-voltage exposures. J Pharm Sci 85:1363-1370.

12. Kochhar C, Imanidis G. 2003. In vitro transdermal iontophoretic delivery of leuprolide – mechanisms under constant voltage application. J Pharm Sci 92:84-96.

13. Turner NG, Guy RH. 1997. Iontophoretic transport pathways: Dependence on penetrant physicochemical properties. J Pharm Sci 86:1385-1389.

14. Bath BD, Scott ER, Phipps JB, White HS. 2000. Scanning electrochemical microscopy on iontophoretic transport in hairless mouse skin. Analysis of the relative contributions of diffusion, migration, and electroosmosis of transport in hair follicles. J Pharm Sci 89:1537-1549.

15. Curdy C, Kalia YN, Guy RH. 2001. Non-invasive assessment of the effects of iontophoresis on human skin in-vivo. J Pharm Pharmacol 53:769-777.

16. Kalia YN, Nonato LB, Guy RH. 1996. The effect of iontophoresis on skin barrier integrity: non-invasive evaluation by impedance spectroscopy and transepidermal water loss. Pharm Res 13:957-960.

17. Kalia YN, Guy RH. 1997. Interaction between penetration enhancers and iontophoresis: effect on human skin impedance in vivo. J Cont Rel 44:33-42.

18. Moser K, Kriwet K, Froehlilch N, Kalia YN, Guy RH. 2001. Permeation enhancement of a highly lipophilic drug using supersaturated systems. J Pharm Sci 90:607-616.

19. Mitragotri S. 2000. Synergistic effect of enhancers for transdermal drug delivery. Pharm Res 17:1354-1359.

20. Mitragotri S. 2001. Effect of bilayer disruption on transdermal transport of low-molecular weight hydrophobic solutes. Pharm Res 18:1018-1023.

21. Yu B, Kim KH, So PTC, Blankschtein D, Langer R. 2003. Visualization of oleic acid-induced transdermal diffusion pathways using two-photon fluorescence microscopy. J Invest Derm 120:448-455.

22. Johnson ME, Mitragotri S, Patel A, Blankschtein D, Langer R. 1996. Synergistic effects of chemical enhancers and therapeutic ultrasound on transdermal drug delivery. J Pharm Sci 85:670-678.

23. Tezel A, Sens A, Tuchscherer J, Mitragotri S. 2002. Synergistic effect of low-frequency ultrasound and surfactants on skin permeability. J Pharm Sci 91:91-100.

24. Tezel A, Sens A, Tuchscherer J, Mitragotri S. 2001. Frequency dependence of sonophoresis. Pharm Res 18:1694-1700.

25. Tezel A, Sens A, Mitragotri S. 2002. A theoretical analysis of low-frequency sonophoresis: Dependence of transdermal transport pathways on frequency and energy density. Pharm Res 19:1841-1846.

26. Tang H, Blankschtein D, Langer R. 2002. Effects of low-frequency ultrasound on the transdermal permeation of mannitol: Comparative studies with in vivo and in vitro skin. J Pharm Sci 91:1776-1794.

27. Tang H, Wang CCJ, Blankschtein D, Langer R. 2002. An investigation of the role of cavitation in low-frequency ultrasound-mediated transdermal drug transport. Pharm Res 19:1160-1169.

28. Alvarez-Román R, Merino G, Kalia YN, Naik A, Guy RH. 2003. Skin permeability enhancement by low-frequency sonophoresis: Lipid extraction and transport pathways. J Pharm Sci 92:1138-1146.

29. Tang H. 2001. Experimental and Theoretical Investigation of the Effects of Low-Frequency Sonophoresis on Transdermal Drug Transport. Ph.D. Thesis. Massachusetts Institute of Technology.

30. Tang H, Mitragotri S, Blankschtein D, Langer R. 2001. Theoretical description of transdermal transport of hydrophilic permeants: Application to low-frequency sonophoresis. J Pharm Sci 90:545-568.

31. Kasting GB, Bowman LA. 1990. DC electrical current properties of frozen, excised human skin. Pharm Res 7:134-143.

32. Tang H, Blankschtein D, Langer R. 2002. Prediction of steady-state skin permeabilities of polar and nonpolar permeants across excised pig skin based on

measurements of transient diffusion: Characterization of hydration effects on the skin porous pathway. J Pharm Sci 91:1897-1907.

33. Deen WM. 1987. Hindered transport of large molecules in liquid-filled pores. AIChE J 33:1409-1425.

34. Tezel A, Sens A, Mitragotri S. 2003. Description of transdermal transport of hydrophilic solutes during low-frequency sonophoresis based on a modified porous pathway model. J Pharm Sci 92:381-393.

35. Bommanan D, Menon GK, Okuyama H, Elias PM, Guy RH. 1992. Sonophoresis. II. Examination of the mechanism(s) of ultrasound-enhanced transdermal drug delivery. Pharm Res. 9:1043-1047.

36. Nemanic MK, Elias PM. 1980. In situ precipitation: A novel cytochemical technique for visualization of permeability pathways in mammalian stratum corneum. J Histochem Cytochem 28:573-578.

37. Squier CA, Lesch CA. 1988. Penetration pathways of different compounds through epidermis and oral epithelia. J Oral Pathol 17:512-516.

38. Michaels AS, Chandraskeran SK, Shaw JE. 1975. Drug permeation through human skin: Theory and in vitro experimental measurement. Am Inst Chem Eng J 21:985-996.

39. Cussler E, Hughes S, Ward W, Aris R. 1988. Barrier membranes. J Memb Sci 38:161-174.

40. Lange-Lieckfeldt R, Lee G. 1992. Use of a model lipid matrix to demonstrate the dependence of the stratum corneum's barrier properties on its internal geometry. J Cont Rel 20:183-194.

41. Edwards DA, Langer R. 1994. A linear theory of transdermal transport phenomena. J Pharm Sci 83:1315-1334.

42. Menton DN. 1976. Minimum-surface mechanism to account for organization of cells into columns in mammalian epidermis. Am J Anat 145:1-22.

43. Mershon MM. 1975. In Applied Chemistry at Protein Interfaces; Gould RF, Ed.; American Chemical Society: Washington, DC.; pp 41-73.

44. Wildnauer RH, Miller DL, Humphries WT. 1975. In Applied Chemistry at Protein Interfaces; Gould RF, Ed.; American Chemical Society: Washington, DC.; pp 74-124.

Chapter 5

Investigation of Transdermal Transport Pathways and Transport Mechanisms in Skin Treated with Low-Frequency Ultrasound and with Chemical Enhancers Using Two-Photon Microscopy

5.1 Introduction

5.1.1 Previous Applications of Two-Photon Microscopy in Transdermal Drug Delivery: Chemical Enhancers and Low-Frequency Ultrasound

In Chapter 1, a brief overview was presented of the visualization techniques that have been utilized in the past to determine the types of transdermal permeation pathways present in the skin.[1-15] One such technique, two-photon microscopy (TPM), has been used in the past to advance our understanding of the permeation pathways present in skin samples treated with chemical enhancers, as well as in skin samples treated with low-frequency sonophoresis.[10-15] Two-photon microscopy is an excellent visualization technique for the analysis of transdermal permeation pathways for two primary reasons: 1) it is a non-invasive imaging technique,[14,16] and 2) it produces higher quality images at

a greater depth into the tissue compared to similar microscopy methods, such as confocal microscopy.[14,17-19] Being a non-invasive technique, it is possible to keep the skin intact while imaging with TPM. This is a significant consideration for the use of *in vivo* imaging of biological tissues. Other imaging techniques used in previous transdermal visualization studies, such as scanning electron microscopy[4,6-8] and transmission electron microscopy,[2,9] require that the skin undergoes special preparations prior to imaging (i.e. coating with gold-palladium;[4] exposure to osmium tertoxide,[6-8] lanthanum nitrate, [6,7] and mercuric chloride;[2] and staining with uranyl acetate[8]) that would be hazardous for *in vivo* applications. In addition to being a safe imaging technique for the skin, TPM offers improved imaging capabilities over confocal microscopy techniques. Specifically, TPM involves a three-body collision of two photons and one fluorescent molecule to create an excitation event, while confocal microscopy involves the collision of a single photon with one fluorescent molecule to create an excitation event.[14,15,17] Because three-body collisions occur with lower frequency than two-body collisions, imaging of fluorophores is restricted to the focal plane of interest.[14,20,21] In addition, the photon flux decreases quadratically as the distance away from the focal plane increases, which allows for discrimination of the fluorescence signal at increased tissue depths.[14,17] These attributes of TPM have made it a useful tool for imaging the delivery of fluorescent permeants in skin samples treated with chemical enhancers and with low-frequency sonophoresis.[10-15]

In the area of chemical enhancers, TPM has been used extensively to further our understanding of the mechanisms of chemically-enhanced transdermal transport. Yu *et al.* used TPM to visualize (image) and to quantify the effect of a chemical enhancer (oleic acid) on the delivery of a model *hydrophilic* fluorescent permeant, sulforhodamine B

Table 5-1: Physical properties of the fluorescent *hydrophilic* probe, Sulforhodamine B (SRB), and the fluorescent *hydrophobic* probe, Rhodamine B Hexyl Ester (RBHE), examined with Two-Photon Microscopy.[14]

Probe	Molecular Weight (Da)	Absorbance/Emission (nm)	Log $K_{O/PBS}$
SRB	559	565/586	-0.45 ± 0.0045
RBHE	627	556/578	2.49 ± 0.18

(SRB), and of a model *hydrophobic* fluorescent permeant, rhodamine B hexyl ester (RBHE) in 112 μm x 112 μm regions of heat-stripped human cadaver skin.[10,14] As Table 5-1 shows, SRB and RBHE are ideal choices since they have similar molecular weights and absorbance/emission peak wavelengths. Through a novel analysis of the fluorescent intensity profiles as a function of skin depth in the imaged skin regions, it was demonstrated that oleic acid primarily enhances the transdermal transport of SRB and RBHE by increasing the permeant vehicle-to-skin partition coefficient as compared to the delivery of SRB and RBHE in untreated skin.[10,14] Imaging studies conducted with High Speed Two-Photon Microscopy (HTPM) demonstrated that a larger number of 112 μm x 112 μm skin samples is required to obtain statistically meaningful data for the hydrophilic permeant, SRB, (12-24 imaged skin sites) than for the hydrophobic permeant, RBHE, (4-6 skin sites).[11,14] Further analysis of HTPM images corresponding to the transdermal delivery of SRB and RBHE with and without oleic acid enhancement demonstrated that the rate-limiting steps for transdermal transport of SRB and RBHE are the vehicle-to-skin partitioning and the lateral diffusion through the lipid lamellar bilayers, respectively.[12,14]

A third TPM technique, *dual-channel TPM*, was used by Yu *et al.* to determine the locations of the SRB and the RBHE probes relative to the intrinsic structure of the stratum corneum. The stratum corneum contains intrinsic fluorophores, including collagen, elastin, aromatic amino acids (such as tryptophan and tyrosine), nicotinamide adenine dinucleotide, porphyrins, and flavin adenine dinucleotide, which have fluorescence emission bands centered at 450 nm and 520 nm.[13,14,22,23] The emission bands of the skin fluorophores are significantly lower than the emission bands of SRB and RBHE (see Table 5-1). By adding filters to the two-photon microscope to capture light emitted from the fluorescent permeants separately from the light emitted from the intrinsic skin fluorophores, it is possible to simultaneously image the location of SRB and RBHE relative to the intrinsic structure of the skin. Using this technique, Yu *et al.* demonstrated that oleic acid increases the localization of RBHE in the intercellular region, while it increases the penetration of SRB into the corneocytes of the stratum corneum.[13,14] These effects of oleic acid effectively reduced the diffusion lag time both in the case of RBHE, by circumventing the corneocytes, which act as sinks to transdermal diffusion, and in the case of SRB, by increasing the partitioning of SRB into the corneocytes, such that the diffusion sinks were filled faster.[13,14]

In the area of low-frequency sonophoresis, some preliminary investigations have been conducted with conventional TPM techniques to understand the differences in transdermal permeation between untreated skin samples and ultrasound-treated skin samples. As part of her Ph.D. thesis work, Tang used TPM to demonstrate that the hydrophilic probe SRB traverses the skin passively via an intercellular pathway. On the other hand, in the presence of ultrasound only (i.e. no surfactant was included in the

coupling medium during the ultrasound treatment), both intercellular and transcellular pathways contribute to the overall transdermal transport of SRB.[15] Additionally, Tang observed heterogeneity in the distribution of SRB on the surface of ultrasound-treated skin.[15] Specifically, a single region containing a large amount of SRB was observed (by the naked-eye since SRB has a red color) beneath the ultrasound transducer.[15] Because of their appearances, these regions were referred to as localized transport regions (LTRs) by Tang.[15] Preliminary investigations of the LTRs with TPM suggested that, near the stratum corneum surface, both intercellular and transcellular permeation pathways were formed as a result of the ultrasound-treatment, while only intercellular pathways were observed in the deeper regions of the stratum corneum.[15] In the surrounding regions of the skin, referred to as inactive transport regions (ITRs) by Tang, TPM imaging demonstrated that intercellular pathways were present, similar to those observed in untreated skin samples.[15] An analysis of the fluorescence intensity profiles as a function of skin depth for untreated skin, the LTRs, and the ITRs: 1) confirmed that the ITRs and the untreated skin samples were statistically similar, and 2) demonstrated that SRB penetrated deeper into the skin within the LTRs as compared to the untreated skin samples and the ITRs.[15]

Prior to the work presented in this chapter, there had been no previous studies conducted with TPM to deduce the types of permeation pathways present in skin treated *simultaneously with low-frequency ultrasound and a chemical enhancer*. In addition, there has been no previous quantitative analysis of the enhancements of key transport properties, such as the vehicle-to-skin partition coefficient, K, and the fluorescent permeant intensity gradient in the skin, dI/dz, for skin treated with low-frequency

sonophoresis (with or without the simultaneous application of a chemical enhancer), as has been examined in the case of a chemical enhancer (oleic acid) by Yu *et al.*[10-14] Finally, there have been no previous investigations with TPM to examine the permeation pathways traversed by a *hydrophobic* permeant in skin treated with low-frequency sonophoresis (with or without the simultaneous application of a chemical enhancer). In the next section, the motivation for investigating these aspects of low-frequency sonophoresis using TPM is provided.

5.1.2 Motivation for Additional Two-Photon Microscopy Studies of Low-Frequency Sonophoresis

In Section 4.4.1, it was demonstrated that the LTRs formed during treatment of full-thickness pig skin samples (an acceptable model for human skin) with low-frequency ultrasound in the presence of a chemical enhancer – the surfactant, sodium lauryl sulfate (SLS) – and a hydrophilic fluorophore, SRB, were indeed localized regions of high permeability for the model *hydrophilic* permeant, calcein.[24] In addition, skin electrical resistivity measurements were used in conjunction with the Aqueous-Pore Pathway Hypothesis to determine the value of the aqueous-pore transport parameter, (ε/τ), for each region of the skin studied: the non-LTRs (note the change in wording from ITRs used by Tang[15]), the LTRs, and the Total skin sample (see Sections 4.2.6 and 4.4.2). By comparing the value of (ε/τ) deduced for each region of the skin studied in Chapter 4 with the threshold value of $(\varepsilon/\tau_{flux})$ for the intercellular regions of the stratum corneum (see Chapter 3 for details), it was hypothesized that transcellular permeation pathways

were present within the LTRs formed in skin samples treated with low-frequency ultrasound in the presence of SLS (see Section 4.5.2 for details).[24]

In this chapter, dual-channel two-photon microscopy (see Section 5.2.6 for an explanation of this technique) was used to determine if, in fact, transcellular pathways are present within the LTRs formed in skin treated simultaneously with low-frequency ultrasound and with the chemical enhancer, SLS (see Section 5.3.3), in the presence of the *hydrophilic* fluorescent permeant, SRB. In addition, the types of pathways present in untreated, SLS-treated, and US-treated skin were also examined in an attempt to understand the differences in the permeation pathways formed as a result of different transdermal enhancing techniques (i.e. a chemical enhancer (SLS), low-frequency sonophoresis (US), and a synergistic method (US combined with SLS)) (see Section 5.3.3). Furthermore, fluorescent intensity profiles as a function of skin depth were generated from the TPM images of the model fluorescent permeant for each of the four skin types listed above (see Section 5.2.7.1 for a discussion of this technique). From the fluorescent intensity profiles, the enhancements in the skin surface partition coefficient, K, and in the permeant intensity gradient, dI/dZ, were determined (see Section 5.3.2.4) for the purpose of furthering our understanding of the mechanism of LTR formation in ultrasound-treated skin (see Section 5.3.4).

The studies listed above were also conducted with RBHE, a *hydrophobic* fluorescent permeant, in place of SRB. In Chapter 4, LTRs were observed in skin treated simultaneously with ultrasound, a chemical enhancer (SLS), and the hydrophilic probe, SRB. The motivation for using RBHE was to determine if the LTRs also form in the presence of a hydrophobic probe, and, if so, what are the differences, if any, in the

permeation pathways, or in the enhancements of the transdermal transport properties, observed using dual-channel TPM imaging methods.

5.2 Materials and Methods

5.2.1 Chemicals

Phosphate buffer saline (PBS; 0.01 M phosphate, 0.137 M NaCl) was obtained from Fluka Chemical (St. Louis, MO). Sulforhodamine B (SRB) and Rhodamine B Hexyl Ester (RBHE) were obtained from Molecular Probes (Eugene, OR). Ethanol and Sodium Lauryl Sulfate (SLS) were obtained from Sigma Chemical Company (St. Louis, MO). All these chemicals were used as received.

5.2.2 Skin Preparation

Human full-thickness skin samples from the abdominal area were obtained from the National Disease Research Institute (NDRI, Philadelphia, PA) and stored at -80°C for up to 3 months prior to use. Human skin was selected, rather than the pig skin model (see Chapter 4), for this investigation since all previous work with TPM for transdermal imaging in our group has used human skin samples.[10-15] Since pig skin is used as a model for human skin, results obtained with human skin are comparable to results obtained with pig skin. In addition, human skin is preferred over pig skin, since human skin is more relevant to the study of transdermal transport for future clinical applications. Prior to its use in the fluorescent permeant diffusion experiments (see Section 5.2.4), the skin was thawed and the subcutaneous fat was removed from the skin using a razor blade. The skin was then sectioned and mounted in vertical Franz diffusion cells (15-mm inner

diameter) obtained from Permegear (Bethlehem, PA). Finally, the initial electrical resistivity of the skin was measured using methods described in Section 4.2.3. Any skin sample with an initial resistivity lower than 50 kOhm*cm^2, which is indicative of the skin sample being compromised,[15] was discarded and replaced with a new skin sample.

5.2.3 Preparation of the Fluorescent Permeant Solutions

For the visualization of SRB in human skin, the following solutions were prepared: Formulation (S-1) – 0.05 mg/ml of SRB in PBS for the delivery of SRB through untreated skin, Formulation (S-2) – 0.005 mg/ml of SRB in PBS for the delivery of SRB through skin treated solely with ultrasound, and Formulation (S-3) – 0.005 mg/ml of SRB in PBS containing 1% (w/v) SLS for the delivery of SRB through chemically-enhanced skin, as well as for the delivery of SRB through skin treated simultaneously with ultrasound and with a chemical enhancer (SLS). For a discussion of the selection of the concentrations of SRB in the various formulations used, see below.

For the visualization of RBHE in human skin, the following solutions were prepared: Formulation (R-1) – 0.05 mg/ml of RBHE in a 50/50 mixture of PBS and ethanol for the delivery of RBHE through untreated skin, Formulation (R-2) – 0.005 mg/ml of RBHE in a 50/50 mixture of PBS and ethanol for the delivery of RBHE through skin treated solely with ultrasound, and Formulation (R-3) – 0.005 mg/ml of RBHE in a 50/50 mixture of PBS and ethanol containing 1% (w/v) SLS for the delivery of RBHE through chemically-enhanced skin, as well for the delivery of RBHE in skin treated simultaneously with ultrasound and with a chemical enhancer. For a discussion of the selection of the concentrations of RBHE in the various formulations used, see below.

The concentrations of SRB and RBHE in formulation S-1 to S-3 and R-1 to R-3 were selected for the following reasons. For the enhanced delivery of SRB and RBHE in the skin, a smaller concentration of 0.005 mg/ml was chosen to enable the detection of both the fluorescent permeant and the intrinsic skin auto-fluorescence signals.[13,14] For the delivery of SRB and RBHE in untreated skin, a larger concentration of 0.05 mg/ml was chosen to ensure that enough fluorescent permeant was present in the skin to be detected with TPM. Ethanol was included in the RBHE solution to enable solubility of RBHE, which is immiscible in PBS due to its relatively high level of hydrophobicity (see Table 5-1). Finally, 1% (w/v) SLS was selected as the amount of chemical enhancer to be consistent with the experiments conducted in Chapters 2 and 4.

5.2.4 Diffusion Experiments Using Fluorescent Permeants

Skin samples were divided into four groups: 1) untreated, 2) SLS-treated (chemical enhancer only), 3) US-treated (low-frequency sonophoresis only), and 4) US/SLS-treated (simultaneous application of low-frequency ultrasound and a chemical enhancer). For the delivery of SRB and RBHE in untreated skin samples, the skin was exposed to Formulation (S-1) and to Formulation (R-1), respectively, for 24 hours. For the delivery of SRB and RBHE in chemically-enhanced skin samples, the skin was exposed to Formulation (S-3) and to Formulation (R-3), respectively, for 24 hours. For the delivery of SRB and RBHE in US-treated skin samples, the skin was exposed to Formulation (S-2) and to Formulation (R-2), respectively, for 24 hours in the presence of ultrasound at the following conditions: frequency – 20 kHz, intensity – 1.6 W/cm^2, duty cycle – 0.1:0.9 sec (ON:OFF), and tip displacement – 3 mm.[15] These ultrasound conditions were

selected to be similar to those used in the preliminary investigation of LTRs with TPM.[15] At the end of the 24-hour exposure period, the skin electrical resistivity was measured to determine the extent to which each formulation had perturbed the structure of the skin. For the delivery of SRB and RBHE in skin samples treated simultaneously with LFS and a chemical enhancer (SLS), the skin was exposed to Formulation (S-3) and Formulation (R-3), respectively, in the presence of ultrasound at the following conditions: frequency – 20 kHz, intensity – 7.5 W/cm^2, duty cycle – 5:5 sec (ON:OFF), and tip displacement – 3 mm,[24] until the skin electrical current reached a value of 225 μAmps, similar to the conditions examined in Chapter 4. Note that this level of skin electrical current was obtained after treating the skin simultaneously with ultrasound and SLS for 5 - 10 minutes.

5.2.5 Preparation of Skin Samples for TPM Imaging

After delivery of SRB and RBHE into the skin, the skin samples were removed from the Franz diffusion cells, and excess formulation was removed from the skin surface. The circular region of the skin exposed to the fluorescent permeants was removed using a razor blade. A few drops of PBS were then added to an imaging chamber (2.5 mm Coverwell, Grace Bio Labs, Bend, OR) covered with a No.1, 22 mm square glass cover slip (VWR Scientific, Media, PA) to ensure good contact of the skin surface with the cover slip. The skin was then inserted into the imaging chamber and subsequently mounted onto a glass microscope slide (VWR Microslides, 25 mm x 75 mm).

5.2.6 Dual-Channel TPM Imaging and Data Collection

Two-photon imaging of the skin samples prepared using the methods outlined in Sections 5.2.4 and 5.2.5 was conducted according to previously published methods,[10-13] which are briefly summarized here. Figure 5-1 shows a schematic illustration of the TPM imaging system.[14] The laser source was provided by a femtosecond ti-sa laser (Tsunami, Spectra-Physics, Mountain View, CA) pumped by 5W diode-pumped, solid state CW laser (Millenia V, Spectra-Physics, Mountain View, CA). For all the dual-channel TPM imaging, the laser power was set at 250 mW to ensure detection of the skin auto-fluorescence signal, while minimizing damage to the skin from the laser. A modified inverted microscope (Axiovert, 100TV, Ziess, Thornwood, NY) with an oil immersion 40X objective lens (Zeiss F Fluar, NA .13) was used to image the skin samples. X-Y scans were made with a scanner unit (6350 Cambridge Technology, Watertown, MA). The emitted photons from the laser excitation are collected by the microscope and then passed through two filters, which split the signal into the *red channel* for the photons emitted by the fluorescent permeant and the *green channel* for the photons emitted by the intrinsic skin fluorophores. The red and green channels are then sent to a photomultiplier and are discriminated against dark noise with a custom built high-speed photon discriminator unit to obtain the final dual-channel TPM image.

In untreated and SLS-treated skin, six 120 μm x 120 μm skin sites were imaged. In US-treated and US/SLS-treated skin, twelve 120 μm x 120 μm skin sites were imaged – six sites for the non-LTRs and six sites for the LTRs. The depth of the TPM imaging varied from a depth of 40 μm, for skin samples where little to no fluorescent permeant

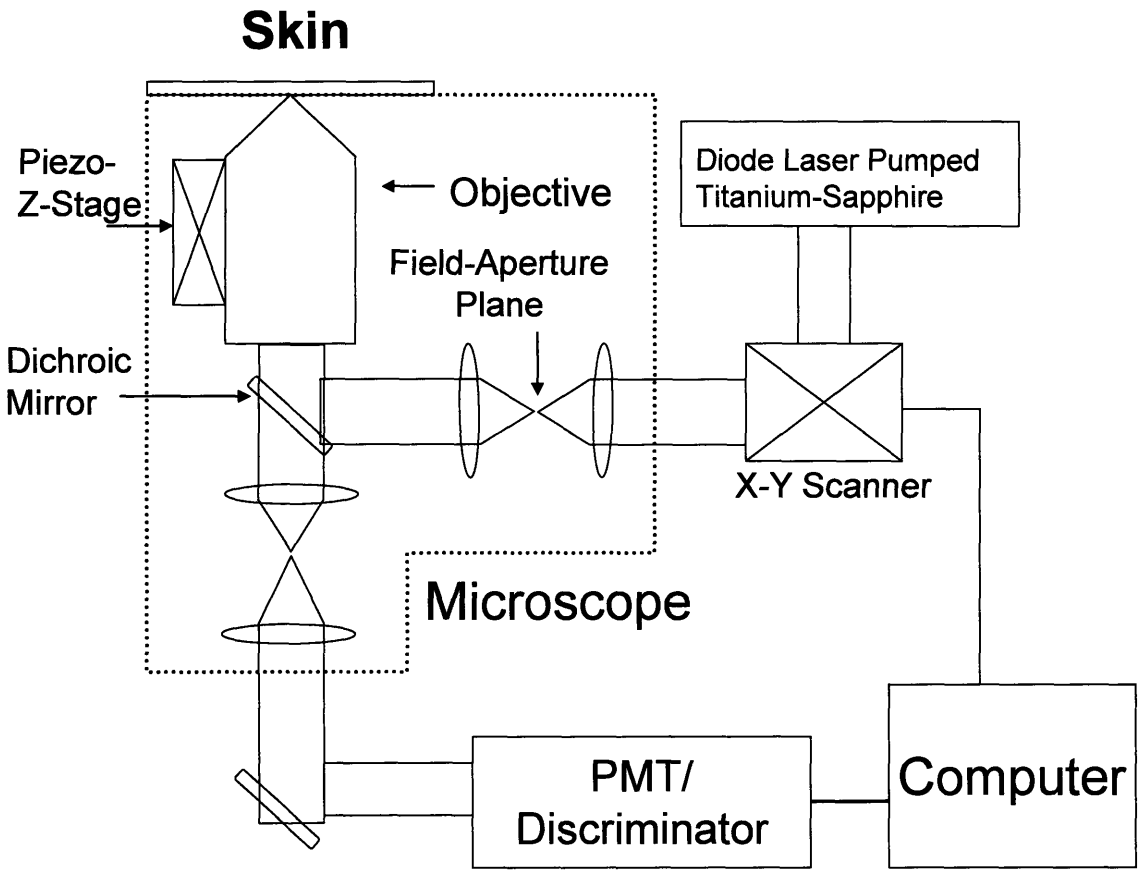

Figure 5-1: Schematic illustration of the TPM imaging system.[14]

penetrated deep into the skin, to a depth of 70 μm, for skin samples where significant fluorescent permeant penetrated deep into the skin.

5.2.7 Analysis of the TPM Images

The techniques that were used to analyze the dual-channel TPM images of both SRB and RBHE are based on previously published methods,[10-15] which are described in this section. These techniques include: 1) generating and analyzing the average fluorescence permeant intensity profiles as a function of skin depth, 2) evaluating the enhancement of the fluorescent permeant vehicle-to-skin partition coefficient, 3) evaluating the enhancement of the fluorescent permeant intensity gradient, 4) evaluating the enhancement of the effective diffusion path length, and 5) evaluating the existence of transcellular permeation pathways in the stratum corneum. All the TPM image processing reported in this section was carried out using MATLAB with the Image Processing Toolbox (Version 7.0.4.365 (R14) Service Pack 2, The Mathworks, Inc.).

5.2.7.1 Generating and Analyzing the Fluorescent Permeant Intensity Profiles as a Function of Skin Depth

The fluorescent permeant intensity profiles as a function of skin depth were generated using an in-lab subroutine in MATLAB, which calculated an average value for the fluorescence intensity, I, for each layer of the skin imaged in the z-direction (the direction perpendicular to the skin surface). The surface of each skin sample, corresponding to z = 0 μm, was defined at the location of the first local maximum in the average value of the intensity of the fluorescent probes as a function of increasing skin depth.[10,14,15] The average value of the fluorescence intensity at z = 0 was then averaged over the 5-7 skin

sites imaged for each of the six types of skin samples examined in this study for delivery of SRB and RBHE: 1) Untreated skin, 2) SLS-treated skin, 3) the non-LTRs of US-treated skin, 4) the LTRs of US-treated skin, 5) the non-LTRs of US/SLS-treated skin, and 6) the LTRs of US/SLS-treated skin. For the fluorescence intensity profiles of SRB and RBHE in the untreated skin, the value of I was divided by 10 to account for the difference in the donor concentration of the fluorescent permeant used for the untreated skin samples (0.05 mg/ml) and for the enhanced skin samples (0.005 mg/ml).

To determine whether treatment of the skin with SLS, US, or US/SLS results in a significant enhancement in the penetration of SRB and RBHE, the average value of the fluorescence permeant intensity in the enhanced skin samples and in the untreated skin samples were analyzed with the t-statistic, over the depth of skin imaged. The t-statistic, t_0, which tests for the difference in two average values where the variances are not equal, was calculated using the following formula:[25]

$$t_0 = \frac{x_{Enhanced} - x_{Untreated}}{\sqrt{\frac{s^2_{Enhanced}}{n_{Enhanced}} + \frac{s^2_{Untreated}}{n_{Untreated}}}} \tag{5.1}$$

where $x_{Enhanced}$ and $x_{Untreated}$ are the average values of the fluorescence intensity corresponding to the enhanced skin samples (i.e. SLS-treated, US-treated, or US/SLS-treated skin samples) and to the untreated skin samples, respectively, $s_{Enhanced}$ and $s_{Untreated}$ are the standard deviations in the average values of the fluorescence intensity corresponding to the enhanced skin samples and to the untreated skin samples, respectively, and $n_{Enhanced}$ and $n_{Untreated}$ are the number of samples examined for the enhanced skin samples and for the untreated skin samples, respectively. The value of t_0

was then compared to the values of t in a standard t distribution table.[25] For a specified value of the number of degrees of freedom, ν, defined by:[25]

$$\nu = \frac{\left(\frac{s^2_{Enhanced}}{n_{Enhanced}} + \frac{s^2_{Untreated}}{n_{Untreated}}\right)^2}{\frac{\left(s^2_{Enhanced}/n_{Enhanced}\right)^2}{n_{Enhanced}+1} + \frac{\left(s^2_{Untreated}/n_{Untreated}\right)^2}{n_{Untreated}+1}} - 2 \tag{5.2}$$

and the level of probability, p, there existed a corresponding value of t. For the case where $t_{\nu,p} > t_0$, $x_{Enhanced}$ and $x_{Untreated}$ are considered to be statistically similar. For the case where $t_{\nu,p} < t_0$, $x_{Enhanced}$ and $x_{Untreated}$ are considered to be statistically different. A value of p = 0.05, corresponding to a 95% confidence, was selected for the analysis of the fluorescent permeant intensity profiles in this study.

5.2.7.2 Evaluating the Enhancement in the Fluorescent Permeant Vehicle-to-Skin Partition Coefficient

The fluorescent permeant vehicle-to-skin partition coefficient, K, is defined as follows:[14]

$$K = \frac{C_s(z=0)}{C_d} \tag{5.3}$$

where $C_s(z = 0)$ is the concentration of the fluorescent permeant at the skin (s) surface and C_d is the concentration of the fluorescent permeant in the bulk donor (d) solution, which is assumed to be constant since $C_d / C_r >> 1$, where C_r is the concentration of the fluorescent permeant in the bulk receiver solution. The enhancement in the fluorescent permeant vehicle-to-skin partition coefficient, E_K, is then calculated using the following equation:

$$E_K = \frac{C_{s,Enhancer}(z=0)/C_{d,Enhancer}}{C_{s,Untreated}(z=0)/C_{d,Untreated}} \tag{5.4}$$

where $C_{i,Enhancer}$ and $C_{i,Untreated}$ (i = s and d) denote the concentrations of the fluorescent permeant in the enhanced skin samples and in the untreated skin samples, respectively. By assuming that the intensity of the fluorescent permeant, I, is directly proportional to its concentration in the skin, E_K can be approximated from the fluorescence intensity profiles using the following equation:[10,14]

$$E_K = \frac{I_{Enhancer}(z=0)}{I_{Untreated}(z=0)} \tag{5.5}$$

where $I_{Enhancer}(z = 0)$ is the average value of the fluorescence intensity of SRB or RBHE at the surface of the enhanced skin samples, and $I_{Untreated}(z = 0)$ is the average value of the fluorescence intensity of SRB or RBHE at the surface of the untreated skin samples. Again, the difference in the concentrations of the fluorescent permeants in the donor solutions has been accounted for in the value of $I_{Untreated}$ as described in Section 5.2.7.1.

5.2.7.3 Evaluating the Enhancement in the Fluorescent Permeant Intensity Gradient

The fluorescent permeant intensity gradient, (dI/dz), in the stratum corneum was evaluated by performing a linear regression using the average intensity values from the first 12 scans from the surface into the stratum corneum, a region which exhibits a significant decrease in the fluorescent probe intensity in the untreated skin, to which the fluorescent probe intensities in the enhanced skin samples are then compared.[10,14] The fluorescent permeant intensity gradient serves as a good approximation of the concentration gradient (dC/dz) of the fluorescent permeant in the skin, since the value of the fluorescence intensity is directly proportional to the concentration of the fluorescent

permeant present in the skin. To calculate the enhancement in the fluorescent permeant intensity gradient, E_G, the following equation was used:[10,14]

$$E_G = \frac{(dI/dz)_{Enhanced}}{(dI/dz)_{Untreated}} \tag{5.6}$$

where $(dI/dz)_{Enhanced}$ and $(dI/dz)_{Untreated}$ are the fluorescent permeant intensity gradients corresponding to the intensity profiles of the enhanced skin samples and of the untreated skin samples, respectively.

5.2.7.4 Evaluating the Enhancement in the Effective Diffusion Path Length

The steady-state flux, J, of permeant through the SC membrane is directly proportional to the concentration gradient, dC/dz, of the permeant in the SC, as embodied in the equation for Fick's First Law of diffusion in one dimension, given by:[26]

$$J = -D\frac{dC}{dz} \tag{5.7}$$

where D is the effective diffusion coefficient of the permeant within the SC. The steady-state permeability, P, is then given by:[27]

$$P = J/\Delta C \tag{5.8}$$

where ΔC is the concentration difference across the SC membrane (i.e. $\Delta C = C_d - C_r$). As discussed in Section 5.2.7.2, $C_d >> C_r$, and, therefore, ΔC can be approximated by C_d. The transdermal permeability can also be defined as follows:[27]

$$P = \frac{KD}{L} \tag{5.9}$$

where L is the effective diffusion path length. Equations (5.7) – (5.9) can be combined to yield the following useful result:

$$L = -\frac{KC_d}{dC/dz} \tag{5.10}$$

Noting that KC_d is equal to $C(z = 0)$ (see Eq. (5.3)), and that the concentration of the fluorescent permeant in the stratum corneum is directly proportional to the intensity of the fluorescence signal, Eq. (5.10) can be written in terms of the fluorescence intensity, I, as follows:

$$L = -\frac{I(z=0)}{dI/dz} \tag{5.11}$$

The enhancement in the effective diffusion path length, E_L, in enhanced skin samples as compared to untreated skin samples is given by:

$$E_L = \frac{L_{Enhanced}}{L_{Untreated}} = \frac{\dfrac{I_{Enhanced}(z=0)}{I_{Untreated}(z=0)}}{\dfrac{(dI/dz)_{Enhanced}}{(dI/dz)_{Untreated}}} = \frac{E_K}{E_G} \tag{5.12}$$

Accordingly, E_L can be evaluated from the values of E_K and E_G, which can be obtained from the fluorescence intensity profiles using Eqs. (5.5) and (5.6), respectively.

5.2.7.5 Evaluating the Existence of Transdermal Permeation Pathways in the Stratum Corneum from the Dual-Channel TPM Images

Following previously published methods,[13,14] a slice, 5 pixels (width) x 256 pixels (length), of the red channel (probe) and the green channel (skin auto-fluorescence) TPM images was selected for analysis of the location of the fluorescent permeant relative to the structure of the skin. At each position along the length of this slice (0 – 255), the intensities of the corresponding 5 pixels along the width were averaged and then normalized. These normalized average values, for both the red channel and the green channel, were plotted as a function of the pixel number along the length of the slice.

Previous studies utilizing this dual-channel TPM image analysis technique have demonstrated that it is possible to determine whether there is an increase, or a decrease, in the penetration of the probe into the corneocytes.[13,14] Specifically, by measuring the width and height of peaks in the normalized average intensity profile of the fluorescent probe in untreated skin, and comparing these values to the peak width and peak height of the fluorescent probe in the enhanced skin samples, enhancements, or reductions, in the penetration of the probe into the corneocytes were evaluated quantitatively. As the height of the peaks increases and the width of the peaks decreases, there is less permeant present inside the corneocytes, which serves as a qualitative indicator of the existence of *intercellular permeation pathways*. Conversely, as the height of the peaks decreases and the width of the peaks increases, there is more permeant present inside the corneocytes, which serves as a qualitative indicator of the existence of *transcellular permeation pathways*. The height of the peaks was determined by evaluating the difference between the height of the peak and the average height of the two valleys that neighbor the peak. The width of the peaks was determined by measuring the width of the peaks at half of the peak height. The skin surface ($z = 0$ μm) was selected as the skin layer to examine for the existence of transcellular permeation pathways. The surface of the skin is the first skin layer that is perturbed by SLS or US, since it is at the skin surface where the enhancing transient acoustic cavitation events take place,[28-30] and where the skin contacts the coupling medium. For samples with transcellular pathways present at $z = 0$ μm, additional measurements were made to deduce the depth that the transcellular pathways penetrate into the stratum corneum.

5.3 Results and Discussion

5.3.1 Qualitative Analysis of the Dual-Channel TPM Images

Figures 5-2 through 5-13 show samples of the 120 μm x 120 μm dual-channel TPM images obtained for the delivery of the fluorescent permeants, SRB and RBHE, in each of the six skin samples examined in this study: 1) untreated skin (see Figure 5-2 for SRB and Figure 5-8 for RBHE), 2) SLS-treated skin (see Figure 5-3 for SRB and Figure 5-9 for RBHE), 3) the non-LTRs of US-treated skin (see Figure 5-4 for SRB and Figure 5-10 for RBHE), 4) the LTRs of US-treated skin (see Figure 5-5 for SRB and Figure 5-11 for RBHE), 5) the non-LTRs of US/SLS-treated skin (see Figure 5-6 for SRB and Figure 5-12 for RBHE), and 6) the LTRs of US/SLS-treated skin (see Figure 5-7 for SRB and Figure 5-13 for RBHE). In each figure, the red channel images show the location of SRB or RBHE in the skin, and the green channel images show the location of the intrinsic skin fluorophores. The dual-channel TPM images are presented as a function of skin depth (z). Specifically, TPM images are presented at z = 0 μm (the skin surface), z = 5 μm, z = 10 μm, z = 20 μm, z = 30 μm, and z = 40 μm to provide qualitative information on how the amount and location of SRB and RBHE changes as a function of skin depth in each of the six skin samples. Note that the thickness of the stratum corneum is, on average, 10 – 20 μm. Where appropriate, the location of a representative corneocyte in the stratum corneum has been indicated with a "C", and the visualization of the stratum spinosum layer of the viable epidermis has been indicated with a "SS". A horizontal white scale bar in the image corresponding to z = 0 μm, representing a length of 24 μm, has been included to aid the reader in approximating dimensions.

5.3.1.1 Qualitative Analysis of SRB Penetration in SLS-Treated and Untreated Skin

From a qualitative analysis of Figures 5-2 and 5-3, the dual-channel TPM images for SRB delivery in untreated and SLS-treated skin, respectively, SRB does not appear to penetrate deeper than 20 μm into the skin, which corresponds approximately to the thickness of the stratum corneum. For the images corresponding to 20 μm, 30 μm, and 40 μm, there is little evidence of appreciable SRB intensity, as well as of little skin auto-fluorescence, indicated by the low values of the upper limits of the intensity scales associated with the TPM images for 20 μm, 30 μm, and 40 μm. In addition, from the images corresponding to z = 0, 5, and 10 μm, the shapes of the corneocyte cells, which have a diameter of 30-40 μm, are clearly observed. This observation suggests that *the penetration of SRB is restricted to the stratum corneum in both SLS-treated skin and untreated skin.*

While the depth of SRB penetration in SLS-treated skin and untreated skin appears to be similar, there is a visible difference between the penetration of SRB into the corneocytes of SLS-treated skin and of untreated skin. In untreated skin (see Figure 5-2, z = 0, 5, and 10 μm), SRB does not penetrate deeply into the corneocytes of the stratum corneum, since the intercellular and corneocyte domains are well defined. On the other hand, in SLS-treated skin (see Figure 5-3, z = 0, 5, and 10 μm), SRB appears to be more evenly distributed between the intercellular region and the interiors of the corneocytes. This observation suggests that *more SRB penetrates into the corneocytes in SLS-treated skin relative to untreated skin.*

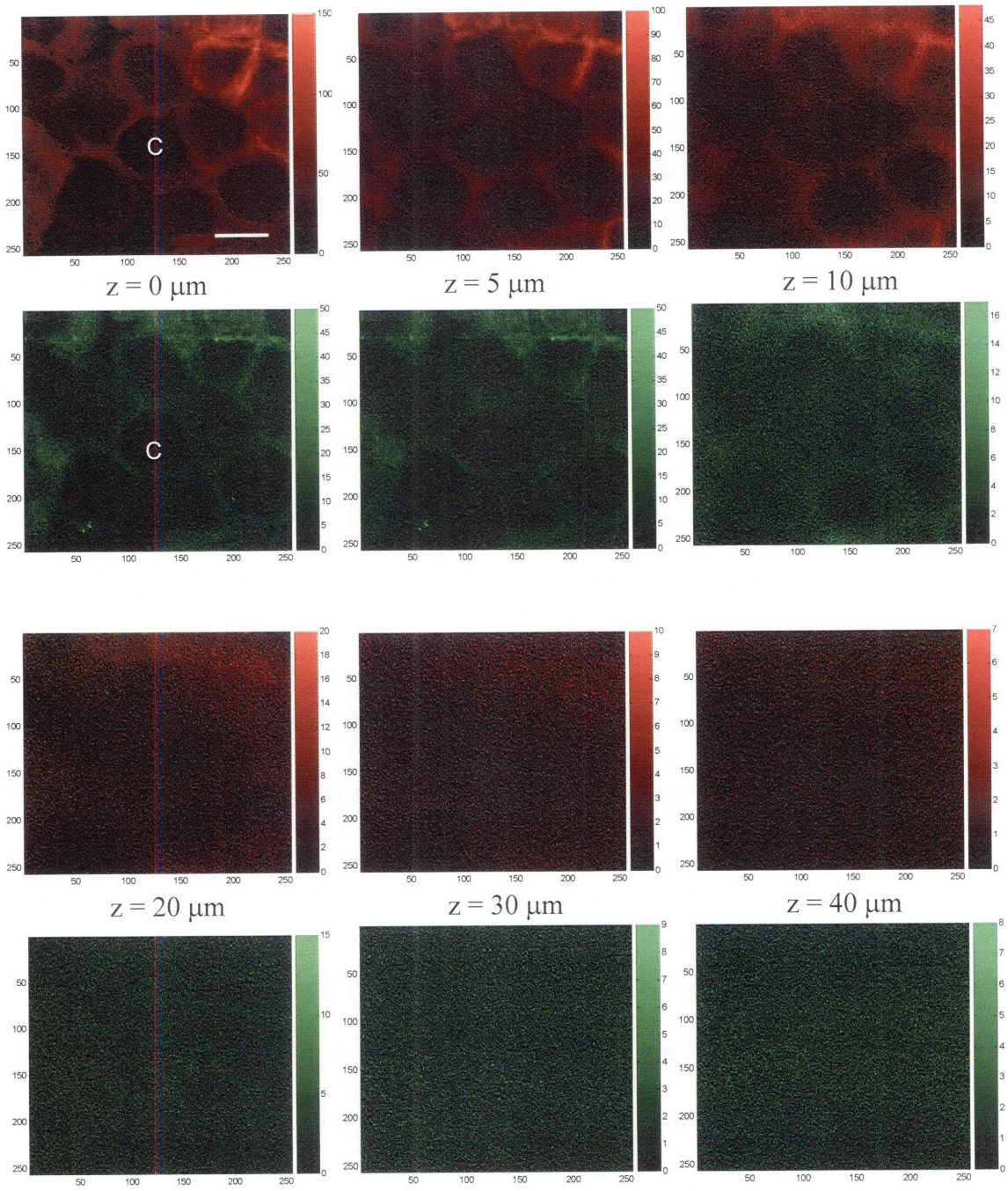

Figure 5-2: Dual-channel two-photon microscopy images of the hydrophilic probe sulforhodamine B (SRB) in untreated skin as a function of skin depth. Key: red – sulforhodamine B, green – skin auto-fluorescence, C – representative corneocyte. Image size: 120 μm x 120 μm. The horizontal white bar in the figure corresponding to z = 0 represents 24 μm.

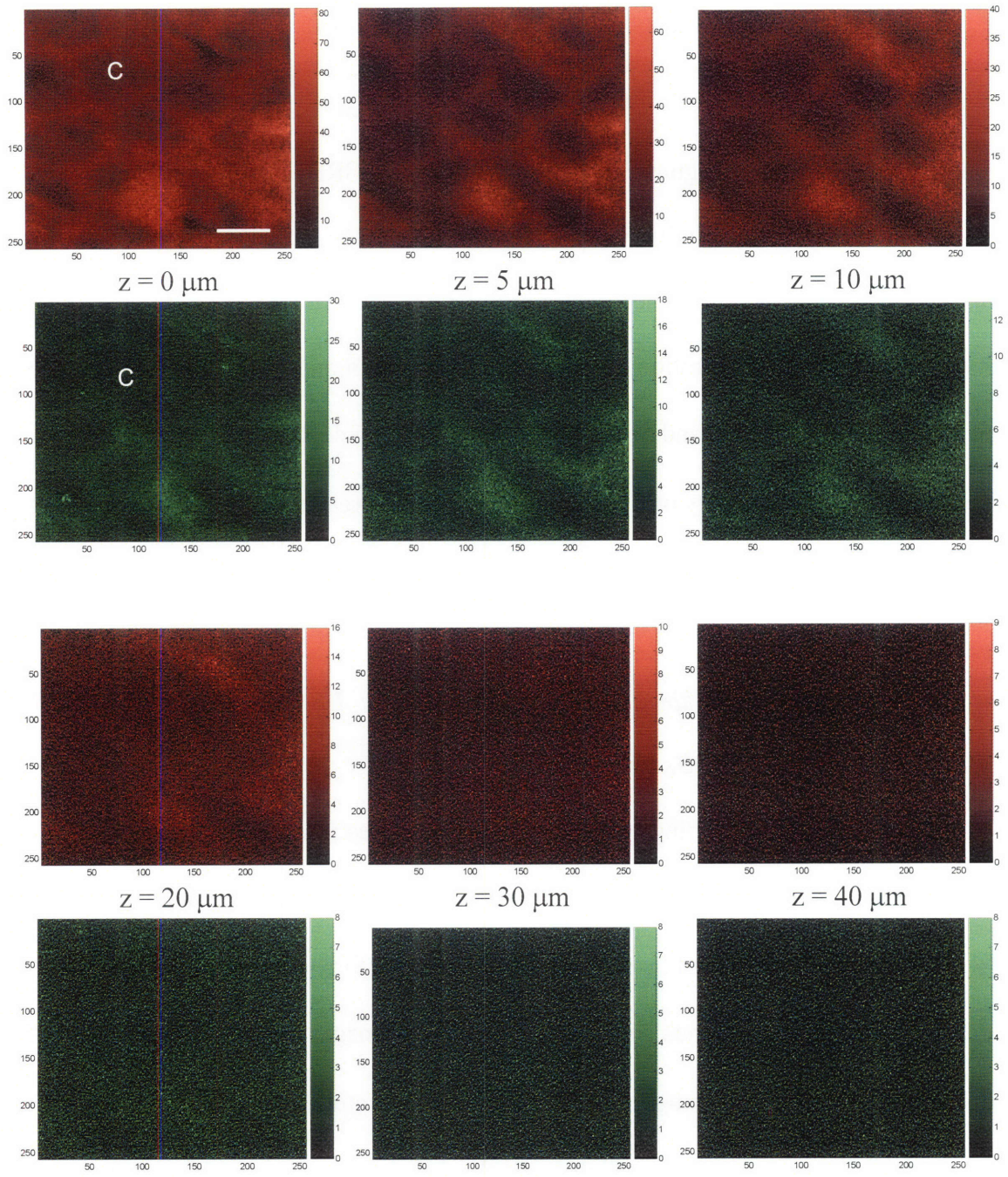

Figure 5-3: Dual-channel two-photon microscopy images of sulforhodamine B in SLS-treated skin as a function of skin depth. Key: red – sulforhodamine B, green – skin auto-fluorescence, C – representative corneocyte. Image size: 120 μm x 120 μm. The horizontal white bar represents 24 μm.

5.3.1.2 Qualitative Analysis of SRB Penetration in US-Treated and Untreated Skin

A qualitative analysis of Figure 5-2 for the delivery of SRB in untreated skin and of Figures 5-4 and 5-5 for the delivery of SRB in the non-LTRs and the LTRs of US-treated skin, respectively, reveals that the penetration of SRB in the LTRs of US-treated skin is much greater than the penetration of SRB in untreated skin and in the non-LTRs of US-treated skin. In Figures 5-2 and 5-4, SRB is visualized to a depth of 10 μm. At depths of 20 μm to 40 μm, the intensity of SRB in the LTRs of US-treated skin is higher relative to the intensity of SRB in untreated skin and in the non-LTRs of US-treated skin. This observation suggests that *SRB penetrates deeper into the skin in the LTRs of US-treated skin relative to untreated skin and to the non-LTRs of US-treated skin, where SRB penetration is restricted to the stratum corneum.*

In addition to suggesting that more SRB penetrates into the skin in the LTRs of US-treated skin, there is also a change in the structure of the skin below 20 μm in the LTRs of US-treated skin (see Figure 5-5). The structure of the corneocytes, which have a diameter of 30-40 μm in human skin, is observed in the images corresponding to z = 0, 5, and 10 μm in Figures 5-2 through 5-5. However, this structural pattern is not observed in Figure 5-5 in the images corresponding to depths greater than 20 μm. Instead, in Figure 5-5, the images corresponding to z = 30 μm and z = 40 μm contain a smaller pattern of dots (2 – 3 μm in diameter). These dots may represent the nuclei of cells in the stratum spinosum (SS) layer of the viable epidermis, which have similar dimensions.[31] This observation suggests that *SRB is able to penetrate into the viable epidermis within the LTRs of US-treated skin.*

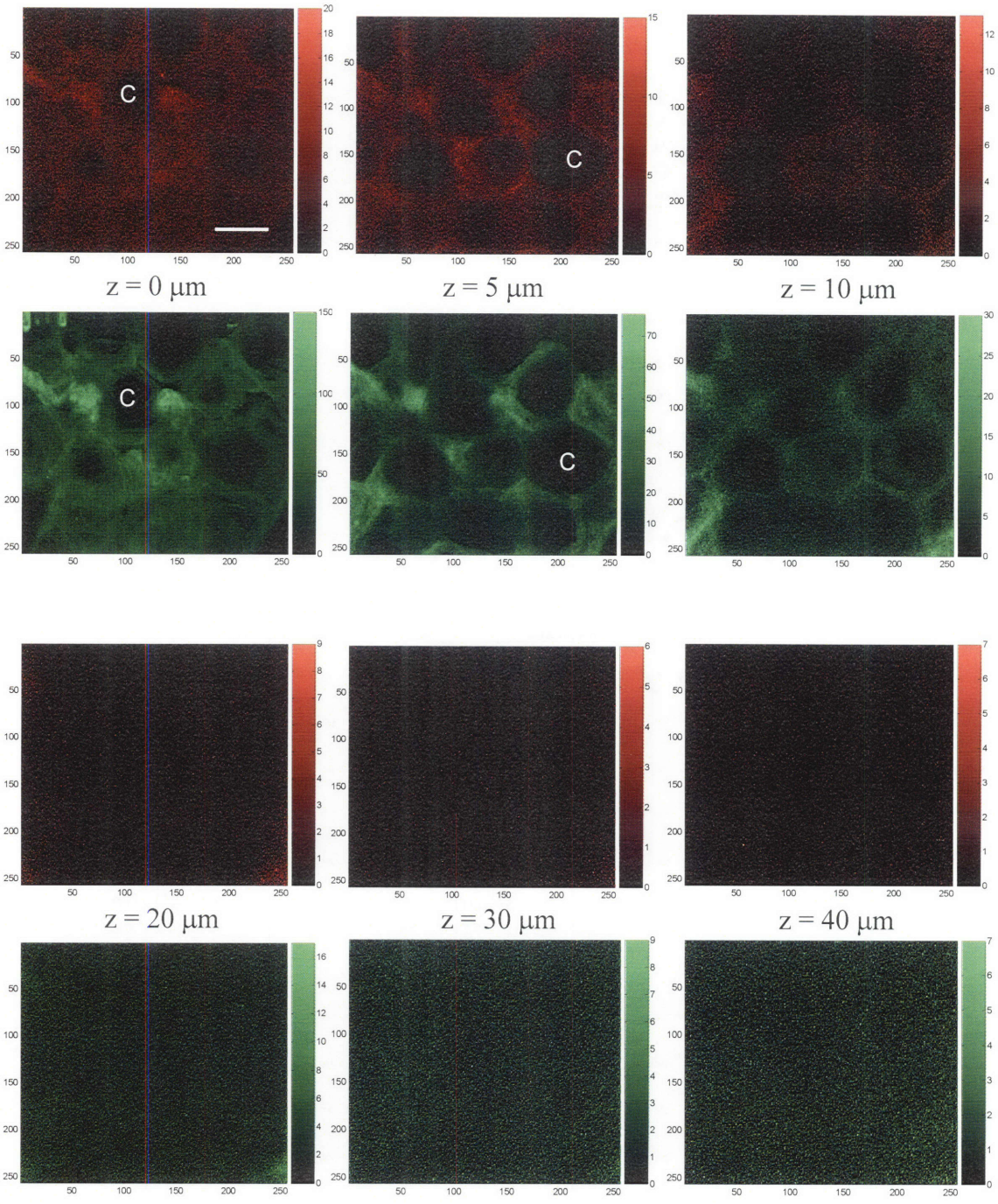

Figure 5-4: Dual-channel two-photon microscopy images of sulforhodamine B in the non-LTRs of US-treated skin as a function of skin depth. Key: red – sulforhodamine B, green – skin auto-fluorescence, C - representative corneocyte. Image size: 120 μm x 120 μm. The horizontal white bar represents 24 μm.

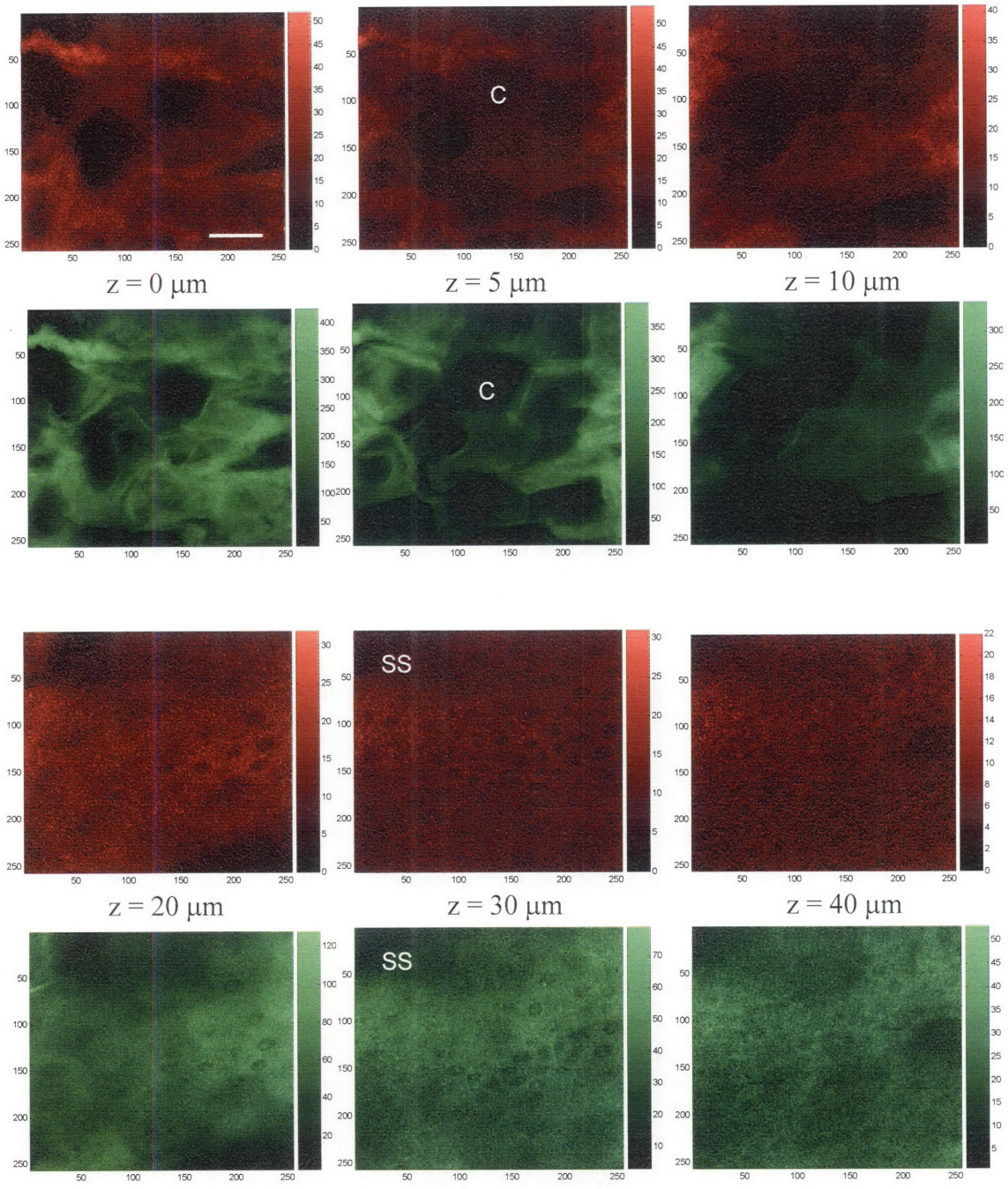

Figure 5-5: Dual-channel two-photon microscopy images of sulforhodamine B in the LTRs of US-treated skin as a function of skin depth. Key: red – sulforhodamine B, green – skin auto-fluorescence, C - representative corneocyte, SS – stratum spinosum. Image size: 120 μm x 120 μm. The horizontal white bar represents 24 μm.

As in the case of the delivery of SRB in SLS-treated skin and in untreated skin, there are qualitative differences in the amount of SRB present in the corneocytes at the surface of the LTRs of US-treated skin as compared to the amount of SRB in the corneocytes at the surface of untreated skin and at the surface of the non-LTRs of US-treated skin. In Figures 5-2 and 5-4, at z = 0 μm, the shapes of the corneocytes can be clearly observed in both the red channel and in the green channel images. However, in Figure 5-5, at z = 0 μm, the intensity of SRB is more uniformly distributed across the region of the skin that was imaged, making it difficult to observe individual corneocyte cells. This observation suggests that *more SRB penetrates into the corneocytes at the skin surface in the LTRs of US-treated skin relative to both untreated skin and to the non-LTRs of US-treated skin.* As z increases from z = 0 to 10 μm within the stratum corneum in Figure 5-5, the shape of the corneocytes becomes more distinct, since more SRB is present in the intercellular domain compared to the corneocytes. This result suggests that less SRB penetrates into the corneocytes in the deeper layers of the stratum corneum within the LTRs of US-treated skin, which agrees with claims made in previous preliminary studies on the penetration of SRB in US-treated skin.[15]

5.3.1.3 Qualitative Analysis of SRB Penetration in US/SLS-Treated and Untreated Skin

For SRB delivery in US/SLS-treated skin relative to SRB delivery in untreated skin, several observations can be made which are similar to the observations made for SRB delivery in US-treated skin relative to untreated skin. Comparing the dual-channel TPM images in Figures 5-2 and 5-6, the *penetration depth of SRB in the non-LTRs of US/SLS-treated skin is restricted to the stratum corneum*, which is similar to the penetration depth

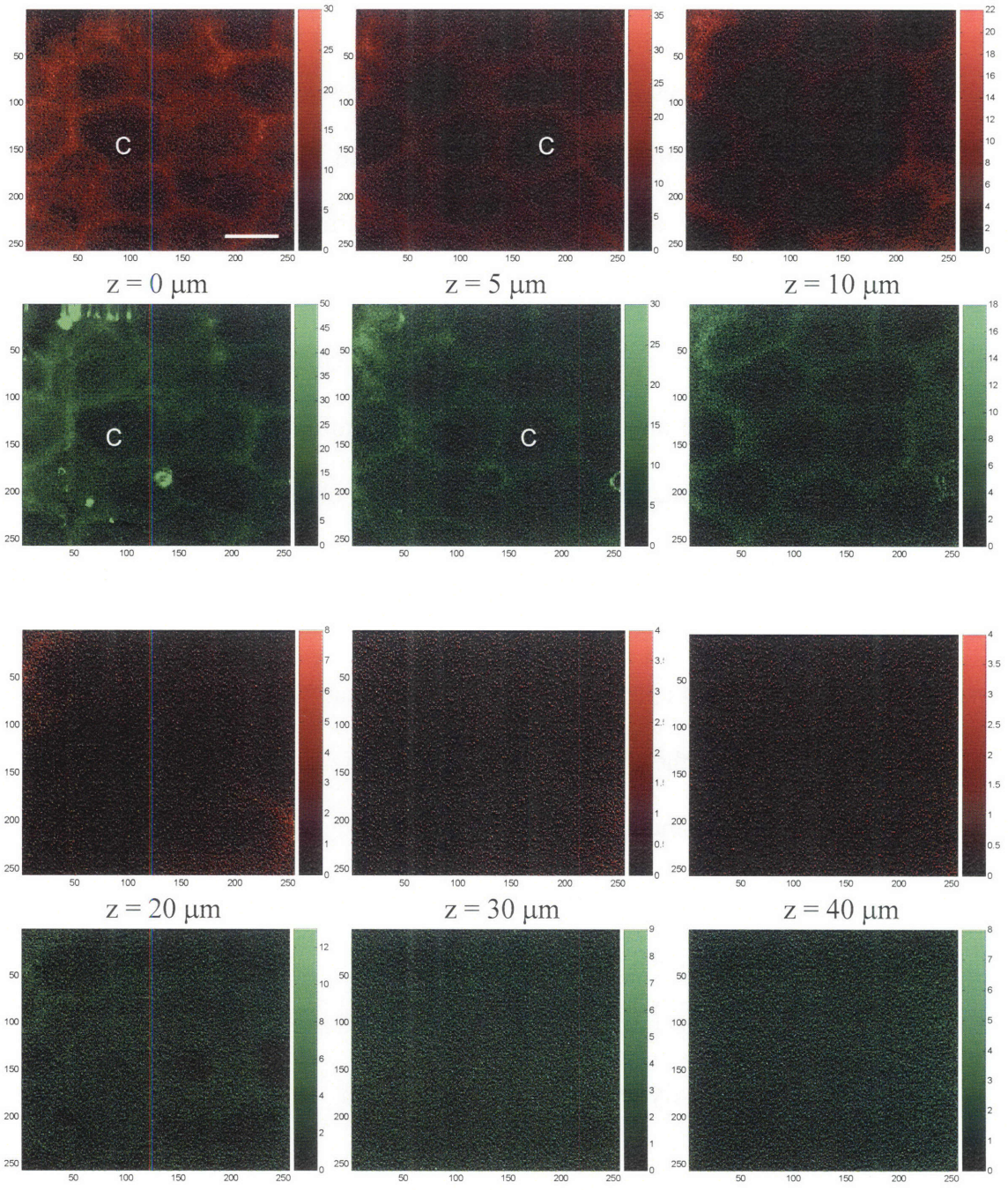

Figure 5-6: Dual-channel two-photon microscopy images of sulforhodamine B in the non-LTRs of US/SLS-treated skin as a function of skin depth. Key: red – sulforhodamine B, green – skin auto-fluorescence, C - representative corneocyte. Image size: 120 μm x 120 μm. The horizontal white bar represents 24 μm.

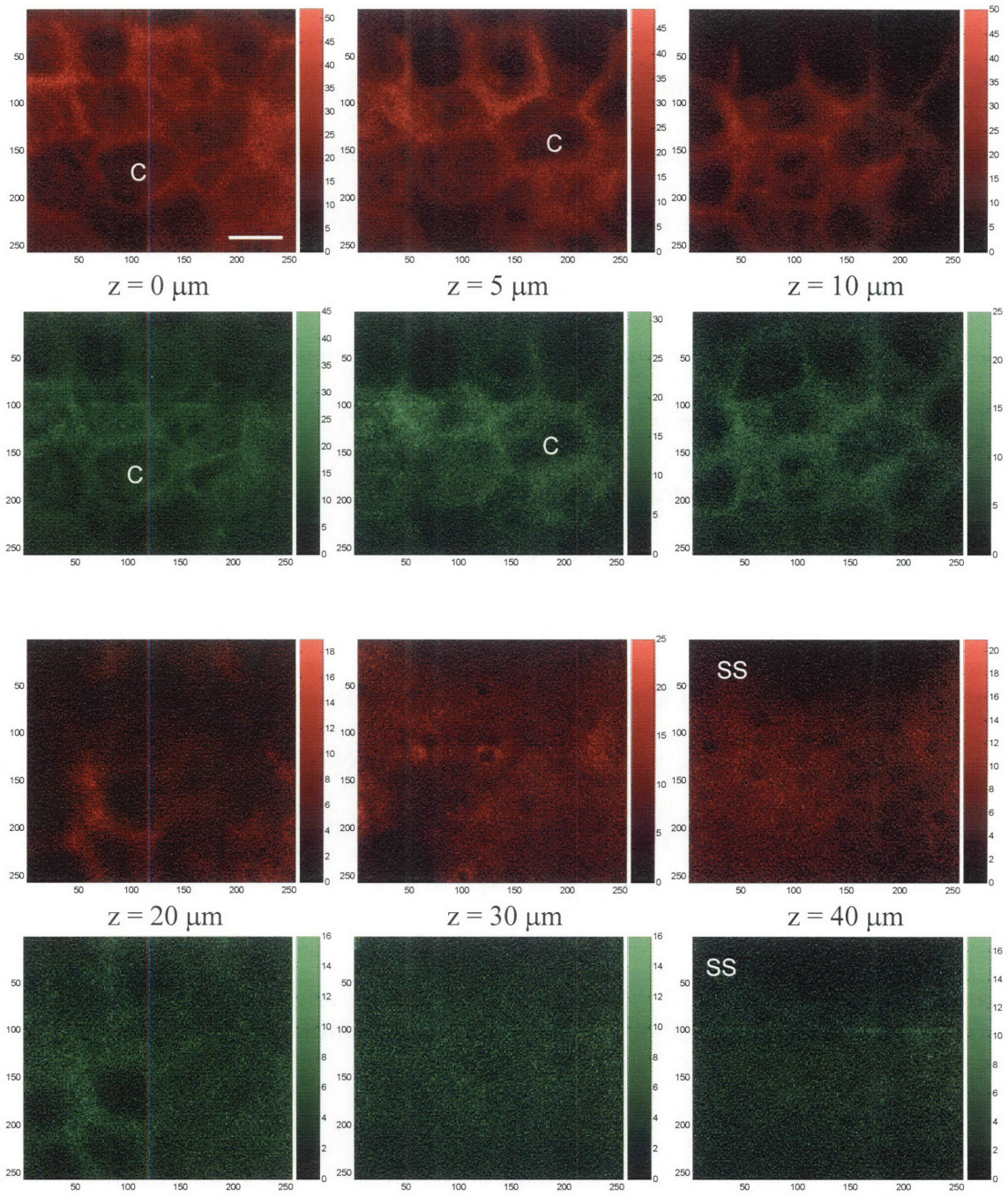

Figure 5-7: Dual-channel two-photon microscopy images of sulforhodamine B in the LTRs of US/SLS-treated skin as a function of skin depth. Key: red – sulforhodamine B, green – skin auto-fluorescence, C – representative corneocyte, SS – stratum spinosum. Image size: 120 μm x 120 μm. The horizontal white bar represents 24 μm.

of SRB in untreated skin. Comparing the dual-channel TPM images in Figure 5-8 with Figures 5-2 and 5-7, *SRB penetrates into the viable epidermis in the LTRs of US/SLS-treated skin* (see z = 40 μm in Figure 5-7). This result is consistent with previous macroscopic digital imaging measurements of the penetration depth of SRB in skin treated with ultrasound and SLS.[32] Furthermore, SRB appears to be more evenly distributed between the corneocytes and the intercellular regions at the skin surface in the LTRs of US/SLS-treated skin (see z = 0 μm in Figure 5-7) relative to the distribution of SRB at the skin surface of both untreated skin (see z = 0 μm in Figure 5-2) and the non-LTRs of US/SLS-treated skin (see z = 0 μm in Figure 5-6). This observation suggests that *more SRB penetrates into the corneocytes at the skin surface in the LTRs of US/SLS-treated skin relative to both untreated skin and to the non-LTRs of US/SLS-treated skin.* As z increases from z = 0 to z = 20 in Figure 5-7, the shapes of the corneocytes in the red channel (SRB) images become more distinct, suggesting that *less SRB penetrates into the corneocytes in the deeper layers of the stratum corneum within the LTRs of US/SLS-treated skin.*

5.3.1.4 Qualitative Analysis of RBHE Penetration in SLS-Treated and Untreated Skin

For the delivery of RBHE in untreated and in SLS-treated skin samples, a qualitative analysis of the dual-channel TPM images in Figures 5-8 and 5-9 reveals that the shapes of the corneocytes in the red channel (RBHE) images are very well defined in both the SLS-treated skin and the untreated skin, contrary to the case of SRB. This result suggests that *unlike the case of SRB, RBHE penetration into the corneocytes does not increase in SLS-treated skin relative to untreated skin.* Furthermore, the dual-channel TPM images

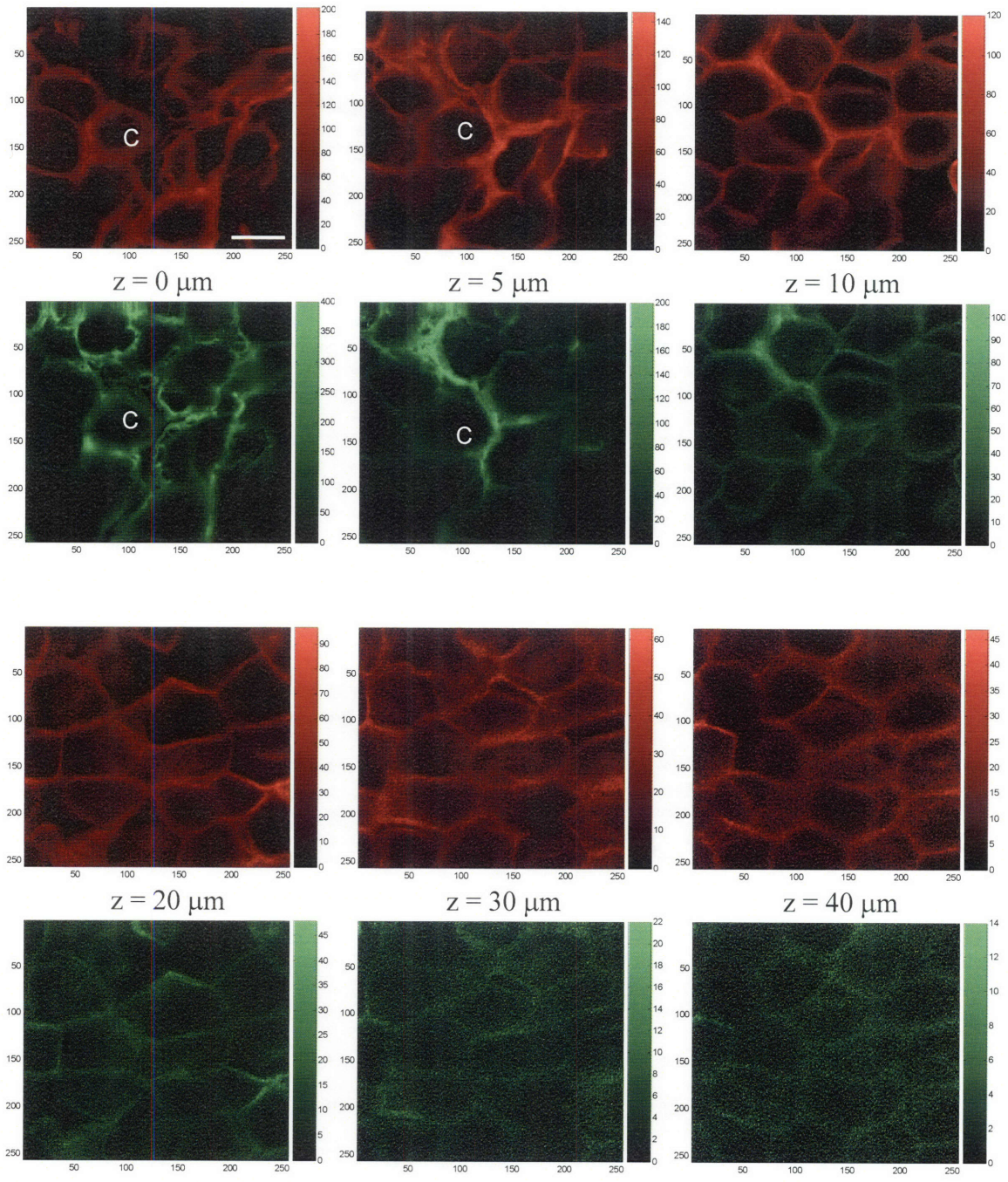

Figure 5-8: Dual-channel two-photon microscopy images of the hydrophobic fluorescent probe rhodamine B hexyl ester (RBHE) in untreated skin as a function of skin depth. Key: red – rhodamine B hexyl ester, green – skin auto-fluorescence, C - representative corneocyte. Image size: 120 μm x 120 μm. The horizontal white bar represents 24 μm.

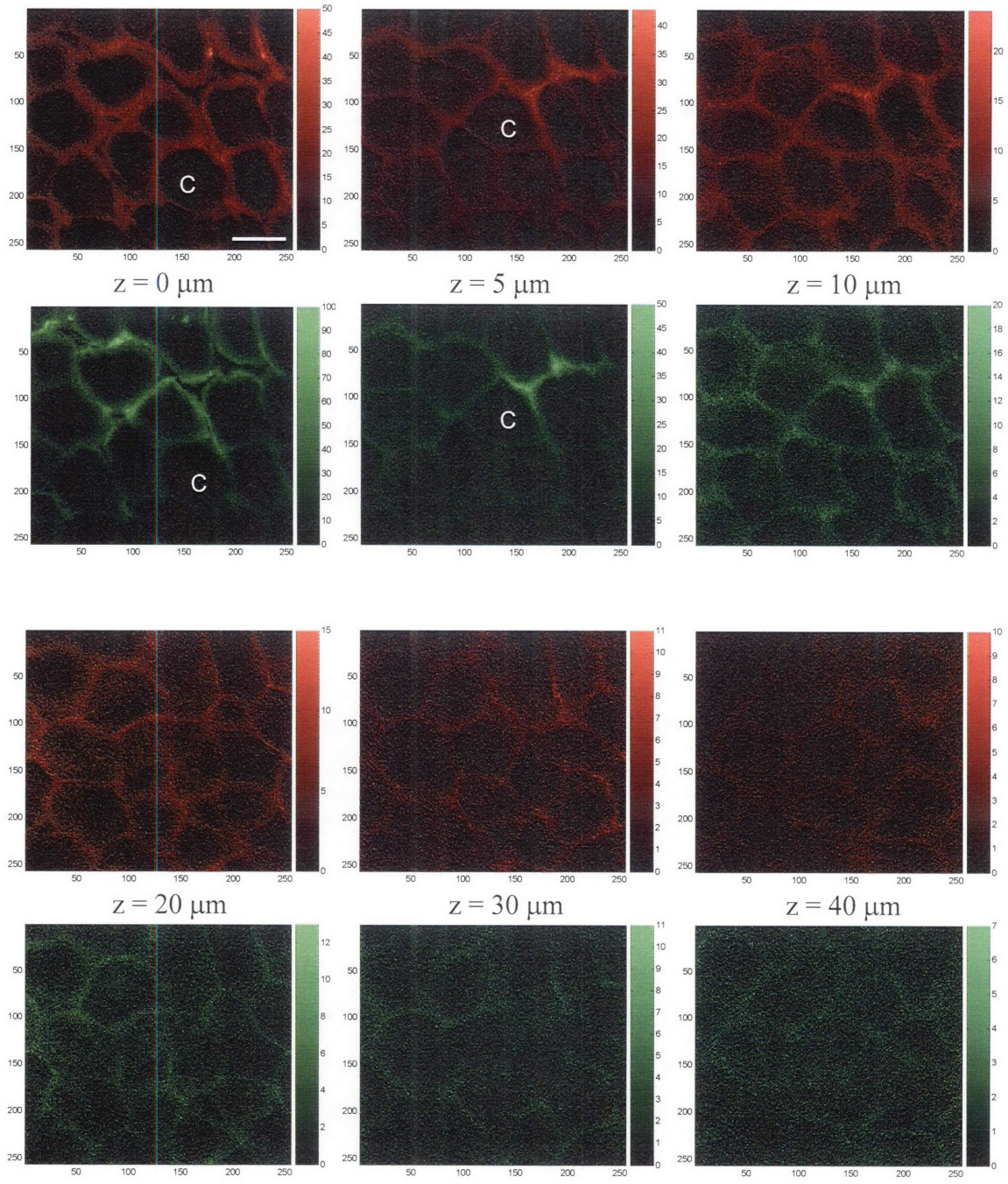

Figure 5-9: Dual-channel two-photon microscopy images of rhodamine B hexyl ester in SLS-treated skin as a function of skin depth. Key: red – rhodamine B hexyl ester, green – skin auto-fluorescence, C - representative corneocyte. Image size: 120 μm x 120 μm. The horizontal white bar represents 24 μm.

also demonstrate that RBHE is able to penetrate deeper into the skin, in both the untreated and the SLS-treated skin samples, relative to the case of SRB. In both Figures 5-8 and 5-9, an observable amount of RBHE is present at depths of up to 40 μm. However, this observed difference may be due solely to the existence of a thicker stratum corneum layer in the skin samples used for the delivery of RBHE in untreated and in SLS-treated skin relative to the skin samples used for the delivery of SRB. (Note that different skin samples were used for each case examined, so some variation in the stratum corneum thickness from sample to sample is possible.) In Figures 5-8 and 5-9, the shapes of the corneocytes are observed in the green channel images for the skin auto-fluorescence even at a depth of 40 μm. This is different from the case of SRB delivery in the LTRs of US-treated and US/SLS-treated skin, where SRB penetration is also observed up to depths of 40 μm (see Figures 5-5 and 5-7). For the case of SRB delivery in the LTRs of US-treated and US/SLS-treated skin, there is also an observed change in the structure of the skin at depths greater than 10 μm in Figure 5-5 and at depths greater than 20 μm in Figure 5-7, which indicates a transition into the viable epidermis (see Section 5.3.1.2 for details). Since there is no observable change in the structure of the skin in Figures 5-8 and 5-9 as the skin depth increases, it is still likely that *penetration of RBHE is restricted to the stratum corneum in both untreated skin and SLS-treated skin, similar to the case of SRB.*

5.3.1.5 Qualitative Analysis of RBHE Penetration in US-Treated and Untreated Skin

For the case of the delivery of RBHE in US-treated skin relative to the delivery of RBHE in untreated skin, there are many similarities with the delivery of SRB in US-treated skin.

First, LTRs are formed with RBHE as the model permeant in US-treated skin. This observation suggests that *LTR formation in skin treated with ultrasound does not depend on whether the model permeant is hydrophilic or hydrophobic.* Second, a comparison of Figures 5-8 (untreated skin), 5-10 (the non-LTRs in US-treated skin), and 5-11 (the LTRs in US-treated skin), indicates that, similar to the case of SRB delivery, there is penetration of RBHE into the viable epidermis within the LTRs of US-treated skin, while the penetration of RBHE in the non-LTRs of US-treated skin and in untreated skin is confined solely to the stratum corneum. This observation suggests that *the penetration of the model permeants into the viable epidermis within the LTRs of US-treated skin also does not depend on whether the model permeant is hydrophilic or hydrophobic.*

Finally, the penetration of RBHE into the corneocytes of the stratum corneum for untreated skin and for the non-LTRs and the LTRs of US-treated skin appears to be similar to the penetration of SRB into the corneocytes of the stratum corneum for the same skin samples. Specifically, a qualitative analysis of the dual-channel TPM images in Figures 5-8 and 5-10 reveals that the shapes of the corneocytes in the red channel (RBHE) images are very well-defined at the skin surface ($z = 0$ μm) in both the non-LTRs of US-treated skin and in the untreated skin. On the other hand, in the image of the skin surface for the LTRs of US-treated skin (see $z = 0$ μm in Figure 5-11) the shapes of the corneocytes are more difficult to identify, since RBHE is distributed more evenly between the corneocytes and the intercellular regions. It also appears that, within the LTRs of US-treated skin, the shape of the corneocytes is more easily identified as the skin depth is increased (see $z = 0$, 5, 10, and 20 μm in Figure 5-11), indicating that less RBHE penetrates into the corneocytes in the deeper layers of the stratum corneum within

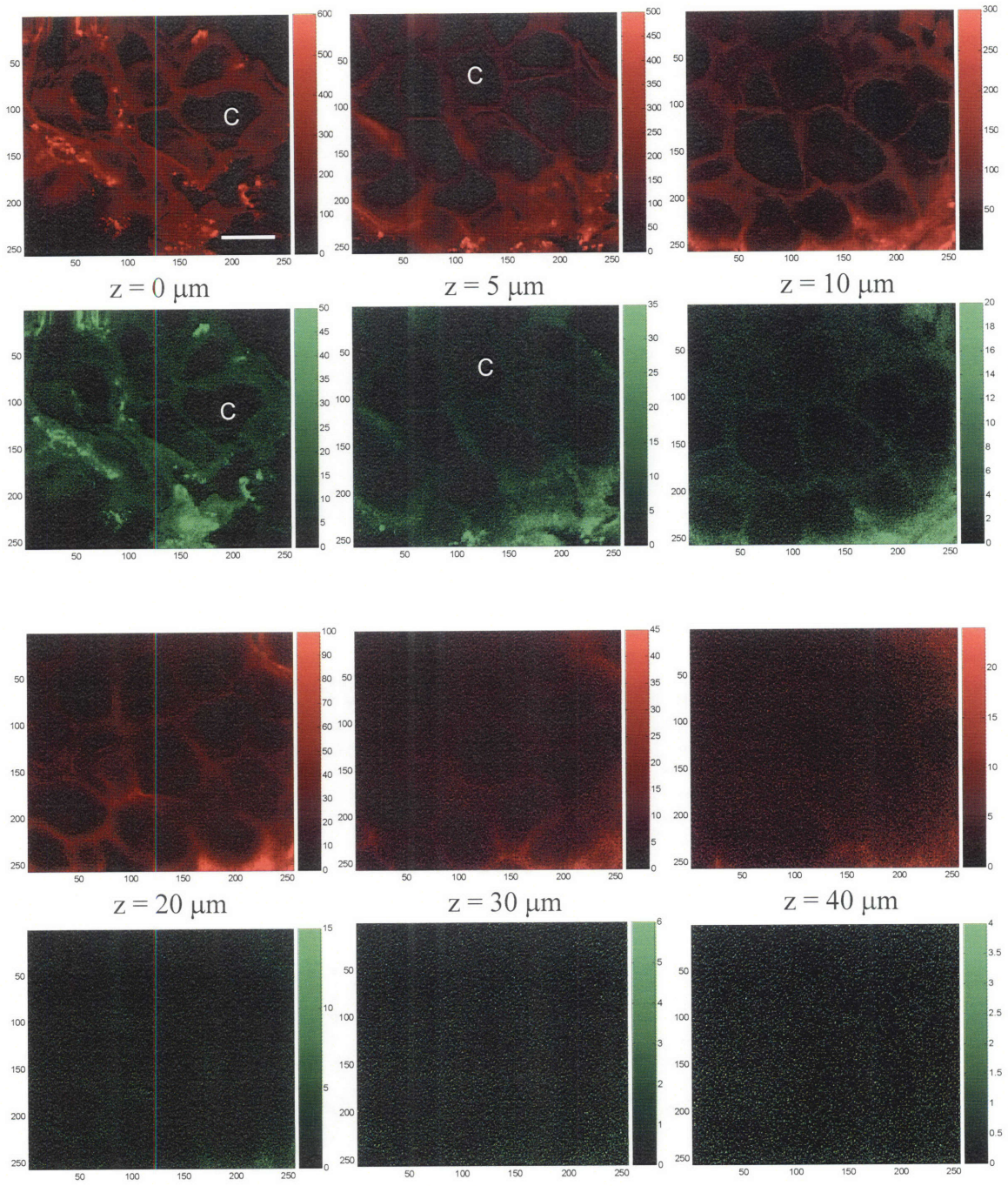

Figure 5-10: Dual-channel two-photon microscopy images of rhodamine B hexyl ester in the non-LTRs of US-treated skin as a function of skin depth. Key: red – rhodamine B hexyl ester, green – skin auto-fluorescence, C - representative corneocyte. Image size: 120 μm x 120 μm. The horizontal white bar represents 24 μm.

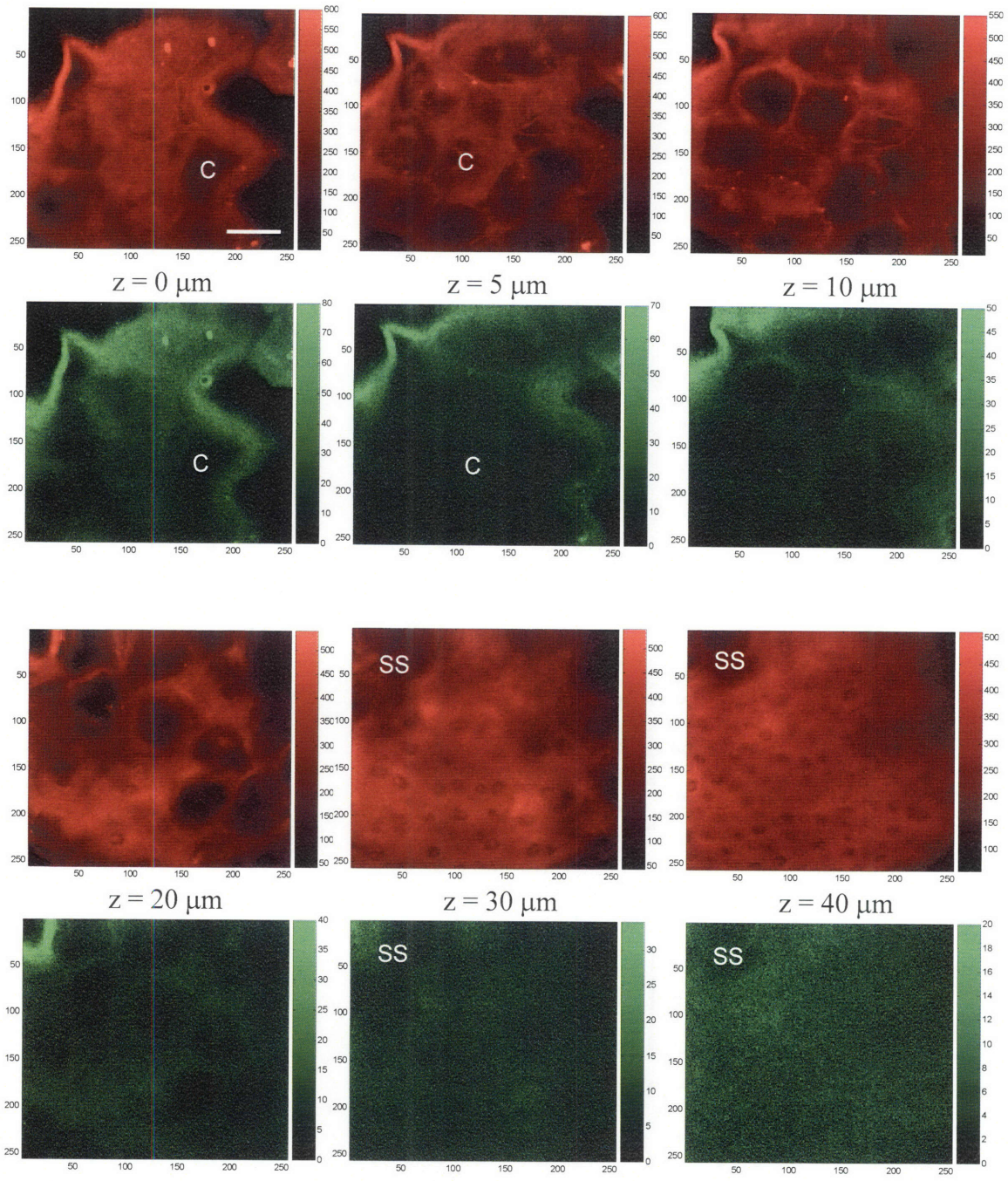

Figure 5-11: Dual-channel two-photon microscopy images of rhodamine B hexyl ester in the LTRs of US-treated skin as a function of skin depth. Key: red – rhodamine B hexyl ester, green – skin auto-fluorescence, C – representative corneocyte, SS – stratum spinosum. Image size: 120 μm x 120 μm. The horizontal white bar represents 24 μm.

the LTRs of US-treated skin, similar to the case of SRB penetration in the LTRs of US-treated skin (see Figure 5-5). This observation suggests that *the level of penetration of the model permeants into the corneocytes of US-treated skin also does not depend on whether the model permeant is hydrophilic or hydrophobic.* Taken together, these three observations further suggest that *the formation of LTRs in US-treated skin, the penetration of the model permeants into the viable epidermis within the LTRs, and the level of penetration of the model permeants into the corneocytes of the stratum corneum within the LTRs depend solely on the effects of localized perturbations in the skin structure due to the ultrasound treatment.*

5.3.1.6 Qualitative Analysis of RBHE Penetration in US/SLS-Treated and Untreated Skin

For the delivery of RBHE in US/SLS-treated skin relative to untreated skin, there are, again, many similarities to the delivery of RBHE in US-treated skin relative to untreated skin. Comparing the dual-channel TPM images for the delivery of RBHE in untreated skin (see Figure 5-8) with the dual-channel images for the delivery of RBHE in the non-LTRs and the LTRs of US/SLS-treated skin (see Figures 5-12 and 5-13, respectively), *RBHE penetrates into the viable epidermis in the LTRs of US/SLS-treated skin, while RBHE penetration is confined solely to the stratum corneum in both untreated skin and in the non-LTRs of US/SLS-treated skin.* Furthermore, RBHE appears to be more evenly distributed between the corneocytes and the intercellular regions at the skin surface in the LTRs of US/SLS-treated skin (see $z = 0$ μm in Figure 5-13) relative to the distribution of SRB at the skin surface of both untreated skin (see $z = 0$ μm in Figure 5-8) and the non-LTRs of US/SLS-treated skin (see $z = 0$ μm in Figure 5-12). This observation suggests

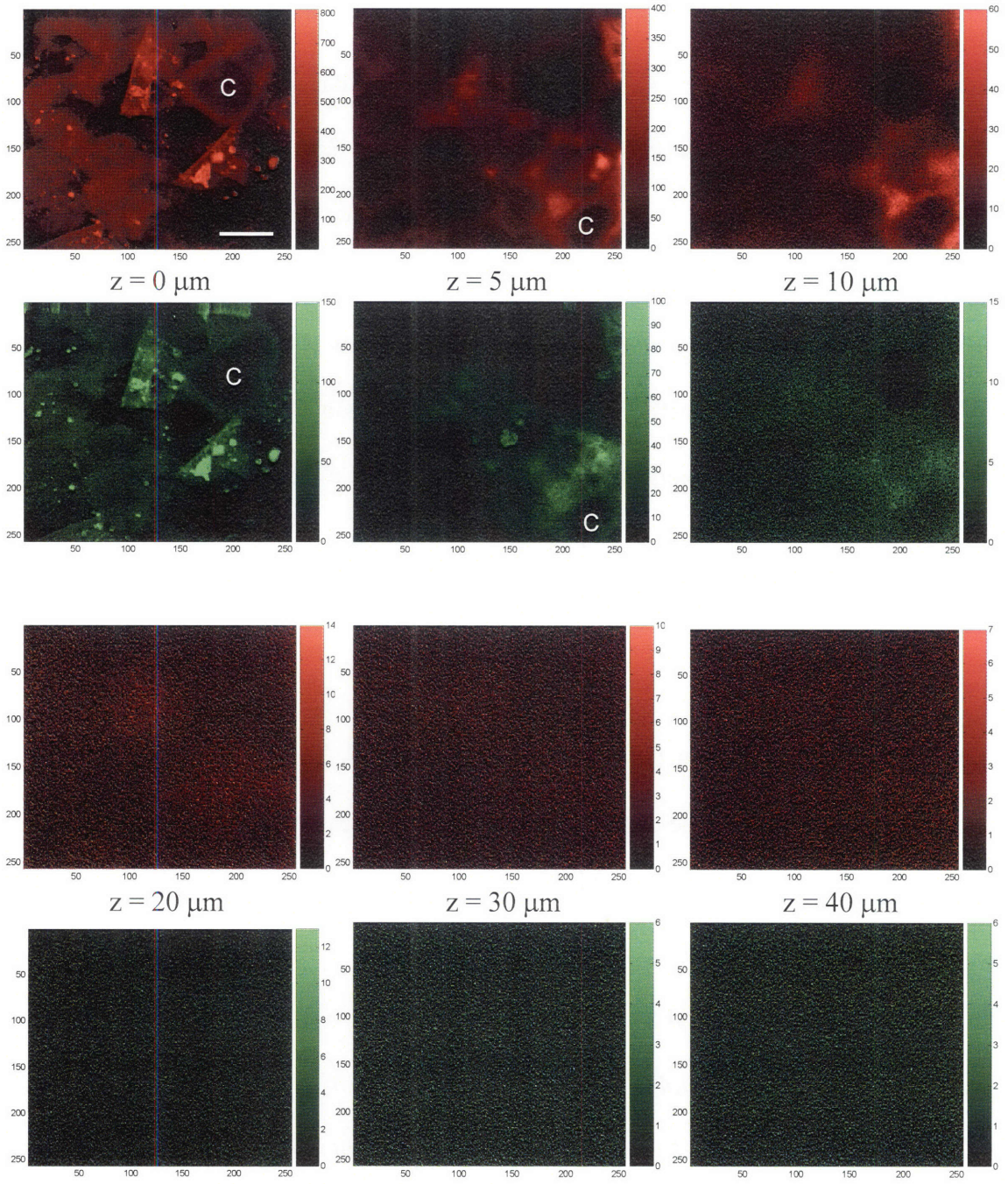

Figure 5-12: Dual-channel two-photon microscopy images of rhodamine B hexyl ester in the non-LTRs of US/SLS-treated skin as a function of skin depth. Key: red – rhodamine B hexyl ester, green – skin auto-fluorescence, C - representative corneocyte. Image size: 120 μm x 120 μm. The horizontal white bar represents 24 μm.

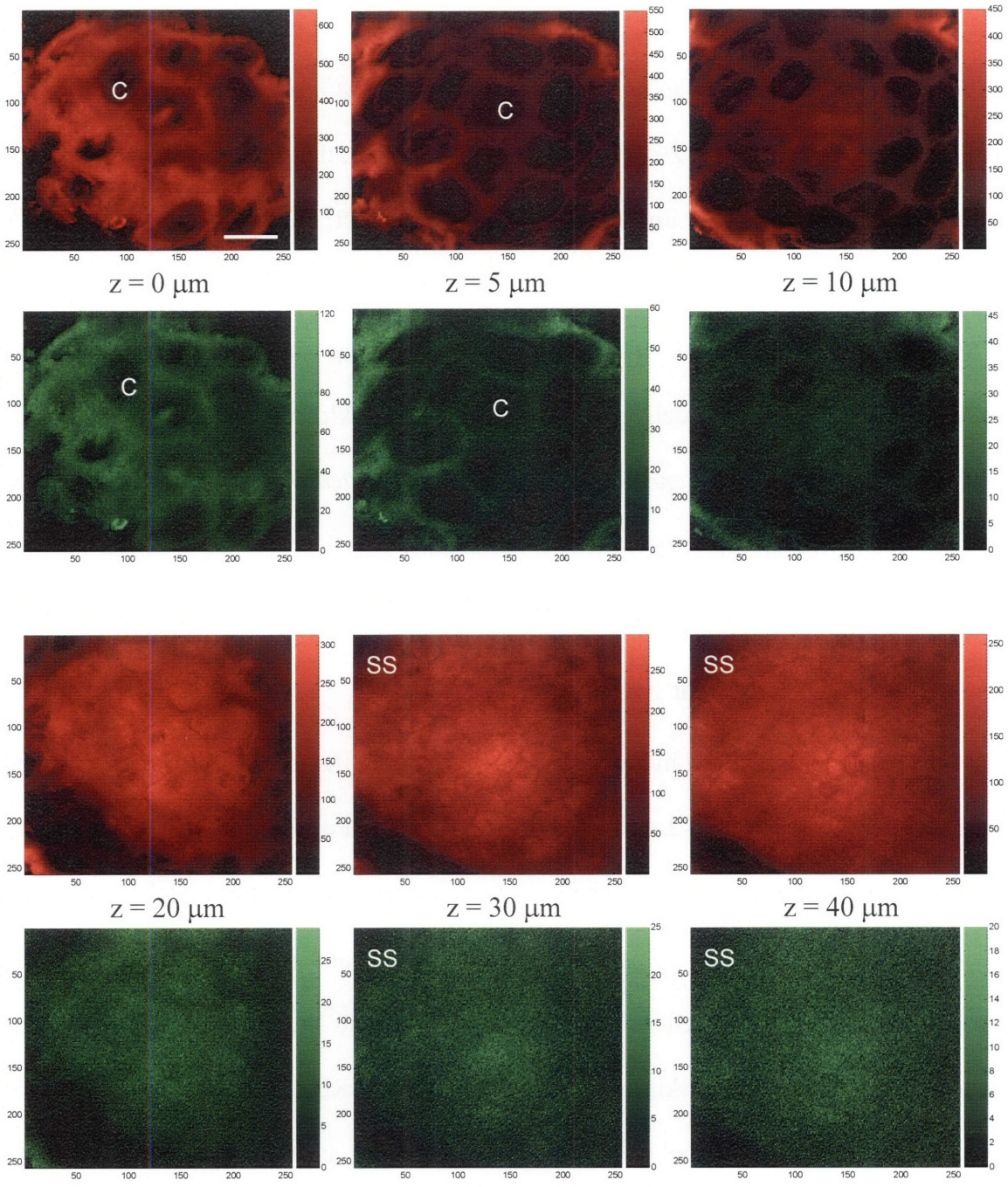

Figure 5-13: Dual-channel two-photon microscopy images of rhodamine B hexyl ester in the LTRs of US/SLS-treated skin as a function of skin depth. Key: red – rhodamine B hexyl ester, green – skin auto-fluorescence, C – representative corneocyte, SS – stratum spinosum. Image size: 120 μm x 120 μm. The horizontal white bar represents 24 μm.

that *more RBHE penetrates into the corneocytes at the skin surface in the LTRs of US/SLS-treated skin relative to both untreated skin and the non-LTRs of US/SLS-treated skin.* As z is increased from z = 0 to z = 10 in Figure 5-13, the shapes of the corneocytes in the red channel (RBHE) images become more distinct, suggesting that *less RBHE penetrates into the corneocytes in the deeper layers of the stratum corneum within the LTRs of US/SLS-treated skin.* These observations are also similar to the observations made for the case of SRB delivery in US/SLS-treated skin relative to untreated skin, suggesting that *the observed enhancements in US/SLS-treated skin are independent of the hydrophobicity/hydrophilicity of the model permeants.*

5.3.1.7 Summary of the Qualitative Investigations of the Dual-Channel TPM Images for SRB and RBHE

From the analyses conducted in Sections 5.3.1.1 – 5.3.1.6, the following key observations can be made from Figures 5-2 through 5-13: 1) formation of the LTRs does not depend on the presence of the chemical enhancer, SLS, or on whether the model permeant is hydrophilic or hydrophobic, 2) penetration of both SRB and RBHE is restricted to the stratum corneum in untreated skin, SLS-treated skin, and the non-LTRs of both US-treated and US/SLS-treated skin, 3) penetration of both SRB and RBHE into the viable epidermis is observed in the LTRs of both US-treated and US/SLS-treated skin, 4) increased penetration of SRB into the corneocytes at the skin surface is observed in SLS-treated skin and in the LTRs of US-treated and US/SLS-treated skin, while increased penetration of RBHE into the corneocytes at the skin surface is observed in the LTRs of US-treated and US/SLS-treated skin, and 5) the increased penetration of both SRB and

RBHE into the corneocytes of the stratum corneum appears to decrease as a function of skin depth in the LTRs of both US-treated and US/SLS-treated skin.

5.3.2 Quantitative Analysis of SRB and RBHE Delivery in Untreated, SLS-Treated, US-Treated, and US/SLS-Treated Skin

5.3.2.1 Statistical Analysis of the Fluorescence Intensity Profiles for SRB

Figure 5-14 shows the average fluorescence intensity profiles of the hydrophilic model permeant, SRB, obtained using the methods discussed in Section 5.2.7.1. In each figure (5-14a – 5-14c), the fluorescence intensity of SRB is plotted on the y-axis and the depth from the skin surface (at $z = 0$ μm), in μm, is plotted on the x-axis. The error bars represent one standard deviation in the average value of the SRB fluorescence intensity (for clarity, only the upper error bars are shown in Figures 5-14a – 5-14c). In addition, the results of the statistical analysis of the fluorescence permeant intensity profiles are also shown in Figure 5-14. Specifically, a bar (solid or dashed) with a single asterisk (*) indicates the range over which the average fluorescence intensity values from the enhanced skin sample are statistically different ($p<0.05$) from the average fluorescence intensity values from the untreated skin samples. A solid bar with a double asterisk (**) indicates the range over which the average fluorescence intensity values of the LTRs is statistically different ($p<0.05$) from the average fluorescence intensity values of the non-LTRs.

In Figure 5-14a, the SRB intensity profile in SLS-enhanced skin (open diamonds) is compared to the SRB intensity profile in untreated skin (black diamonds). As indicated by the solid bar with a single asterisk (*) in Figure 5-14a, there is a significant

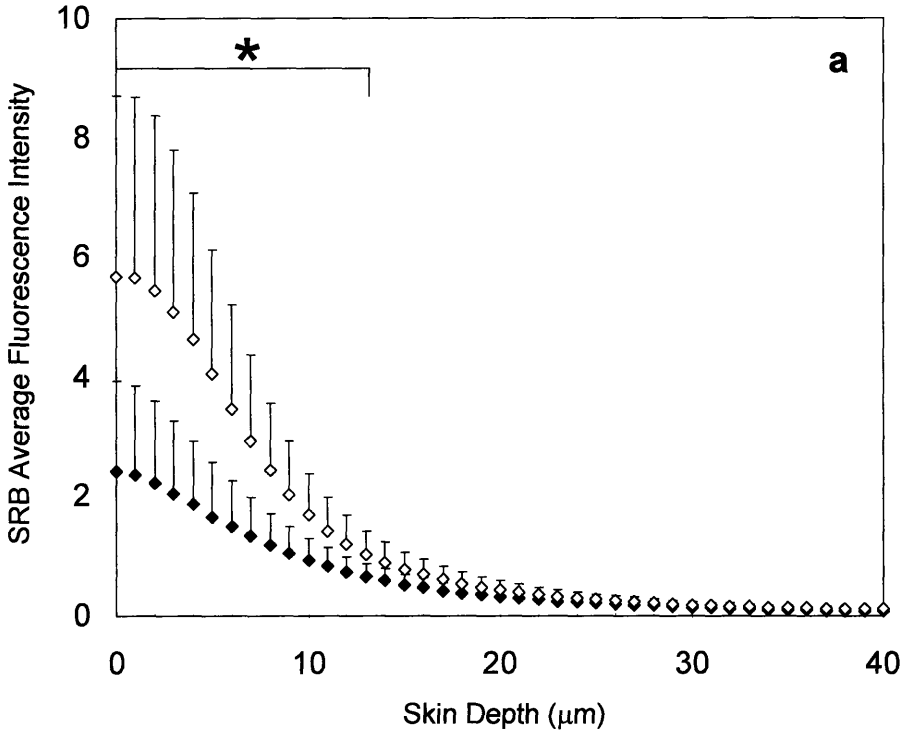

Figure 5-14: SRB fluorescence intensity profiles as a function of skin depth from the skin surface (at z = 0): (a) SLS-treated skin versus untreated skin, (b) the non-LTRs and the LTRs of US-treated skin versus untreated skin, and (c) the non-LTRs and the LTRs of US/SLS-treated skin versus untreated skin. Key: black diamonds – untreated skin samples, open diamonds – SLS-treated skin samples, open triangles – the non-LTRs, and open circles – the LTRs. Error bars represent one standard deviation in the average value of 5 – 7 skin samples. For clarity, only the upper error bars are shown. Single asterisks (*) indicate the region of significant difference ($p<0.05$) between SRB delivery in enhanced skin and in untreated skin. Double asterisks (**) indicate the region of significant difference ($p<0.05$) between SRB delivery in the non-LTRs and in the LTRs. In (c), the dashed line with the single asterisk (*) corresponds to the confidence interval for the non-LTRs.

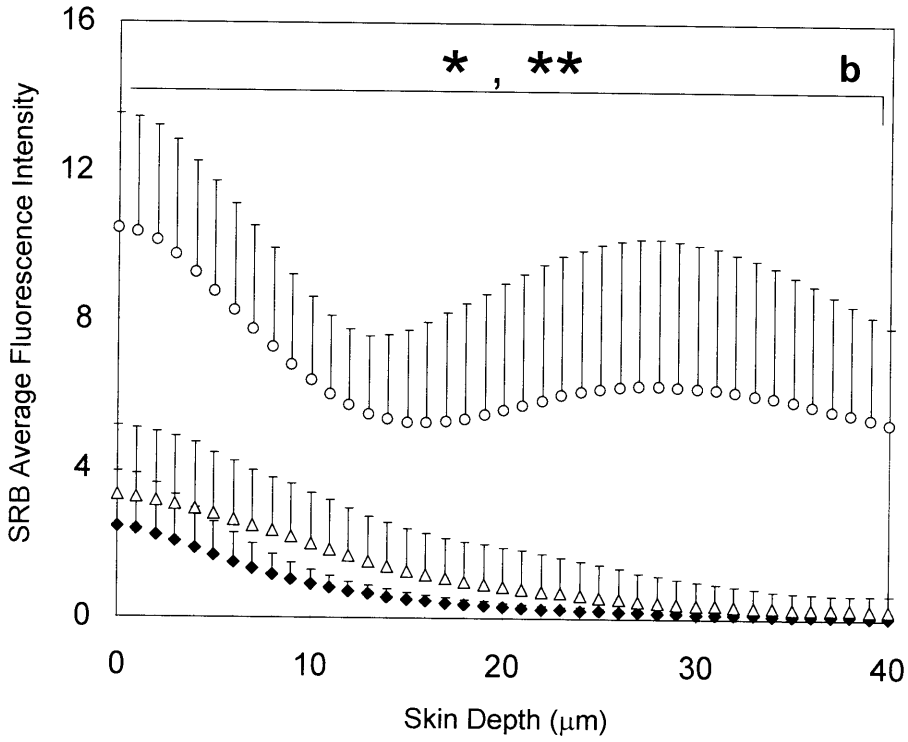
16
12
8
4
0
SRB Average Fluorescence Intensity
* , **
b
0
10
20
30
40
Skin Depth (μm)

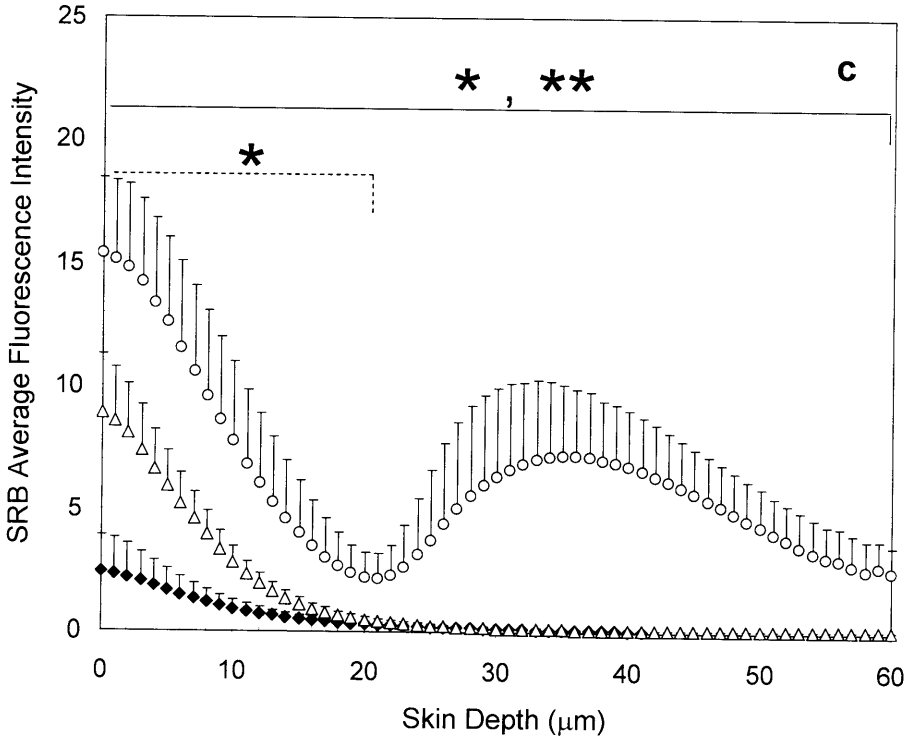
25
20
15
10
5
0
SRB Average Fluorescence Intensity
* , **
*
c
0
10
20
30
40
50
60
Skin Depth (μm)

indicates that *more SRB penetrates in the skin as a result of SLS-treatment of the skin relative to the case of untreated skin.* In addition, there is a sharp decrease in the average increase ($p<0.05$) in the intensity of SRB in the first 14 layers of the SLS-treated skin as compared to the intensity of SRB in the first 14 layers of the untreated skin. In addition, SRB fluorescence intensity decreases to near zero values over the first 20 layers of both SLS-treated and untreated skin, indicating that *the stratum corneum provides the primary barrier to the delivery of SRB in SLS-treated skin, similar to untreated skin.* Furthermore, there is little penetration of SRB into the skin deeper than 20 μm in both SLS-treated skin and untreated skin, confirming that *SRB penetration is restricted to the stratum corneum in SLS-treated and untreated skin.*

In Figure 5-14b, the SRB intensity profiles of the non-LTRs (open triangles) and of the LTRs (open circles) in US-enhanced skin are compared to the SRB intensity profile in untreated skin (black diamonds). As shown by the solid bar with a single asterisk (*) in Figure 5-14b, the intensity of SRB within the LTRs of US-treated skin is significantly greater ($p<0.05$) than the intensity of SRB in untreated skin up to a depth of 40 μm, indicating that *more SRB penetrates in the skin within the LTRs as a result of US-treatment of the skin relative to the case of untreated skin.* On the other hand, the intensity of SRB within the non-LTRs is not significantly greater ($p>0.05$) than the intensity of SRB in untreated skin up to a depth of 40 μm, and, therefore, no asterisked bar for the non-LTRs is reported in Figure 5-14b, indicating that *SRB penetration in the non-LTRs of US-treated skin is similar to SRB penetration in the case of untreated skin.* Furthermore, the intensity of SRB within the LTRs of US-treated skin is significantly greater ($p<0.05$) than the intensity of SRB in the non-LTRs of untreated skin up to a

depth of 40 μm, as shown by the solid bar with a double asterisk (**) in Figure 5-14b, indicating that *more SRB penetrates into the skin within the LTRs as a result of US-treatment of the skin relative to the non-LTRs of US-treated skin.* These results are in good agreement with previous studies examining the penetration of hydrophilic fluorescent permeants in US-treated skin,[15,33] and suggest that *ultrasound only perturbs discrete regions of the skin to enhance the transdermal penetration of model permeants.*

In Figure 5-14c, the SRB intensity profiles of the non-LTRs (open triangles) and of the LTRs (open circles) in US/SLS-enhanced skin are compared to the SRB intensity profile in untreated skin (black diamonds). Similar to the SRB delivery in US-treated skin, the intensity of SRB in the LTRs of US/SLS-treated skin is significantly ($p<0.05$) greater than the intensity of SRB in both untreated skin (see solid bar with a single asterisk (*) in Figure 5-14c) and the non-LTRs of US/SLS-treated skin (see solid bar with a double asterisk (**) in Figure 5-14c) over the depth of skin imaged. This result indicates that *more SRB penetrates into the skin within the LTRs as a result of US/SLS-treatment of the skin relative to both untreated skin and the non-LTRs of US/SLS-treated skin.* Contrary to the SRB delivery in US-treated skin, the intensity of SRB in the first 21 layers of the non-LTRs of US/SLS-treated skin is also significantly greater ($p<0.05$) than the intensity of SRB in the first 21 layers of untreated skin (see dashed bar with a single asterisk (*) in Figure 5-14c). This result indicates that *more SRB penetrates into the skin within the non-LTRs as a result of US/SLS-treatment of the skin relative to untreated skin.* Furthermore, the intensity of SRB in the non-LTRs of US/SLS-treated skin is not significantly ($p>0.05$) different from the intensity of SRB in untreated skin at depths greater than 21 μm (i.e. deeper than the average stratum corneum depth), indicating that

the depth of SRB penetration in the non-LTRs of US/SLS-treated skin is similar to the depth of SRB penetration in untreated skin. This result confirms that *SRB penetration in the non-LTRs of US/SLS-treated skin is confined solely to the stratum corneum, while SRB penetration in the LTRs of US/SLS-treated skin extends into the viable epidermis.* Combining the results from the depth and intensity of SRB delivered into the LTRs and the non-LTRs of US/SLS-treated skin relative to untreated skin, one may conclude that *two levels of skin perturbation take place in skin treated simultaneously with ultrasound and the chemical enhancer, SLS.* This result independently confirms the presence of two levels of enhancement in skin treated simultaneously with ultrasound and SLS made in Chapter 4 using skin electrical resistivity measurements.

5.3.2.2 Statistical Analysis of the Fluorescence Intensity Profiles for RBHE

Figure 5-15 shows the average fluorescence intensity profiles of the hydrophobic model permeant, RBHE, obtained using the methods discussed in Section 5.2.7.1. In each figure (5-15a – 5-15c), the fluorescence intensity of RBHE is plotted on the y-axis and the depth from the skin surface (at $z = 0$ μm), in μm, is plotted on the x-axis. The error bars represent one standard deviation in the average value of the RBHE fluorescence intensity (again, for clarity, only the upper error bars are shown in Figures 5-15a – 5-15c). Specifically, a bar (solid or dashed) with a single asterisk (*) indicates the range over which the average fluorescence intensity values from the enhanced skin sample are statistically different ($p<0.05$) from the average fluorescence intensity values from the untreated skin samples. A solid bar with a double asterisk (**) indicates the range over

which the average fluorescence intensity values of the LTRs was statistically different ($p<0.05$) from the average fluorescence intensity values of the non-LTRs.

In Figure 5-15a, the RBHE intensity profile in SLS-enhanced skin (open diamonds) is compared to the RBHE intensity profile in untreated skin (black diamonds). There is a significant increase ($p<0.05$) in the intensity of RBHE in the first 40 layers of SLS-treated skin below the skin surface compared to the intensity of RBHE in the first 40 layers of untreated skin below the skin surface (see solid bar with a single asterisk (*) in Figure 5-15a). The RBHE intensity curves for the SLS-treated skin and for the untreated skin decrease toward zero intensity in the region in which the stratum corneum is present (for the location of the stratum corneum in untreated and SLS-treated skin see $z = 0$ μm – 40 μm in Figures 5-8 and 5-9). Therefore, this result suggests that *RBHE penetration is restricted to the stratum corneum in SLS-treated and untreated skin*, similar to the case of SRB delivery in SLS-treated and untreated skin.

In Figure 5-15b, the RBHE intensity profiles of the non-LTRs (open triangles) and of the LTRs (open circles) in US-enhanced skin are compared to the RBHE intensity profile in untreated skin (black diamonds). Similar to the SRB delivery in US-treated skin, the intensity of RBHE in the LTRs of US-treated skin was found to be significantly ($p<0.05$) greater than the intensity of RBHE in both untreated skin (see solid bar with a single asterisk (*) in Figure 5-15b) and the non-LTRs of US/SLS-treated skin (see solid bar with a double asterisk (**) in Figure 5-15b) over the depth of skin imaged. This result indicates that *more RBHE penetrates into both the stratum corneum and the viable epidermis within the LTRs as a result of US-treatment of the skin relative to both*

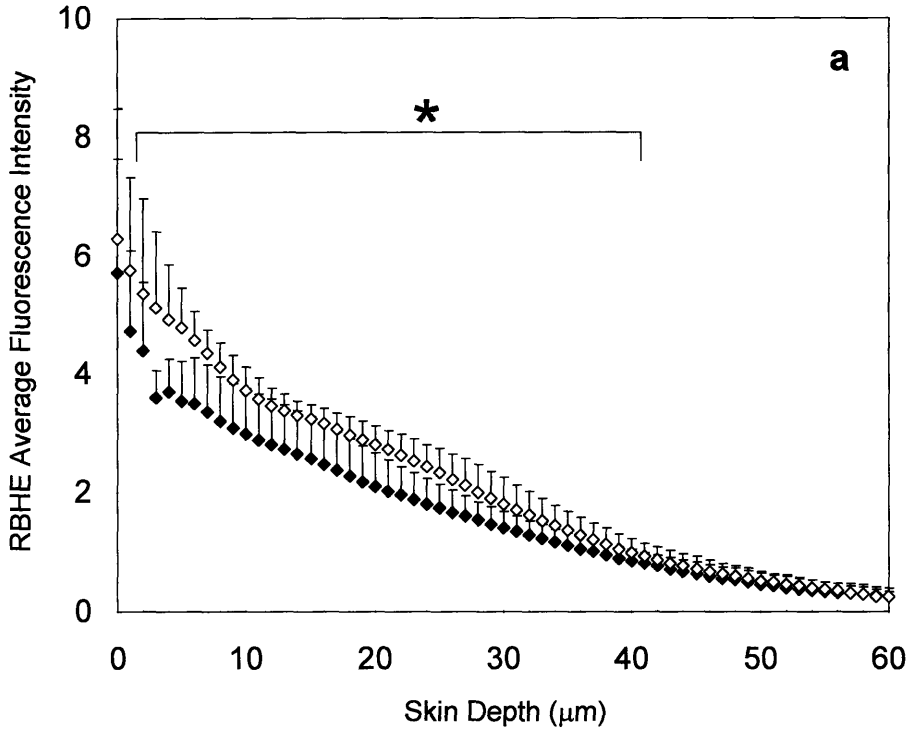

Figure 5-15: RBHE fluorescence intensity profiles as a function of skin depth from the skin surface (at z = 0): (a) SLS-treated skin versus untreated skin, (b) the non-LTRs and the LTRs of US-treated skin versus untreated skin, and (c) the non-LTRs and the LTRs of US/SLS-treated skin versus untreated skin. Key: black diamonds – untreated skin samples, open diamonds – SLS-treated skin samples, open triangles – the non-LTRs, and open circles – the LTRs. Error bars represent one standard deviation in the average value of 5 – 7 skin samples. For clarity, only the upper error bars are shown. Single asterisks (*) indicate the region of significant difference ($p<0.05$) between RBHE delivery in enhanced skin and in untreated skin. Double asterisks (**) indicate the region of significant difference ($p<0.05$) between RBHE delivery in the non-LTRs and in the LTRs. In (b) and (c), the dashed line with the single asterisk (*) corresponds to the confidence interval for the non-LTRs.

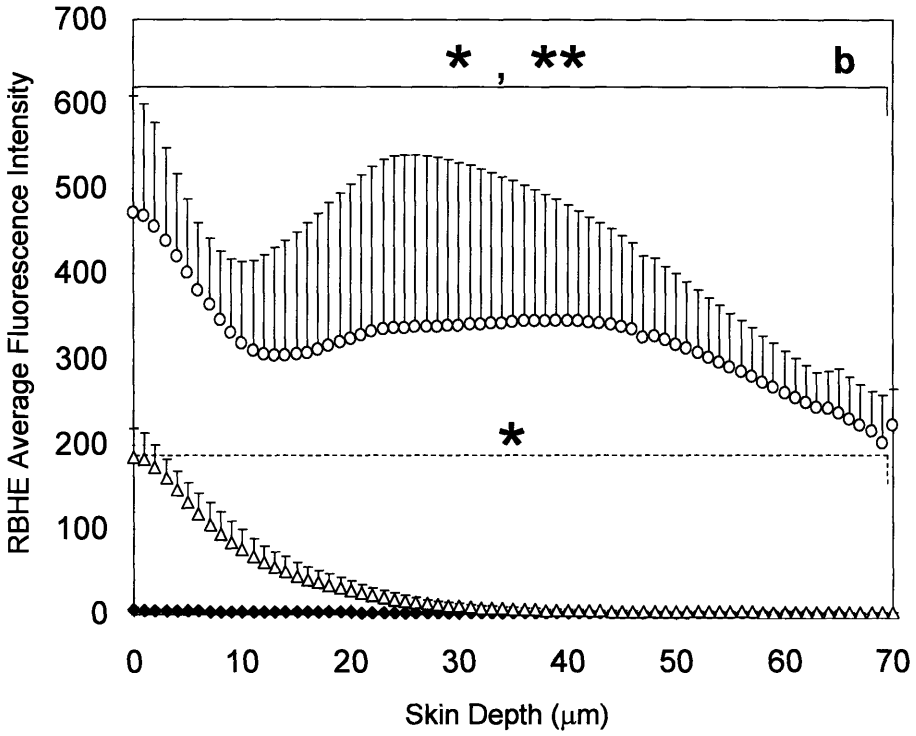
700
600
500
400
300
200
100
0
RBHE Average Fluorescence Intensity
* , **
b
*
0
10
20
30
40
50
60
70
Skin Depth (μm)

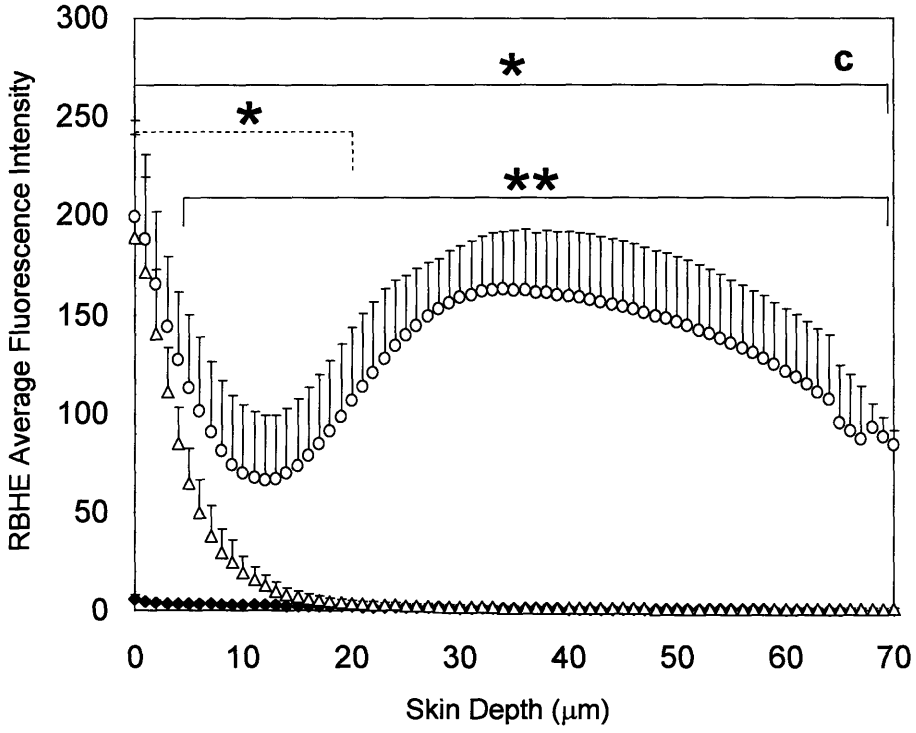
300
250
200
150
100
50
0
RBHE Average Fluorescence Intensity
*
c
*
**
0
10
20
30
40
50
60
70
Skin Depth (μm)

untreated skin and the non-LTRs of US-treated skin. Contrary to the SRB delivery in US-treated skin, the intensity of RBHE of the non-LTRs of US/SLS-treated skin is also significantly greater ($p<0.05$) than the intensity of RBHE of untreated skin (see dashed bar with a single asterisk (*) in Figure 5-15b) over the entire depth of skin imaged. This result indicates that *more RBHE penetrates into the skin within the non-LTRs as a result of US-treatment of the skin relative to untreated skin.* Combining these results, one may conclude that *two levels of skin perturbation also take place for the RBHE delivery in US-treated skin,* similar to the case of SRB delivery in US/SLS-treated skin.

In Figure 5-15c, the RBHE intensity profiles of the non-LTRs (open triangles) and of the LTRs (open circles) in US/SLS-enhanced skin are compared to the RBHE intensity profile in untreated skin (black diamonds). Similar to the SRB delivery in US/SLS-treated skin, the intensity of SRB in the LTRs of US/SLS-treated skin is significantly ($p<0.05$) greater than the intensity of SRB in both untreated skin (see solid bar with a single asterisk (*) in Figure 5-15c) over the depth of skin imaged and the non-LTRs of US/SLS-treated skin (see solid bar with a double asterisk (**) in Figure 5-15c) at depths greater than 4 μm. This result indicates that *more RBHE penetrates into the skin within the LTRs as a result of US/SLS-treatment of the skin relative to both untreated skin and the non-LTRs of US/SLS-treated skin.* In addition, the intensity of RBHE in the first 21 layers of the non-LTRs of US/SLS-treated skin is significantly greater ($p<0.05$) than the intensity of RBHE in the first 21 layers of untreated skin (see dashed bar with a single asterisk (*) in Figure 5-15c). This result indicates that *more RBHE penetrates into the skin within the non-LTRs as a result of US/SLS-treatment of the skin relative to untreated skin.* Furthermore, the intensity of RBHE in the non-LTRs of US/SLS-treated

skin is not significantly ($p>0.05$) different from the intensity of SRB in untreated skin at depths greater than 21 μm (i.e. deeper than the average stratum corneum depth), indicating that the depth of RBHE penetration in the non-LTRs of US/SLS-treated skin is similar to the depth of RBHE penetration in untreated skin. This result confirms that *RBHE penetration in the non-LTRs of US/SLS-treated skin is confined solely to the stratum corneum, while SRB penetration in the LTRs of US/SLS-treated skin extends into the viable epidermis.* Combining the results from the depth and intensity of RBHE delivered into the LTRs and the non-LTRs of US/SLS-treated skin relative to untreated skin, one may conclude that *two levels of skin perturbation take place in skin treated simultaneously with ultrasound and the chemical enhancer, SLS.*

5.3.2.3 Impact of Changes in Skin Morphology and Barrier Properties on the Shape of the Probe Fluorescence Intensity Curves within the LTRs of US-Treated and US/SLS-Treated Skin

For the delivery of SRB and RBHE in untreated, SLS-treated, and the non-LTRs of US-treated and US/SLS-treated skin, the fluorescence intensity profiles decrease linearly in the regions of the skin corresponding to the stratum corneum (see Figures 5-14a – 5-14c and 5-15a – 5-15c), approaching and maintaining near zero values in the deeper layers of the skin. However, in Figures 5-14c and 5-15c, after a similar initial linear decrease of the fluorescent permeant intensity in the LTRs in the region of the skin corresponding to the stratum corneum ($z = 0$ to $z = 15 – 20$ μm), there is an increase in the fluorescence intensity with increased skin depth. This unique shape of the fluorescence intensity profile for SRB and RBHE in the LTRs of US/SLS-treated skin can be attributed to two effects: (i) changes in the skin morphology as a function of depth, and (ii) differences in

the penetration of SRB and RBHE into the corneocytes of the SC and into the keratinocytes of the viable epidermis. First, the diameter of the skin cells increases from the viable epidermis (diameter = 10-12 μm)[27] up to the stratum corneum (diameter ~ 40 μm).[34] Also, the intercellular porosity of the viable epidermis (15%)[27] is much larger than the intercellular porosity of the stratum corneum (8-9%).[34] This decrease in the cell diameter, and the corresponding increase in the intercellular porosity, takes place in the stratum granulosum, which is the layer of the viable epidermis between the stratum corneum and the stratum spinosum layer of the viable epidermis. The location of this layer of the skin is in good agreement with the location of the observed increase in the fluorescence intensity curve for the LTRs in Figures 5-14c and 5-15c. Second, SRB and RBHE should be able to more easily penetrate across the cell membranes of the keratinocytes in the viable epidermis than across the cell membranes of the corneocytes in the stratum corneum. Indeed, it is well known that the corneocyte cell membranes contain a highly cross-linked network of covalently bound proteins and lipids, which form a cornified envelope.[27] This cornified envelope, which provides a large barrier to diffusion, begins to form in the upper layers of the stratum spinosum, and continues to form through the stratum granulosum layer of the viable epidermis.[27] Therefore, as a result of changes in the skin morphology and in the barrier properties of the skin cell membranes, the average intensity of SRB and RBHE in the upper layers of the epidermis could be larger than the average intensity of SRB and RBHE in the lower layers of the stratum corneum over the same area of the skin.

This effect is also observed in the fluorescence intensity profiles of SRB and RBHE in the LTRs of US-treated skin (see Figures 5-14b and 5-15b, respectively). In

these figures, the increase in the intensity of SRB and RBHE in the upper layers of the viable epidermis is less pronounced. Recall from Section 5.2.4 that for the case of US-treatment, the skin is exposed to SRB and RBHE for 24 hours prior to imaging, while for the case of US/SLS-treatment, the skin is exposed to SRB and RBHE for only 5 – 10 minutes prior to imaging. Therefore, for the US-treated experiments, SRB and RBHE have more time to fully penetrate into the upper layers of the viable epidermis, allowing for a more uniform distribution of SRB and RBHE in the viable epidermis as a function of depth. These results also indicate that *the shape of the fluorescence intensity profile curve in the LTRs does not depend on the presence of SLS during US treatment of the skin, or on the physicochemical properties of SRB and RBHE.*

5.3.2.4 Enhancements in the Vehicle-to-Skin Partition Coefficient, the Intensity Gradient, and the Effective Diffusion Path Length for SRB and for RBHE

Tables 5-2 and 5-3 report the values of the enhancement of the vehicle-to-skin partition coefficient, E_K, the enhancement of the intensity gradient, E_G, and the enhancement of the effective diffusion path length, E_L for the delivery of SRB and RBHE, respectively, in each of the three types of enhanced skin samples examined in this study – SLS-treated skin, US-treated skin, and US/SLS-treated skin. The values reported in Tables 5-2 and 5-3 were obtained from the experimental data presented in Figures 5-14 and 5-15 using the methods discussed in Sections 5.2.7.2 – 5.2.7.4. The errors reported for E_K, E_G, and E_L are presented as ± 1 standard deviation.

Using Eq. (5.5), the observed increase in the intensity of SRB at the surface in SLS-treated skin relative to the intensity of SRB at the surface in untreated skin results in

Table 5-2: Calculated values of the vehicle-to-skin partition coefficient enhancement, the intensity gradient enhancement, and the effective diffusion path length enhancement for the delivery of SRB in each of the skin samples examined.[a,b]

Skin Type	E_K	E_G	E_L
SLS-Treated	2.34 ± 1.93	2.78 ± 0.14	0.84 ± 0.70
US-Treated (non-LTRs)	1.35 ± 1.06	0.86 ± 0.05	1.58 ± 1.25
US-Treated (LTRs)	4.32 ± 2.79	2.79 ± 0.14	1.55 ± 1.00
US/SLS-Treated (non-LTRs)	3.69 ± 1.47	4.02 ± 0.16	0.92 ± 0.37
US/SLS-Treated (LTRs)	6.36 ± 2.12	5.26 ± 0.26	1.21 ± 0.41

a – E_K was calculated using Eq. (5.5), E_G was calculated using Eq. (5.6), and E_L was calculated using Eq. (5.10).
b – The errors in E_K, E_G and E_L are 1 S.D.

a value of E_K which is greater than 1 (see Table 5-2). Additionally, there is a corresponding enhancement in the intensity gradient ($E_G > 1$) for SLS-treated skin, but no difference in the effective diffusion path length of SRB (see Table 5-2). Therefore, using Eq. (5.12), the observed increase in the intensity gradient is directly due to the increased partitioning of SRB at the surface of SLS-treated skin, suggesting that *SLS primarily enhances the delivery of SRB into the skin by increasing the vehicle-to-skin partition coefficient*. For the case of SRB delivery in US-treated skin, the values for E_K and E_L corresponding to the non-LTRs of US-treated skin are not different from unity, indicating that the values of K and L corresponding to the delivery of SRB in the non-LTRs of US-treated skin are not significantly different from the values of K and L corresponding to the delivery of SRB in untreated skin. For the case of E_G, there is a slight decrease in the value of the intensity gradient in the non-LTRs of US-treated skin, as compared to

untreated skin. These results further indicate that the non-LTRs of US-treated skin are similar to untreated skin. For the delivery of SRB in the LTRs of US-treated skin, both the values of E_K and E_G are greater than unity, while E_L is not different from unity. In addition, the values of E_K, E_G, and E_L corresponding to the delivery of SRB in the LTRs of US-treated skin behave similarly to the values of E_K, E_G, and E_L corresponding to the delivery of SRB in SLS-treated skin. This similarity suggests that *US also enhances transdermal delivery, in part, by increasing the vehicle-to-skin partition coefficient.* For the case of SRB delivery in US/SLS-treated skin, Table 5-2 indicates that the values of E_K and E_G for the non-LTRs and the LTRs are both greater than unity. However, the values for E_K and E_G for the non-LTRs are both lower than the values of E_K and E_G for the LTRs, further confirming *the existence of two levels of skin perturbation in skin treated simultaneously with ultrasound and the chemical enhancer, SLS.*

For the case of RBHE delivery in SLS-treated skin, the values of E_K, E_G, and E_L are not different from unity, suggesting that *SLS has little effect on the amount of RBHE delivered into the skin relative to untreated skin.* For the case of RBHE delivery in US-treated skin, a significant enhancement of the values of E_K and E_G corresponding to both the non-LTRs and the LTRs is observed in Table 5-3. There is also a reduction in the effective diffusion path length, L, in the non-LTRs of US-treated skin relative to untreated skin. However, this result is due to the difference in the thickness of the stratum corneum in the skin used for the US-treated skin samples and in the skin used for the untreated skin samples. Recall that the stratum corneum is observed up to a depth of 40 μm in the skin auto-fluorescence images of untreated skin presented in Figures 5-8. In addition, the values of E_K and E_G are greater for the LTRs relative to the non-LTRs,

Table 5-3: Calculated values of the vehicle-to-skin partition coefficient enhancement, the intensity gradient enhancement, and the effective diffusion path length enhancement for the delivery of RBHE in each of the skin samples examined.[a,b]

Skin Type	E_K	E_G	E_L
SLS-Treated	1.23 ± 0.63	1.35 ± 0.24	0.91 ± 0.49
US-Treated (non-LTRs)	32.5 ± 8.5	56.6 ± 4.1	0.57 ± 0.16
US-Treated (LTRs)	82.5 ± 28.0	78.8 ± 3.4	1.05 ± 0.36
US/SLS-Treated (non-LTRs)	33.0 ± 13.1	78.5 ± 8.16	0.42 ± 0.17
US/SLS-Treated (LTRs)	34.9 ± 12.8	60.7 ± 7.6	0.57 ± 0.22

a – E_K was calculated using Eq. (5.5), E_G was calculated using Eq. (5.6), and E_L was calculated using Eq. (5.10).
b – The errors in E_K, E_G and E_L are 1 S.D.

which confirms that *two levels of skin perturbation are also present in skin treated with ultrasound for the delivery of RBHE.* For the case of RBHE delivery in US/SLS-treated skin, Table 5-3 indicates that the values of E_K and E_G for the non-LTRs and the LTRs are both greater than unity. In addition, the value for E_G for the non-LTRs is different from the value of E_G for the LTRs, further confirming *the existence of two levels of skin perturbation in skin treated simultaneously with ultrasound and the chemical enhancer, SLS.*

5.3.2.5 Impact of Ethanol, a Chemical Enhancer, on the Delivery of RBHE

From a comparison of the results for the delivery of SRB and RBHE reported in Sections 5.3.2.1, 5.3.2.2, and 5.3.2.4, there are two cases where the results for SRB and RBHE differ. The first case is for SLS-treated skin relative to untreated skin. In this case, SLS has a large impact on the delivery of SRB (see Figure 5-14a and Table 5-2), but does not

have a large impact on the delivery of RBHE (see Figure 5-15a and Table 5-3), relative to untreated skin. The second case is for the non-LTRs of US-treated skin relative to untreated skin. In this case, SRB delivery in the non-LTRs of US-treated skin is similar to the delivery of untreated skin (see Figure 5-14b and Table 5-2), while RBHE delivery in the non-LTRs of US-treated skin is increased relative to untreated skin (see Figure 5-15b and Table 5-3).

The observed differences can be attributed to the presence of ethanol in the RBHE donor solution. Recall from Section 5.2.3 that ethanol was used in a 50:50 mixture with PBS to solubilize RBHE, which is a hydrophobic permeant. However, ethanol can also serve as a chemical enhancer for the transdermal delivery of hydrophobic permeants.[35-40] Noting that ethanol was present at a concentration of 50% (v/v) while SLS was present only at a concentration of 1% (w/v), the enhancing effect of SLS on the transdermal delivery is expected to be small relative to the enhancing effect of ethanol. This can explain why the RBHE fluorescence intensity profiles for the SLS-treated skin and for the untreated skin in Figure 5-15a are similar, as well as explain why the values of E_K, E_G, and E_L for SLS-treated skin are not different from unity in Table 5-3. Furthermore, the presence of ethanol in the RBHE coupling medium during US-treatment can also explain the increased penetration of RBHE into the non-LTRs of US-treated skin relative to untreated skin, albeit not to the same extent observed in the LTRs of US-treated skin. This result for RBHE is similar to the observation for SRB delivery in skin treated simultaneously with ultrasound and with a chemical enhancer, SLS. *Therefore, ethanol also acts as a chemical enhancer to create two levels of perturbation for the case of RBHE delivery in US-treated skin.*

5.3.2.6 Summary of Results from the Qualitative Analysis of SRB and RBHE Delivery in Untreated, SLS-Treated, US-Treated, and US/SLS-Treated Skin

From a quantitative analysis of the SRB and RBHE fluorescence permeant intensity profiles (see Figures 5-14 and 5-15) and the enhancements in the vehicle-to-skin partition coefficient, the intensity gradient, and the effective diffusion path length (see Tables 5-2 and 5-3), the following key observations can be made: 1) two levels of perturbation, measured by probe delivery into the skin, are observed in skin samples treated simultaneously with ultrasound and a chemical enhancer (i.e. ethanol or SLS), and 2) in the absence of a chemical enhancer, ultrasound enhances only discrete regions (the LTRs) of the treated skin sample, while the remaining regions of the skin (the non-LTRs) are not significantly perturbed compared to untreated skin.

5.3.3 Investigation of the Existence of Transcellular Permeation Pathways in the Stratum Corneum

Figures 5-16 and 5-17 show plots of the normalized average fluorescence intensity across a five pixel wide slice of the dual-channel TPM images of SRB and RBHE, respectively, as a function of the length of the slice, given in pixel numbers (i.e. 0 – 255). The case of SRB and RBHE delivery in untreated skin are presented in Figures 5-16a and 5-17a, respectively. The case of SRB and RBHE delivery in SLS-treated skin are presented in Figures 5-16b and 5-17b, respectively. The case of SRB and RBHE delivery in the non-LTRs of US-treated skin are presented in Figures 5-16c and 5-17c, respectively. The

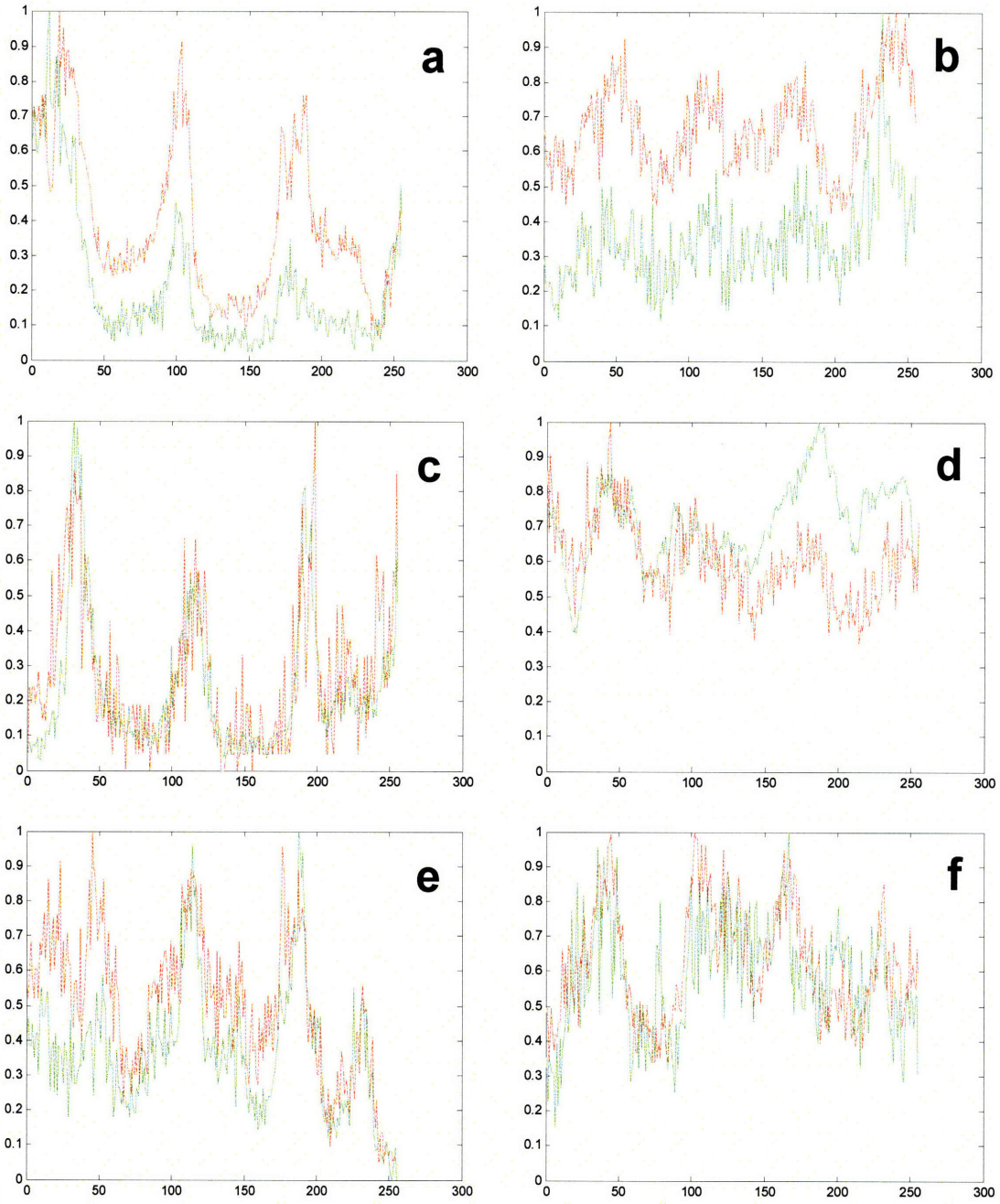

Figure 5-16: SRB and skin auto-fluorescence intensity (plotted on the y-axis) as a function of the pixel number along the length of the image slice (plotted on the x-axis). Key: red – SRB, green – skin auto-fluorescence. (a) Untreated skin, (b) SLS-treated skin, (c) the non-LTRs of US-treated skin, (d) the LTRs of US-treated skin, (e) the non-LTRs of US/SLS-treated skin, and (f) the LTRs of US/SLS-treated skin.

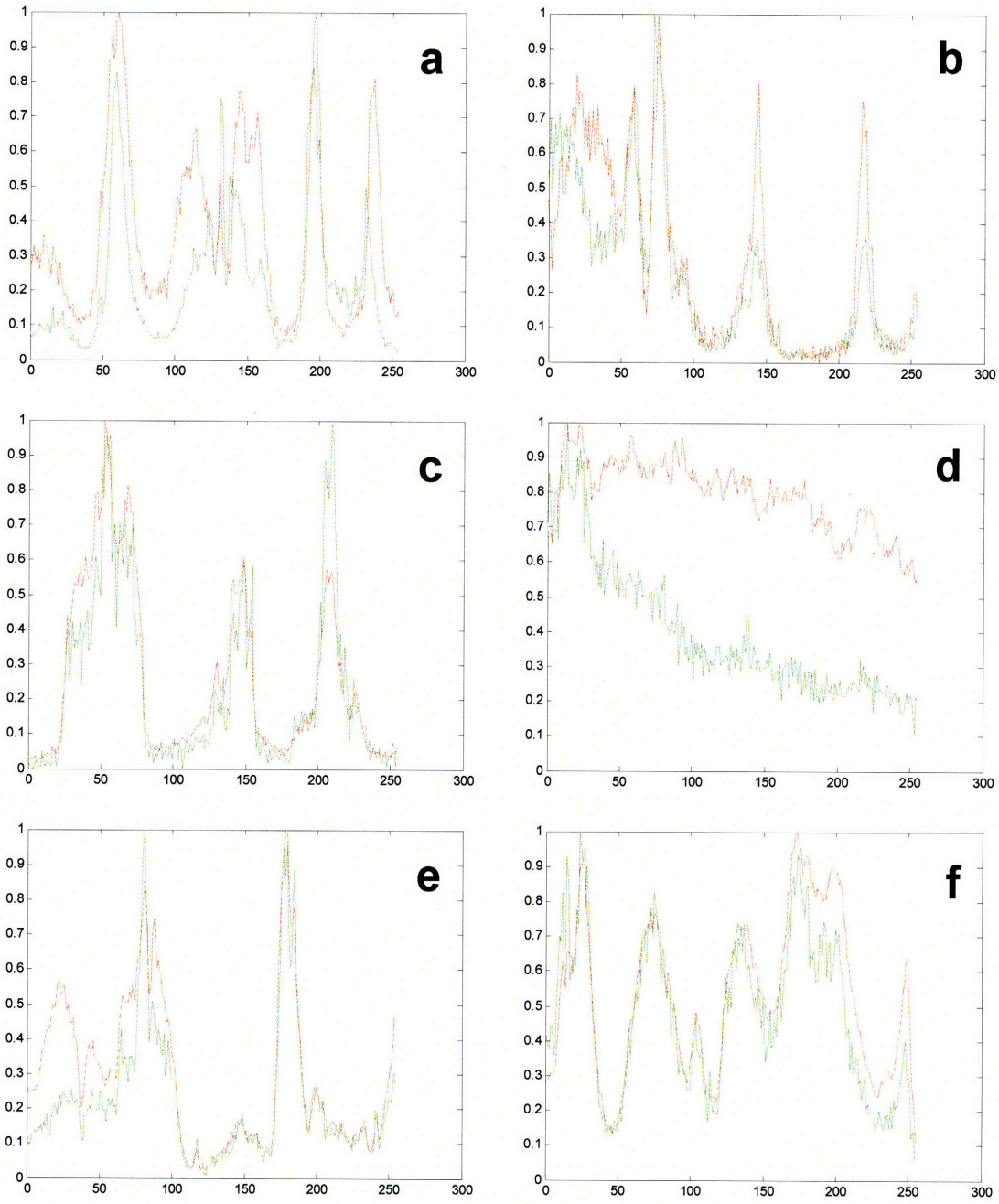

Figure 5-17: RBHE and skin auto-fluorescence intensity (plotted on the y-axis) as a function of the pixel number along the length of the image slice (plotted on the x-axis). Key: red – RBHE, green – skin auto-fluorescence. (a) Untreated skin, (b) SLS-treated skin, (c) the non-LTRs of US-treated skin, (d) the LTRs of US-treated skin, (e) the non-LTRs of US/SLS-treated skin, and (f) the LTRs of US/SLS-treated skin.

case of SRB and RBHE delivery in the LTRs of US-treated skin are presented in Figures 5-16d and 5-17d, respectively. The case of SRB and RBHE delivery in the non-LTRs of US/SLS-treated skin are presented in Figures 5-16e and 5-17e, respectively. The case of SRB and RBHE delivery in the LTRs of US/SLS-treated skin are presented in Figures 5-16f and 5-17f, respectively. In each figure, the normalized average fluorescence intensity is plotted on the y-axis, while the pixel number along the length of the slice, ranging in value from 0-255, is plotted on the x-axis. The red curves in Figures 5-16 and 5-17 correspond to the normalized average fluorescence intensity curves of SRB and RBHE, respectively. The green curves in Figures 5-16 and 5-17 correspond to the normalized average fluorescence intensity curves of the skin auto-fluorescence.

Table 5-4 reports the measured values of the average height and the average width of the peaks in the red curves from Figure 5-16, corresponding to the delivery of SRB, and from Figure 5-17, corresponding to the delivery of RBHE, which were obtained using the methods discussed in Section 5.2.7.5. The values are reported as the average measurements, ± 1 standard deviation, of the height and the width of 3 – 5 peaks, which were determined by the actual number of peaks present in Figures 5-16 and 5-17. Values of peak widths and peak heights shown in bold are significantly different ($p<0.05$) from the values of peak widths and peak heights corresponding to SRB and RBHE delivery in untreated skin.

As the results in Table 5-4 show, the heights of the SRB peaks in SLS-treated skin are significantly lower ($p<0.05$) than the heights of the SRB peaks in untreated skin. Likewise, the widths of the SRB peaks in SLS-treated skin are significantly higher

Table 5-4: Measured values of the average peak height and of the average peak width[a] for the delivery of SRB and RBHE at the surface (z = 0 μm) of the skin samples examined in Figures 5-16 and 5-17.[b,c]

	SRB		RBHE	
Skin Type	Height[d]	Width[e]	Height[d]	Width[e]
Untreated Skin	0.61 ± 0.07	17 ± 3	0.65 ± 0.15	14 ± 5
SLS-Treated	**0.46 ± 0.07**	**30 ± 6**	0.82 ± 0.09	**8 ± 1**
US-Treated (non-LTRs)	0.79 ± 0.16	16 ± 5	0.68 ± 0.24	25 ± 15
US-Treated (LTRs)	**0.25 ± 0.11**	**38 ± 4**	**no discernible peaks**	
US/SLS-Treated (non-LTRs)	0.53 ± 0.12	17 ± 5	0.65 ± 0.28	23 ± 11
US/SLS-Treated (LTRs)	**0.24 ± 0.05**	21 ± 5	0.58 ± 0.14	**30 ± 9**

a – The peak width was evaluated at half of the height of the peaks.
b – The errors are presented as 1 S.D. in the average.
c – Values in bold are significantly different ($p<0.05$) from the values for untreated skin.
d – The height is presented as a dimensionless quantity, normalized by the maximum value of the fluorescent permeant intensity at z = 0 μm.
e – The width is presented in units of pixels.

($p<0.05$) than the widths of the SRB peaks in untreated skin. These quantitative results indicate that more SRB is able to penetrate into the corneocytes at the surface of SLS-treated skin samples, than at the surface of untreated skin samples. Mechanistically, this result suggests that *SLS increases the partitioning of SRB, a hydrophilic permeant, from the intercellular region (a hydrophobic environment) and into the corneocyte domain (a hydrophilic environment).* In Table 5-5, a significant increase ($p<0.05$) in the penetration of SRB into the corneocytes is also observed down to a depth of 3 μm in SLS-treated skin relative to untreated skin. This result suggests that *transcellular permeation pathways play a larger role in the transdermal delivery of SRB in SLS-treated skin than in*

Table 5-5: Measured Values of the Depth of Transcellular Pathways in the Stratum Corneum.[a]

Skin Type	SRB	RBHE
SLS-Treated	3 μm	N/A
US-Treated (LTRs)	5 μm	5 μm
US/SLS-Treated (LTRs)	2 μm	3 μm

a – Depth of the transcellular pathways was determined by comparing the heights and the widths of the fluorescent permeant intensity peaks in the enhanced skin with the heights and the widths of the fluorescent permeant intensity peaks in untreated skin as a function of skin depth. Transcellular pathways are deemed present in a layer if either the height of the peaks is significantly smaller ($p<0.05$), or the width of the peaks is significantly larger ($p<0.05$), than the height and the width of the peaks in untreated skin.

untreated skin. For the case of RBHE delivery in SLS-treated skin relative to untreated skin, measurements of the average peak heights and the average peak widths reported in Table 5-4 indicate that the width of the RBHE fluorescence peaks in SLS-treated skin is significantly smaller ($p<0.05$), and that the height of the RBHE fluorescence peaks is approximately 20% larger, than the RBHE peaks in untreated skin. This result suggests that *SLS localizes RBHE within the intercellular lipid domain of the stratum corneum, suggesting that intercellular transport dominates the delivery of RBHE in SLS-treated skin.* These results for the delivery of SRB and RBHE in SLS-treated skin are consistent with previous studies on the role of the chemical enhancer, oleic acid, on the transdermal delivery of SRB.[13,14]

For the delivery of SRB and RBHE in the non-LTRs of US-treated skin and US/SLS-treated skin, there is no significant difference ($p>0.05$) in the heights and the widths of the fluorescence peaks in Figures 5-16c and 5-15e when compared to the heights and the widths of the SRB fluorescence peaks in Figure 5-16a (see also Table 5-

4). For the delivery of RBHE in the non-LTRs of US-treated skin and US/SLS-treated skin, there is no significant difference ($p>0.05$) in the heights and in the widths of the fluorescence peaks in Figures 5-17c and 5-17e when compared to the heights and the widths of the SRB fluorescence peaks in Figure 5-17a (see also Table 5-4). This data provides further evidence that *the delivery of SRB and RBHE in the non-LTRs in US-treated skin occurs primarily via the intercellular route*, similar to untreated skin.

The existence of transdermal pathways at the surface of the LTRs in US-treated and US/SLS-treated skin for both SRB and RBHE is confirmed quantitatively from the measurements of the heights and the widths of the fluorescence peaks in Figures 5-16d, 5-16f, 5-17d, and 5-17f. A comparison of the data reported in Table 5-4 for the delivery of SRB in untreated skin and in the LTRs of US-treated skin demonstrates that the peak widths are significantly larger ($p<0.05$), and the peak heights are significantly smaller ($p<0.05$), in the US-treated skin samples than in the untreated skin samples. For the case of RBHE delivery in the LTRs of US-treated skin, there are no discernable peaks present in Figure 5-17d, due to the uniform distribution of RBHE in the corneocytes and in the intercellular regions. Therefore, no peak width or peak height is reported in Table 5-4. Comparing the values of the heights and the widths of the peaks in the SRB fluorescence curve for the LTRs of US/SLS-treated skin (see Figure 5-16f) and untreated skin (see Figure 5-16a) presented in Table 5-4, the heights of the peaks in the LTRs of US/SLS-treated skin are significantly lower ($p<0.05$) than the heights of the peaks in untreated skin, and the widths of the peaks are 25% larger in the LTRs of US/SLS-treated skin than in untreated skin. These results suggest that more SRB is present in the corneocytes at the surface of the LTRs of US/SLS-treated skin relative to untreated skin than in the

corneocytes at the surface of the non-LTRs of US/SLS-treated skin relative to untreated skin. Comparing the measurements of the heights and the widths of the peaks in the RBHE fluorescence curves in the non-LTRs and in the LTRs of US/SLS-treated skin (see Figures 5-17e and 5-17f, respectively) with the measurements of the heights and the widths of the peaks in the RBHE fluorescence curves in untreated skin (see Figure 5-17a) reported in Table 5-4, no significant difference ($p>0.05$) is observed between the values of the peak heights and the peak widths for untreated skin and for the non-LTRs of US/SLS-treated skin, while a significant increase ($p<0.05$) in the peak widths and an insignificant decrease ($p>0.05$) in the peak height are observed in the LTRs of US/SLS-treated skin relative to untreated skin. These trends are indicative of increased penetration of SRB and RBHE in the corneocytes at the surface of the LTRs of US-treated and US/SLS-treated skin relative to the penetration of SRB and RBHE in the corneocytes at the surface of untreated skin. A significant increase ($p<0.05$) in the penetration of SRB into the corneocytes down to a depth of 5 μm and 2 μm is also observed in the LTRs of US-treated and of US/SLS-treated skin relative to untreated skin, respectively. Likewise, a significant increase ($p<0.05$) in the penetration of RBHE into the corneocytes down to a depth of 5 μm and 3 μm is also observed in the LTRs of US-treated and of US/SLS-treated skin relative to untreated skin, respectively. Using the penetration of SRB and RBHE in the corneocytes as a marker for transcellular permeation pathways in the stratum corneum, these results further suggest that *transcellular permeation pathways are utilized in the delivery of SRB and RBHE in the LTRs in US-treated skin.* This observation, resulting from an analysis of the dual-channel TPM images, independently confirms that transcellular pathways are traversed by

hydrophilic permeants in the LTRs of US/SLS-treated skin, as previously suggested from an analysis of the skin electrical resistivity data in the context of the aqueous-pore pathway hypothesis (see Chapter 4 for details).

5.3.4 Proposed Mechanisms of Enhancement in SLS-Treated, US-Treated, and US/SLS-Treated Skin

A possible mechanism for the observed difference in the location of SRB and RBHE in SLS-treated skin is that SLS facilitates the diffusion of water into the corneocytes of SLS-treated skin by disrupting the cornified envelope which surrounds the corneocytes. Indeed, there is ample evidence that SLS increases the hydration of the stratum corneum.[41-46] If these observed hydration effects are localized to the corneocytes, the corneocytes in SLS-treated skin will become more hydrophilic, due to the increased amount of water present inside the corneocytes. As a result of the increased hydrophilicity of the SLS-treated corneocytes, SRB, a hydrophilic molecule, should partition more favorably into the corneocytes of the SLS-treated skin than into the corneocytes of the untreated skin. Likewise, RBHE, a hydrophobic molecule, should partition less favorably into the more hydrophilic corneocytes of the SLS-treated skin than into the corneocytes of the untreated skin. The proposed mechanism of SLS disrupting the cornified envelope of the corneocytes to increase water partitioning into the corneocytes provides a simple, single mechanism that can be invoked to effectively explain the observation and results obtained from an analysis of the dual-channel TPM images for the delivery of SRB and of RBHE in SLS-treated skin and in untreated skin.

From previous studies of ultrasound-enhanced transdermal drug delivery, it has been demonstrated that *transient acoustic cavitation events near the skin surface are the primary mechanism for the enhancement of transdermal transport.*[28-30] An analysis of dual-channel TPM imaging of the delivery of SRB in US-treated skin suggests that transient acoustic cavitation events near the skin surface are localized to discrete regions of the ultrasound-treated skin. In these regions of the skin, the LTRs, which are regions of high transdermal permeability,[24] are formed as a result of the ultrasound exposure. For the delivery of SRB, the remaining regions of US-treated skin, the non-LTRs, are comparable to untreated skin, both in the intensity of SRB and in the depth of the SRB penetration, suggesting that little to no transient acoustic cavitation events take place near the surface of this region of US-treated skin.

Similar to the delivery of SRB in US-treated skin, LTRs are observed in skin treated simultaneously with ultrasound and a chemical enhancer (i.e. SLS or ethanol). These results suggest that ultrasound-induced *localized transient acoustic cavitation events near the skin surface* are required for the formation of LTRs. Contrary to the delivery of SRB in US-treated skin, the intensity of SRB and RBHE in the non-LTRs in skin treated simultaneously with ultrasound and a chemical enhancer was found to be higher than the intensity of SRB and RBHE in untreated skin. This result suggests *the presence of a chemical enhancer in the coupling medium during ultrasound treatment of the skin is required to achieve two levels of enhancement in skin treated with ultrasound.* Acoustic streaming in the coupling medium, another effect of ultrasound treatment of the skin, may be responsible for enhancing the delivery of the chemical enhancer into the skin during ultrasound treatment. Specifically, the existence of acoustic streaming in the

coupling medium during ultrasound treatment provides an additional convective driving force to assist in the penetration of the chemical enhancer into the skin. Once the chemical enhancer has penetrated the skin, it is then able to enhance the transdermal delivery of SRB and RBHE by disordering the intercellular lipid bilayers, disrupting the corneocyte cornified envelope, or extracting lipids from the stratum corneum. Therefore, the enhancement of the non-LTRs in skin treated simultaneously with ultrasound and with a chemical enhancer may be due to increased transdermal penetration of the chemical enhancer, which results from convective driving forces that are supplied by acoustic streaming in the coupling medium during ultrasound exposure.

For the delivery of SRB and RBHE in skin treated with ultrasound and a chemical enhancer (i.e. SLS or ethanol), SRB and RBHE penetration in the non-LTRs was found to be restricted to the stratum corneum similar to untreated skin, while SRB and RBHE penetration in the LTRs extended into the viable epidermis. The penetration of SRB and RBHE into the viable epidermis of the LTRs in both US-treated and US/SLS-treated skin may be the result of high-velocity microjets, which form during transient cavitation bubble collapse, impinging repeatedly on the surface of the skin where transient acoustic cavitation events take place. Additionally, the high-velocity microjets may be responsible for the formation of transcellular permeation pathways near the skin surface in the LTRs of US-treated and US/SLS-treated skin. Since the corneocytes represent over 99% of the skin surface, it is highly probable that the high-velocity microjets contact the skin primarily in the corneocyte region, rather than in the intercellular lipid region, pushing the fluorophore-containing coupling medium into the corneocytes near the skin surface.

5.4 Conclusions

Dual-channel two-photon microscopy images were generated and analyzed to compare the transdermal delivery of SRB, a fluorescent hydrophilic permeant, and RBHE, a fluorescent hydrophobic permeant, in skin treated with SLS (a chemical enhancer), ultrasound, and the simultaneous application of ultrasound and SLS, with the transdermal delivery of SRB and RBHE in untreated skin. From an analysis of the dual-channel TPM images as a function of skin depth for SRB and for RBHE, it was observed that both SRB and RBHE penetrate into the viable epidermis in the LTRs of US-treated and of US/SLS-treated skin, while the penetration of SRB and RBHE was confined solely to the stratum corneum in untreated skin, in SLS-treated skin, and in the non-LTRs of US-treated and US/SLS-treated skin.

From an analysis of the average fluorescence intensity profiles and the values of E_K, E_G, and E_L, which were obtained from the average fluorescence intensity profiles, it was observed that two significant levels of skin perturbation exist when the skin is treated simultaneously with ultrasound and with a chemical enhancer (i.e. SLS or ethanol). Greater perturbation of the skin was observed in the LTRs of skin treated with ultrasound and a chemical enhancer relative to the extent of skin perturbation observed in the non-LTRs of skin treated with ultrasound and a chemical enhancer. These results are consistent with our previous conclusions reached using the skin electrical resistivity measurements of the non-LTRs and the LTRs presented in Chapter 4. In the absence of a chemical enhancer during ultrasound treatment of the skin, the non-LTRs were found not to be significantly enhanced by ultrasound, as compared to untreated skin. This result suggests that ultrasound, in the absence of a chemical enhancer, discretely enhances the

skin through the mechanism of transient acoustic cavitation near the skin surface. This result also suggests that the presence of a chemical enhancer in the coupling medium during ultrasound treatment of the skin is required to obtain two levels of significant enhancements in the perturbation of the skin structure.

Finally, by comparing the heights and the widths of the fluorescence intensity peaks obtained from the dual-channel TPM images, transcellular pathways were observed in the LTRs of US-treated and of US/SLS-treated skin for both SRB and RBHE, as well as in SLS-treated skin for SRB. These observations provided confirmation of the results presented in Chapter 4 based on an analysis of the skin electrical resistivity data in the context of the aqueous-pore pathway hypothesis, which suggested that transcellular pathways may be present in the LTRs of skin treated simultaneously with ultrasound and a chemical enhancer.

In the next chapter, the differences of the non-LTRs and the LTRs formed in skin treated simultaneously with ultrasound and SLS will be investigated further to build on the knowledge gained in this chapter and in Chapter 4. Specifically, the aqueous-pore pathway hypothesis will be utilized to analyze the differences in the porosity, the tortuosity, and the pore distribution for the aqueous pore pathways in the non-LTRs and in the LTRs to gain additional mechanistic information on how the US/SLS enhancement system can produce two different levels of perturbation in the skin.

5.5 References

1. Hou SYE, Mitra AK, White SH, Menon GK, Ghadially R, and Elias PM. 1991. Membrane structures in normal and essential fatty acid deficient stratum corneum: characterization by ruthenium tetroxide staining and X-ray diffraction. J Invest Derm 96:215-223.
2. Bodde HE, van der Brink I, Koerten HK, and de Haan FHN. 1991. Visualization of in vitro percutaneous penetration of mercuric chloride; transport through intercellular space versus cellular uptake through desmosomes. J Cont Rel 15:227-236.
3. Sznitowska M, Janciki S, and Williams AC. 1998. Intracellular or intercellular localization of the polar pathway across stratum corneum. J Pharm Sci 87:1109-1114.
4. Yamashita N, Tachibana K, Ogawa K, Tsujita N, Tomita A. 1997. Scanning electron microscopic evaluation on the skin surface after ultrasound exposure. The Anatomical Record 247:455-461.
5. Hatanaka T, Manabe E, Sugibayashi K, Morimoto Y. 1994. An application of the hydrodynamic pore theory to percutaneous absorption of drugs. Pharm Res 11:654-658.
6. Menon GK, Bommannan DB, Elias PM. 1994. High-frequency sonophoresis: permeation pathways and structural basis for enhanced permeability. Skin Pharmacol 7:130-139.
7. Menon GK and PM Elias. 1997. Morphological basis for a pore-pathway in mammalian stratum corneum. Skin Pharmacol 10:235-246.

8. Bommannan D, Menon GK, Okuyama H, Elias PM, Guy RH. 1992. Sonophoresis II: examination of the mechanism(s) of ultrasound-enhanced transdermal delivery. Pharm Res 9:1043-1047.

9. Boucaud A, Montharu J, Lebertre M, Patat F, Vaillant L, Machet L. 1999. Biological effects of low frequency ultrasound on the skin. IEEE Ultrasonics Symposium.

10. Yu B, Dong C, So PTC, Blankschtein D, Langer RS. 2001. In vitro visualization and quantification of oleic acid induced changes in transdermal transport using two-photon fluorescence microscopy. J Invest Dermatol 117:16-25.

11. Yu B, Kim KH, So PTC, Blankschtein D, Langer RS. 2002. Topographic heterogeneity in transdermal transport revealed by high-speed two-photon microscopy: Determination of representative skin sample sizes. J Invest Dermatol 118:1085-1088.

12. Yu B, Kim KH, So PTC, Blankschtein D, Langer RS. 2003. Visualization of oleic acid-induced transdermal diffusion pathways using two-photon fluorescence microscopy. J Invest Dermatol 120:448-455.

13. Yu B, Kim KH, So PTC, Blankschtein D, Langer RS. 2003. Evaluation of fluorescent probe surface intensities as an indicator of transdermal permeant distributions using wide-area two-photon fluorescence microscopy. J Pharm Sci 92:2354-2365.

14. Yu B. Elucidation of Chemically-Induced Transdermal Transport Processes. Ph.D. Thesis, MIT (2002).

15. Tang H. Low-Frequency Sonophoresis in Transdermal Drug Delivery. Ph.D. Thesis, MIT (2001).

16. Masters BR, So PTC, Gratton E. 1998. Optical biopsy of in vivo human skin: Multiphoton excitation microscopy. Lasers Med Sci 13:196-203.

17. Denk W, Strickler JH, Webb WW. 1990. Two-photon laser scanning fluorescence microscopy. Science 248:73-76.

18. Diaspro A. 1999. Introduction to two-photon microscopy. Microsc Res Tech 47:163-164.

19. Soeller C, Cannell MB. 1999. Two-photon microscopy: Imaging in scattering samples and three dimensionally resolved flash photolysis. Microsc Res Tech 47:182-195.

20. Masters BR, So PTC, Gratton E. 1997. Multiphoton excitation fluorescence microscopy and spectroscopy of in vivo human skin. Biophys J 72:2405-2412.

21. Periasamy A, Skoglund P, Noakes C, Keller R. 1999. An evaluation of two-photon excitation versus confocal and digital deconvolution fluorescence microscopy imaging in xenopus morphogenesis. Microsc Res Tech 47:172-181.

22. Na R, Stender I-M, Ma L, Wulf HC. 2000. Auto-fluorescence spectrum of the skin: Component bands and body site variations. Skin Res Technol 6:112-117.

23. Na R, Stender I-M, Ma L, Wulf HC. 2001. Auto-fluorescence of human skin is age-related after correction for skin pigmentation and redness. J Invest Dermatol 116:536-540.

24. Kushner J, Blankschtein D, and Langer R. 2004. Experimental demonstration of highly permeable localized transport regions in low-frequency sonophoresis. J Pharm Sci. 93:2733-2745.

25. Montgomery DC, Runger GC, Hubele NF. Engineering Statistics. John Wiley & Sons, Inc. New York (1998).

26. Peck KD, Srinivasan V, Li SK, Higuchi WI, Ghanem A-H. 1996. Quantitative description of the effect of molecular size upon electroosmotic flux enhancement during iontophoresis for a synthetic membrane and human epidermal membrane. J Pharm Sci 85:781-788.

27. Schaefer H, Redelmeier TE. Skin Barrier. Basel: Karger (1996).

28. Tang H, Wang CCJ, Blankschtein D, Langer R. 2002. An investigation of the role of cavitation in low-frequency ultrasound-mediated transdermal drug transport. Pharm Res 19:1160-1169.

29. Tezel A, Mitragotri S. 2003. Interactions of inertial cavitation bubbles with stratum corneum lipid bilayers during low-frequency sonophoresis. Biophys J 85:3502-3512.

30. Tezel A, Sens A, Mitragotri S. 2002. Investigations of the role of cavitation in low-frequency sonophoresis using acoustic spectroscopy. J Pharm Sci 91:444-453.

31. Montaga W, Klingman AM, Carlisle KS. Atlas of Normal Human Skin. Springer-Verlag, New York (1992).

32. Tezel A, Sens A, Mitragotri S. 2002. A theoretical analysis of low-frequency sonophoresis: Dependence of transdermal transport pathways on frequency and energy density. Pharm Res 19:1841-1846.

33. Alvarez-Román R, Merino G, Kalia YN, Naik A, Guy RH. 2003. Skin permeability enhancement by low-frequency sonophoresis: Lipid extraction and transport pathways. J Pharm Sci 92:1138-1146.

34. Johnson ME, Blankschtein D, and Langer R. 1997. Evaluation of solute permeation through the stratum corneum: Lateral bilayer diffusion as the primary transport mechanism. J Pharm Sci 86:1162-1172.

35. Femenia-Fonta A, Balaguer-Fernandez C, Merino V, Rodilla V, Lopez-Castellano A. 2005. Effect of chemical enhancers on the in vitro percutaneous absorption of sumatriptan succinate Eur J Pharm Biopharm 61:50-55.

36. Pillai O, Nair V, Panchagnula R. 2004. Transdermal iontophoresis of insulin: IV. Influence of chemical enhancers. Int J Pharm 269:109-120.

37. Magnusson BM, Runn P. 1999. Effect of penetration enhancers on the permeation of the thyrotropin releasing hormone analogue pGlu-3-methyl-His-Pro amide through human epidermis. Int J Pharm 178:149-159.

38. Bhatia KS, Gao S, Freeman TP, Singh J. 1997. Effect of penetration enhancers and iontophoresis on the ultrastructure and cholecystokinin-8 permeability through porcine skin. J Pharm Sci 86:1011-1015.

39. Johnson ME, Mitragotri S, Patel A, Blankschtein D, Langer R. 1996. Synergistic effects of chemical enhancers and therapeutic ultrasound on transdermal drug delivery. J Pharm Sci 85:670-678.

40. Peck KD, Ghanem AH, and Higuchi WI. 1994. Hindered diffusion of polar molecules through and effective pore radii estimates of intact and ethanol treated human epidermal membrane. Pharm Res 11:1306-1314.

41. Mizushima J, Kawasaki Y, Tabohashi T, Kitano T, Sakamoto K, Kawashima M, Cooke R, Maibach HI. 2000. Effect of surfactants on human stratum corneum: electron paramagnetic resonance study. Int J Pharm 197:193-202.

42. Wilhelm KP, Cua AB, Wolff HH, Maibach HI. 1993. Surfactant-induced stratum corneum hydration in vivo: prediction of the irritation potential of anionic surfactants. J Invest Dermatol 101:310-315.

43. Rhein LD, Robbins CR, Ferne K, Cantore R. 1986. Surfactant structure effects on swelling of isolated human stratum corneum. J Soc Cosmet Chem 37:125-139.

44. Miyazawa K, Ogawa M, Mitsui T. 1984. The physico-chemical properties and protein denaturation potential of surfactant mixtures. Int J Cosm Sci 6:33 46.

45. Goffin V, Pierard-Franchimont C, Pierard GE. 1999. Passive sustainable hydration of the stratum corneum following surfactant challenge. Clin Experim Dermatol 24:308-311.

46. Uhoda E, Leveque JL, Pierard GE. 2005. Silicon image sensor technology for in vivo detection of surfactant- induced corneocyte swelling and drying Dermatol 210:184-188.

Chapter 6

Evaluation of the Porosity, the Tortuosity, and the Hindrance Factor for the Transdermal Delivery of Hydrophilic Permeants in the LTRs and in the Non-LTRs of Skin Treated Simultaneously with a Chemical Enhancer and Low-Frequency Ultrasound

6.1 Introduction

In Chapter 4, I demonstrated that the red spots that are formed in skin treated simultaneously with a chemical enhancer and low-frequency ultrasound in the presence of the hydrophilic fluorescent probe, sulforhodamine B (SRB), are indeed localized regions of high permeability. Using calcein, another hydrophilic fluorescent probe, I also demonstrated that the localized transport regions (LTRs) are approximately 80-fold more permeable than the surrounding regions of the skin (the non-LTRs).[1] The difference in the enhancements of the LTRs and the non-LTRs due to treatment of the skin with a chemical enhancer and low-frequency sonophoresis was confirmed using skin electrical

resistivity measurements.[1] For these measurements, the skin electrical resistivity in the LTRs was found to be approximately 30-fold lower than in the non-LTRs.[1] This result is consistent with the skin permeability measurements utilizing calcein, since the skin electrical resistivity is inversely proportional to the skin permeability. In addition, the skin electrical resistivity measurements indicated that both the LTRs and the non-LTRs were significantly enhanced relative to untreated skin. Specifically, the skin electrical resistivity of the non-LTRs was found to be approximately 170-fold lower than that of untreated skin, while the skin electrical resistivity of the LTRs was found to be approximately 5000-fold lower than that of untreated skin.[1] This important result indicated that there are two levels of enhancement in skin treated simultaneously with a chemical enhancer and low-frequency ultrasound, which was subsequently confirmed in Chapter 5 using two-photon microscopy. Using the results of the skin electrical resistivity measurements, values of the porosity-to-tortuosity ratio, (ε/τ), were determined in the non-LTRs and in the LTRs,[1] and compared to the threshold value of (ε/τ) for the intercellular regions of the stratum corneum,[2] which was obtained in Chapter 3. This analysis suggested that transcellular pathways may be present in the LTRs formed in skin treated simultaneously with a chemical enhancer and low-frequency ultrasound. The presence of transcellular pathways in the LTRs was subsequently confirmed in Chapter 5 using two-photon microscopy.[3]

In light of the work discussed above, it would be instructive to deepen our understanding of the differences between the LTRs and the non-LTRs by further examining the differences in the porosity, the tortuosity, and the aqueous pore radii in these two regions of ultrasound/chemical enhancer treated skin. In Chapter 4, because a

single fluorescent permeant was delivered across the skin, only the ratio, (ε/τ), could be determined from the available experimental permeation data. By utilizing the theoretical and experimental methods introduced in Chapter 2 to carry out and analyze permeability experiments using *two radiolabeled permeants*, in conjunction with the methods introduced in Chapter 4 to analyze the sizes of the LTRs and the non-LTRs, as well as to carry out diffusion masking experiments, it will be possible to separately evaluate the porosity, ε, the tortuosity, τ, and the aqueous pore radii, r_{pore}, in the non-LTRs and in the LTRs (see Materials and Methods, Section 6.2). Specifically, the permeability data obtained from the LTRs and the non-LTRs (see Section 6.3.1) will be analyzed using the three approaches presented in Chapter 2. In the first approach (see Section 6.3.2), the steady-state permeability data are analyzed using the methods of Peck *et al.*[4] and Tang *et al.*,[5] who assumed that the porosity and the tortuosity of the aqueous pore channels are independent of the radii of the permeants which are delivered across the skin, to evaluate a single average pore radius for the aqueous pore channels present in the skin. In the second approach (see Section 6.3.3), the methods presented in Section 2.4.6 are used to evaluate the porosity, the tortuosity, and the hindrance factor, $H(\lambda)$, for the case of a distribution of pore radii, as proposed by Tezel *et al.*[6] In the final approach (see Section 6.3.4), the methods of Section 2.4.6 are used to evaluate the porosity and the tortuosity as a function of the extent of skin perturbation and of the radius of the permeant for the limiting case of infinitely-large aqueous pores, where $r_{pore} \rightarrow \infty$ and $H(\lambda) = 1$. The results of these investigations will highlight the differences in the structure of the aqueous pore channels present in the LTRs and in the non-LTRs, which should further increase our mechanistic understanding of how these two distinct regions of the skin are formed as a

result of a single treatment of low-frequency ultrasound in the presence of a chemical enhancer (see Section 6.3.5).

6.2 Materials and Methods

6.2.1 Chemicals

Four hydrophilic permeants, ^{14}C-Urea (MW = 60.1 Da), ^{3}H-Mannitol (MW = 182.2 Da), ^{3}H-Raffinose (MW = 504.4 Da), and ^{3}H-Inulin (MW = 5,000 Da), were obtained from American Radiolabeled Chemicals, Inc. (St. Louis, MO). Phosphate Buffer Saline and Sodium Lauryl Sulfate (SLS) were obtained from Sigma-Aldrich (St. Louis, MO). Sulforhodamine B (SRB) was obtained from Molecular Probes (Eugene, OR). All these chemicals were used as received.

6.2.2 Skin Preparation

Full-thickness human cadaver skin was obtained from the National Disease Research Institute (Philadelphia, PA) and stored at -80^{o}C until use. Prior to use in the diffusion experiments, the skin was thawed and the subcutaneous fat was removed from the skin using a razor blade. The skin was then sectioned and mounted in vertical Franz diffusion cells (15-mm inner diameter) obtained from Permegear (Bethlehem, PA).

6.2.3 Skin Electrical Resistivity Measurements

Prior to ultrasound pre-treatment, the electrical resistance of the skin mounted on the diffusion cells was measured according to previously published methods,[7] which are

summarized next. A 100 mV AC voltage source at 10 Hz was generated using a signal generator (Hewlett-Packard, model HP 33120A) and applied across the skin membrane using two Ag/AgCl electrodes (In Vivo Metrics, Healdsburg, CA) for 5-10 seconds. The skin electrical current was measured using a Fluke Multimeter (Model 139, Fluke Corporation). The skin electrical resistance was obtained from the skin electrical current using Ohm's Law. Since this measurement also includes the resistance of the donor and the receiver cell solutions, a background electrical resistance measurement of just the PBS solution was made separately, and was then subtracted from the electrical resistance of the skin in the diffusion cell to determine the actual skin electrical resistance. The electrical resistance, R, of all the skin samples was measured and multiplied by the skin area available to ultrasound exposure in the diffusion cell (A = 1.77 cm^2) to obtain the skin electrical resistivity. Any skin sample with an initial RA value of <50 kOhm*cm^2, corresponding to an initial current of 3.3 μAmps, was considered damaged and was discarded, and was subsequently replaced with an intact skin sample.[7]

6.2.4 Ultrasound Pre-Treatment Protocol

Ultrasound, in the presence of a coupling medium containing 1% (w/v) SLS and 0.5% (w/v) SRB in PBS, was applied to the intact human full-thickness skin samples following previously published methods.[8,9] Ultrasound (VCX 400, Sonics and Materials, Inc., Newtown, CT) was applied to the skin samples at the following conditions: frequency - 20 kHz, intensity - 7.2 W/cm^2, pulse length - 5 sec on, 5 sec off, and tip displacement - 3 mm,[8,9] until the skin electrical current reached approximately ~ 225 μAmps. This value of the skin electrical current was selected because it was the lowest value of the skin

electrical current investigated in Chapter 4 for the formation of LTRs in ultrasound-treated skin.[1] After each minute of ultrasound exposure, the coupling medium was changed to minimize the impact of thermal effects on the permeation enhancement of the skin,[8,9] and measurements of the skin electrical current were conducted to determine if the target skin electrical current had been reached. Once the desired skin electrical current was attained, the skin sample was removed from the diffusion cell and was rinsed for 15 minutes in PBS to remove all excess coupling medium from the skin surface in preparation for digital imaging of the skin surface to quantify the areas of the LTRs and the non-LTRs (see Section 4.2.5 for details).

6.2.5 Dual Radiolabeled Masking Experiments

Following digital imaging of the skin surface, the ultrasound-treated skin samples were divided into two groups: A) non-LTRs and B) LTRs. The surface of the skin was masked with vacuum grease (High Vacuum Grease, Dow Corning, Midland, MI) according to the methods presented in Section 4.2.6.[1] In the non-LTR group, the LTRs were masked with vacuum grease to permit permeation only through the non-LTRs, while for the LTR group, the non-LTRs were masked with vacuum grease to permit permeation only through the LTRs.

After masking of the skin, dual radiolabeled diffusion experiments were carried out using vertical Franz diffusion cells. In each experiment, urea, which is carbon-14 labeled, was paired with a tritium-labeled permeant – mannitol, raffinose, or inulin. 2 ml of a solution containing 1 μCi/ml of urea and 1 μCi/ml of one of the three tritium-labeled permeants was placed in the donor chamber. Aliquots (~400 μL) of the receiver chamber

were taken at predetermined time points over a period of 48 hours to ensure transition into the steady-state regime for each of the permeants and skin sample types considered. The radioactivity of these aliquot samples was then measured using the dual radiolabeled counting mode in a scintillation counter (Packard, Tri-Carb®, 2200 CA) to measure the cumulative mass of permeant delivered into the receiver cell as a function of time, M(t). To evaluate the cumulative mass of permeant *per unit area*, Q(t), delivered through the LTRs and the non-LTRs, the following expressions are used:

$$Q(t)_{LTRs} = \frac{M(t)}{A_{LTRs}} \tag{6.1}$$

$$Q(t)_{non-LTRs} = \frac{M(t)}{A_{non-LTRs}} \tag{6.2}$$

where A_{LTRs} and $A_{non\text{-}LTRs}$ are the areas of the skin surface available for transport in the LTRs and in the non-LTRs, respectively. Plots of $Q(t)_{LTRs}$ and $Q(t)_{non\text{-}LTRs}$ versus time were then generated from the results of the scintillation counting of the aliquots taken from the receiver cells.

6.2.6 Regression Analysis of the Experimental Diffusion Data to Evaluate the Steady-State Permeability, the Porosity, the Tortuosity, and the Aqueous Pore Radii in the LTRs and in the Non-LTRs

As in Chapter 2, the Q(t) versus time data generated from the dual radiolabeled masking experiments were analyzed using DataFit 8.1 (Oakdale Engineering). Equations (2.35a) and (2.35b) were used as the model equations for the nonlinear regression analysis, and the quantities, $(\varepsilon C_d \tau L)$ and $[DH(\lambda)/(\tau L)^2]$, were selected as the regression parameters for

analysis of the experimental data sets. DataFit 8.1 uses the Levenberg-Marquardt method as the algorithm to adjust the values of the initial estimates of the regression parameters to improve the fit of the nonlinear regression model. Once ($\varepsilon C_d \tau L$) and [$D^{\infty}H(\lambda)/(\tau L)^2$] were determined for both urea and the selected tritium-labeled permeant, the porosity, the tortuosity, and the aqueous pore radii in the non-LTRs and in the LTRs could be determined using the theoretical methods presented in Eqs. (2.36) – (2.40) (see Section 2.4.6).

6.3 Results and Discussion

6.3.1 Dual Radiolabeled Diffusion Experimental Data

Figures 6-1a and 6-1b show the cumulative amounts of radiolabeled permeant delivered across the skin, Q(t), as a function of time, t, for the LTRs and for the non-LTRs, respectively. In each plot, the black diamonds correspond to the delivery of urea, the open circles correspond to the delivery of mannitol, the open squares correspond to the delivery of raffinose, and the open triangles correspond to the delivery of inulin. Each data point represents an average of 5 – 6 skin samples. Representative error bars, corresponding to $\pm$ 1 S.D., have been included to provide an estimate of the error in the average value of Q(t).

From the data presented in Figures 6-1a and 6-1b, two trends may be observed. First, in both Figures 6-1a and 6-1b, Q(t) decreases as the size of the permeant increases. This observation follows the expected trend that permeability decreases as the radius of the permeant increases, since larger permeants generally have smaller diffusion coefficients, according to the Stokes-Einstein equation.[10] Second, the value of Q(t)

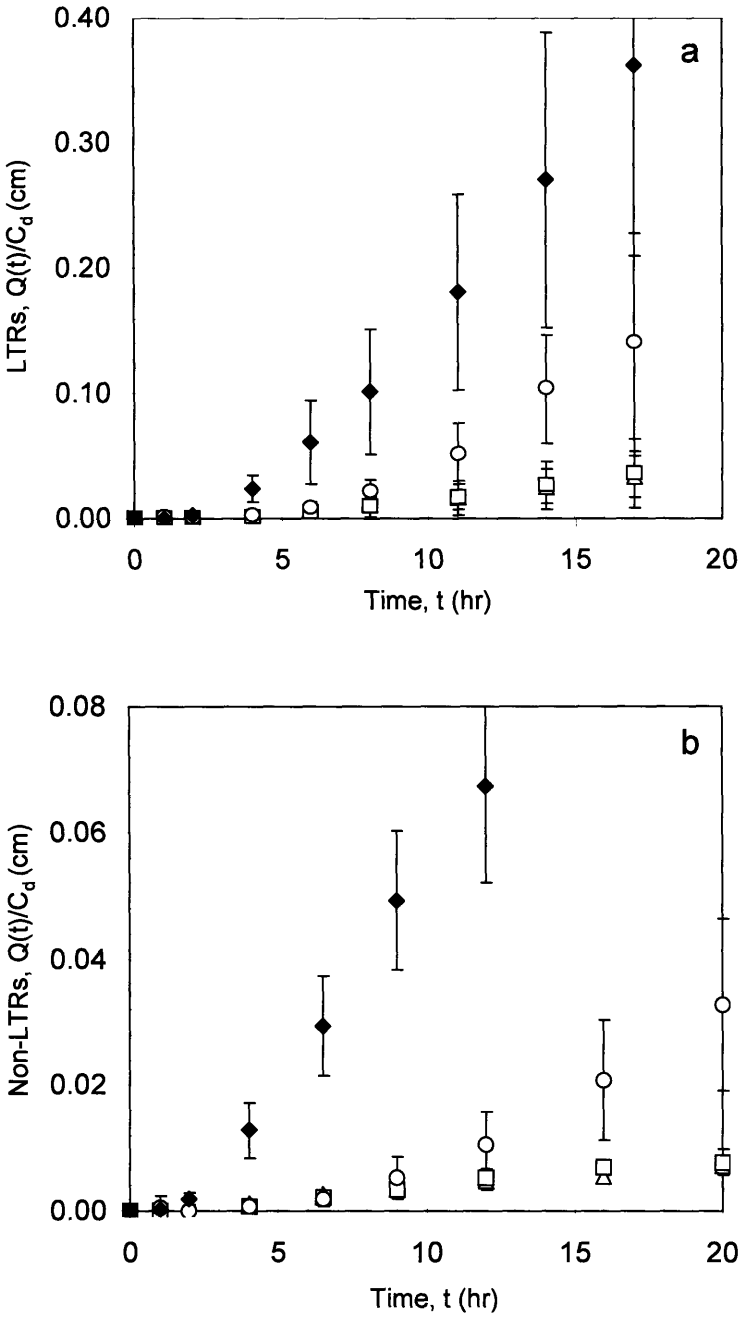

Figure 6-1: Plots of the cumulative amount of hydrophilic permeant, Q(t), delivered across the skin as a function of time, t, normalized by the initial donor concentration, C_d. (a) LTRs and (b) non-LTRs. Key: Urea – black diamonds, mannitol – open circles, raffinose – open squares, inulin – open triangles. Sample error bars correspond to $\pm$ 1 S.D.

corresponding to the LTRs for each of the four permeants is larger than the value of Q(t) corresponding to the non-LTRs for each of the four permeants. For the four permeants considered, the permeabilities in the LTRs were 3-fold to 10-fold higher than the permeabilities in the non-LTRs formed in full-thickness human skin. This result is in qualitative agreement with the results presented in Chapter 4, in which the permeability of calcein in the LTRs was shown to be 80-fold higher than that in the non-LTRs formed in full-thickness pig skin.[1]

6.3.2 Evaluation of the Average Aqueous Pore Radii in the LTRs and in the Non-LTRs from an Analysis of Log P_{3H} vs. Log P_{Urea} Plots using Steady-State Analysis Methods

Figure 6-2 shows plots of the permeability data from the three dual radiolabeled systems examined in this experimental study. The ^{3}H-mannitol – ^{14}C-urea permeability data is presented in Figure 6-2a, the ^{3}H-raffinose – ^{14}C-urea permeability data is presented in Figure 6-2b, and the ^{3}H-inulin – ^{14}C-urea permeability data is presented in Figure 6-2c. The values of the permeability for both the tritium-labeled permeant and urea were calculated from the regression parameters, $(\varepsilon C_d \tau L)$ and $[D^{\infty} H(\lambda)/(\tau L)^2]$, by using Eq. (2.41) in the time interval from 0 – 20 hours. The open circles and the open triangles correspond to the permeability data from the non-LTRs and the LTRs, respectively, while the black diamonds, the black circles, the black squares, and the black triangles correspond to the permeability data obtained in Chapter 2 for the delivery in untreated, low dose US-treated, high dose US-treated, and dermis skin samples, respectively. Note that each data point in Figures 6-2a through 6-2c represents a single diffusion experiment.

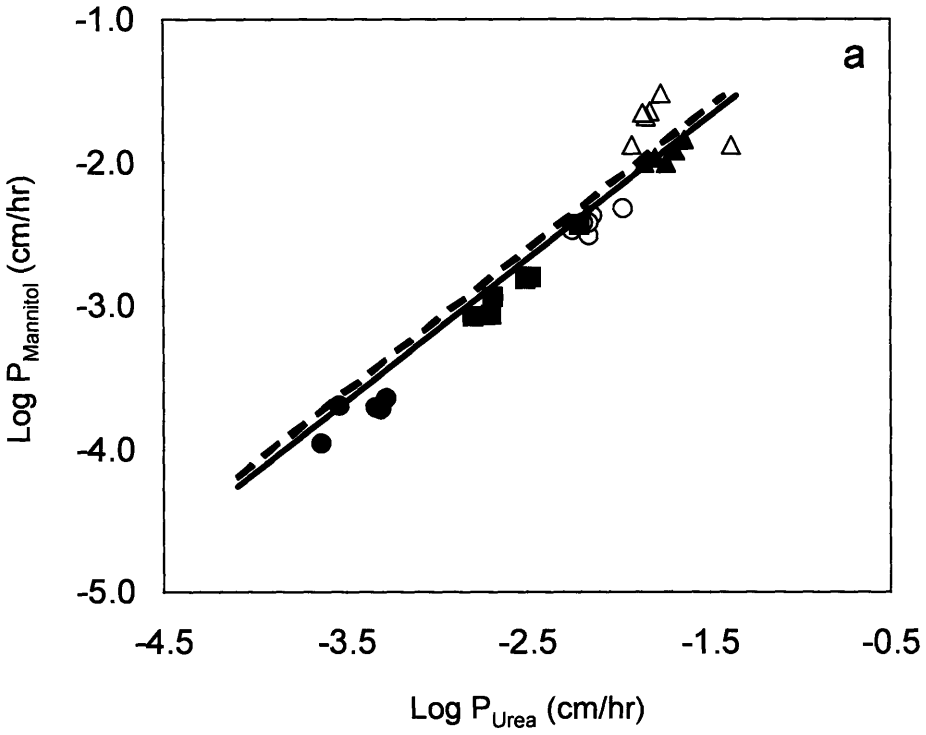

Figure 6-2: Log P of the tritium-labeled permeants plotted against log P of urea, the carbon-14 labeled permeant. (a) Mannitol-Urea, (b) Raffinose-Urea, and (c) Inulin-Urea. Key: LTRs – open triangles, non-LTRs – open circles, untreated skin – black diamonds, low dose US-treated – black circles, high dose US-treated skin – black squares, dermis – black triangles, ideal slope of 1 – solid line, and the limiting case of infinitely large aqueous pore channels – dashed line.

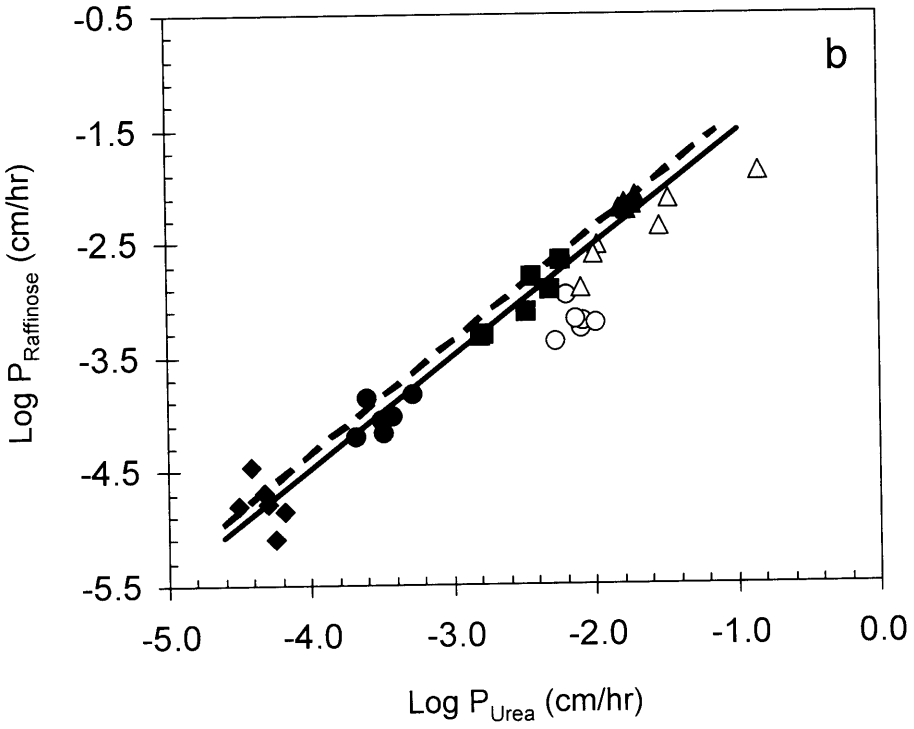
b
-0.5
-1.5
-2.5
-3.5
-4.5
-5.5
-5.0
-4.0
-3.0
-2.0
-1.0
0.0
Log $P_{Raffinose}$ (cm/hr)
Log P_{Urea} (cm/hr)

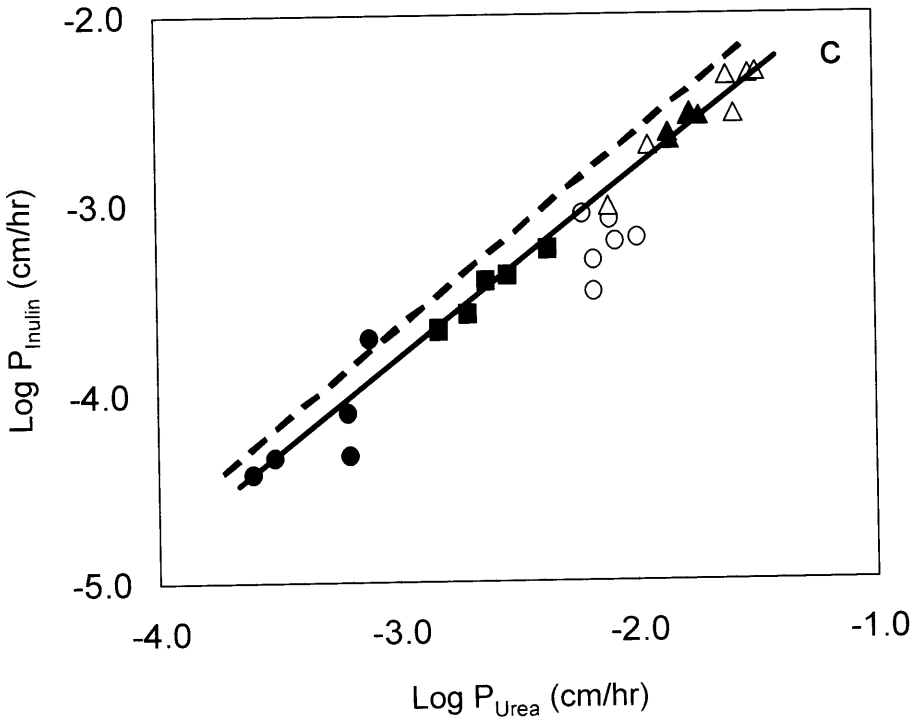
c
-2.0
-3.0
-4.0
-5.0
-4.0
-3.0
-2.0
-1.0
Log P_{Inulin} (cm/hr)
Log P_{Urea} (cm/hr)

In addition, a solid line through the data from Chapter 2, representing the ideal slope of 1 predicted by Eq. (2.4b), and a dashed line, representing the limiting case of infinitely large aqueous pores (see Eq. (2.42), where $r_{pore} \rightarrow \infty$ and $H(\lambda) = 1$, have been added for reference.

From an examination of Figures 6-2a through 6-2c, one may again conclude that the LTRs (see the open triangles) are more permeable than the non-LTRs (see the open circles) for each of the three delivery systems considered. If it is assumed that the porosity and the tortuosity ratios are unity (as was done by Peck *et al.* and by Tang *et al.*),[4,5] it is then possible to determine the value of the hindrance factor ratio using Eq. (2.4b), from which the average available pore radii, r_{pore}, may be determined. The values of the hindrance factor ratios and of the average available pore radii are reported in Table 6-1. An examination of the values of the hindrance factor ratios reveals that the hindrance factor ratio in the LTRs is significantly larger ($p<0.05$, using the t-statistic for the difference in the two means[11]) than in the non-LTRs. This observed difference in the hindrance factor ratios in the LTRs and in the non-LTRs also leads to a difference in the average available pore radii in the LTRs and in the non-LTRs. From Table 6-1, the average available pore radius in the LTRs is also significantly larger ($p<0.05$) than the average available pore radius in the non-LTRs. These results, obtained using the analysis methods of Peck *et al.* and of Tang *et al.*,[4,5] suggest that the aqueous pores formed in the LTRs have a larger average radius than the aqueous pores formed in the non-LTRs. This observation further supports the hypothesis presented in Chapters 4 and 5,[1,2] that there are two distinct mechanisms of enhancement operating in skin treated simultaneously with a chemical enhancer (SLS) and low-frequency ultrasound. This observation also

Table 6-1: Values of the Hindrance Factor Ratio, $H(\lambda)_{3H}/H(\lambda)_{Urea}$, and of the Average Available Pore Radii of the LTRs and the non-LTRs Calculated from the Steady-State Permeability Data Obtained from the Mannitol-Urea, the Raffinose-Urea, and the Inulin-Urea Delivery Systems.

Delivery System	Skin Type	$\frac{H(\lambda)_{3H}}{H(\lambda)_{Urea}}$	Average Available Pore Radii[b] (Å)		
			Low	Average	High
Mannitol-Urea	Non-LTRs	0.87 ± 0.11[a]	38	70	450
	LTRs	2.10 ± 0.85	∞	∞	∞
Raffinose-Urea	Non-LTRs	0.23 ± 0.10	15	18	22
	LTRs	0.49 ± 0.19	21	32	54
Inulin-Urea	Non-LTRs	0.37 ± 0.15	36	51	72
	LTRs	0.66 ± 0.13	74	108	182

a – Errors correspond to $\pm$ 1 S.D.
b – The high and the low values reported correspond to 1 standard deviation from the average value of the aqueous pore radii.

contradicts the claim made by Tang *et al.*[5] and by Tezel *et al.*[6] that ultrasound only forms additional aqueous pore channels that have similar structural properties to those present in untreated skin. However, in the previous studies, the hindrance factor ratio and the average available pore radius were evaluated over the entire region of ultrasound-treated skin, since it was assumed that low-frequency ultrasound perturbed the skin uniformly over the entire area of exposed skin. As my studies in Chapters 4 and 5 have demonstrated, this assumption on the uniformity of ultrasound enhancement of the skin can no longer be considered valid.

6.3.3 Evaluation of the Distribution of Pore Radii, the Porosity, and the Tortuosity as a Function of both the Radius of the Hydrophilic Permeant and the Extent of Skin Perturbation Induced in the LTRs and in the Non-LTRs

In the previous section, the hindrance factor ratio and the average available pore radius were evaluated in the context of the aqueous pore pathway hypothesis using two simplifying assumptions: (1) the porosity and the tortuosity of the aqueous pore channels do not depend on the radius of the permeant delivered across the skin, and (2) the two permeants being delivered across the skin are able to access the same aqueous pore channels. In this section, the permeability data obtained from the three delivery systems considered are again analyzed in the context of the aqueous pore pathway hypothesis to evaluate the hindrance factor, the porosity, and the tortuosity as a function of both the extent of skin perturbation and the radius of the permeant considered. The results are reported in Table 6-2. In this analysis, the possible existence of a distribution of aqueous pore radii in the skin is considered, as proposed by Tezel *et al.* (see Eq. (2.40)),[6] which, in turn, also allows for the possibility that the porosity and the tortuosity of the aqueous pore channels may depend on the radius of the permeant which is delivered across the skin.

An initial examination of the data reported in Table 6-2 indicates that some of the values obtained for the porosity and the tortuosity are physically unrealizable. For the porosity, the upper bound of physically realizable values is unity, which corresponds to the entire surface area of the skin being available for transport. From Table 6-2, the average values of the porosities of urea, of mannitol, and of raffinose in the LTRs are all

Table 6-2: Values of the Hindrance Factor, $H(\lambda)$, the Porosity, ε, and the Tortuosity, τ, of the LTRs and the non-LTRs Calculated from the Permeability Data Obtained from the Mannitol-Urea, the Raffinose-Urea, and the Inulin-Urea Delivery Systems Using the Methods Presented in Section 2.4.6 for the Case of a Distribution of Pore Radii.[a]

Permeant	Non-LTRs			LTRs		
	$H(\lambda)$	ε	τ	$H(\lambda)$	ε	τ
Urea	0.49 ± 0.37	0.28 ± 0.15	1.44 ± 0.61	0.69 ± 0.39	1.01 ± 1.10	2.04 ± 0.77
Mannitol	0.94 ± 0.15	0.20 ± 0.03	3.35 ± 0.41	0.84 ± 0.39	1.40 ± 0.80	2.87 ± 1.14
Raffinose	0.02 ± 0.02	0.27 ± 0.05	0.20 ± 0.24	0.40 ± 0.48	1.54 ± 2.01	1.01 ± 0.95
Inulin	0.03 ± 0.03	0.18 ± 0.06	0.20 ± 0.13	0.53 ± 0.51	0.56 ± 0.37	0.95 ± 0.71

a – The errors correspond to $\pm$ 1 S.D.

greater than the upper bound of unity. Since the error bars associated with these values of the porosity do include unity, one may claim that the porosity of urea, of mannitol, and of raffinose in the LTRs is not statistically greater than the upper bound of unity. For the tortuosity, the lower bound of physically realizable values is also unity, which corresponds to the permeant traversing the skin along a straight path perpendicular to the skin surface. From Table 6-2, the average values of the tortuosities of raffinose and of inulin in the non-LTRs, and of inulin in the LTRs, are all less than the lower bound of unity. Since the error bars associated with the value of the tortuosity of inulin in the LTRs includes unity, one may claim that the tortuosity of inulin is not statistically less than the lower bound of unity. However, for the values of the tortuosities of raffinose and of inulin in the non-LTRs, the error bars do not include unity, and, therefore, one

must conclude that the values of the tortuosities of raffinose and of inulin in the non-LTRs are statistically less than the lower bound of unity.

Comparing the values of the hindrance factor, of the porosity, and of the tortuosity reported for the four permeants for delivery in the non-LTRs, there is considerable statistically significant variation in the values of the hindrance factors and of the tortuosities, while there appears to be little statistically significant variation in the values of the porosities. Specifically, five of the six permeant pairs (urea-mannitol, urea-raffinose, urea-inulin, mannitol-raffinose, and mannitol-inulin) have significant differences ($p<0.05$) in the values of the hindrance factors and of the tortuosities, while raffinose-inulin is the only permeant pair that has a significant difference ($p<0.05$) in the porosity. This result for the porosity would suggest that the porosity in the LTRs can be considered to be independent of the permeant radius, and, therefore, to be an intrinsic property of the skin, which is consistent with the observations made in Chapter 2. Even though there is evidence that the values of these parameters depends on the radii of the permeants, due to the large values of the hindrance factor and of the tortuosity corresponding to mannitol, there is no clear decreasing trend in these values as the radius of the permeant increases, as was observed in Chapter 2.

In the LTRs, there is less statistically significant variation in the hindrance factor, in the porosity, and in the tortuosity for the four permeants considered. There is no statistically significant difference ($p>0.05$) in the values of the hindrance factors for any of the six permeant pairs considered. This result suggests that there is no dependence of the hindrance factor on the radius of the permeant, which is contrary to the result expected based on Eqs. (2.2) and (2.3). In addition, only one permeant pair, mannitol-

inulin, has a significant difference ($p<0.05$) in the corresponding values of the porosities. Similar to the results obtained for the non-LTRs, this result would again suggest that the porosity in the LTRs can be considered to be independent of the permeant radius, and, therefore, to be an intrinsic property of the skin, which is consistent with the observations made in Chapter 2. These statistical results for the hindrance factor and for the porosity, however, are primarily due to the large variations in the calculated values of the hindrance factor, of the porosity, and of the tortuosity, especially for the data corresponding to the LTRs, as indicated by the large values of the standard deviations reported in Table 6-2. Finally, for the tortuosity, only three permeant pairs, urea-inulin, mannitol-raffinose, and mannitol-inulin, have statistically significant differences ($p<0.05$) in their tortuosity values. Based on this statistical analysis, there is no significantly observable increasing, or decreasing, trend in the value of the tortuosity in the LTRs as a function of the radius of the permeant.

Comparing the values of the hindrance factor, the of porosity, and of the tortuosity reported in Table 6-2 in the non-LTRs and in the LTRs for each of the four permeants, in all cases except one, the calculated p value from the t-test is greater than 0.05, corresponding to less than 95% confidence. This result would suggest that there is little statistical difference between the values of these structural parameters reported for the non-LTRs (lower extent of skin perturbation due to ultrasound) and for the LTRs (higher extent of skin perturbation due to ultrasound). This statistical result is again due to the large variations in the calculated values of the hindrance factor, the porosity, and the tortuosity, especially for the data corresponding to the LTRs, as indicated by the large values of the standard deviations reported in Table 6-2. These large standard deviation

values are the result of large variations in the shape of the distribution of pore radii, characterized by the value of σ in Eq. (2.40), which were found to range in value from 3 Å to infinity.

As in Chapter 2, given that the values reported for the porosity and the tortuosity corresponding to some permeants are physically unrealizable, and that there is a large variation in the value of σ for the distribution of pore radii, it is questionable whether hindered transport, as modeled by the distribution of pore radii proposed by Tezel *et al.*,[6] is useful to the overall modeling of hydrophilic transdermal transport. Therefore, it is instructive to evaluate the porosity and the tortuosity of the aqueous pore channels in the LTRs and in the non-LTRs as a function of the extent of skin perturbation and of the permeant radius for the limiting case of infinitely large pores, for which $r_{pore} \rightarrow \infty$ and $H(\lambda) = 1$ (see Eqs. (2.2) and (2.3)).

6.3.4 Evaluation of the Porosity and the Tortuosity as a Function of Both the Radius of the Hydrophilic Permeant and the Extent of Skin Perturbation in the LTRs and in the non-LTRs for the Limiting Case of Infinitely Large Aqueous Pores

In this section, the analysis carried out in Section 6.3.3 is repeated for the limiting case of infinitely large aqueous pore channels, where $r_{pore} \rightarrow \infty$ and $H(\lambda) = 1$. The values of the porosity and the tortuosity of the aqueous pore channels present in the LTRs and in the non-LTRs for each of the four permeants considered are reported in Table 6-3. By assuming that the aqueous pores are infinitely large, and, therefore, that hindered

Table 6-3: Values of the Porosity, ε, and the Tortuosity, τ, of the LTRs and the non-LTRs Calculated from the Permeability Data Obtained from the Mannitol-Urea, the Raffinose-Urea, and the Inulin-Urea Delivery Systems Using the Methods Presented in Section 2.4.6 for the Case of Infinitely Large Aqueous Pores.[a]

Permeant	Non-LTRs		LTRs	
	ε	τ	ε	τ
Urea	0.15 ± 0.04	2.25 ± 0.26	0.50 ± 0.30	2.63 ± 0.53
Mannitol	0.21 ± 0.03	3.47 ± 0.21	1.00 ± 0.29	3.34 ± 0.43
Raffinose	0.03 ± 0.02	1.70 ± 0.55	0.20 ± 0.11	2.43 ± 0.38
Inulin	0.03 ± 0.01	1.20 ± 0.23	0.23 ± 0.11	1.51 ± 0.12

a – The errors correspond to ± 1 S.D.

transport does not contribute to the transdermal transport of the hydrophilic permeants, more physically realizable results for both the porosity and the tortuosity can be obtained. Specifically, the average values of the tortuosities, τ, in both the LTRs and in the non-LTRs, are all greater than the lower bound of 1. Likewise, the average values of the porosities, ε, in both the LTRs and in the non-LTRs, are all lower than, or equal to, the upper bound of 1. These results, physically, are an improvement over the results reported in Table 6-2, which include porosity values that are greater than 1 (see the delivery of urea, mannitol, and raffinose in the LTRs in Table 6-2) and tortuosity values that are lower than 1 (see the delivery of raffinose and inulin in the non-LTRs, and the delivery of inulin in the LTRs in Table 6-3).

In addition, the values of the porosities and the tortuosities reported in Table 6-3 also indicate that these quantities do depend on the nature of the permeant delivered transdermally. In the non-LTRs, there is a significant difference ($p<0.05$) in the porosity values of all the permeant pairs except for raffinose and inulin, which have statistically similar porosity values. Likewise, there is a significant difference in the tortuosity values of urea and mannitol, urea and inulin, mannitol and raffinose, and mannitol and inulin. However, as with the data reported in Table 6-2, there is no clear decreasing trend in the porosity values and in the tortuosity values as a function of the permeant radius in the LTRs and in the non-LTRs, since the values of the porosity and the tortuosity of mannitol are higher than those of urea.

Finally, a comparison of the porosity and the tortuosity values corresponding to the LTRs with those corresponding to the non-LTRs reported in Table 6-3 suggests that there is a greater difference in the porosity of the LTRs and of the non-LTRs than in the tortuosity values of the LTRs and of the non-LTRs for the four permeants considered. Specifically, the porosity values reported for the LTRs are 3-fold to 8-fold larger than those reported for the non-LTRs for the four permeants considered, while there is only a significant difference ($p<0.05$) in the reported tortuosity values of the non-LTRs and the LTRs for raffinose and inulin. These results suggest that the primary difference between the non-LTRs and the LTRs, under the assumption that the aqueous pore channels are infinitely large, is that a greater fraction of the skin surface is made available for transport in the LTRs than in the non-LTRs. In fact, the observed difference in the porosity values of the LTRs and the non-LTRs is in excellent agreement with the observed difference in the permeability values of the LTRs and the non-LTRs reported in Section 6.3.1 (3-fold

to 10-fold). These differences further confirm that there are two distinct levels of skin perturbation induced by the simultaneous treatment of the skin with a chemical enhancer (SLS) and low-frequency ultrasound leading to the formation of the LTRs and the non-LTRs.

6.3.5 Proposed Mechanism of Enhancement in Skin Treated Simultaneously with a Chemical Enhancer and Low-Frequency Ultrasound

Prior to the studies carried out as part of this thesis, transient cavitation events near the skin surface were thought to be the primary mechanism responsible for the observed enhancement of the transdermal transport of hydrophilic permeants in skin treated simultaneously with SLS, a chemical enhancer, and low-frequency ultrasound,[12] as well as in skin treated solely with low-frequency ultrasound.[13] Furthermore, from an analysis of the skin permeability and the skin electrical resistivity measurements in the context of the aqueous pore pathway hypothesis, it was demonstrated that new aqueous pore channels, similar in radius to those present in untreated skin, were formed in skin treated simultaneously with a chemical enhancer and low-frequency ultrasound,[6] as well as in skin treated solely with low-frequency ultrasound.[5] Finally, it was assumed that the observed enhancement due to ultrasound treatment of the skin was uniform over the entire surface of the treated skin sample.

In Chapter 2, it was shown that ultrasound treatment of the skin: (i) increases the porosity values by orders of magnitude, while the tortuosity decreases at most by a factor of 3-fold, and (ii) results in no significant increase, or decrease, in the hindrance factor,

over the range of ultrasound conditions studied. These results suggest that the observed enhancement in the transdermal transport of hydrophilic permeants result primarily from an interaction of the skin surface with the low-frequency ultrasound waves and the surfactant, SLS. These results, then, provide further support for the idea that ultrasound enhancement is the result of transient cavitation events, which are triggered by the ultrasound acoustic field, acting near the skin surface.

In Chapter 4, the skin permeability and the skin electrical resistivity of both the LTRs and the non-LTRs were evaluated for this first time. The results of this investigation clearly demonstrated that two distinct levels of enhancement can be observed in skin treated simultaneously with SLS and low-frequency ultrasound. In addition, the porosity-to-tortuosity ratio corresponding to the LTRs was compared to a threshold value of the porosity-to-tortuosity ratio corresponding to the intercellular domains of the stratum corneum, calculated in Chapter 3, to demonstrate that transcellular permeation pathways may be present in the LTRs formed in skin treated simultaneously with SLS and low-frequency ultrasound. Both of these observations – the presence of two levels of enhancement and of transcellular permeation pathways in the LTRs – were confirmed in Chapter 5 using Two-Photon Microscopy. These results suggested that skin treated simultaneously with SLS and low-frequency ultrasound is not uniformly enhanced, as was previously assumed.

In the analyses presented in this chapter, the key observations made in Chapters 4 and 5, that ultrasound-treated skin is not uniformly enhanced, are again confirmed. The steady-state analysis methods of Peck *et al.*[4] and of Tang *et al.*[5] revealed that the values of the hindrance factor and of the average available pore radius are significantly larger in

the LTRs than in the non-LTRs for the each of the three delivery systems (mannitol-urea, raffinose-urea, and inulin-urea) considered. This result suggests that a single application of low-frequency ultrasound produces aqueous pore channels having different radii in different regions of the skin. Evaluation of the porosities and the tortuosities in the LTRs and in the non-LTRs for the case where $r_{pore} \rightarrow \infty$ and $H(\lambda) = 1$ revealed that the differences observed in the porosity values in the LTRs and in the non-LTRs for each of the four permeants considered were much larger than the difference in the tortuosity values in the LTRs and in the non-LTRs. This result suggests that a surface-related phenomenon is primarily responsible for the observed difference in the transdermal transport of hydrophilic permeants in the LTRs and in the non-LTRs. Since the value of the porosity is much higher in the LTRs than in the non-LTRs, this surface-related phenomenon appears to cause a greater increase in the fraction of the skin surface occupied by the aqueous pore channels in the LTRs than in the non-LTRs. Since previous studies have demonstrated that transient cavitation events near the skin surface are the primary ultrasound enhancement mechanism,[12,13] it is likely that a greater number of these transient cavitation events occur over the surface of the skin where the LTRs will eventually form relative to the number of transient cavitation events that occur over the surface of the skin where the non-LTRs will eventually form. This hypothesis may be confirmed by future studies (see Section 7.2.3) which would need to demonstrate: 1) the existence of spatial variations in the density of transient cavitation events near the skin surface (defined as the number of cavitation events per unit area), and 2) that high density regions of transient cavitation events near the skin surface result in the formation of the highly permeable LTRs which are observed in ultrasound-treated skin.

6.4 Conclusions

In this chapter, I evaluated the hindrance factor, the porosity, and the tortuosity of the LTRs and the non-LTRs formed in skin treated simultaneously with a chemical enhancer (the surfactant, SLS) and low-frequency sonophoresis, for four hydrophilic permeants, using three different analysis approaches.

In the first analysis approach, steady-state permeabilities were used to evaluate the hindrance factor and the average available pore radius for the case where the porosity and the tortuosity were assumed to be independent of the radius of the permeant being delivered transdermally. The results obtained using this analysis approach revealed that both the hindrance factor and the average available pore radius are significantly larger in the LTRs than in the non-LTRs. These results suggest that ultrasound treatment results in larger aqueous pore channels in the LTRs than in the non-LTRs, an indication that two separate enhancing mechanisms are exploited by ultrasound to make the skin more permeable to hydrophilic permeants.

In the second analysis approach, transient and steady-state diffusion data were used to evaluate the hindrance factor, the porosity, and the tortuosity for the case where a distribution of pore radii was assumed to exist in the skin. The results of this analysis approach revealed little statistical difference in the values of the hindrance factor, of the porosity, and of the tortuosity of the LTRs as compared to those of the non-LTRs due to the large values of the standard deviations in the hindrance factor, in the porosity, and in the tortuosity calculated from the experiments conducted in the LTRs. Because of the large variation in the σ parameter, which determines the shape of the function characterizing the distribution of pore radii, from 3 Å to infinity, and some physically

unrealizable values of the porosity and the tortuosity, it is questionable whether the distribution of pore radii given in Eq. (2.40) accurately describes the range of aqueous pore radii present in the skin. This finding is consistent with observations made in Chapter 2 using this analysis approach.

In the final analysis approach, transient and steady-state diffusion data were again used to evaluate the porosity and the tortuosity for the limiting case where the aqueous pore channels are infinitely large, such that hindered transport may be neglected (i.e. $H(\lambda) = 1$). The results of this analysis approach revealed that the primary difference between the LTRs and the non-LTRs is in the values of the porosity. For the four permeants considered, the porosity values of the LTRs are 3-fold to 8-fold larger than the porosity values of the non-LTRs, which is excellent agreement with the observed difference in the permeability values of the LTRs and the non-LTRs (3-fold to 10-fold) There is also a small difference in the tortuosity values of the LTRs and the non-LTRs for the four permeants considered, but the difference is much smaller, only 50% difference in the tortuosity values, compared to the observed differences in the porosity values. These results suggest that the difference in the permeabilities of the LTRs and of the non-LTRs is due to the creation of more aqueous channels in the LTRs than in the non-LTRs.

The observations made using these three analysis approaches provide additional support for the hypothesis put forward in Chapters 4 and 5 that enhancement of the skin due to ultrasound treatment does not occur via a uniform, homogeneous process. From the data obtained on the structural parameters of the aqueous pore channels in the LTRs and in the non-LTRs, it appears that transient cavitation events near the skin surface, which were previously shown to be the primary enhancing mechanism of low-frequency

ultrasound, occur more frequently over the areas of the skin which eventually become the LTRs. It is the main closing hypothesis of this thesis, then, that these high density domains of transient cavitation events near the skin surface (defined as the number of cavitation events per unit area) are responsible for the formation of the highly permeable LTRs, as well as for the formation of transcellular pathways associated with the transdermal transport of hydrophilic permeants within the LTRs.

6.5 References

1. Kushner J, Blankschtein D, and Langer R. 2004. Experimental demonstration of highly permeable localized transport regions in low-frequency sonophoresis. J Pharm Sci. 93:2733-2745.
2. Kushner J, Deen W, Blankschtein D, and Langer R. First-principles, structure-based transdermal transport model to evaluate lipid partition and diffusion coefficients of hydrophobic permeants solely from stratum corneum permeation experiments. (Submitted to J Pharm Sci).
3. Kushner J, Kim D, So PTC, Blankschtein D, and Langer R. Dual-channel two-photon microscopy study of transdermal transport in skin treated with low-frequency ultrasound and a chemical enhancer. (Submitted to J Invest Dermatol).
4. Peck KD, Ghanem AH, and Higuchi WI. 1994. Hindered diffusion of polar molecules through and effective pore radii estimates of intact and ethanol treated human epidermal membrane. Pharm Res 11:1306-1314.
5. Tang H, Mitragotri S, Blankschtein D, Langer RS. 2001. Theoretical description of transdermal transport of hydrophilic permeants: Application to low-frequency sonophoresis. J Pharm Sci 90:545-568.
6. Tezel A, Sens A, and Mitragotri S. 2003. Description of transdermal transport of hydrophilic solutes during low-frequency sonophoresis based on a modified porous pathway model. J Pharm Sci. 92: 381-393.
7. Tang H, Blankschtein D, Langer R. 2002. Effects of low-frequency ultrasound on the transdermal permeation of mannitol: Comparative studies with in vivo and in vitro skin. J Pharm Sci 91:1776-1794.

8. Tang H, Mitragotri S, Blankschtein D, Langer RS. 2001. Theoretical description of transdermal transport of hydrophilic permeants: Application to low-frequency sonophoresis. J Pharm Sci 90:545-568.

9. Tezel A, Sens A, Tuchscherer J, Mitragotri S. 2002. Synergistic effect of low-frequency ultrasound and surfactants on skin permeability. J Pharm Sci 91:91-100.

10. Deen W. 1998. Analysis of Transport Phenomena. Oxford: New York. P. 19.

11. Montgomery DC, Runger GC, Hubele NF. 1998. Engineering Statistics. John Wiley & Sons, Inc. New York.

12. Tezel A, Sens A, Mitragotri S. 2002. Investigations of the role of cavitation in low-frequency sonophoresis using acoustic spectroscopy. J Pharm Sci 91:444-453.

13. Tang H, Wang CCJ, Blankschtein D, Langer R. 2002. An investigation of the role of cavitation in low-frequency ultrasound-mediated transdermal drug transport. Pharm Res 19:1160-1169.

Chapter 7

Thesis Summary and Proposed Future Research Directions

7.1 Thesis Summary

The central goal of this thesis has been to build upon, and to extend, previous research in the areas of both passive and ultrasound-enhanced transdermal drug delivery. Specifically, I have further examined the theoretical modeling of the transdermal transport of both hydrophilic permeants (Chapter 2) and of hydrophobic permeants (Chapter 3). These modeling studies were subsequently used to further our understanding of the mechanism by which low-frequency ultrasound enhances transdermal drug delivery. My investigations in the field of low-frequency sonophoresis focused on furthering our understanding of the localized transport regions (LTRs), and the surrounding regions of the skin (the non-LTRs), that form in skin treated with low-frequency ultrasound in the presence of a chemical enhancer, the surfactant – sodium lauryl sulfate (SLS). Specifically, these studies examined: 1) if the LTRs are, in fact, regions of high permeability through the use of diffusion masking experiments (Chapter 4), 2) what types of permeation pathways exist in the LTRs and in the non-LTRs through

the use of dual-channel two-photon microscopy (Chapter 5), and 3) the differences in the values of the porosity, the tortuosity, and the hindrance factor associated with the aqueous-pore channels located in the LTRs and in the non-LTRs that form in skin treated simultaneously with low-frequency sonophoresis and the chemical enhancer SLS through the use of the aqueous-pore pathway hypothesis (Chapter 6). The key results from each of these five research topics are summarized in greater detail below.

In Chapter 2, the aqueous pore pathway hypothesis was extended to model the transient domain of the transdermal transport of hydrophilic permeants, in addition to the previously-investigated steady-state domain, to verify various assumptions regarding the behavior of the hindrance factor, the tortuosity, and the porosity as a function of both permeant radius and the extent of skin perturbation. Diffusion experiments were conducted with ^{14}C-urea combined with tritium-labeled mannitol, tritium-labeled raffinose, or tritium-labeled inulin as the model permeants. An analysis of the cumulative amount of the permeant delivered per unit area, Q(t), as a function of time, t, showed that the lag time to reach steady-state was 10-fold to 40-fold lower in the dermis than in untreated full-thickness skin, indicating that the tortuosity of the aqueous pore channels does not increase with increasing skin perturbation, contrary to a suggestion made previously by Tezel *et al.*[11]

Analysis of the steady-state permeability data by linear regression revealed that the slope of the best-fit line through the steady-state permeability data was statistically similar to the predicted slope of 1 over the range of permeant radii investigated in this study (r_p = 2.6 Å – 12 Å). Using steady-state analysis methods, I showed that the average available aqueous pore radius ranges in size from 41 Å to infinity. Given the

large range of values for the average available aqueous pore radius, as well as the large value of the standard deviation in the average available pore radius (in some cases varying from 21 Å to infinity), it is questionable whether the inclusion of a hindrance factor improves the overall modeling of transdermal transport of hydrophilic permeants.

To further investigate the need to include the hindrance factor, as well as to investigate how the porosity and the tortuosity vary as a function of the permeant radius and the of extent of skin perturbation, the Q(t) vs. t data were analyzed with the proposed model equations describing the transdermal transport of hydrophilic permeants in the transient and the steady-state domains. For the case where a distribution of pore radii exists in the skin, as proposed by Tezel *et al.*,[11] my results indicated that: 1) the value of the hindrance factor depends on the radius of the permeant delivered through the skin, while there is little change in the value of the hindrance factor as a function of the extent of skin perturbation, 2) the value of the porosity does not depend on the radius of the permeant delivered, while the value of the porosity increases as the extent of skin perturbation increases, and 3) the value of the tortuosity decreases as the radius of the permeant increases, while there is little evidence that the tortuosity depends on the extent of skin perturbation. These trends would seem to suggest that ultrasound treatment of the skin results in the formation of aqueous pore channels that are structurally similar to those found in untreated skin.

Because the tortuosity values of inulin where found to be statistically significantly lower than unity, and because of the large standard deviations in the hindrance factor values of urea, mannitol, and raffinose, the values of the porosity and the tortuosity were also evaluated in the limiting case of infinitely large aqueous pores ($r_{pore} \rightarrow \infty$). This

analysis showed that, similar to the previous case where a distribution of aqueous pore channels was assumed to exist in the skin, the tortuosity exhibited some dependence on the radius of the permeant, while the porosities of urea, of mannitol, and of raffinose were found to be statistically similar. In addition, a significant decrease in the tortuosity of each permeant was observed as a function of the extent of skin perturbation. While the use of infinitely large pores resulted in tortuosity values of inulin which were greater than unity, the value of the porosity for inulin was found to be significantly lower than those of the other three permeants considered, suggesting that there were some aqueous pore channels which could not be accessed by inulin due to its larger radius. These results indicate that additional studies are needed to improve the model for the distribution of the aqueous pore radii in the skin to better understand the transdermal transport of inulin, and other large hydrophilic permeants, in the context of the aqueous pore pathway hypothesis.

In Chapter 3, a new theoretical model that describes Fickian diffusion of hydrophobic molecules which diffuse through the intercellular lipid domains of the stratum corneum was developed from first principles. This new theoretical model, the two-tortuosity model, utilized the structural parameters of the stratum corneum to evaluate the porosity and the tortuosity parameters. The novel feature in the model was the introduction of two tortuosity factors in the model equations, which accounted for: 1) the total amount of lipids in the SC, and 2) the impact of parallel diffusion pathways on the diffusive flux through the SC. Based on a regression analysis of data obtained from the simulated stratum corneum diffusion experiments performed with FEMLAB, the two-tortuosity model deduced K_b, the vehicle-lipid partition coefficient, and D_b, the diffusion coefficient of the permeant in the lipid bilayers, to within a 2-3% error for native stratum

corneum structures, out-performing all the five previous structure-based transport models considered. The regressed values of K_b = 233 ($\pm$44) and D_b = 1.6*10^{-7} ($\pm$0.3*10^{-7}) cm^2/s for naphthol and of K_b = 100 ($\pm$31) and D_b = 1.8*10^{-8} ($\pm$0.5*10^{-8}) cm^2/s for testosterone, obtained using the two-tortuosity model, were comparable to the values obtained using two previously published experimental techniques: 1) permeation experiments combined with octanol-water partition experiments, and 2) permeation experiments combined with solute-release experiments. This result demonstrated that K_b and D_b values of hydrophobic permeants can be evaluated solely from permeation experiments using the new theoretical model, which should greatly simplify the experimental method used to evaluate K_b and D_b of hydrophobic permeants.

In Chapter 4, the focus of the thesis shifted from examining transdermal transport models to examining the mechanism of enhancement in skin samples treated with ultrasound in the presence of a chemical enhancer (the surfactant, SLS). Specifically, a series of diffusion masking experiments with ultrasound-treated full-thickness pig skin were performed for the purpose of demonstrating quantitatively that the patterns of "red spots" observed on the skin when the red-colored hydrophilic permeant SRB and the chemical enhancer SLS are used in the ultrasound coupling medium are, indeed, markers for localized regions of high transdermal permeability. The results of these experiments, carried out over a range of skin electrical currents (225 – 325 μAmps), revealed that the transdermal permeability of the LTRs is 80-fold higher, on average, than the transdermal permeability of the less permeable non-LTRs. Although most of the transdermal delivery occurs in the more permeable LTRs, an analysis of the skin electrical resistivity data also indicated that there is a significant enhancement in both the highly permeable LTRs and

in the less permeable non-LTRs when compared to untreated skin (~5000-fold and ~170-fold, respectively). This suggests that the skin may be experiencing two levels of structural perturbation in the ultrasound/SLS system. Finally, by comparing the (ε/τ) values of the less permeable non-LTRs and of the highly permeable LTRs with the (ε/τ) value of the intercellular regions of the SC obtained in Chapter 3 for steady-state transport ($3.6*10^{-4}$), it was suggested that the transdermal transport pathways that exist in the less permeable non-LTRs may be entirely intercellular, while the transdermal transport pathways that exist in the more permeable LTRs are likely to be both intercellular and transcellular.

In Chapter 5, dual-channel two-photon microscopy (TPM) studies were performed to confirm the existence of transcellular transdermal transport pathways in the more permeable LTRs, as well as to better understand how two levels of structural perturbation may be induced in skin samples treated simultaneously with low-frequency ultrasound and SLS, which were both observed in Chapter 4. Dual-channel TPM images were generated and analyzed to compare the transdermal delivery of SRB, a fluorescent hydrophilic permeant, and of RBHE, a fluorescent hydrophobic permeant, in skin treated with SLS (a chemical enhancer), with ultrasound, and with the simultaneous application of ultrasound and SLS, with the transdermal delivery of SRB and of RBHE in untreated skin. From an analysis of the dual-channel TPM images as a function of skin depth for SRB and for RBHE, it was observed that both SRB and RBHE penetrate into the viable epidermis in the LTRs of US-treated and of US/SLS-treated skin, while the penetration of SRB and of RBHE was confined solely to the stratum corneum in untreated skin, in SLS-treated skin, and in the non-LTRs of US-treated and of US/SLS-treated skin. From an

analysis of the average fluorescence intensity profiles and the values of E_K (the enhancement in the vehicle-skin partition coefficient), E_G (the enhancement in the fluorescent permeant intensity gradient in the skin), and E_L (the enhancement in the effective diffusion path length), which were obtained from the average fluorescence intensity profiles, it was observed that two significant levels of skin perturbation exist when the skin is treated simultaneously with ultrasound and with a chemical enhancer (i.e. SLS or ethanol). Greater perturbation of the skin was observed in the LTRs of skin treated with ultrasound and a chemical enhancer relative to the extent of skin perturbation observed in the non-LTRs of skin treated with ultrasound and a chemical enhancer. These results are consistent with our previous conclusions reached using the skin electrical resistivity measurements of the non-LTRs and of the LTRs presented in Chapter 4. In the absence of a chemical enhancer during ultrasound treatment of the skin, the non-LTRs were found not to be significantly enhanced by ultrasound, as compared to untreated skin. This result suggests that ultrasound, in the absence of a chemical enhancer, discretely enhances the skin through the mechanism of transient acoustic cavitation near the skin surface. This result also suggests that the presence of a chemical enhancer in the coupling medium during ultrasound treatment of the skin is required to obtain two levels of significant enhancement in the perturbation of the skin structure. Finally, by comparing the heights and the widths of the fluorescence intensity peaks obtained from the dual-channel TPM images, transcellular pathways were observed in the LTRs of US-treated and of US/SLS-treated skin for both SRB and RBHE, as well as in SLS-treated skin for SRB. These observations provided confirmation of the results presented in Chapter 4 based on an analysis of the skin electrical resistivity data in the

context of the aqueous-pore pathway hypothesis, which suggested that transcellular pathways may be present in the LTRs of skin treated simultaneously with ultrasound and a chemical enhancer.

In Chapter 6, I evaluated the hindrance factor, the porosity, and the tortuosity of the LTRs and the non-LTRs formed in skin treated simultaneously with a chemical enhancer (the surfactant, SLS) and low-frequency sonophoresis, for four hydrophilic permeants, using three different analysis approaches.

In the first analysis approach, steady-state permeabilities were used to evaluate the hindrance factor and the average available pore radius for the case where the porosity and the tortuosity were assumed to be independent of the radius of the permeant being delivered transdermally. The results obtained using this analysis approach revealed that both the hindrance factor and the average available pore radius are significantly larger in the LTRs than in the non-LTRs. These results suggest that ultrasound treatment results in larger aqueous pore channels in the LTRs than in the non-LTRs, an indication that two separate enhancing mechanisms are exploited by ultrasound to make the skin more permeable to hydrophilic permeants.

In the second analysis approach, transient and steady-state diffusion data were used to evaluate the hindrance factor, the porosity, and the tortuosity for the case where a distribution of pore radii was assumed to exist in the skin. The results of this analysis approach revealed little statistical difference in the values of the hindrance factor, of the porosity, and of the tortuosity of the LTRs as compared to those of the non-LTRs due to the large values of the standard deviations in the hindrance factor, in the porosity, and in the tortuosity calculated from the experiments conducted in the LTRs. Because of the

large variation in the σ parameter, which determines the shape of the function characterizing the distribution of pore radii, from 3 Å to infinity, and some physically unrealizable values of the porosity and the tortuosity, it is questionable whether the distribution of pore radii given in Eq. (2.40) accurately describes the range of aqueous pore radii present in the skin. This finding is consistent with observations made in Chapter 2 using this analysis approach.

In the final analysis approach, transient and steady-state diffusion data were again used to evaluate the porosity and the tortuosity for the limiting case where the aqueous pore channels are infinitely large, such that hindered transport may be neglected (i.e. $H(\lambda) = 1$). The results of this analysis approach revealed that the primary difference between the LTRs and the non-LTRs is in the values of the porosity. For the four permeants considered, the porosity values of the LTRs are 3-fold to 8-fold larger than the porosity values of the non-LTRs, which is excellent agreement with the observed difference in the permeability values of the LTRs and the non-LTRs (3-fold to 10-fold) There is also a small difference in the tortuosity values of the LTRs and the non-LTRs for the four permeants considered, but the difference is much smaller, only 50% difference in the tortuosity values, compared to the observed differences in the porosity values. These results suggest that the difference in the permeabilities of the LTRs and of the non-LTRs is due to the creation of more aqueous channels in the LTRs than in the non-LTRs.

The observations made using these three analysis approaches provide additional support for the hypothesis put forward in Chapters 4 and 5 that enhancement of the skin due to ultrasound treatment does not occur via a uniform, homogeneous process. From the data obtained on the structural parameters of the aqueous pore channels in the LTRs

and in the non-LTRs, it appears that transient cavitation events near the skin surface, which were previously shown to be the primary enhancing mechanism of low-frequency ultrasound, occur more frequently over the areas of the skin which eventually become the LTRs. It is the main closing hypothesis of this thesis, then, that these high density domains of transient cavitation events near the skin surface (defined as the number of cavitation events per unit area) are responsible for the formation of the highly permeable LTRs, as well as for the formation of transcellular pathways associated with the transdermal transport of hydrophilic permeants within the LTRs.

7.2 Proposed Future Research Directions

7.2.1 Generalization of the Two-Tortuosity Model to More Complex Transdermal Transport Problems

In Chapter 3, the Two-Tortuosity model was developed to model the transdermal transport of permeants, which are confined to the intercellular regions of the stratum corneum. As such, the Two-Tortuosity model, in its present form, is applicable for transdermal drug delivery in specific cases (i.e. hydrophobic permeant delivery). Several avenues are available to generalize the Two-Tortuosity model to more accurately and broadly describe transport through human skin for a variety of permeants, including accounting for: 1) penetration into the corneocytes, 2) diffusion through the viable epidermis and the dermis, 3) non-uniformity in the stratum corneum structure as a function of depth, which can lead to a dependence of the partition and the diffusion coefficients on skin depth, and 4) the existence of shunt pathways – sweat glands and hair follicles – in the skin. Each of these added complexities to the Two-Tortuosity model of

transdermal transport could be introduced via a first-principles approach, similar to the methods used to derive the original Two-Tortuosity model from first principles (see Section 3.3 for details). To account for penetration into the corneocytes, a partition coefficient describing permeant partitioning between the intercellular and the corneocyte domains would need to be added to the Two-Tortuosity model, as well as adding a diffusion coefficient describing permeant transport in the corneocyte domain. Diffusion through the viable epidermis and the dermis may be addressed in a similar manner to penetration into the corneocyte domain (i.e. partition and diffusion coefficients for both the viable epidermis and the dermis would need to be incorporated into the model), with the additional requirement of estimating the skin structural parameters characterizing the viable epidermis and the dermis. Transport models for the viable epidermis and the dermis can then be added, in series, to the transport model for the stratum corneum to obtain an overall skin transport model. Variation in the SC structure as a function of skin depth can also be addressed in a similar manner to the addition of the viable epidermis and the dermis to the overall skin transport model. The stratum corneum consists of two layers: i) the stratum disjunctum, which comprises the outer layers of the stratum corneum and where desquamation of the corneocytes occurs, and ii) the stratum compactum, which comprises the inner layers of the stratum corneum and is more densely packed than the stratum disjunctum.[1] Specifically, these two layers can be modeled as two skin layers in series, similar to what was proposed to model the viable epidermis and the dermis. Finally, the presence of shunt pathways can be incorporated into the Two-Tortuosity model by modeling these pathways *in parallel* to transport through the stratum corneum. Transport through hair follicles and sweat glands may be

incorporated using modeling techniques similar to those used in the aqueous-pore pathway hypothesis, since transport through small, cylindrical-shaped channels is common to both hydrophilic transport through the skin and to transport through the shunt pathways. In addition, future modeling efforts should also be directed to better understanding how the tortuosity should be modeled in a 3-D representation of the stratum corneum. This investigation would help determine the accuracy of the 2-D modeling of transdermal transport relative to modeling transdermal transport with a 3-D representation of the stratum corneum.

7.2.2 Identification of Classes of Permeants that Exhibit Enhanced Delivery in the LTRs

In Chapters 4 and 6, I examined the transdermal delivery of several hydrophilic permeants, ranging in molecular weight from 182 Da to 5,000 Da, to evaluate the differences in their permeabilities in the LTRs and in the non-LTRs formed in skin treated simultaneously with low-frequency ultrasound and a chemical enhancer (SLS). Further studies examining the transdermal transport of several additional permeants through the LTRs and the non-LTRs should be conducted to determine what additional classes of permeants would benefit the most from the formation of the highly-permeable LTRs during ultrasound treatment of the skin. These permeants may include: 1) a low molecular weight hydrophobic permeant (for example, estradiol, MW = 272.4), 2) a high molecular weight hydrophobic permeant (for example, erythropoietin, MW = 34,000 Da), 3) drug-containing nanoparticles (diameter: 200-400 nm), 4) oligonucleotides (20 base pairs, ~12,000 Da), and 5) drug-containing liposomes (diameter: 70-200 nm). These

representative permeants should allow the determination of which classes of permeants would benefit the most from LTR formation in ultrasound-treated skin.

Specifically, *in vitro* diffusion masking experiments (see Section 4.2.6 for details) may be conducted with full-thickness pig skin as the model skin membrane for the five model permeants listed above. The skin should be pretreated with ultrasound, both in the presence and in the absence of SLS, according to the ultrasound pre-treatment protocol outlined in Section 4.2.4. Skin electrical current measurements can be carried out using the procedures outlined in Section 4.2.3. After ultrasound pretreatment, the skin can be digitally imaged, following the protocol outlined in Section 4.2.5, to determine the areas of the LTRs and of the non-LTRs on the skin. After digital imaging, the skin samples should be masked according to the protocol outlined in Section 4.6. After masking, a solution containing one of the five model permeants listed above, which should be radiolabeled, can be placed in the donor compartment of the diffusion cell. Diffusion of the radiolabeled permeant should continue under passive conditions for 48 hours, with samples being taken from the receiver cell at predetermined time points. These samples should be analyzed in a scintillation counter to determine the quantity of permeant delivered across the unmasked regions of the skin membrane. The permeability through these unmasked regions can be evaluated using Eq. (4.1). Transdermal permeability experiments with the radiolabeled permeants through untreated full-thickness pig skin samples should also be conducted to evaluate the permeability of each skin region relative to the permeability of untreated skin.

7.2.3 Mechanisms of LTR Formation in Low-Frequency Sonophoresis

In previous work, our group demonstrated that transient acoustic cavitation events near the skin surface are primarily responsible for the structural perturbations in skin exposed to low-frequency ultrasound, which lead to the observed enhancements in the transdermal permeabilities and in the skin electrical current measurements.[2] Because the LTRs consist of the most perturbed regions of the skin, I have hypothesized that transient acoustic cavitation events near the skin surface play a significant role in the formation of the LTRs (see Section 5.3.4). In order to better understand the formation of the LTRs formed by low-frequency ultrasound, I first propose demonstrating that transient acoustic cavitation events near the skin surface are required for LTR formation (see Section 7.2.3.1). I then propose examining how ultrasound, the skin surface topography, and the presence of a chemical enhancer (e.g. SLS) in the coupling medium affects LTR formation in skin exposed to low-frequency ultrasound (see Sections 7.2.3.2 and 7.2.3.3, respectively).

7.2.3.1 Investigation of the Role of Acoustic Cavitation in LTR Formation

In this set of experiments, full-thickness pig skin samples can be treated with low-frequency ultrasound at previously-investigated conditions (i.e. frequency – 20 kHz, intensity – 7.5 W/cm^2, duty cycle – 5 sec ON: 5 sec OFF, and tip displacement – 3 mm) using different coupling media to determine if acoustic cavitation events are indeed necessary for the formation of LTRs. The coupling media that can be used in these experiments include: i) castor oil, ii) degassed PBS, iii) regular PBS, and iv) gas-filled microspheres (e.g. Albunex) in a PBS solution. Castor oil, since it is highly viscous, has been shown to suppress acoustic cavitation events.[2,3] Also, degassed PBS will have reduced acoustic cavitation activity compared to regular PBS, since the dissolved gases,

which nucleate into cavitation bubbles, have been removed from the solution prior to ultrasound exposure. The coupling medium containing gas-filled microspheres should exhibit increased acoustic cavitation activity compared to regular PBS due to an increased amount of dissolved gas in the coupling medium, which should lead to an increase in the number of cavitation bubbles formed by exposure to low-frequency ultrasound.[2] The goal of this investigation would be to demonstrate that the size of the LTRs formed in the skin increases with the amount of dissolved gases in the coupling medium, and, therefore, with the amount of cavitation activity in the coupling medium.

7.2.3.2 Investigation of the Role of Ultrasound and Surface Topography in LTR Formation

In this section, I discuss how ultrasound and the surface topography affect the location of acoustic cavitation events in the skin. Specifically, investigations are proposed to examine how the dissolved gases in the coupling medium interact with the acoustic field generated by the ultrasound transducer and the surface topography to control where transient cavitation events occur, which lead to the formation of the LTRs on the skin surface. *Transient cavitation events near the skin surface* may be induced by dissolved gases in the coupling medium or on the skin surface. The skin surface may contain crevices, folds, and/or pores which can trap gases that lead to the acoustic cavitation events which result in LTR formation. For a material with a smooth surface, which would be unable to trap any gases, any *transient cavitation events near the skin surface* should result from the acoustic field interacting with the coupling medium. Similarly, for a material with a smooth surface, any variation in the pattern of acoustic cavitation activity would be the result of variations in the ultrasound acoustic field. Based on our

preliminary studies, when full-thickness pig skin samples are treated with identical US conditions in the presence of SLS, a variety of LTR patterns are generated.[4]

The following set of experiments is proposed to decouple the effect of the skin surface topography from the effect of the acoustic field on the location of *transient cavitation events near the skin.* (Recall that, as discussed in Section 7.2.3.1, it will be demonstrated that *transient cavitation events near the skin surface* are necessary to produce the LTRs.) A material with a smooth surface (for example, aluminum foil or another highly polished metal surface) may be exposed to identical ultrasound conditions, both in the presence and in the absence of the surfactant SLS. The size, location, and distribution of the pits formed from *transient cavitation events near the surface* can be recorded and compared for each sample. Since there is no variation in the surface topography, or in the ultrasound exposure conditions, there should be no variation in the pattern of pits on the material surface. (However, if a variation in the pattern of pits is observed when the samples are exposed to identical ultrasound conditions, one may conclude that *transient cavitation events near the skin surface* are chaotic and irreproducible.) The acoustic field used to treat the smooth-surfaced material may be varied by changing the transducer diameter and/or the ultrasound operating conditions. Again, any variations in the pattern of pits on the material surface would be a result of variations in the acoustic field. Finally, using identical ultrasound conditions, the surface smoothness may be varied by roughening selected portions of the material surface, to determine if the surface topography induces variations in the pattern of pits in the material surface. From these experiments, it should be possible to determine whether the

acoustic field, the surface topography, or both, are responsible for the pattern of pits on the material surface that result from *transient cavitation events near the material surface.*

7.2.3.3 Investigation of the Role of Chemical Enhancers in Low-Frequency Sonophoresis

From previous work, our group has demonstrated that SLS enhances the effect of ultrasound on the skin, significantly reducing the amount of time required to reach a desired level of skin perturbation.[5,6] I have also demonstrated that the presence of a chemical enhancer in the coupling medium during ultrasound treatment is required to achieve significant perturbation in the non-LTRs relative to untreated skin (see Chapter 5). I propose a series of experiments to determine how SLS, a model chemical enhancer, impacts LTR formation in ultrasound-treated skin, as well as the enhancement of the non-LTRs. SLS may be added to the coupling medium prior to ultrasound exposure at concentrations of 0%, 0.01%, 0.03% (the critical micelle concentration, beyond which SLS micelles form), 0.2%, and 1% (w/v). Ultrasound can then be applied to full-thickness pig skin and the patterns of LTRs may be observed for significant trends in formation and distribution. In addition, since acoustic cavitation events are the source of skin perturbation, and, therefore, likely the source of the LTRs, experiments with aluminum foil may also be conducted at the same SLS concentrations to determine if there are any changes in the pitting of the aluminum foil (observed by measuring the pit diameter and the pit depth) produced by the cavitation events. Skin electrical resistance measurements of the non-LTRs as a function of the concentration of SLS in the coupling medium may provide clues into the mechanisms by which a chemical enhancer produces a second, less perturbing level of enhancement in the non-LTRs. To investigate how the

non-LTRs are enhanced in the presence of a chemical enhancer during ultrasound treatment of the skin, additional mechanistic studies should be performed focusing on the secondary effects of ultrasound treatment of the skin – acoustic streaming, thermal effects, and microjet formation resulting from transient cavitation bubble collapse. Each of these three secondary mechanisms can be investigated in the following manner: 1) for acoustic streaming, experiments can be performed where the donor chamber is continuously mixed with a stir bar to approximate fluid velocities generated in the coupling medium during ultrasound treatment, 2) for thermal effects, the coupling medium can be heated to approximate temperatures reached in the coupling medium as a result of ultrasound treatment, and 3) for microjet formation, the results of Section 7.2.3.1 should allow determination of whether microjet formation is required for enhancement of the non-LTRs. Enhancements in the permeability and the electrical resistivity of the skin from these three experiments, relative to untreated skin, can then be compared to the enhancements in the skin permeability and the skin electrical resistivity for the non-LTRs formed in skin treated simultaneously with ultrasound and a chemical enhancer to determine which secondary mechanism, if any, is responsible for the observed enhancement in the non-LTRs. These investigations should better elucidate how SLS impacts the acoustic cavitation events leading to the formation of the LTRs, as well as the enhancement in the perturbation of the non-LTRs.

7.2.4 Additional Investigations of the Non-LTRs and the LTRs using Dual-Channel Two-Photon Microscopy (TPM)

While significant progress was made using dual-channel TPM to elucidate the types of transport pathways and mechanisms of enhancement in skin treated with ultrasound and chemical enhancers in Chapter 5, there are three additional areas of study that may be explored using TPM: 1) investigation of the non-LTRs and the LTRs using wide-field TPM, 2) investigation of the number of samples required to achieve representative results from TPM images in the non-LTRs and in the LTRs, and 3) investigation of the depth of transcellular pathway penetration in the LTRs. I provide details of (1) – (3) below.

7.2.4.1 Investigation of the Non-LTRs and the LTRs Using Wide-Field TPM

Wide-field TPM has been previously used by our group in the area of chemical enhancers.[7] Compared to conventional TPM imaging, which captures a sample size of 100 μm x 100 μm, wide-field TPM has been used to capture regions of the skin up to 2 mm x 2 mm in size, which is equivalent to 400 adjacent conventional TPM images. The advantage offered by wide-field TPM, compared to conventional TPM, is the ability to image a larger region of the skin. By imaging a larger region of the non-LTRs and of the LTRs, it would be possible to determine the uniformity of the penetration of the fluorescent probe in the non-LTRs and in the LTRs. In addition, it would be possible to observe the transition between the LTRs and the non-LTRs in a single TPM image. From the results of Chapter 5, it was demonstrated that there is significant penetration of the probe into the corneocytes and into the viable epidermis within the LTRs, while the probe is restricted to the intercellular domain of the stratum corneum in the non-LTRs. Wide-field TPM imaging would allow investigation into the boundary region between the LTRs

and the non-LTRs, furthering our understanding of the differences between these two regions of US-treated skin.

7.2.4.2 Investigation of Representative Sample Sizes Required for Imaging of the Non-LTRs and the LTRs

Previous studies with chemical enhancers demonstrated that a larger number of TPM images is required to obtain reproducible results for hydrophilic permeants (12-24 samples) in human skin as compared to hydrophobic permeants (4-6 samples).[8] A larger number of samples is required for hydrophilic permeants due to the heterogeneous distribution of the hydrophilic permeants in the skin. It would be worthwhile to evaluate the number of TPM images required to obtain reproducible results for the non-LTRs and for the LTRs of skin treated with ultrasound, both in the presence and in the absence of a chemical enhancer. Using the wide-field TPM images discussed in Section 7.2.4.1, which contain the equivalent of 400 conventional TPM images, values of E_K, E_G, and E_L can be determined from image subsets having a size of 6, 12, 18, 24, and 30 images. Several image subsets can be selected for each total number of images by randomly selecting the location of the individual TPM images in the wide-field image. The appropriate number of TPM images for the non-LTRs and for the LTRs can then be determined by evaluating the size of the standard deviation in the values of E_K, E_G, and E_L as a function of the number of samples examined.

7.2.4.3 Investigation of the Depth of Transcellular Pathway Penetration in the LTRs

In Chapter 5, a preliminary investigation of the penetration depth of the transcellular pathways observed in the LTRs of ultrasound-treated and of US/SLS-treated skin, as well

as in SLS-treated skin, for the hydrophilic permeant, SRB, and for the hydrophobic permeant, RBHE, was conducted. Additional studies should be conducted to confirm the results presented in Chapter 5. One challenge that will need to be overcome in this area is obtaining significant penetration of the fluorescent probe deep into the stratum corneum to obtain fluorescence signals that are much stronger than the background noise. Since the method for evaluating the penetration of the probe into the corneocyte domain presented in Chapter 5 depends on the normalized difference in the fluorescent signal in the intercellular domain and in the corneocyte domain, a low signal-to-noise ratio in the fluorescence data from the deeper layers of the stratum corneum can produce a false positive result. This false positive result would then suggest that transcellular pathways are present in the deeper layers of the stratum corneum, when, in effect, the penetration of the fluorescent probe is confined solely to the intercellular domain. In order to increase the signal-to-noise ratio, a higher concentration of SRB and RBHE in the coupling medium would be required to increase the fluorescence signal of the exogenous permeants. However, this increase in the fluorescent permeant concentration would need to be balanced against the signal of the skin auto-fluorescence, since too much exogenous fluorescent permeant may mask the skin auto-fluorescence signal.

7.2.5 Investigations of the Safety of LTR Formation

Previous studies have shown that low-frequency ultrasound is safe for the skin, inducing no permanent damage to the skin or to the underlying tissues.[9] However, these studies were conducted without recognizing that ultrasound-treated skin samples experience heterogeneous structural perturbation through the formation of the LTRs and of the non-

LTRs. Therefore, it is possible that the previous safety analysis may not have specifically examined the LTRs, which are the most structurally-perturbed regions of the ultrasound-treated skin, since it was previously assumed that low-frequency ultrasound uniformly perturbs the skin structure. Therefore, it is necessary to examine the safety of LTR formation to determine if low-frequency ultrasound is truly safe for the skin and for the underlying tissues. Specifically, the safety issues involved in LTR formation resulting from ultrasound exposure can be classified into: i) reversibility of the changes induced in the skin barrier properties by LTR formation, and ii) biological effects of LTR formation on the skin membrane and on the underlying tissues. Below, I discuss each issue in detail, as well as propose experiments to investigate each of them.

7.2.5.1 Reversibility of the Changes Induced in the Skin Barrier Properties by LTR Formation

Although ultrasound pretreatment enhances skin permeability for several hours, the skin permeability should eventually return to its baseline level, in both the LTRs and the non-LTRs. A detailed investigation of the recovery of structural changes in the SC, as well as of the skin barrier properties, after sonophoresis, should be conducted. Using Yorkshire pig as the *in vivo* animal model, the skin can be pre-treated using 20 kHz ultrasound over a range of intensities (0 – 30 W/cm^2). The skin samples should then be masked using the methods described in Chapter 4 and the time dependence of the transdermal flux of radiolabeled mannitol may be tracked in the LTRs and in the non-LTRs by measuring the amount of mannitol excreted in the pig urine. Over time, the amount of mannitol excreted in the urine should decrease as the ultrasound-treated skin restores its barrier properties. Skin electrical resistance measurements may also be used to quantify the

reversibility of the skin permeability changes in the LTRs and in the non-LTRs due to ultrasound application. Over time, the skin electrical resistance will increase as the ultrasound-treated skin restores its barrier properties. The electrical resistance of the skin is inversely proportional to the mobility of the ions in the skin. Because of the small size of an ion, a small structural change in the skin causes a significant change in its electrical resistance. Consequently, the electrical resistance of the skin is a very sensitive indicator of its barrier properties. Furthermore, measurements of electrical resistance are much more sensitive to structural changes in the skin than permeability measurements. Measurements of the skin permeability and of the skin electrical resistance in the LTRs and in the non-LTRs can be made separately using the protocols discussed in Chapter 4.

7.2.5.2 Biological Effects of Localized Transport Regions on the Skin

In vivo studies with the Yorkshire pig animal model can be conducted in which the effect of LTR formation in the skin is compared with untreated skin samples to determine the biological effects of LTR formation. The skin should be exposed to 20 kHz ultrasound, with SLS (1.0% w/v) and without SLS, in the presence of SRB at several sites and at different ultrasound intensities (0 – 30 W/cm^2). The skin should be perturbed by low-frequency ultrasound, using the ultrasound pre-treatment protocol outlined in Section 4.2.4, until the skin reaches the desired level of skin perturbation. The skin can then be harvested so that the LTR and the non-LTR skin samples formed under different ultrasound intensities can be compared with untreated skin samples to assess the existence of any damage induced to the skin. For the histology studies, the LTRs and the non-LTRs can be harvested separately from the same ultrasound-treated skin tissues. Damage may be assessed by erosion of the stratum corneum layer and by the necrosis of

cells in the epidermal layer, the dermal layer, and/or the underlying tissues. This investigation should determine the range of US intensities that are safe to induce LTR formation in the skin.

7.3 References

1. Schaefer H, Redelmeier TE. Skin Barrier. Basel: Karger (1996).
2. Tang H, Wang CCJ, Blankschtein D, Langer R. 2002. An investigation of the role of cavitation in low-frequency ultrasound-mediated transdermal drug transport. Pharm Res 19:1160-1169.
3. Terahara T, Mitragotri S, Langer R. 2002. Porous resins as a cavitation enhancer for low-frequency sonophoresis. J Pharm Sci 91:753-759.
4. Kushner J, Blankschtein D, Langer R. 2004. Experimental demonstration of the existence of highly permeable localized transport regions in low-frequency sonophoresis. J Pharm Sci 93:2733-2745.
5. Johnson ME, Mitragotri S, Patel A, Blankschtein D, Langer R. 1996. Synergistic effects of chemical enhancers and therapeutic ultrasound on transdermal drug delivery. J Pharm Sci 85:670-678.
6. Tezel A, Sens A, Tuchscherer J, Mitragotri S. 2002. Synergistic effect of low-frequency ultrasound and surfactants on skin permeability. J Pharm Sci 91:91-100.
7. Yu B, Kim KH, So PTC, Blankschtein D, Langer RS. 2003. Evaluation of fluorescent probe surface intensities as an indicator of transdermal permeant distributions using wide-area two-photon fluorescence microscopy. J Pharm Sci 92:2354-2365.
8. Yu B, Kim KH, So PTC, Blankschtein D, Langer RS. 2002. Topographic heterogeneity in transdermal transport revealed by high-speed two-photon microscopy: Determination of representative skin sample sizes. J Invest Dermatol 118:1085-1088.

9. Tang H, Blankschtein D, Langer R. 2002. Effects of low-frequency ultrasound on the transdermal permeation of mannitol: Comparative studies with in vivo and in vitro skin. J Pharm Sci 91:1776-1794.